

165

SATELLITE & MESOMETEOROLOGY
RESEARCH PROJECT

Department of the Geophysical Sciences
The University of Chicago

WORKBOOK
Of TORNADOES and HIGH WINDS

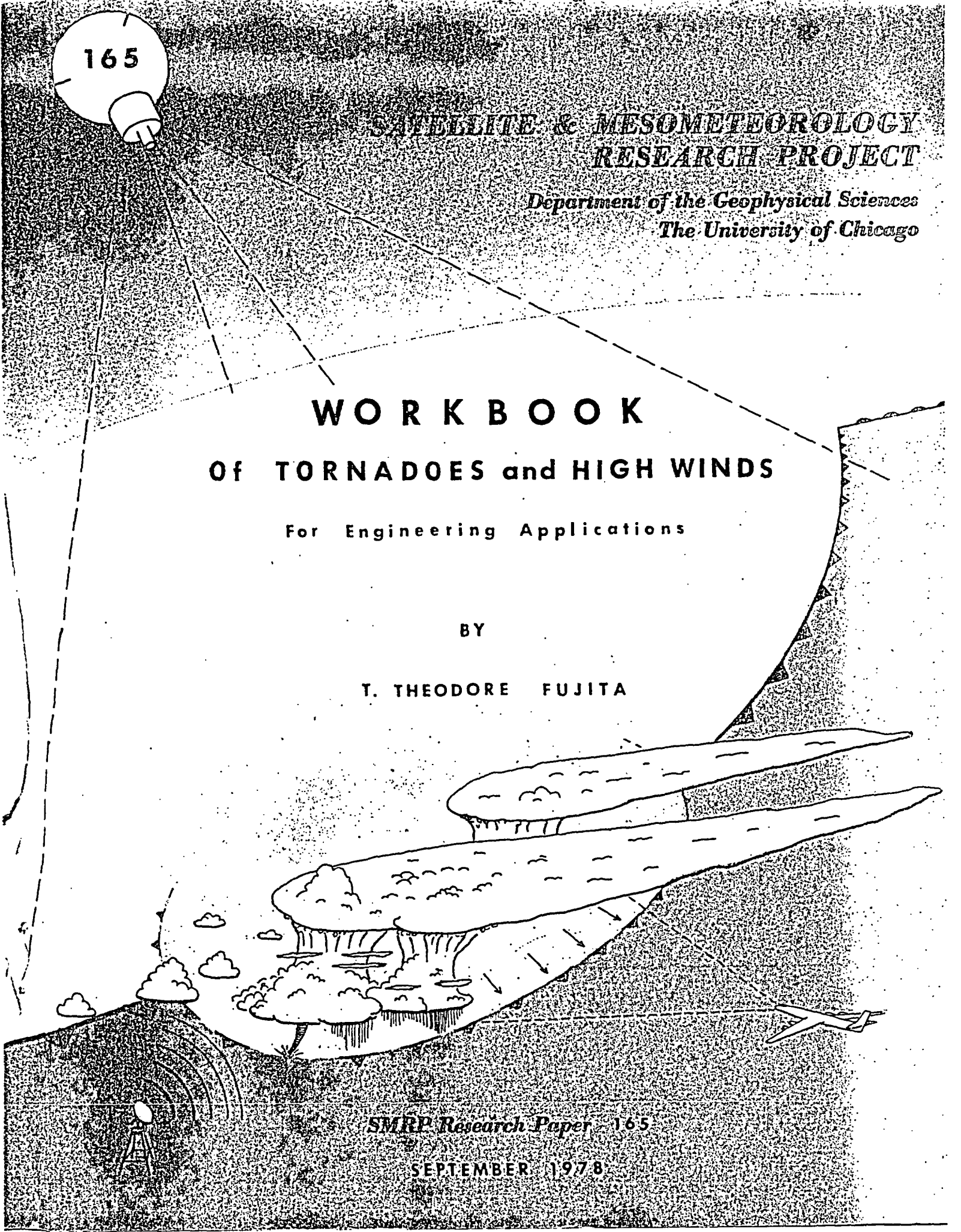
For Engineering Applications

BY

T. THEODORE FUJITA

SMRP Research Paper 165

SEPTEMBER 1978



W O R K B O O K
of
T O R N A D O E S A N D H I G H W I N D S
for
Engineering Applications

by
T. Theodore Fujita
Professor of Meteorology
The University of Chicago

September 1978

This workbook was prepared by T. Theodore Fujita under Argonne National Laboratory Contract No. 31-109-38-4500 for use in the Department of Energy, Division of Operational and Environmental Safety, Workshops on Tornadoes and High Winds. (July and September 1978 at Argonne National Laboratory)

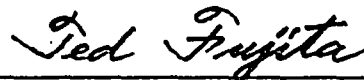
- ② Design-basis tornado (DBT-77) in Chapter 6 was finalized in the summer of 1977 under ANL Contract No. 31-109-38-3731.
 - ③ Basic concept of DBT-78 leading to the computation of new DAPPLE values was developed under NRC Contract No. AT(49-24)-0239.
-

PREFACE

At the request of Mr. W. J. McCool, DOE, two workshops on tornadoes and high winds were organized and a workbook prepared for DOE personnel. The emphasis in the workshops, held at Argonne National Laboratory, Illinois in July and September, 1978 is on the understanding of meteorological phenomena related to severe local storms in general and the tornado in particular.

The workshops cover a range of topics dealing with terminology, meteorology aspects, photogrammetric analyses, aerial surveys, statistical data base, hazard probabilities and analytical models of tornadoes that incorporate suction vortices. This workbook, prepared by the principal lecturer, outlines the current state-of-knowledge of the above subjects. The workshop and workbook are not meant to provide definitive answers to the modeling tornadoes or assessing their hazard probability, but rather to provide an introduction for use by anyone desiring to develop a basic understanding of the tornado and severe storm phenomena.

The contents of the workbook will not substitute for detailed analyses performed by the principal lecturer or others. Consequently, the conclusions presented in the workbook should not be blindly applied without achieving adequate background and understanding of the principles involved. As is the nature of scientific research, the concepts and conclusions presented in the workshop will change as new information and insight become available. With this in mind, this workbook is provided as a detailed written summary and reference book to those topics presented at the two DOE tornadoes and high winds workshops.



T. Theodore Fujita
Principal Lecturer

September 1, 1978

T A B L E O F C O N T E N T S

CHAPTER ONE	INTRODUCTION TO SEVERE LOCAL WINDSTORMS	
1.	Synoptic mapping of airflow	3
2.	Divergence and rotation	8
3.	Definition of severe local windstorms	10
4.	Annual frequencies of U.S. tornadoes	13
CHAPTER TWO	METEOROLOGICAL ASPECTS OF TORNADOES AND DOWNBURSTS	
1.	How do tornadoes form?	17
2.	How do downbursts form?	18
3.	How do tornadoes and downbursts interact?	22
4.	Specific examples	23
CHAPTER THREE	PHOTOGRAMMETRIC ANALYSES OF TORNADOES	
1.	Angular measurements and triangulation	28
2.	Distant tornado on vertical image plane	31
3.	Model tornado on vertical image plane	32
4.	Determination of tornado parameters	36
5.	Example of parameter computations	38
CHAPTER FOUR	AERIAL SURVEY FOR STORM STRUCTURE	
1.	Microburst	43
2.	Downburst	44
3.	Small tornado	47
4.	Large tornado	50
5.	Suction vortex	52
6.	Aerial survey of Grand Gulf tornado	57
CHAPTER FIVE	TORNADO STATISTICS AND DATA BASE	
1.	F-scale statistics of 1916-77 tornadoes	65
2.	Bi-monthly distribution of 1916-77 tornadoes	69
3.	3-hourly distribution of 1916-77 tornadoes	75
CHAPTER SIX	ANALYTICAL MODEL OF TORNADOES	
1.	Geometric features	83
2.	Definition of windspeeds	84
3.	Tangential velocity, V	86
4.	Radial velocity, U	88
5.	Crossing angle, α	91
6.	Vertical velocity, W	94
7.	Summary of three component velocities	96
CHAPTER SEVEN	TORNADO PARAMETERS FOR ENGINEERING	
1.	Core diameters of tornado and suction vortex	98
2.	Maximum total windspeed	100
3.	Maximum pressure drop	104
4.	Maximum rate of pressure change	106
CHAPTER EIGHT	RISK COMPUTATION BY DAPPLE METHOD	
1.	Weighted mean F scale	112
2.	Definition of damage area	115
3.	Concept of DAPPLE	117
4.	Determination of DAPPLE	119
5.	Wind field of tornado and embedded suction vortex	121
6.	Computation of isovel widths from DBT-78	126
7.	Comparison of DAPPLE values from AF-75 and DBT-78	133

CHAPTER ONE

INTRODUCTION TO SEVERE LOCAL WINDSTORMS

The original meaning of the term "synoptic", which is frequently used in meteorology, is the "simultaneous view of meteorological parameters over a large area." The area of view may be as large as the entire earth or as small as a cornfield.

A synoptic map, therefore, includes both data and analyses which describe the state of atmosphere over a large area at a given moment in time.

Since the 1920s, when Norwegian meteorologists began analyzing numerous synoptic maps, the strict definition of "simultaneous" was modified into "nearly instantaneous", because it is not feasible to complete weather observations of a number of meteorological elements simultaneously. A few minutes of time difference in data collections is regarded as "simultaneous" as long as daily synoptic maps are concerned.

In severe weather meteorology a few minutes difference in observation times can no longer be regarded as "simultaneous". During tornadoes, for instance, the variations of wind and pressure must be measured simultaneously with an accuracy of "one second" in order to obtain a synoptic view of these storms.

1. Synoptic Mapping of Airflow

Wind is a vector quantity which includes both "direction" and "speed". The wind direction is expressed by the azimuth "from which" the air is moving, while the wind speed denotes the rate of air movement at a given point and time.

As shown in Figure 1.1, a wind vector is expressed by "a shaft and barbs". The shaft extends from a station (observation point) toward the direction of wind. The numbers of barbs are proportional to the windspeed, each barb representing 10 kts.

When windspeeds are extremely high, a group of five barbs are replaced by a "flag", each representing a 50 kts windspeed (see Table 1.1).

Beaufort Force 10 (B 10) denotes approximately a 50-kt wind while a 100-kt wind corresponds to about B 16. (For Beaufort force and specifications, see Table 1.2).

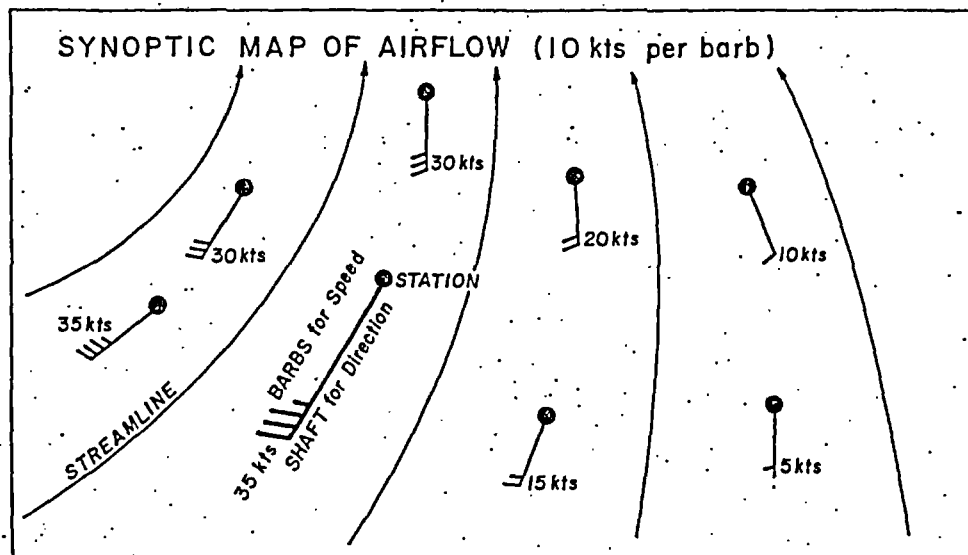


Figure 1.1 A synoptic map of airflow expressed by 10 kts per barb wind symbols.

Table 1.1 Wind barbs currently used internationally for synoptic maps (left) and those used by Fujita for mapping windstorms (right). Beaufort force and Fujita scale corresponding to these wind barbs are also shown in this table.

FOR SYNOPTIC MAPS			FOR WINDSTORM MAPS			
B force	m/sec	knots		mph	m/sec	F scale
B 3	5	10		25	11	F -
B 5	10	20		50	22	F 0
B 7	15	30		75	33	F 1
B 8	20	40		100	44	F 1
B 10	25	50		125	55	F 2
B 11	30	60		150	66	F 2
B 12	35	70		175	77	F 3
B 13	40	80		200	88	F 3
B 15	45	90		225	99	F 4
B 16	50	100		250	110	F 4
B 17	55	110		275	121	F 5
B 18	60	120		300	132	F 5

Table 1.2 Beaufort Force (1 to 17) windspeeds and damage specifications. Based on Smithsonian Meteorological Table No. 36 (1958).

Force	Wind types	Windspeeds		Specifications
		(mph)	(m/sec)	
B 0	Calm	less than 1	0.0-0.2	Smoke rises vertically
B 1	Light air	1-3	0.3-1.5	Smoke drifts
B 2	Breeze, light	4-7	2-3	Wind felt on face
B 3	Breeze, gentle	8-12	4-5	Wind extends light flags
B 4	Breeze, moderate	13-18	6-7	Raises dust and loose papers
B 5	Breeze, fresh	19-24	8-10	Crested wavelets on inland waters
B 6	Breeze, strong	25-31	11-13	Telephone wires whistle
B 7	Gale, moderate	32-38	14-16	Whole trees in motion
B 8	Gale, fresh	39-46	17-20	Breaks twigs off trees
B 9	Gale, strong	47-54	21-24	Slight structural damage occurs
B 10	Gale, whole	55-63	25-28	Seldom experienced inland
B 11	Storm	64-72	29-32	Wide-spread damage
B 12	Hurricane	73-82	33-36	-----
B 13	Hurricane	83-92	37-41	-----
B 14	Hurricane	94-103	42-45	-----
B 15	Hurricane	104-114	46-50	-----
B 16	Hurricane	115-125	51-56	-----
B 17	Hurricane	126-136	57-61	-----

Table 1.3 Fujita scale (0 to 12), windspeeds and damage specifications. Based on Fujita (1971).

Scale	Damage types	Windspeeds		Specifications
		(mph)	(m/sec)	
F 0	Light	40-72	17-32	TV antennae bent; breaks twigs off trees; mobile homes pushed over
F 1	Moderate	73-112	33-49	Mobile homes overturned; weak trees uprooted; outbuildings blown down
F 2	Considerable	113-157	50-69	Roofs off houses; light-object missiles generated; weak structures smashed
F 3	Severe	158-206	70-92	Walls torn off houses; trees in forest flattened; large missiles generated
F 4	Devastating	207-260	93-116	Well-constructed houses flattened; large missiles generated; some trees debarked
F 5	Incredible	261-318	117-142	Strong structures blown off; trees debarked by wind; high-speed missiles generated
F 6	-----	319-380	143-169	-----
F 7	-----	381-445	170-199	-----
F 8	-----	446-513	200-229	-----
F 9	-----	514-585	230-261	-----
F 10	-----	586-660	262-294	-----
F 11	-----	661-737	295-329	-----
F 12	-----	738-818	330-365	738 mph (330 m/sec) is the speed of sound at -3°C

Fujita (1971) proposed a new wind scale (F scale) designed to express speeds of damaging winds. The beginning of the F1 scale corresponds to that of B12 while that of F12 is chosen as Mach 1, the speed of sound in the free atmosphere (see Table 1.3 and Figure 1.3).

In order to avoid too many flags in expressing high windspeeds, such as 200 or 300 mph, a "25 mph per barb" system has been devised for mapping damaging winds (see Table 1.1).

A hypothetical synoptic map of a 250-mph tornado is shown in Figure 1.2. In this model tornado, a 25 m/sec (56 mph) translational velocity toward the east-northeast was used. The core area of the tornado was chosen to be circular. The wind direction at one point inside the core should be calm at a given moment. The calm spot, called the "instantaneous center of rotation", moves with the parent tornado, resulting in a sudden decrease and subsequent increase of windspeeds at a fixed point on the earth.

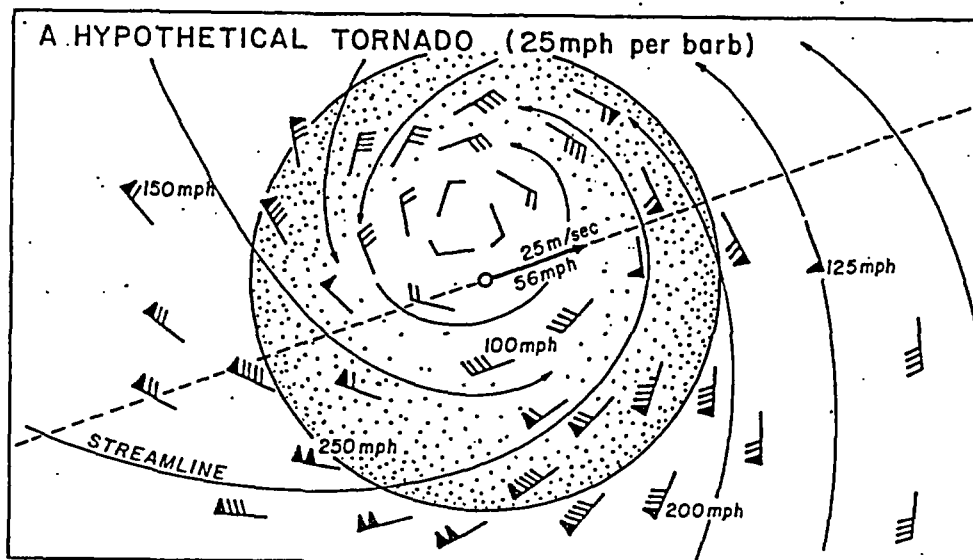


Figure 1.2 A synoptic map of a hypothetical tornado expressed by 25 mph per barb wind symbols.

Three important lines in analyzing the airflow in and around storms are

- A. **STREAMLINE** -- A line of airflow on a synoptic map showing the instantaneous air motion. The wind direction at any point must be tangent to the streamline through the point.
- B. **TRAJECTORY** -- The path of an air parcel obtained by tracing its movement on successive synoptic maps. If the flow remains unchanged (steady-state), the trajectories and streamlines are identical.
- C. **STREAK LINE** -- A line connecting air parcels which passed successively through a specific point or a source. If the source is fixed on the earth the line extends downwind from the fixed point (smoke from a chimney). If the point moves the orientation of the streak line varies according to both air flow and the movement of the source (smoke from a moving ship).

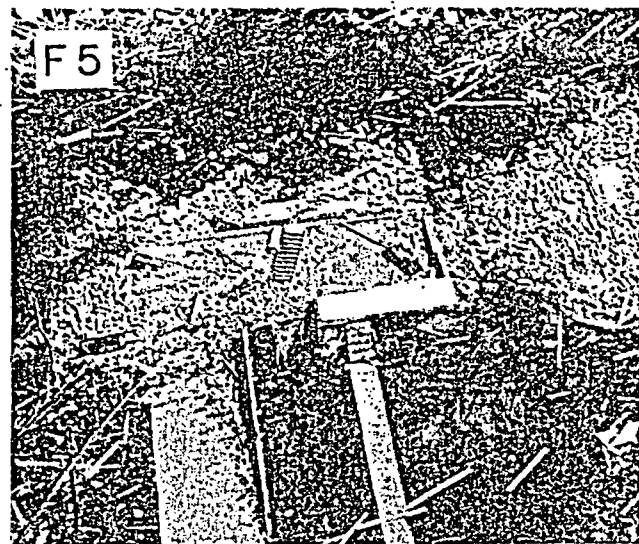
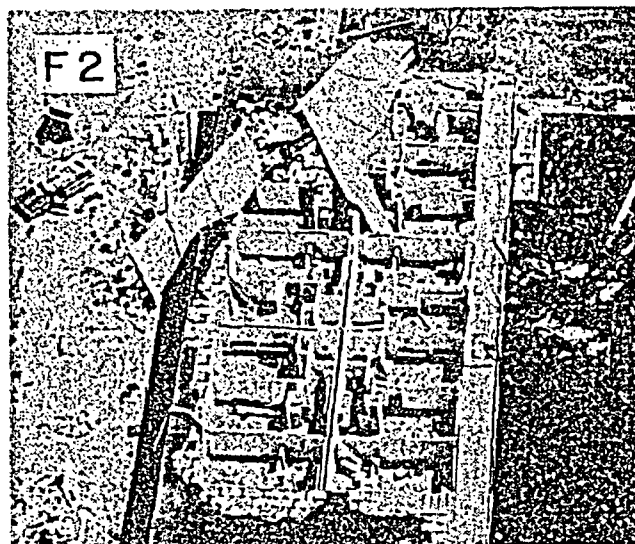
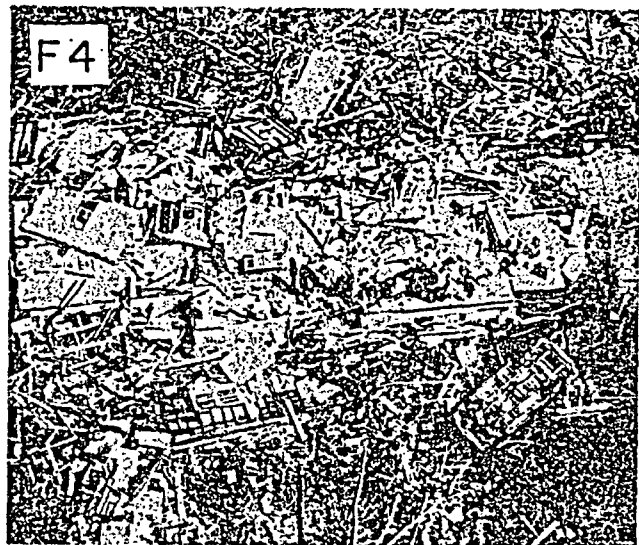
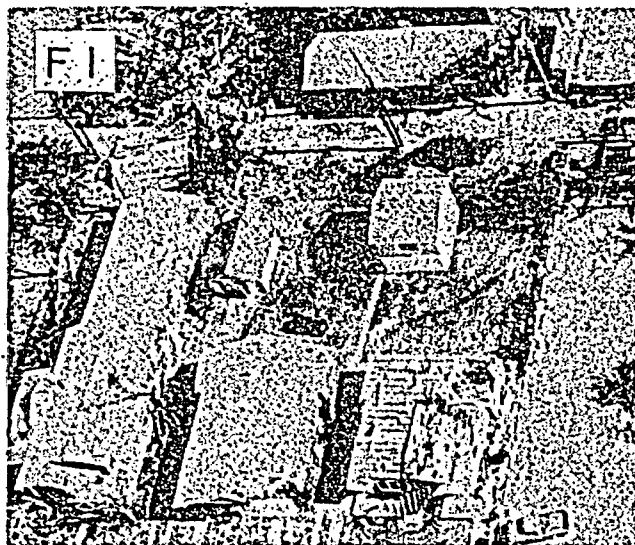
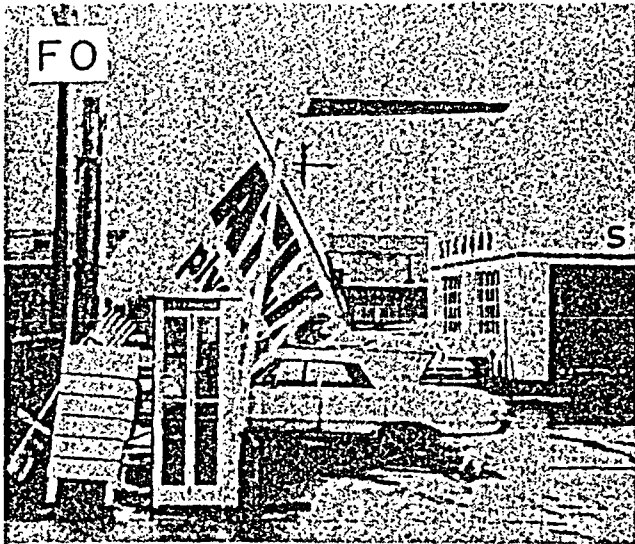


Figure 1.3 Reference pictures in determining F scale based on damage characteristics. Outbuildings or mobile homes could be blown away by F2 or F3 winds. Even well-constructed structures can be destroyed by F5 winds. For original pictures of F scale damage, refer to Fujita (1971).

2. Divergence and Rotation

Airflow in and around storms can be characterized by both direction and speed of an air parcel (a group of air molecules). Patterns of air flow analyzed on successive synoptic maps are useful in determining streamlines, trajectories, and streak lines induced by storms.

In addition to the analyses of these vector quantities, we have to know their derivatives both in time and space.

- A. TRANSLATION -- The time rate of change of the center of gravity of an air parcel.
- B. DIVERGENCE -- The time variation of the area of an air parcel. The area may increase with time (divergence) or decrease with time (convergence). If the air flow on the surface is divergent, the air inside the parcel must sink to fill up the space caused by the increased area. If the air flow is convergent, there must be a rising motion inside the parcel.
- C. ROTATION -- The degree of rotation of an air parcel, positive counter-clockwise and negative clockwise. The rotation of the earth is positive in the northern hemisphere and negative in the southern hemisphere.
- D. DEFORMATION -- The rate of stretch of an air parcel in one direction and shrinking in the other direction. A deformation may occur with or without divergence and/or rotation.

For simple mathematical expressions of above four derived quantities, see Figure 1.4.

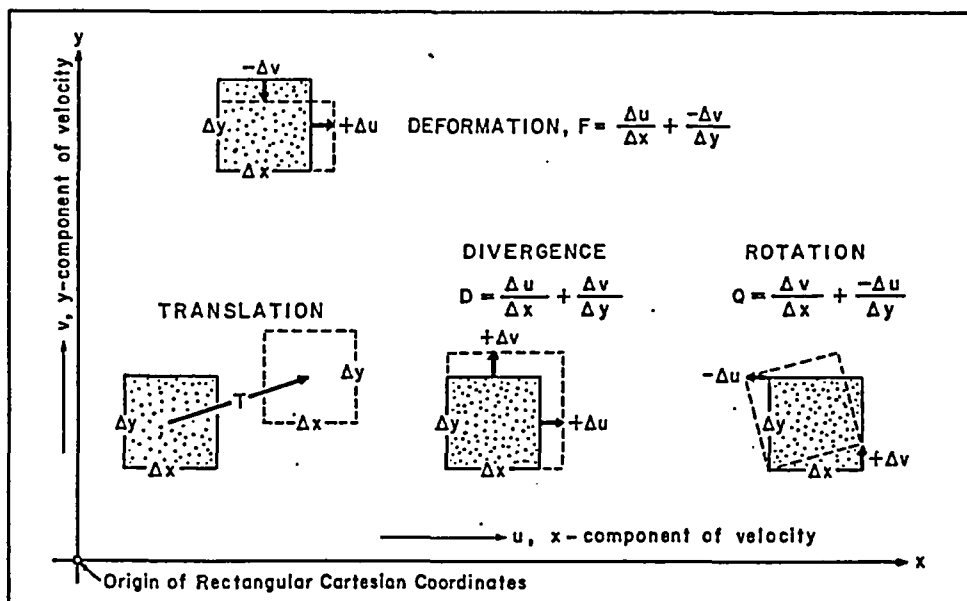


Figure 1.4 Mathematical definitions of translation, divergence, rotation, and deformation. A small air parcel may be characterized by a combination of these quantities.

"Outflow and inflow" are used frequently in describing the state of a local air flow. The total outflow is defined by a line integral,

$$B = \oint U ds$$

where U denotes the flow velocity perpendicular to the line element, ds . The integration should be performed along a closed line around an area, A . The mean divergence averaged over the entire area can be computed by

$$\bar{D} = \frac{B}{A},$$

the unit of which is $(\text{m}/\text{sec}) \times (\text{m}) \div (\text{m}^2) = \text{sec}^{-1}$.

"Rotation or vorticity" is a measure of local rotation of an air flow. The (total) circulation is defined by a line integral,

$$\Gamma = \oint V ds$$

where V denotes the flow velocity tangent to the line element, ds . The integration should be performed along a closed line around an area, A . The mean vorticity averaged over the entire area can be computed by

$$\bar{Q} = \frac{\Gamma}{A},$$

the unit of which is $(\text{m}/\text{sec}) \times (\text{m}) \div (\text{m}^2) = \text{sec}^{-1}$.

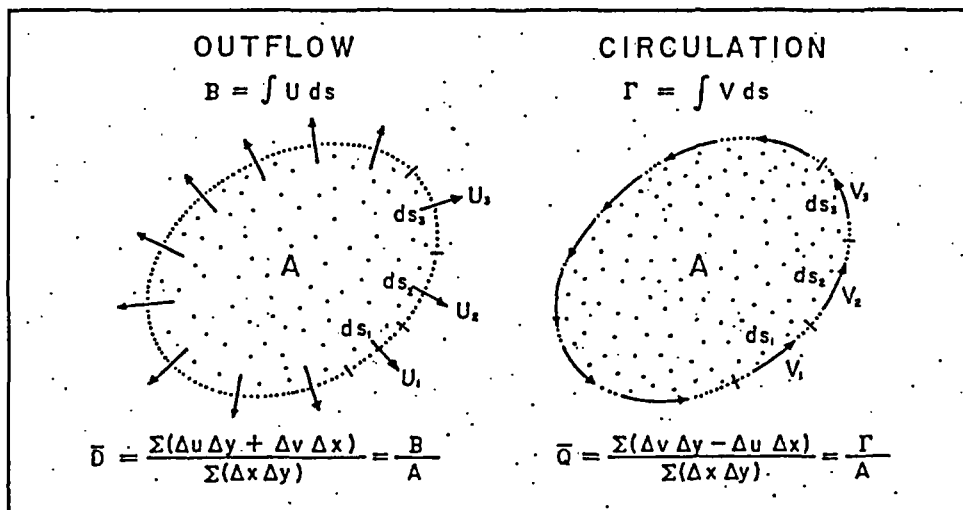


Figure 1.5 Definitions of outflow and circulation in relation to mean divergence and mean vorticity.

3. Definition of Severe Local Windstorms

Severe local windstorms are characterized by extreme values of divergence and/or vorticity. A simple breakdown of these windstorms are given in Table 1.4. Their definitions are

Table 1.4 Severe local windstorms characterized predominantly by either divergent or rotational flow field. * Downslope winds are usually non-divergent and irrotational.

Divergent Windstorms	Rotational Windstorms
Downbursts	Tornadoes
Gust fronts	Waterspouts
* Downslope winds	Dust devils

- A. **TORNADO** -- A violently rotating column of air, pendant from the base of a convective cloud, and often observable as funnel cloud attached to the cloud base. A tornado must be accompanied by damaging winds (F0 or stronger) at structure levels. If not, the windstorm is classified as "funnel aloft".

About 90% of tornadoes are spawned by thunderstorms. The ones formed by hook-echo thunderstorms are usually strong and long-lived. 10% of tornadoes, mostly weak and short-lived, form beneath towering cumuli in their rapidly growing stages.

The length and diameter of the funnel cloud inside a tornado depends upon the maximum windspeed as well as the moisture drawn into the storm. Over dry land a tornado may not be characterized by a funnel cloud. On the other hand, even a weak tornado on wet ground could be accompanied by a rope-shaped funnel reaching the surface.

58% of tornadoes are F1 (112 mph) or weaker, 97% are F3 (206 mph) or weaker and only 3% are rated as F4 (207-260 mph). 127 tornadoes out of 24,148 during the 1916-77 period were rated as F5. The occurrence frequency was 0.07%.

- B. **WATERSPOUT** -- A fast-rotating column of air over water. The formative stage of a waterspout is a dark spot above the water surface seen from the air. A funnel cloud pendant from a convective cloud is often observed from the ground. A mature waterspout induces a spray vortex, leaving a wake of foam along its path.

Waterspouts commonly form over warm tropical and subtropical waters. When a waterspout moves inland it must be identified, by definition, as a tornado. Likewise, a tornado is identified as a waterspout during its passage over a large body of water.

- C. DUST DEVIL -- A rotating column of air which forms over dry ground heated by strong solar radiation. The direction of rotation is not unique, affected by the environmental flow field during the formation stage.

Most dust devils are F0 (72 mph) or weaker. Occasionally F1 (73-112 mph) dust devils damage outbuildings or garages.

The central region of a dust devil is characterized by a descending motion and relatively clear air.

- D. SUBVORTEX -- A spinning column of air embedded inside tornado, waterspout, and dust devil. A large windstorm may be accompanied by several subvortices simultaneously. The travel of these subvortices is governed by the airflow in and around the parent storm.

Strong subvortices in tornadoes often induce vertical acceleration of the air several meters above the surface estimated to be a few tenths of g , the gravitational acceleration. These strong subvortices are called "suction vortices". The spinning rate of suction vortices is estimated at 50 to 100 mph while the vortex diameter rarely exceeds 100 ft.

A condensation funnel is often visible inside a strong suction vortex. The rate of pressure change due to suction vortices is often one order of magnitude larger than that of parent tornado.

- E. DOWN-SLOPE WIND -- A hot (warm), dry downslope wind descending from its source region at high elevations. Strong winds along the east slope of the Rockies often reach F1 (73-112 mph) at Boulder, Colorado.

Santa Ana wind blows generally from the northeast or east in the winter months. The wind originates over the southwest desert, reaching its peak intensity as it blows through mountain gaps.

Downslope wind from interior Antarctica induces strong wind rushing out from the continent. The winds through glacier gaps are often so strong that snow devils move out into the field of sea ice.

- F. GUST FRONT -- A line of gusty wind moving out from a squall line or an area of severe thunderstorms. A gust front extends 10s of miles parallel to the line of thunderstorms.

At the leading edge of a gust front, wind direction shifts abruptly from toward the storm (inflow) to away from the storm (outflow).

The gustiness factor, the ratio of the total range of windspeed between gusts and lulls divided by the mean windspeed, is very large in gust front, often reaching 0.5 to 0.7. Peak gust speeds are usually less than F2 (113 mph).

About 75% of waterspouts form beneath towering cumuli while 25% are spawned by cumulonimbus clouds.

90% of waterspouts are F1 (112 mph) or weaker; F4 (207 mph) or stronger waterspouts are rare and exceptional.

- G. DOWNBURST -- A strong downward current of air which induces an outward burst of damaging wind on or near the ground. Practically all downbursts occur beneath cumulonimbus clouds during their precipitation stages.

Downburst winds are highly divergent, covering an area up to 30 miles long and 10 miles wide. The peak windspeed of downbursts is less than mid-F3 (180 mph).

Due to a rapidly sinking motion, the descending air successively hits the surface to burst out. As a result, the gustiness factor of downbursting winds is only 0.1 to 0.3.

Most downbursts are highly divergent but irrotational. However, some downbursts are rotational with a curved airflow identified as the "twisting downburst". Small tornadoes frequently form on the edge of a twisting downburst.

- H. MICROBURST -- A small downburst with its horizontal scale of less than the square root of 10 miles (3.16 miles = 5.1 km) is called microburst. The mature life of microbursts is only a few to 10 minutes, making their detection and warning extremely difficult.

The maximum windspeed of microbursts is less than mid-F1 (90 mph). Damage caused by microbursts is limited mostly to outbuildings and mobile homes.

An aircraft attempting to fly through a microburst near the ground could encounter serious difficulties. 112 persons were killed at John F. Kennedy Airport, New York City, when Eastern 66 crashed in a microburst. Since then one to two aircraft accidents related to microbursts have been suspected.

Frequencies of the above defined severe local windstorms by parent-cloud types and by F-scale windspeeds are given in Tables 1.5 and 1.6, respectively.

Table 1.5 Frequencies of severe local windstorms by parent-cloud types. Subject to revision in future years.

Parent clouds	Down- bursts	Gust fronts	Downslope winds	Tornadoes	Water- spouts	Dust devils
Hook-echo Tsm	30 %	10 %	nil	40 %	5 %	nil
Bow-echo Tsm	40 %	20 %	nil	20 %	rare	nil
Other Tsm	30 %	70 %	nil	30 %	20 %	nil
Towering Cu	nil	nil	nil	10 %	75 %	nil
No cloud	nil	nil	100 %	nil	nil	100 %

Table 1.6 Frequencies of severe local windstorms by F-scale windspeeds. Subject to revision in future years.

Scale	Down-bursts	Gust fronts	Downslope winds	Tornadoes	Water-spouts	Dust devils
F 5	nil	nil	nil	rare	nil	nil
F 4	nil	nil	nil	3 %	rare	nil
F 3	2 %	nil	nil	10 %	2 %	nil
F 2	19 %	rare	rare	29 %	8 %	nil
F 1	32 %	10 %	25 %	35 %	20 %	rare
F 0	47 %	90 %	75 %	23 %	70 %	100 %

4. Annual Frequencies of U. S. Tornadoes

Since 1916 when the official collection of U. S. tornado data began, 24,148 tornadoes had been reported by the end of 1977. The average frequency during these 62 years was 389 tornadoes per year.

Only 78 tornadoes per year were reported during the 1910s, the first decade of the tornado data collection. The annual frequencies increased gradually up to the 1940s when a 165-per year frequency was reported. In the 1950s a significant jump in frequency occurred; from 202 in 1950 to 605 in 1959. This increasing trend has

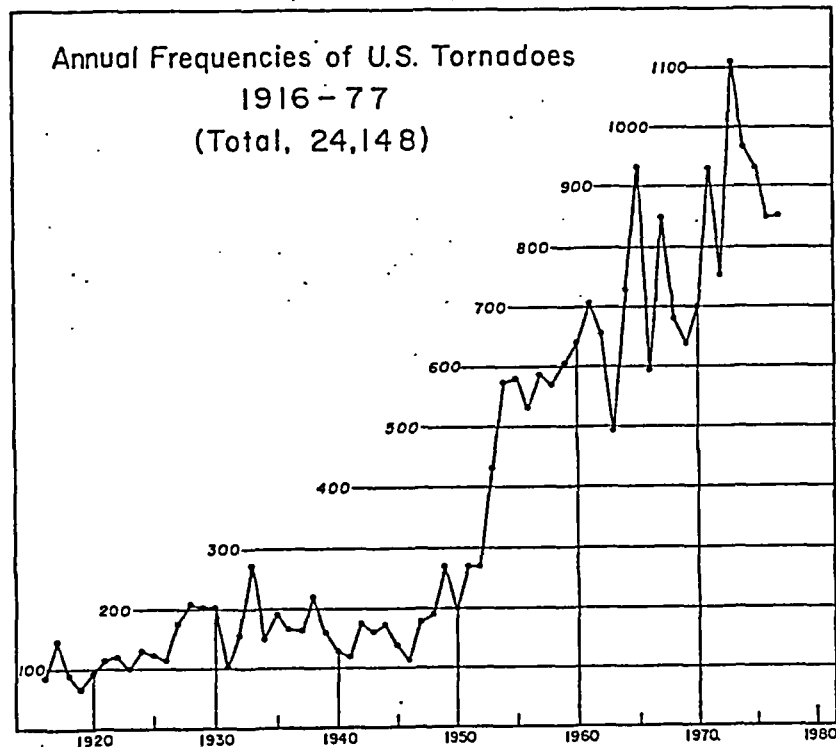


Figure 1.6 Annual frequencies of U.S. tornadoes during the 62-year period, 1916-77.

Table 1.7 Annual frequencies of U.S. tornadoes by F-scale.
Based on 24,148 tornadoes (1916-77) in the DAPPLE Tornado Tape.

Scale	1910	1911	1912	1913	1914	1915	1916	1917	1918	1919	Total	in %
F 5	--	--	--	--	--	--	0	10	2	1	13	3 %
F 4	--	--	--	--	--	--	4	11	3	6	24	6 %
F 3	--	--	--	--	--	--	9	31	17	12	69	18 %
F 2	--	--	--	--	--	--	29	55	42	25	151	39 %
F 1	--	--	--	--	--	--	28	33	24	17	102	26 %
F 0	--	--	--	--	--	--	16	7	2	7	32	8 %
Scale	1920	1921	1922	1923	1924	1925	1926	1927	1928	1929	Total	in %
F 5	8	4	0	1	1	2	0	7	0	5	28	2 %
F 4	6	4	3	6	9	5	3	5	6	7	54	4 %
F 3	17	19	28	27	39	23	27	42	47	41	310	22 %
F 2	34	52	57	34	57	63	50	79	83	81	590	42 %
F 1	20	31	27	28	21	29	30	33	61	56	336	24 %
F 0	8	5	7	4	4	3	6	10	12	14	73	5 %
Scale	1930	1931	1932	1933	1934	1935	1936	1937	1938	1939	Total	in %
F 5	1	1	0	5	1	0	3	0	5	2	18	1 %
F 4	12	1	13	10	10	4	14	3	10	7	84	5 %
F 3	33	14	11	37	17	33	27	22	35	24	253	14 %
F 2	105	46	58	109	62	71	54	81	80	57	723	40 %
F 1	35	26	41	62	33	62	39	31	66	46	441	25 %
F 0	19	15	33	50	26	26	29	27	23	25	273	15 %
Scale	1940	1941	1942	1943	1944	1945	1946	1947	1948	1949	Total	in %
F 5	1	1	2	2	3	1	1	4	4	4	23	1 %
F 4	7	5	18	13	13	15	11	12	21	19	134	8 %
F 3	19	14	38	29	35	31	18	35	49	55	323	20 %
F 2	58	53	67	74	68	58	45	79	76	96	674	41 %
F 1	27	25	26	28	34	25	25	34	32	64	320	19 %
F 0	17	23	24	16	19	8	13	13	10	31	174	11 %
Scale	1950	1951	1952	1953	1954	1955	1956	1957	1958	1959	Total	in %
F 5	0	0	0	3	0	1	1	4	0	1	10	0 %
F 4	6	4	24	11	8	3	9	22	2	11	100	2 %
F 3	32	27	54	63	68	57	52	97	47	57	554	11 %
F 2	60	73	94	137	184	159	157	237	112	159	1372	28 %
F 1	82	116	74	142	202	231	186	296	246	238	1813	37 %
F 0	22	50	24	76	112	128	127	230	162	139	1070	22 %
Scale	1960	1961	1962	1963	1964	1965	1966	1967	1968	1969	Total	in %
F 5	0	2	0	1	2	5	2	2	3	1	18	0 %
F 4	17	13	12	13	13	25	6	18	15	14	146	2 %
F 3	63	94	41	58	50	77	41	68	62	56	610	9 %
F 2	172	193	146	155	164	207	148	229	190	187	1791	26 %
F 1	264	235	231	161	289	333	206	284	219	173	2395	35 %
F 0	123	170	226	106	211	286	190	246	192	207	1957	28 %
Scale	1970	1971	1972	1973	1974	1975	1976	1977	Total	in %		
F 5	2	2	0	1	7	1	3	1	17	0 %		
F 4	10	20	12	23	30	10	13	10	128	2 %		
F 3	70	73	46	80	102	47	56	51	525	7 %		
F 2	214	253	180	286	204	197	179	171	1684	24 %		
F 1	226	389	344	501	382	370	353	362	2927	41 %		
F 0	177	193	171	219	241	307	245	256	1809	26 %		

Table 1.8 Frequencies of tornadoes in each decade since 1916.
Based on the DAPPLE Tornado Tape.

Scale	1910s (5 yr)	1920s (10 yr)	1930s (10 yr)	1940s (10 yr)	1950s (10 yr)	1960s (10 yr)	1970s (7 yr)	1916-77 (62 yr)
F 5	13	28	18	23	10	18	17	127
F 4	24	54	84	134	100	146	128	670
F 3	69	310	253	323	554	610	525	2644
F 2	151	590	723	674	1372	1791	1684	6985
F 1	102	336	441	320	1813	2395	2927	8334
F 0	32	73	273	174	1070	1957	1809	5388
Total	391	1391	1792	1648	4919	6917	7090	24148

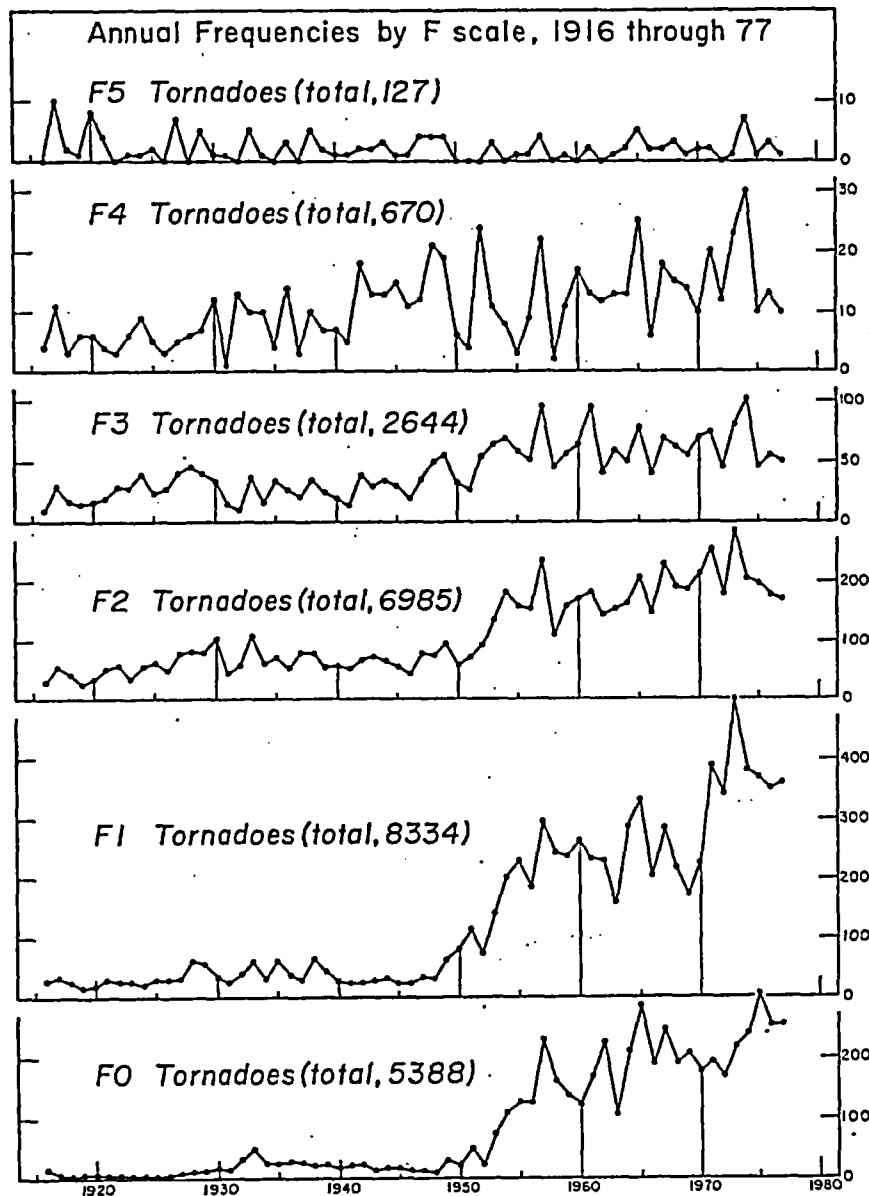


Figure 1.7 Breakdown of the annual frequencies of U.S. tornadoes by F scale. Note that weak tornadoes increased significantly since 1950s.

Table 1.9 Percent frequencies of tornadoes in each decade since 1916. Based on the DAPPLE Tornado Tape.

Scale	1910s (5 yr)	1920s (10 yr)	1930s (10 yr)	1940s (10 yr)	1950s (10 yr)	1960s (10 yr)	1970s (7 yr)	1916-77 (62 yr)
F 5	3.3	2.0	1.0	1.4	0.2	0.2	0.2	0.5
F 4	6	4	5	8	2	2	2	2.8
F 3	18	22	14	20	11	9	7	10.9
F 2	39	42	40	41	28	26	24	28.9
F 1	26	24	25	19	37	35	41	34.5
F 0	8	5	15	11	22	28	26	22.8

continued since then, and in 1973, 1110 tornadoes--the highest frequency in U. S. history--were reported (see Tables 1.7; 1.8 and Figure 1.6).

Are U. S. tornadoes increasing? The answer to this question is, "Yes, they are, as far as the reported numbers are concerned." On the other hand, there is no reason to believe that "true activities" of tornadoes increased during the past 62 years. The increase in the reported frequencies is a result of the improved data collection efficiency through public awareness, the communications system, the compiling method, etc.

The F-scale breakdown of tornadoes in Table 1.7 and Figure 1.7 reveals a tremendous increase in the F0 and F1 tornadoes while the stronger tornadoes, such as F2, F3, and F4, increased less significantly. F5 tornadoes, on the contrary, have decreased since 1916, suggesting that reporters over-emphasized and exaggerated tornado phenomena. Table 1.9 shows that 3.3% of tornadoes per year in the 1910s were rated as F5 while only 0.2% were F5 in the 1970s.

CHAPTER TWO

METEOROLOGICAL ASPECTS OF TORNADOES AND DOWNBURSTS

Of the variety of severe local windstorms, both tornadoes and downbursts are the most damaging to various structures on the surface. Since these storms have been defined in Chapter 1, their characteristics will be discussed further.

1. How do Tornadoes form?

Though this is a simple question, it is difficult to answer. First of all, not all tornadoes form under identical circumstances and environment. Some are small and short-lived while others are large and last for several hours.

Table 1.5 in Chapter 1 shows that 40% of all tornadoes are spawned by hook-echo thunderstorms; 20% by bow-echo thunderstorms; 30% by other thunderstorms; and 10% by towering cumuli. A breakdown of these parent clouds in relation to tornado formations, is presented in Figure 2.1.

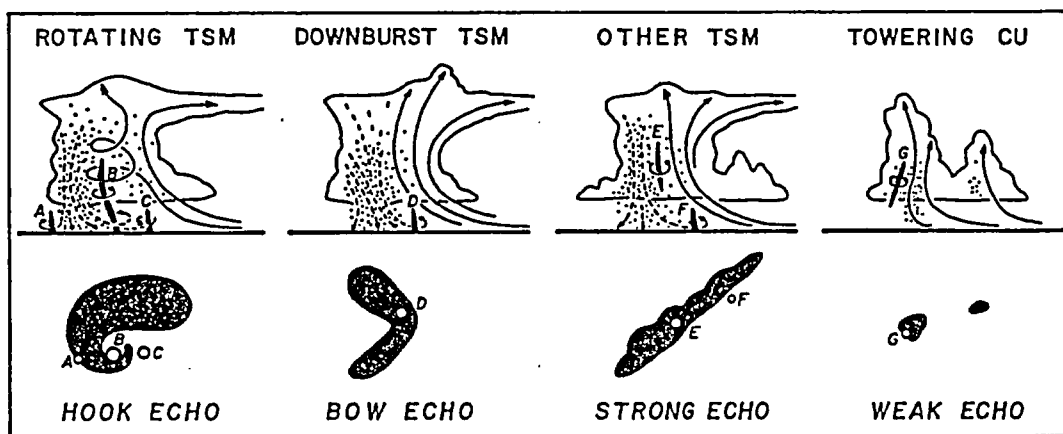


Figure 2.1 Four types of parent clouds which spawn tornadoes. Refer to Table 1.5.

HOOK ECHO, somewhat like a giant fishhook in the sky, appears on a radarscope when the radar beam scans through the relatively low elevation of a rotating thunderstorm.

A radar echo appears when the microwave emitted by a radar antenna hits the raindrops which reflect back the microwave toward the same antenna. Thus, the appearance of a radar echo on the scope reveals the presence of raindrops in the direction and at the range of the echo relative to the radar.

Existence of a hook echo implies that raindrops deep inside the storm cloud are influenced by the swirling motion of the incloud air. A rotating thunderstorm is likely to spawn tornadoes at various locations inside the cloud. These locations as shown in Figure 2.1 are

- A, where the downdraft air makes an anticyclonic turn. An anticyclonic tornado may develop at this location.
- B, where the major downdraft from the hook echo region turns cyclonically back toward the left. An intense cyclonic tornado may develop.
- C, near the advancing edge of a hook where a shear line forms between inflow and outflow winds.

BOW ECHO forms when a portion of a thunderstorm translates faster than other parts of the storm. The fast-moving cell often generates a series of downbursts near its pointed end, with its shape like that of a bow.

Tornadoes, mostly weak and short-lived ones, form near the ground on the left side of the downburst outflow (see location D in Figure 2.1).

STRONG ECHOES are characterized by strong up- and downdrafts. The cloud spinning motion at location E in Figure 2.1 may extend downward, inducing damaging winds near the surface.

A tornado, similar to C and D in Figure 2.1, may form at F which is located near the leading edge of the outflow from strong thunderstorm regions.

TOWERING CUMULI are not always characterized by significant precipitation. They are often accompanied by strong updrafts which could induce an incloud vortex at location G in Figure 2.1. Such an incloud vortex may extend down to the ground to become a weak tornado.

2. How do Downbursts form?

Downbursts are a specific pattern of thunderstorm-induced winds which were defined by the author in 1975. Due to their short research history, the phenomenon itself is not understood very well.

One explanation offered by the author is described in Figure 2.2. During the updraft stage, air parcels rise inside the cloud, maintaining a temperature (virtual temperature) several degrees warmer than that of their environment. The buoyancy force

$$B = g \frac{T' - T}{T}$$

where T denotes the temperature of the environment; T' , that of a rising parcel; and g the gravitational acceleration.

A positive buoyancy will act upon the rising parcel until reaching the crossover height where $T' - T$ becomes zero. Above the crossover height, the negative buoyancy acts against the rising parcel by virtue of its inertia. After forming an overshooting dome atop the storm's anvil cloud, the rising motion comes to an end.

Toward the end of the overshooting period the rising parcel stores a large potential energy against the environmental air temperature. When the root of the updraft beneath the overshooting top is weakened or cut off, the overshooting top sinks by converting the potential energy into kinetic energy of the downward flow at the cloud top.

The impact of this downward motion upon underlying, incloud precipitation initiates a strong downward current which extends throughout the entire depth of the cloud (see Figure 2.2).

A strong downdraft, thus developed inside a thunderstorm, hits the surface inducing an outburst of damaging winds.

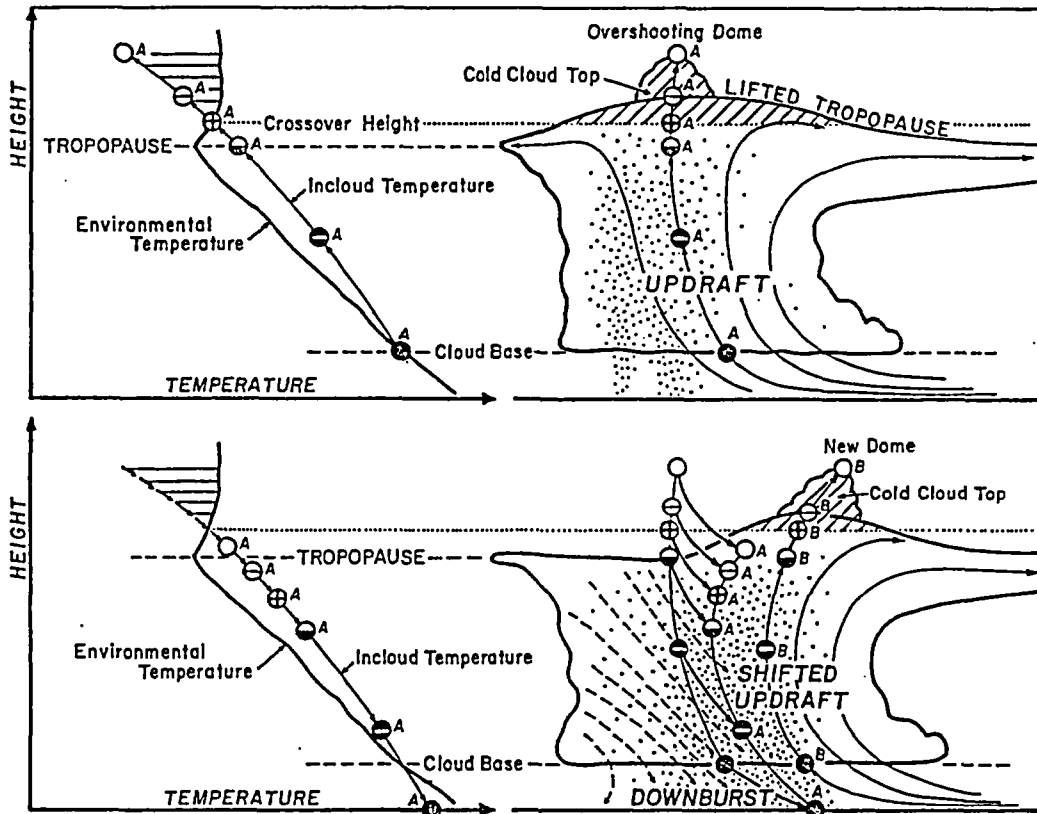


Figure 2.2 Fujita model of downburst thunderstorm. In this model, it is assumed that the potential energy of the cold air, lifted above the crossover height, descends violently when the potential energy is converted into the kinetic energy of the descending air. One of the Black Sunday storms on June 25, 1978 showed an extensive descending motion throughout the entire depth of the cloud.

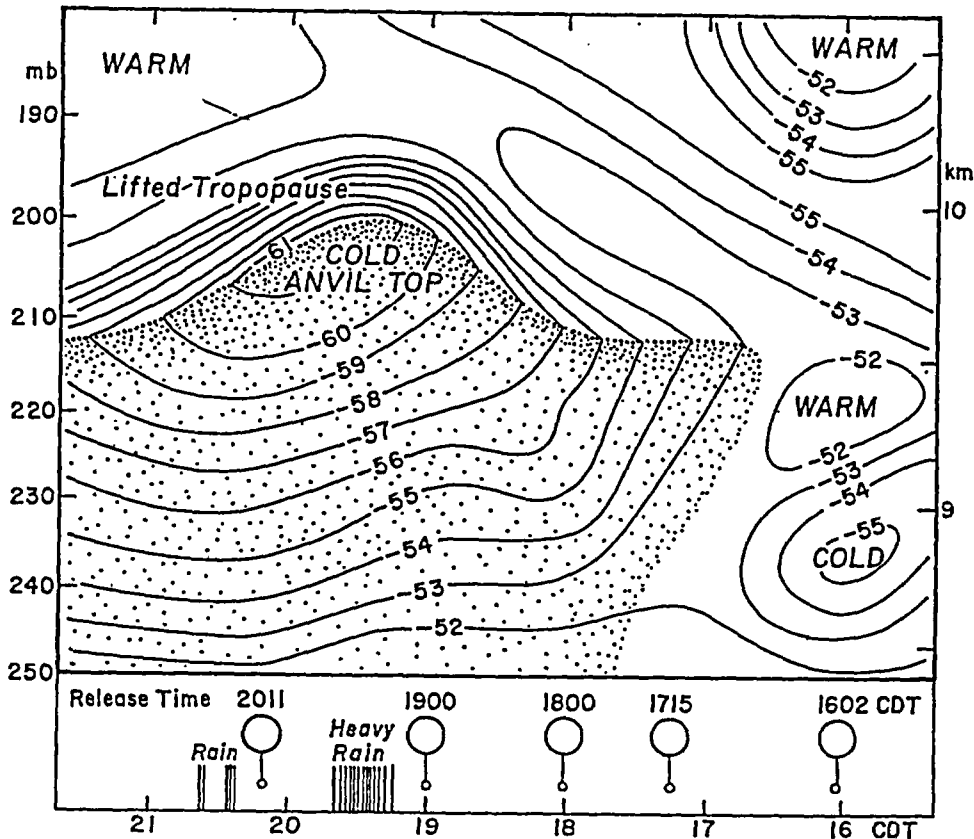


Figure 2.3 Cold anvil top revealed by serial ascents of rawinsondes from Yorkville, Illinois on May 12, 1978. From operation summary of Project NIMROD.

On June 17, 1978 a Doppler radar of Project NIMROD at Yorkville, Illinois confirmed such a complicated cloud-top activity in relation to a downburst on the surface.

The Doppler beam, pointing vertically at Yorkville, measured a 17 m/sec (38 mph) upward velocity at 16.2 km. 19 seconds later, at 05h02m34s, the cloud top sank 1.2 km to 15.0 km. Three minutes later, at 05h05m06sec, the top sank further to 14.0 km with 5 m/sec (11 mph) sinking motion at the cloud top and an 18 m/sec (40 mph) downward motion at the 12 km level in the cloud.

At 0507 CDT, a 14 m/sec (31 mph) peak wind from the north occurred at the Yorkville radar site. Horizontal scanning of the Doppler radar also depicted the velocity signature of this downburst from its birth to dissipation.

The cooling of the anvil top through the successive pumping action of the downdrafts has been measured by a serial ascent of radiosonde balloons (see Figure 2.3). This example shows that the tropopause is lifted during a two-hour period of convective activities. Lifted, cold tropopause is a characteristic feature of this type of convective modification.

Downburst and gust front are different in various aspects of their wind structure. A downburst usually lasts up to about 30 minutes and a microburst dies out in less than 15 minutes. A gust front can often be identified for 30 minutes to over 120 minutes.

Wind direction changes 60 to 180 degrees in a down- or microburst while the directional change is only less than 60 degrees in a gust front. The gustiness factor in downbursts is about one-third of that in a gust front characterized by extremely gusty winds. Namely, the flow inside a downburst is relatively smooth.

A microburst which occurred near O'Hare Airport was depicted by one of the surface stations of the Project NIMROD network (see Figure 2.4). The microburst wind began shortly after 2220 CDT, reached its maximum (41.4 mph) 2 to 3 minutes later, and ended at 2226 CDT. The whole event was over in only 6 minutes.

A gust front arrived at the same station a few minutes later. The gust front, like most others, was accompanied by gusty wind.

Microburst is an aviation hazard because the wind direction inside the downburst changes within a short distance of several kilometers. During both the takeoff and landing phases of an aircraft, a microburst could reduce the airspeed such that the aircraft encounters a dangerous sinking motion. A list of aircraft accidents caused by microburst penetrations is presented in Table 2.1.

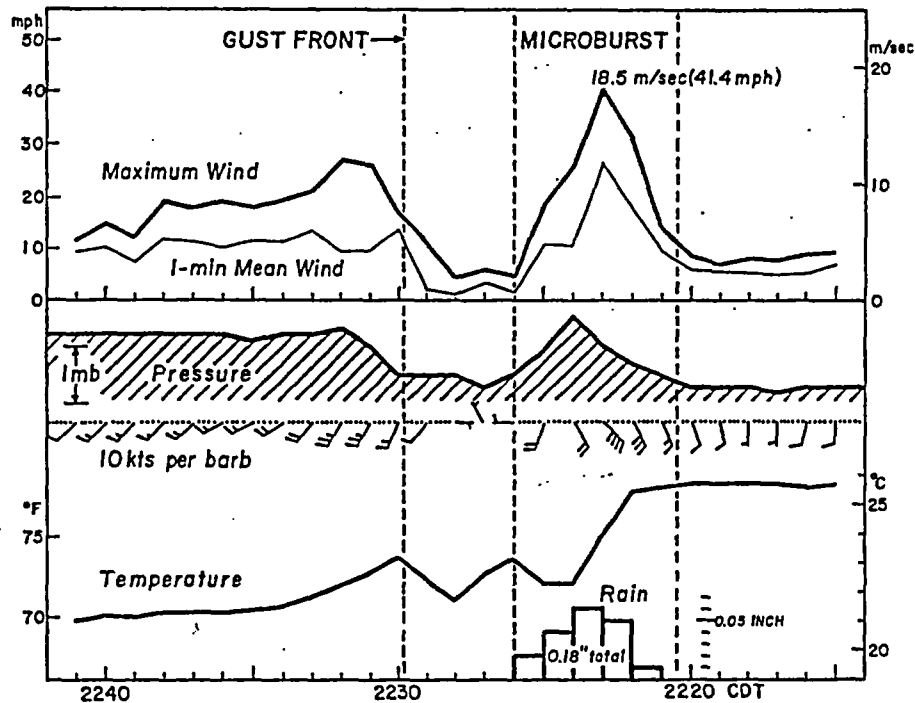


Figure 2.4 A microburst and a gust front recorded by a PAM station near O'Hare airport on May 29, 1978. From operation summary of Project NIMROD.

Table 2.1 List of five accident cases attributed to strong wind shear inside microbursts, 2.8 to 5.2 km (1.8 to 3.2 miles) in horizontal dimensions. The 1956 accident occurred at Kano, Nigeria. He, Ta, and Do in wind shear denote headwind, tailwind, and downward wind, respectively.

Years	1975	1975	1976	1977	1956
Dates	June 24	August 7	June 23	June 3	June 24
Local time	3:05 pm	4:11 pm	4:12 pm	12:59 pm	5:23 pm
Airport	JFK	Denver	Philadelphia	Tucson	Kano
Airlines	EA 66	CO 426	AL 121	CO 63	BOAC 252/773
Flt. Phase	Landing	Takeoff	Landing	Takeoff	Takeoff
Fatalities	112	zero	zero	zero	32
Injuries	12	15	106	zero	7
Microburst dimensions	4.1 km 2.5 mi	5.0 km 3.1 mi	2.8 km 1.8 mi	3.1 km 1.9 mi	3.5 km 2.2 mi
Wind shear	16 kts He to 13 Do	10 kts He to 50 Ta	65 kts He to zero	30 kts He to 30 Ta	20 kts He to strong Ta

3. How do tornadoes and downbursts interact?

Recent investigation by the author and his collaborators revealed that downbursts and/or microbursts near a tornado influence both the tornado's path and internal structure.

A downburst to the left of a traveling tornado pushes the tornado toward the right, resulting in a "right-turn tornado". Likewise, a "left-turn tornado" occurs when a downburst is to the right of a tornado. Even a "U-turn tornado" is seen when one or more downbursts deviate a tornado course significantly (see Figure 2.5).

The axisymmetric structure of a tornado is destroyed when a nearby downburst or microburst intensifies the inflow air from a specific direction. Quite often, so-called "suction vortices" form where the convergence into the tornado core is the largest (see Figure 2.6).

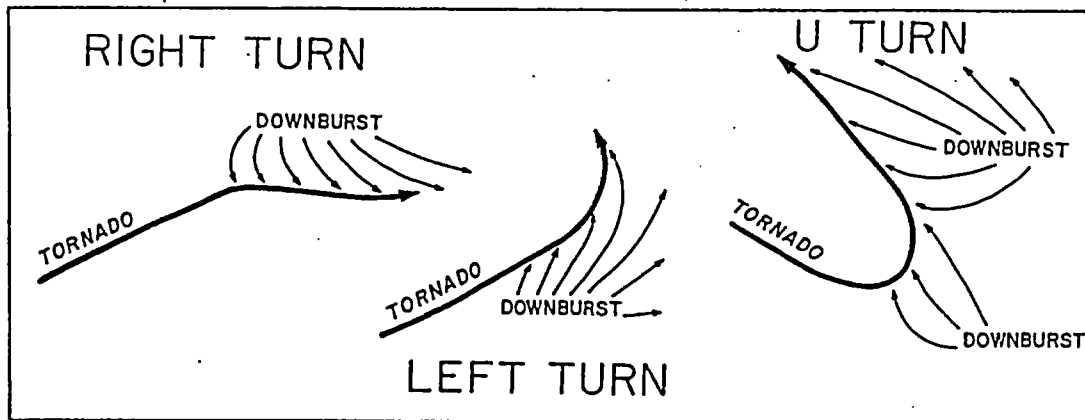


Figure 2.5 Deviation (turning) of the course of tornado due to nearby downburst. Detailed aerial surveys revealed repeatedly this type of interaction between tornado and downburst.

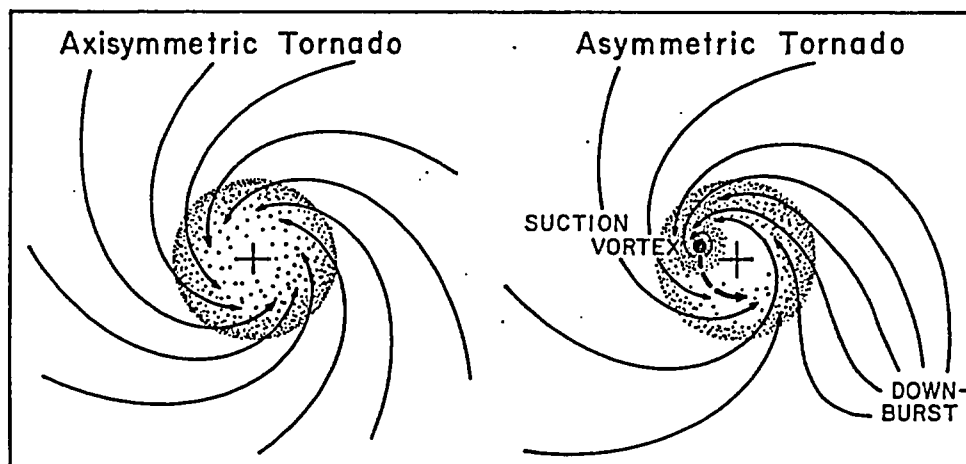


Figure 2.6 Axisymmetric structure of tornado can be destroyed by the flow that originates in nearby downburst. Destruction of axisymmetry often results in successive formations of suction vortices. Two to five suction vortices in their various stages can be seen simultaneously within a tornado.

4. Specific Examples

The Rainsville tornado, Indiana, on April 3, 1974 which crossed US-41 toward the northeast was characterized by cycloidal marks left in a plowed field. Shortly after the highway crossing, the marks were interrupted and the course deviated to the right (see Figure 2.7).

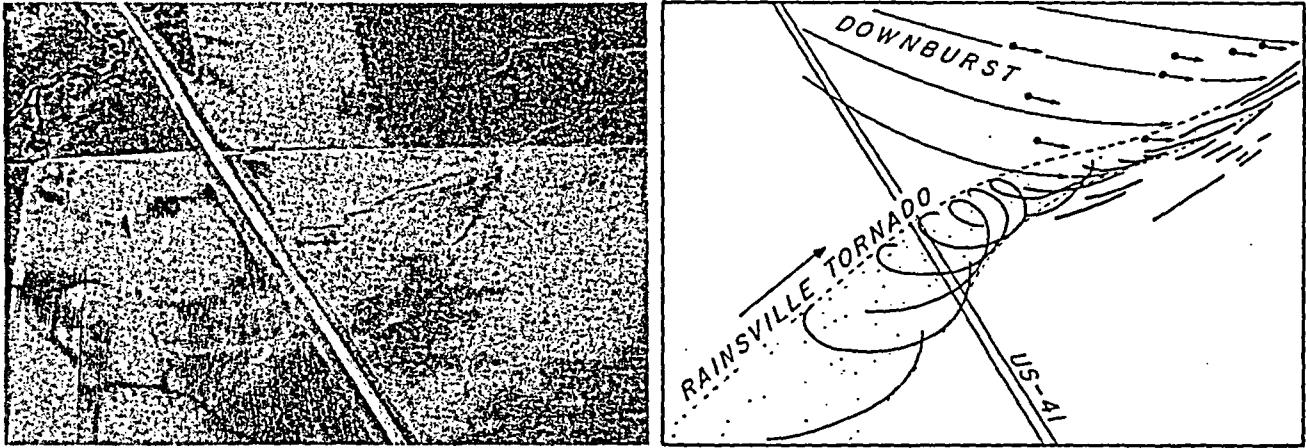


Figure 2.7 Rainsville tornado of April 3, 1974 affected by the downburst winds from the rear left. The tornado weakened abruptly while deviating to the right.

Mapping of tree damages around the right-turn area confirmed the existence of strong winds from the northwest. Since the tree damage on the left (northwest) side of the path started near US-41, the flow was caused probably by a downburst which descended to the northwest of the tornado.

The right-turn of the Louisville tornado of April 3, 1974 was documented by a series of still pictures taken by Mr. Cundiff of Crestwood, Kentucky (see Figure 2.8). Cundiff watched the Louisville tornado with its dark, parent cloud travel from left (southwest) to right across the western sky. Within a few minutes the whole funnel emerged from the dark cloud, turning into a tall, grayish-white funnel cloud. Thereafter, the funnel moved from left (west) to right, in front of the parent cloud.

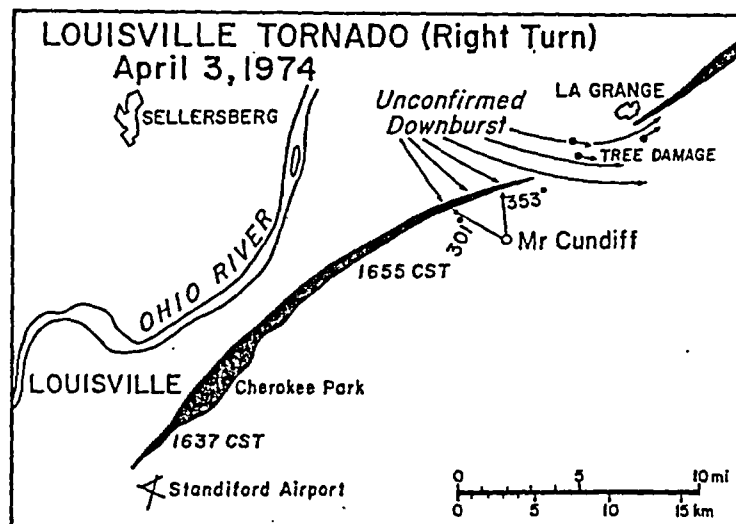


Figure 2.8 Louisville tornado which made a right turn during its dissipating stage. A sequence of pictures taken by Mr. Cundiff revealed that the tornado emerged from the parent cloud toward the south, apparently in response to a downburst from the north.

In view of the scattered tree damage to the southwest of La Grange, where a new tornado had started, we may speculate on the existence of a downburst on the left (northwest) side of the tornado (see Figure 2.8).

The left-turn tornadoes of April 3, 1974 have been mapped and discussed by Fujita (1974), (1975) and Forbes (1977), (1978) in detail. The left-turn paths of tornadoes in a family are very unique and unmistakable when determined by an aerial survey.

The first tornado is characterized by a cone-shaped funnel when it appears. Then, the funnel is steered by the parent cloud for 10 to 20 minutes, until the tornado vortex at the ground deviates to the left while reducing its translational speed. As a result, the vortex on the ground is left behind, to the left of its original location relative to the parent cloud. Meanwhile, the funnel shape changes from that of a cone into a trunk, and finally into a rope (see Figure 2.9).

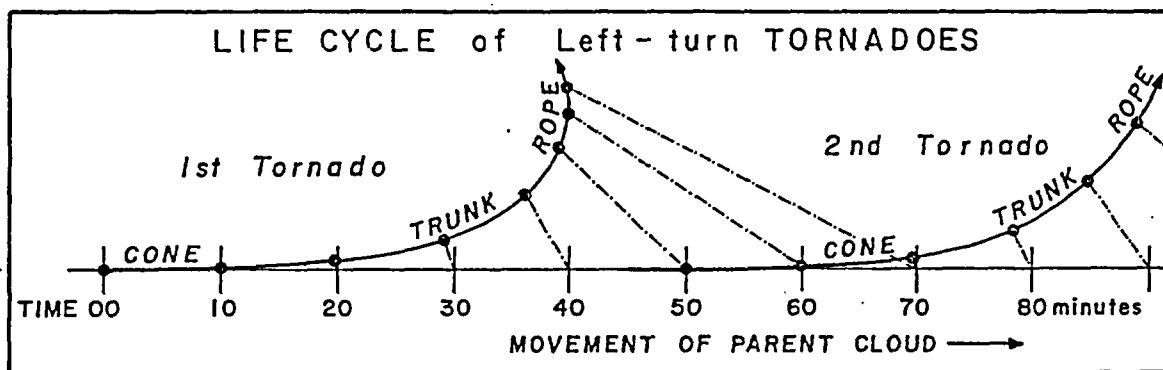


Figure 2.9 Typical paths of successive left-turn (LT) tornadoes spawned by a single parent cloud. Note that there are chances of observing a rope-shaped funnel and a cone-shaped funnel simultaneously.



Figure 2.10 Two pictures taken almost simultaneously from two different locations in Cincinnati, Ohio. The rope-shaped funnel (left) was photographed by Mr. Jay Carter and the cone-shaped funnel (right) by Mr. Mark Carter who happened to be his nephew. Pictures were taken at 1640 CST, April 3, 1974.

Rare simultaneous pictures of a disintegrating rope and a newly-forming cone were taken by Messrs. Jay and Mark Carter. The cone funnel (right), at the formative stage of the Mason tornado, Ohio, was located near the center of the parent cloud over the northeast suburb of Cincinnati, Ohio. The rope funnel of the Sayler Park tornado on the ground was about 7 miles to the west of the cone funnel and was swirling practically under the blue sky (see Figure 2.10).

During its dissipating stage, the ground position of the rope funnel of a left-turn tornado is located outside the parent cloud. If the initial cone funnel forms inside the hook echo of a parent cloud, the vortex on the ground of a left-turn tornado will have to move out of the parent hook, somehow.

An example of a complicated tornado, affected by a downburst and a microburst simultaneously, is shown in Figure 2.11. Two suction vortices, "B" and "C", were probably induced by a downburst flow from the rear-left. A single-turn vortex, "A", enlarged in the left and center pictures of Figure 2.12 was the result of a microburst to the right of the tornado path.

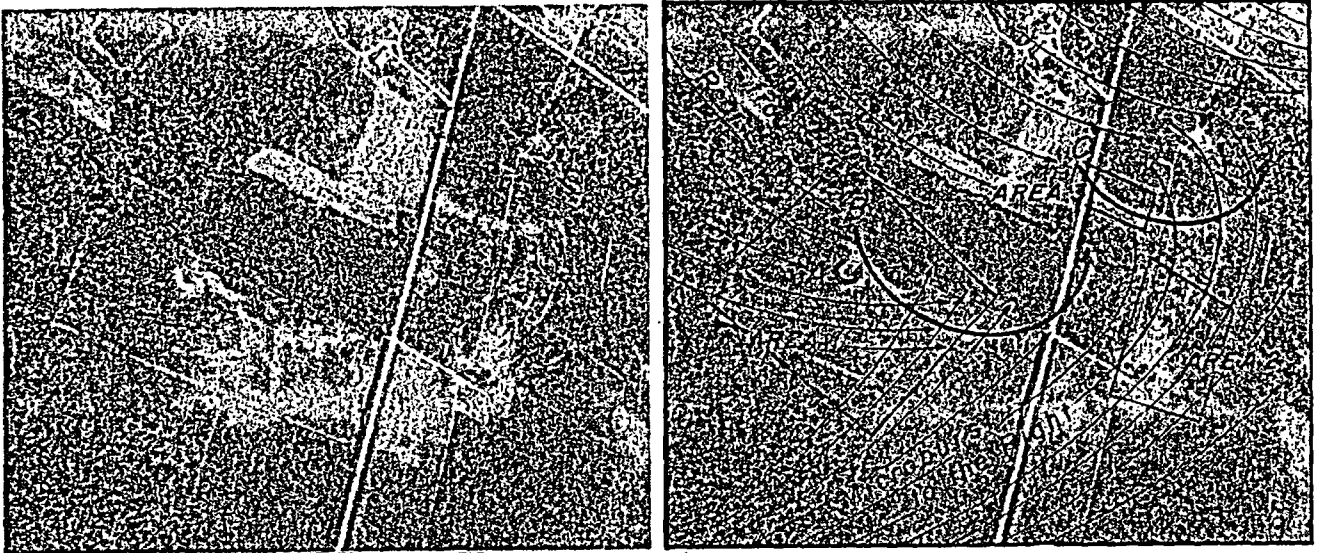


Figure 2.11 Rather complicated ground marks left by the Bloomer, Wisconsin tornado of July 30, 1977. A microburst to the right and a downburst from the rear left were affecting the tornado simultaneously.

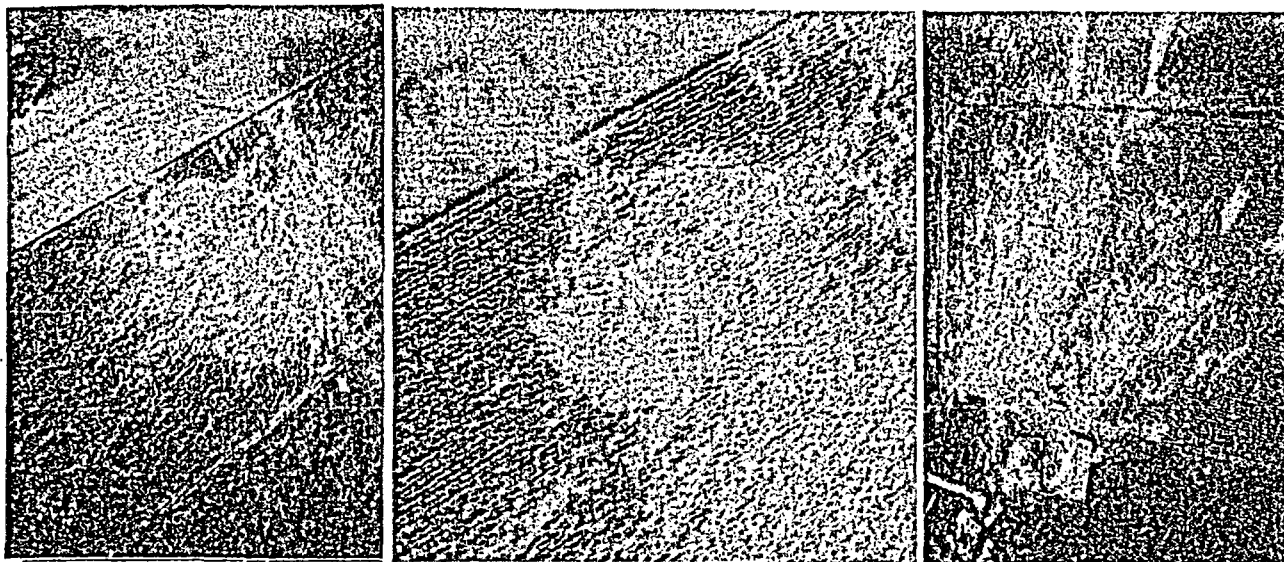


Figure 2.12 A stationary suction vortex in Area 1 induced by a microburst to the right (left picture) and its enlargement (center). A farm in Area 2 smashed by the microburst winds drawn violently into the tornado (right).

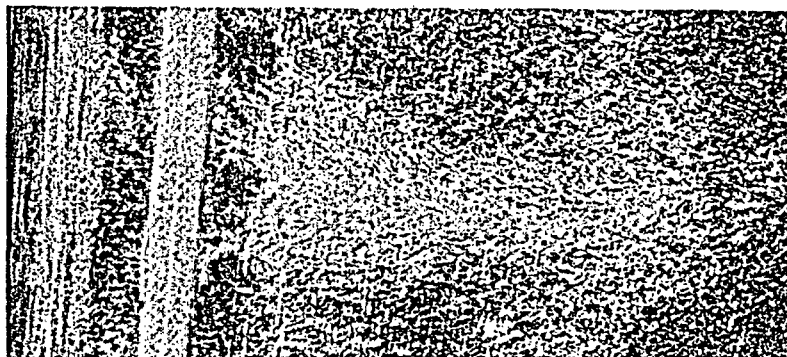


Figure 2.13 A close-up view (Area 3) of suction-vortex swath "C"; probably induced by the downburst from the rear left. Swath "B" preceded "C".

CHAPTER THREE

PHOTOGRAMMETRIC ANALYSES OF TORNADOES

Tornado parameters for engineering purposes are R_c , the core radius; V_m , the maximum tangential velocity; T , the translational velocity; and H_i , the height of inflow layer. These parameters can be obtained photogrammetrically by analyzing still and motion pictures of tornadoes.

1. Angular Measurements and Triangulation

Tornado pictures taken by professional meteorologists and/or photographers are fewer in number than those taken by the general public. Thus, it is necessary to collect pictures and movies taken by those who happened to be in or near the paths of tornadoes.

The first step of photogrammetric analysis is to determine the exact locations and viewing angles of the collected pictures. For this purpose, we visit each photographic site with a calibrated camera. It is rather easy to get to the exact photographic site and to shoot horizontal pictures toward the direction of the tornado which had existed days, weeks, or even months ago. These post-tornado pictures, called "reference pictures", must be taken with a zero elevation angle or at a horizontal aim, otherwise, the azimuth lines in the reference pictures will not be perpendicular to the horizon.

It is not necessary to obtain from the photographers the focal length of the camera used in taking the tornado pictures. Picture dimensions are highly dependent upon the size of the prints. The "effective focal distance" of each print must be computed from the reference picture.

An example of the triangulation of the Ash Valley tornado of August 30, 1974 is shown in Figure 3.1. The figure includes 45 azimuths of the tornado center viewed from 21 photographic locations. The tornado moved toward the southeast leaving a 6.3-mile path of disturbance. The tornado made a looping path shortly before it dissipated.

The life cycle of this tornado is shown by a drawing (Figure 3.2) and four pictures (Figure 3.3). There was no evidence of a typical tornado funnel until the storm reached its dissipating stage. During the mature stage, a small funnel, less than 200 m (600 ft) long, was hanging from the cloud base at about 1500 m (4900 ft) above the ground. The funnel failed to descend toward the ground during the storm's mature stage.

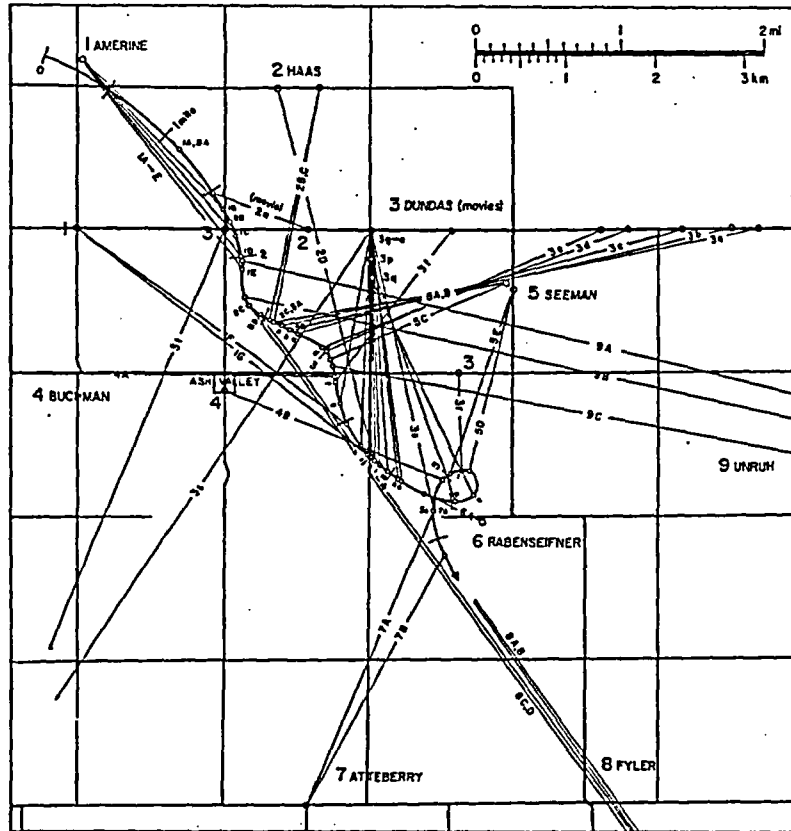


Figure 3.1 Locations of the center of the Ash Valley tornado of August 30, 1974 determined by triangulation method. Photographers are identified by numbers 1, 2, 3..., and photographic locations by each photographer by A, B, C....

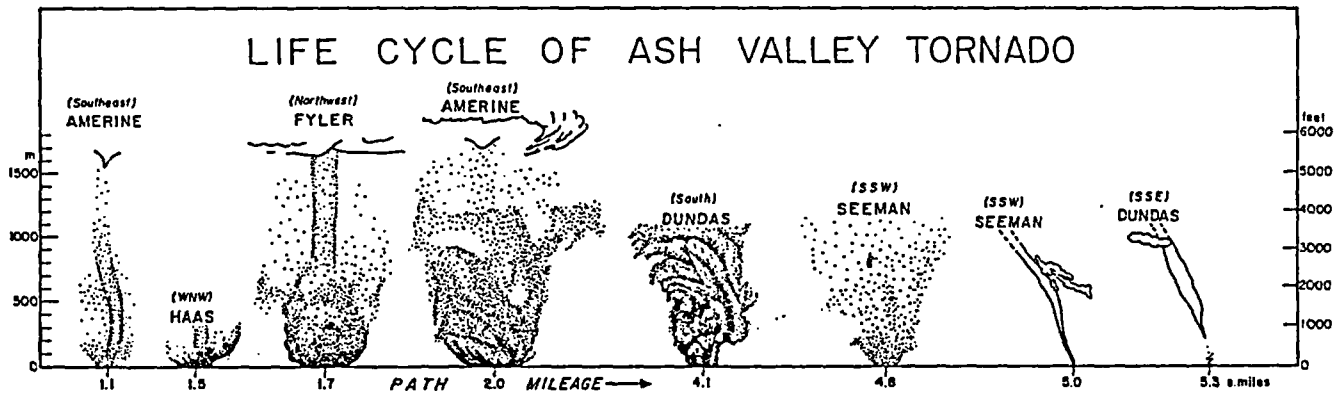


Figure 3.2 Variation of the Ash Valley tornado. The funnel cloud was insignificant until reaching the 4.8 path mileage. Thereafter the tornado was undercut by a cold downdraft from the northeast. A waterspout-like funnel cloud extended down to the wet ground at paths mileages 5.0 and 5.3 miles.

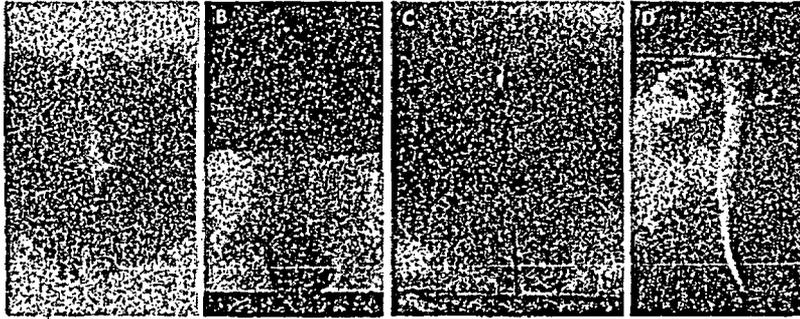


Figure 3.3 Photographic evidence by A, Amerine (1A); B, Fyler (8B); C, Seeman (5D); and D, Buckman (4B). For (1A), (8B), etc. refer to Figure 3.1.

It was shortly after the cold downdraft air moved into the tornado area that a small funnel cloud suddenly extended all the way to the wet ground. This evidence clearly shows that we cannot estimate tornado windspeeds based solely on the length of the funnel cloud.

The core radius, R_0 , can be estimated from the viewing angles of the dust column and the distance to the tornado center. Funnel diameter should not be used as the core diameter because a funnel cloud is a measure of the tornado's pressure field made visible by condensed water droplets. We should always look for the region of high winds where airborne dust and light objects swirl around the tornado center.

Figure 3.4 shows the variation of the core radius which increased to 185 m (600 ft). The diameter remained 120 m (400 ft) for a while until it suddenly decreased to zero.

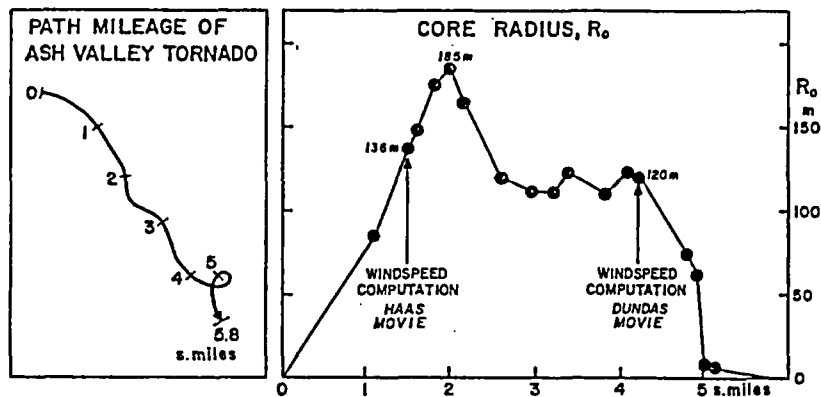


Figure 3.4 Variation of R_0 , the core radius from the birth to death of the Ash Valley tornado.

2. Distant Tornado on Vertical Image Plane

Projection of a nearby tornado on an image plane is rather complicated because the lines of sight diverge within the viewing angle of the storm. To avoid this difficulty, tornado pictures are projected on vertical image planes from an infinite distance.

Let the core diameter of a tornado be R_0 with its cylindrical core extending vertically to infinity. The angle θ called the "center angle" is defined as zero at C, the tornado center on the image (see Figure 3.5). The center angle of the left edge is -90° and that of the right edge $+90^\circ$.

The X ordinate of the left and right edges on the image plane are $+X_0$ and $-X_0$, respectively. The ordinate of a point on the core boundary can be written as

$$X = R_0 \sin \theta. \quad (3.1)$$

The horizontal velocity of the airflow at the core boundary, expressed by S_H , intersects the core boundary with an angle, α_0 , called the crossing angle at R_0 .

The horizontal velocity, S_H , of airflow projected on the image plane is

$$I_H = S_H \cos (\alpha_0 + \theta) \quad (3.2)$$

where I_H denotes the image-plane component of S_H .

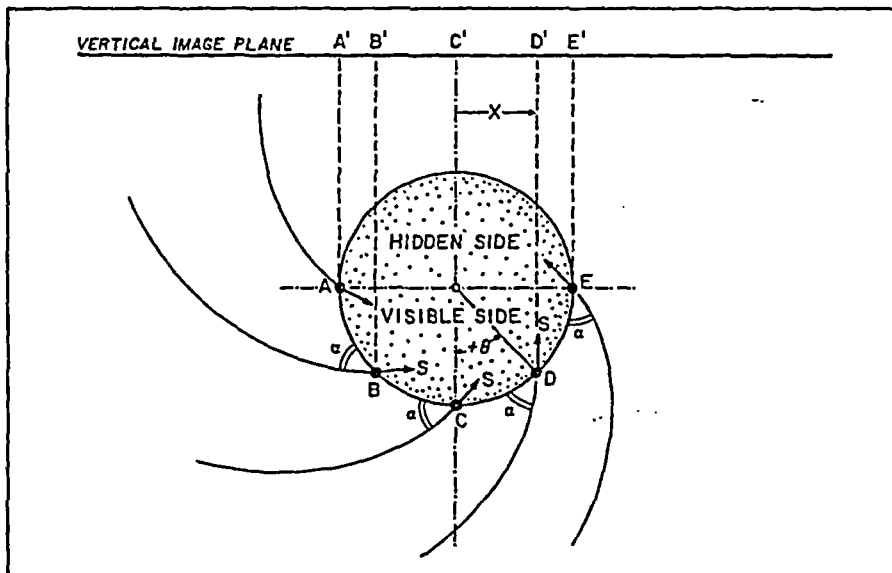


Figure 3.5 Projection of a tornado on a vertical plane from the infinite distance. α is the crossing angle which denotes the angle between the direction of airflow and the tornado-centric circle at their crossover point.

Although we cannot photograph (like an X-ray) the air motion hidden inside a thick cloud of dust, the tornado's flow field is likely to be characterized by

- A. An inflow layer with its top height H_i ;
- B. Radial and tangential velocity fields with velocities, U_o and V_o , respectively, at the core boundary;
- C. An inner core with its outer radius $n R_o$. This core rotates with insignificant or no vertical motion.
- D. An outer core with its outer radius R_o . Violent vertical motions exist inside this core.

A schematic diagram of the above characteristics is presented in Figure 3.6.

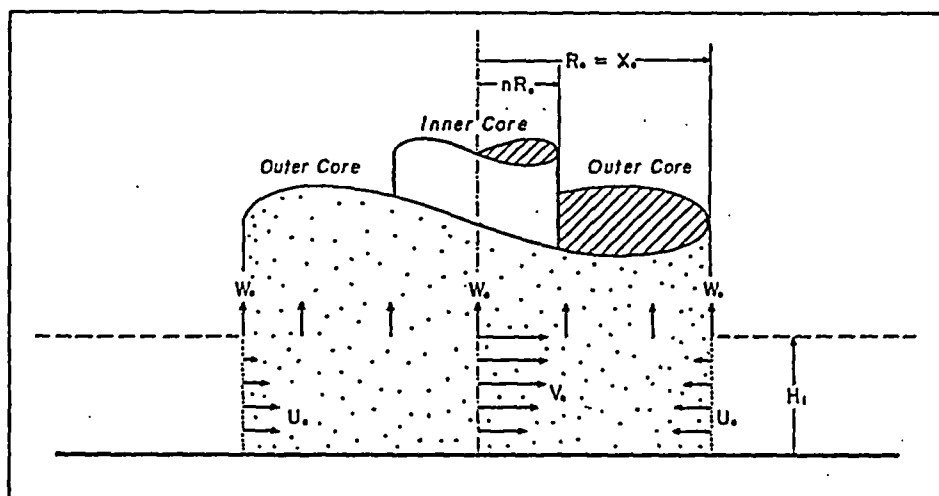


Figure 3.6 Tornado parameters which can be determined by photogrammetric analyses of tornado movies.

3. Model Tornado on Vertical Image Plane

Examination of a model tornado projected onto a vertical image plane is helpful in learning the nature of movement on a movie screen. For this purpose, Fujita's model tornado described in Chapter 6 was used to determine the expected air motion on an image plane.

Referring to the equations in Chapter Six, we summarize the tornado parameters as:

- A. Inflow height, $H_1 = iR_0$, where i is the "inflow index". See Eq. (6.3).
- B. Inner-core radius, $R_n = nR_0$, where n is the "core ratio". See Eq. (6.1).
- C. Tangential velocity, V_0 at R_0 below H_1 is expressed by $V_0 = V_m h^{\frac{1}{6}}$ where V_m denotes the maximum tangential velocity; $h = H/H_1$, the normalized height. See Eqs. (6.9) and (6.12).
- D. Radial velocity, U_0 at R_0 below H_1 is expressed by $U_0 = V_0 \tan \alpha_0$ where $\tan \alpha_0 = -A_m(1 - h^{\frac{5}{2}})$. See Eq. (6.18)
- E. Vertical velocity W_0 at R_0 below H_1 is expressed by

$$W_0 = \frac{3}{28} \frac{i}{1-n^2} A_m h^{\frac{1}{6}} (16 - 7h^{\frac{5}{2}}) V_m$$

See Eq. (6.39).

We shall now project these velocities onto the vertical plane with a perspective looking from infinity.

By definition of α_0 and V_0 , horizontal velocity S_H can be written as

$$S_H = V_0 \sec \alpha_0 \quad (3.3)$$

Equations (3.2) and (3.3) show that the image-plane component of S_H is

$$I_H = V_0 \frac{\cos(\alpha_0 + \theta)}{\cos \alpha_0} \quad (3.4)$$

Rising angle, β , is defined as the elevation angle of the velocity vector of air motion on the image. Since vertical velocity, W_0 , remains unchanged upon projection on the vertical image plane, we write

$$\tan \beta_0 = \frac{W_0}{I_H} = \frac{W_0}{V_0} \frac{\cos \alpha_0}{\cos(\alpha_0 + \theta)} \quad (3.5)$$

Numerical values of α_0 , V_0 , and W_0 of the model tornado are shown in Table 3.1. Special cases of this rising angle are:

$$\tan \beta = W_0/V_0 \cot \alpha_0 \quad \text{when } \theta = -90^\circ \text{ (left edge)} \quad (3.6)$$

$$\tan \beta = W_0/V_0 \quad \text{when } \theta = 0^\circ \text{ (center axis)} \quad (3.7)$$

$$\tan \beta = -W_0/V_0 \cot \alpha_0 \quad \text{when } \theta = +90^\circ \text{ (right edge)} \quad (3.8)$$

$$\tan \beta = W_0/V_0 \cos \alpha_0 \quad \text{when } \theta = -\alpha_0 \quad (3.9)$$

$$\beta = 90^\circ \quad \text{when } \theta = 90^\circ - \alpha_0 \quad (3.10)$$

Table 3.1 Crossing angles, α_0 , and normalized velocities, v_0 and w_0 , as functions of normalized height, h .

(Locations)	$h = H/H_1$	α_0	$v_0 = V_0/V_m$	$w_0 = W_0/V_m$	W_0/V_0
	10	+0.29°	0.763	0.376	0.493
	7	+0.21	0.835	0.387	0.463
	5	+0.14	0.888	0.393	0.443
	3	+0.07	0.942	0.397	0.421
(Top of inflow)	1	0.0	1.000	0.398	0.398
	0.9	-6.3°	0.983	0.392	0.391
	0.8	-12.0	0.963	0.374	0.388
	0.7	-17.3	0.942	0.347	0.368
	0.6	-21.9	0.918	0.310	0.338
	0.5	-25.9	0.891	0.266	0.299
	0.4	-29.2	0.858	0.216	0.252
	0.3	-32.1	0.818	0.161	0.197
	0.2	-34.3	0.765	0.104	0.136
	0.1	-36.0	0.681	0.047	0.069
(Surface)	0.0	-36.9	0.000	0.000	0.000

Magnitude of the total velocity vectors on the image plane can be computed from

$$I_T = (I_H^2 + W_0^2)^{\frac{1}{2}}$$

$$\text{or } I_T = W_0 \operatorname{cosec} \beta \quad (3.11)$$

where I_T denotes the total image velocity.

Velocity vectors in Figure 3.7 were computed from Eqs. (3.5) and (3.11). See Table 3.2 for numerical values. Only vectors on the front side were plotted because we will not be able to see the other side of the swirling dust column.

It should be noted that the inflow air from both sides moves into the outer core, forming an apparent convergence line near the lower right edge of the outer core.

The maximum image velocity, I_m , is located on the tornado's center line at the top of the inflow layer. I_m is larger than V_m , the maximum tangential velocity, because the former includes W_m , the maximum vertical velocity at the top of the inflow layer. Thus we write

$$I_m = (V_m^2 + W_m^2)^{\frac{1}{2}} \quad (3.12)$$

Isotachs of image velocity (total) are drawn in Figure 3.8.

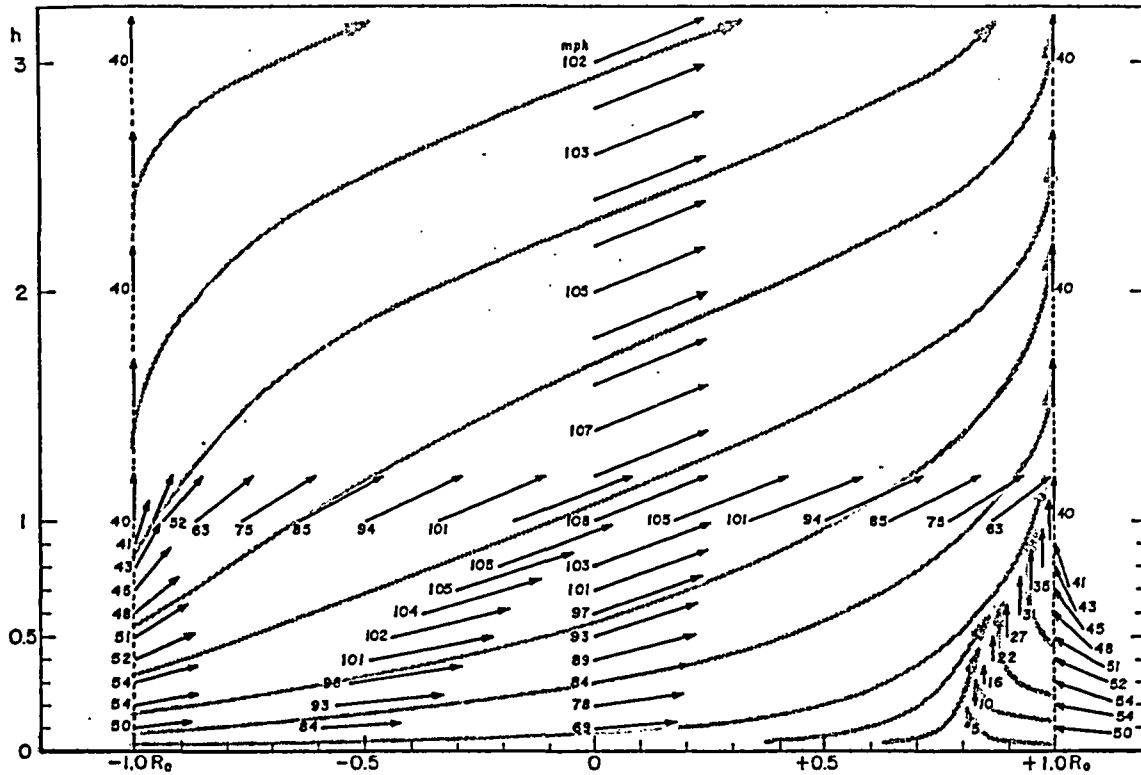


Figure 3.7 Total velocity vectors on image plane (total image velocities). Vectors on the front side only were plotted because those on the other side are hidden behind a swirling column of dust.

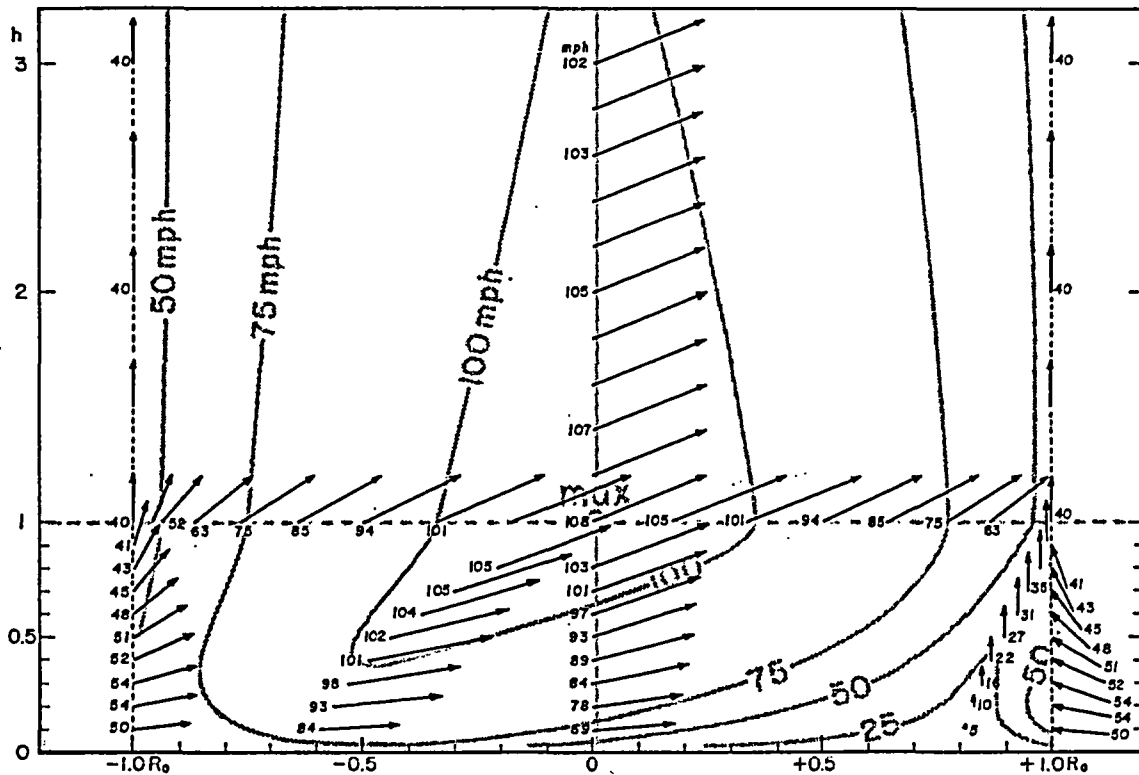


Figure 3.8 Isotachs of total image velocities. Note that the maximum velocity is located on the center line at the top of the inflow layer.

Table 3.2 Rising angle, β in degree and image velocity, I_T in mph tabulated as a function of normalized height, h and center angle, θ . In computing image velocity, the maximum tangential velocity was assumed $V_m = 100$ mph.

Normalized height, h	Crossing angle, α_0	Center angle, θ				
		-90°	$-\alpha_0$	zero	$90^\circ - \alpha_0$	$+90^\circ$
10	+0.29	91-38 _{mph}	26-85 _{mph}	26-85 _{mph}	90-38 _{mph}	89-38 _{mph}
7	+0.21	91-39	25-92	25-92	90-39	90-39
5	+0.14	90-39	24-97	24-97	90-39	90-39
3	+0.07	90-40	23-102	23-102	90-40	90-40
1	0.00	90-40	22-108	22-108	90-40	90-40
0.9	-6.3	74-41	21-108	21-108	90-39	106-41
0.8	-12.0	61-43	21-105	21-103	90-37	119-43
0.7	-17.3	50-45	19-105	20-101	90-35	130-45
0.6	-21.9	40-48	17-104	19-97	90-31	140-48
0.5	-25.9	32-51	15-102	17-93	90-27	149-51
0.4	-29.2	24-52	12-101	14-89	90-22	156-52
0.3	-32.1	17-54	10-98	11-84	90-16	163-54
0.2	-34.3	11-54	06-93	08-78	90-10	169-54
0.1	-36.0	05-50	03-84	04-69	90-05	175-50
0.0	-36.9	00-00	00-00	00-00	90-00	180-00

4. Determination of Tornado Parameters

Some of the tornado parameters can be determined based on photogrammetric quantities. Figure 3.9 shows schematically how parameters can be determined.

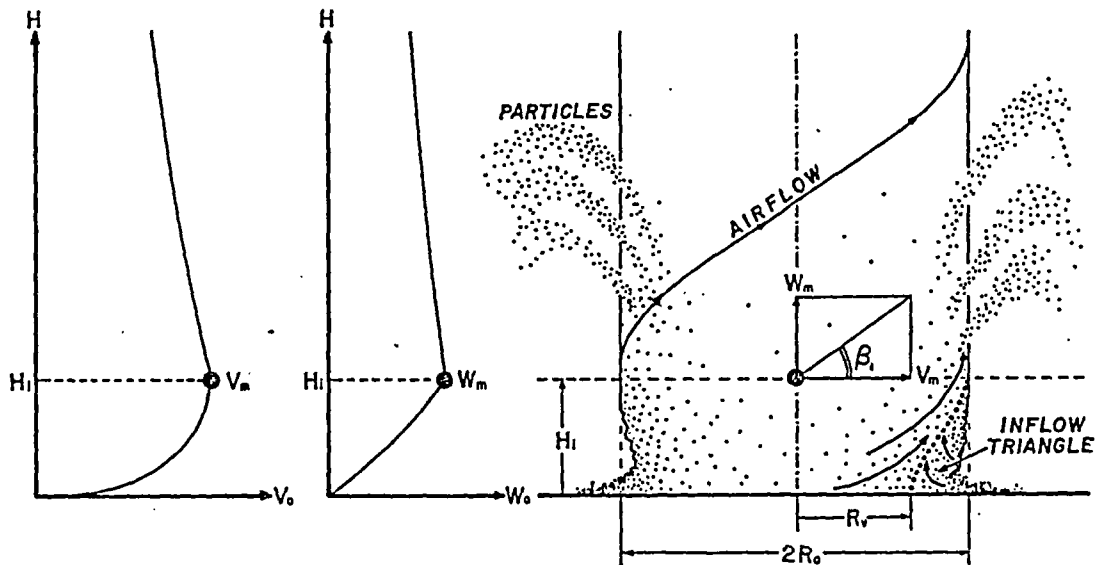


Figure 3.9 Schematic diagrams to determine tornado parameters.

Step I. Determination of Inflow Height, H_1

The domain of the upward motion near the lower right portion decreases as the height increases. At the top of the inflow layer the inflow triangle (see Figure 3.9) disappears. The height at which the inflow triangle disappears denotes H_1 , the top of inflow layer.

Step II. Computation of Crossing Angle, α_0

X ordinates of the vertical current along the left side of the inflow triangle are computed as a function of the height above the ground. Let X_v be the ordinate, then Eqs. (3.1) and (3.10) permit us to write

$$X_v = R_0 \sin(90^\circ - \alpha_0) = R_0 \cos \alpha_0$$

$$\text{or} \quad \cos \alpha_0 = X_v / R_0 \quad (3.12)$$

Values of X_v measured on the image as a function of height will give us the crossing angles of the inflow air from the ground to the inflow top.

Step III. Maximum vertical, W_m , and maximum tangential, V_m , velocities can be obtained from

$$\begin{aligned} W_m &= I_m \sin \beta_1 \\ \text{and} \quad V_m &= I_m \cos \beta_1 \end{aligned} \quad (3.13)$$

where I_m denotes the maximum image velocity on the center axis at H_1 ; and β_1 , the rising angle of the air at the same location.

Step IV. Determination of core ratio, n .

The size of the central core (eye of tornado) can be estimated from

$$\tan \beta_1 = \frac{W_m}{V_m} = \frac{27}{28} A_m \frac{i}{1 - n^2} \quad (3.14)$$

where $A_m = -\tan \alpha_0$.

From predetermined values of α_0 , β_1 , and i , core ratio, n is computed as

$$n^2 = 1 - \frac{27}{28} i (-\tan \alpha_0) \cot \beta_1 \quad (3.15)$$

where α_0 is negative inside the inflow layer.

Computation steps I through IV permit us to determine the following basic parameters of the tornado flow field. They are

- $H_i = i R_o$, the inflow height
- α_o , the crossing angle
- V_m , the maximum tangential velocity
- W_m , the maximum vertical velocity
- $n = R_n/R_o$, the core ratio

These computations are based on the assumptions that V_o varies along the vertical in proportion to $h^{\frac{1}{6}}$ and that $\tan \alpha_o$, to $(1 - h^{\frac{3}{2}})$.

It is not necessary, however, to be dependent upon the above assumptions. Both I_T , the total image velocity and β , the rising angle can be computed along the tornado's center line to determine

$$V_o = I_T \cos \beta = f(H) \quad (3.16)$$

where V_o and β are functions of height.

The crossing angle is also determined as a function of height. Equation (3.12) can readily be used to obtain $\alpha_o = F(H)$ from values of X_v measured on the image plane.

5. Example of Parameter Computations

A detailed analysis of the Ash Valley tornado movie taken by Mr. Robert Dundas of Great Bend, Kansas was performed by Umenhofer and Fujita (1977). Their analytical results were used in determining the tornado parameters.

The inflow height measured from image-velocity vectors in Figure 3.10 is 70 m (230 ft) while its core radius was $R_o = 120$ m (390 ft). Thus, we obtain the "inflow index", i , to be

$$i = H_i/R_o = 0.58 \quad (3.17)$$

The crossing angle at the surface is computed from the measured value of $X_v = 95$ m (310 ft). From Eq. (3.12) we have

$$\alpha_o = 37.7^\circ \quad (3.18)$$

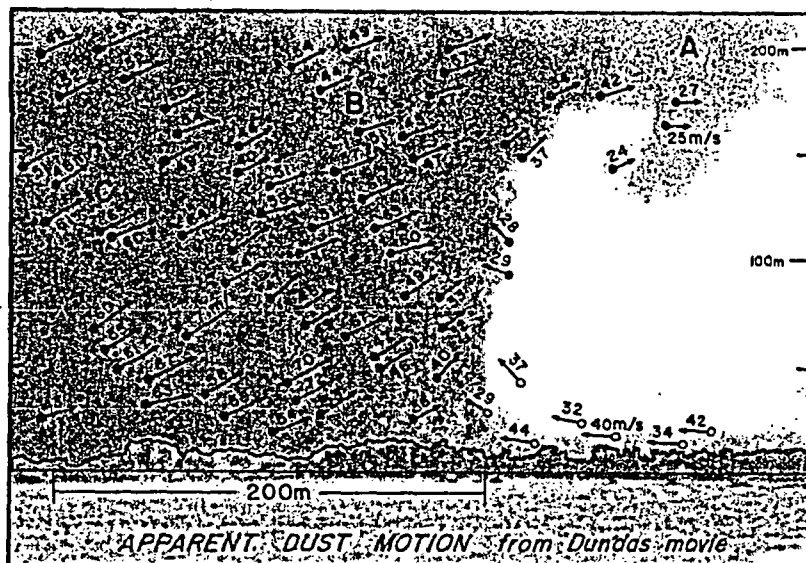


Figure 3.10 Velocity vector superimposed upon a telophoto view of Dundas Movie of the Ash Valley tornado. Vectors with open circles denote inflow.

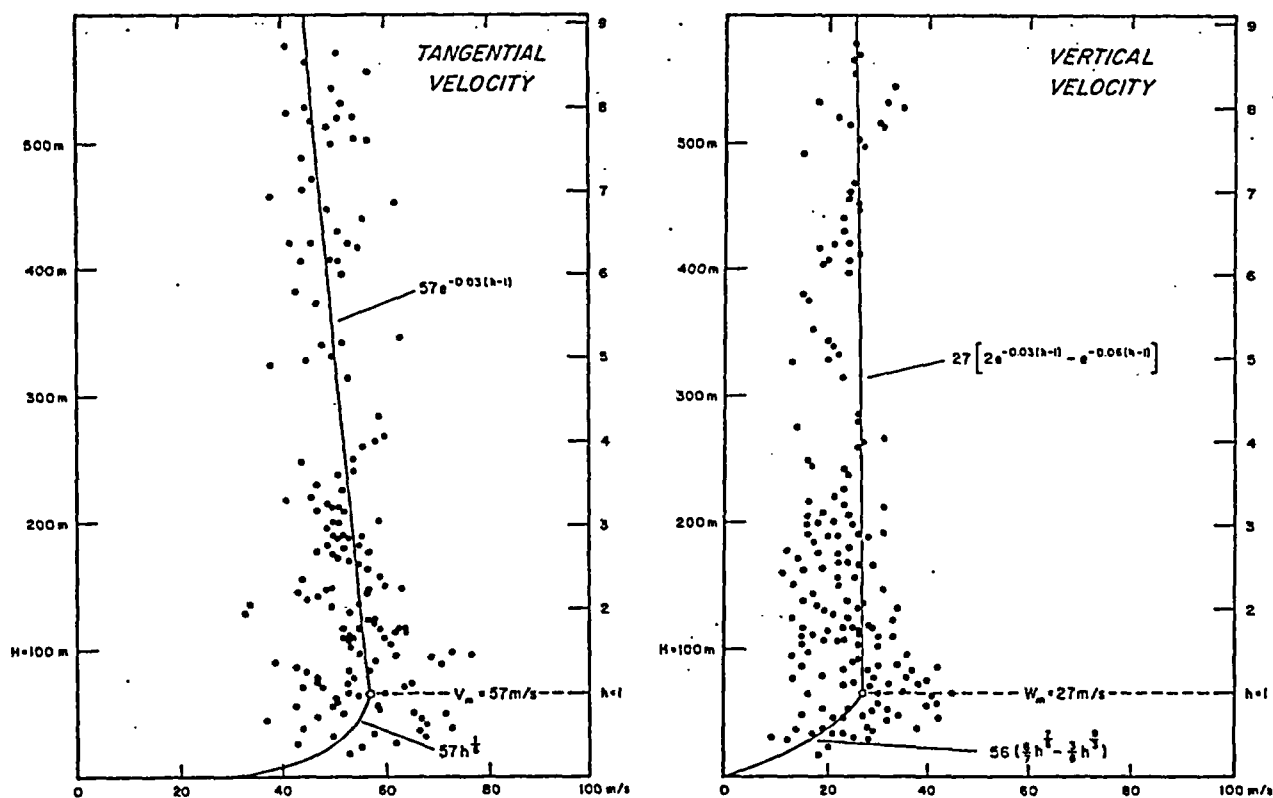


Figure 3.11 Vertical distribution of tangential velocity (left) and that of vertical velocity (right) computed from Dundas Movie.

Tangential and vertical velocities were plotted as functions of height. Their maximum values in Figure 3.11 are

$$V_m = 57 \text{ m/sec and } W_m = 27 \text{ m/sec}$$

These values are used to compute n , the core ratio, from Eq. (3.15). Thus, we have

$$n = 0.296 \quad (3.19)$$

A large number of photogrammetric analyses of tornado movies will be required before we will be able to establish reasonable parameters of a tornado model. Such an example, nevertheless, reveals important tornado parameters which cannot be determined otherwise.

The Xenia tornado of April 3, 1974 was analyzed by Fujita (1975). The tornado was characterized by a huge mass of swirling dust cloud with numerous debris embedded.

Since the motions of the debris and dust clouds are not expected to be similar to each other, "dust" and "debris" were tracked separately. Image velocities (apparent motions) thus computed are shown in Figures 3.12 (dust) and 3.13 (debris).

Embedded debris, by virtue of their fall velocities, showed rising angles much smaller than those of dust. Although we cannot determine the difference between dust and air motions, it is natural to postulate that extremely small particles move with the wind.

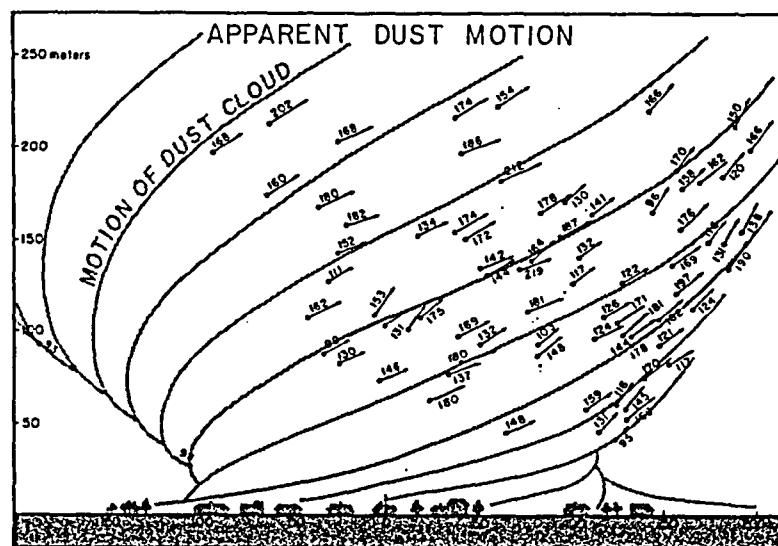


Figure 3.12 Velocities of dust clouds on the image plane. Xenia tornado of April 3, 1974.

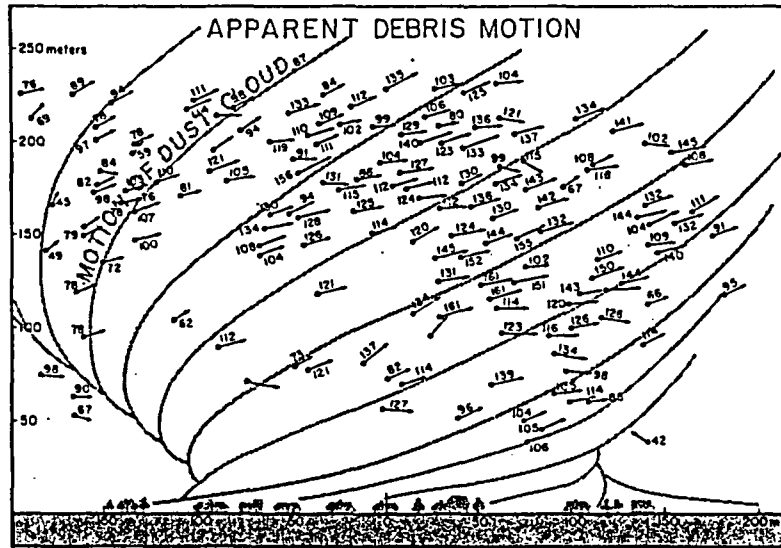


Figure 3.13 Velocities of debris corresponding to those in Figure 3.12. Flow patterns are those of dust clouds.

The Xenia tornado was characterized by a non-cylindrical dust column, the diameter of which increased significantly with height. It is difficult to judge if the cone-shaped column was created by the expansion of particle trajectories or if the original flow pattern itself was a tapered cone.

Vertical (right) and tangential (left) velocities of dust clouds are shown in Figure 3.14. A heavy line in each diagram denotes the upper limit of the velocity points. In plotting tangential velocities, dust clouds on the front and back sides were distinguished.

The Xenia tornado movie was analyzed in 1974 when our photogrammetric method was still in the process of improvement. We have learned, since then, that special skill and a knowledge of photogrammetric analyses do improve the final results. Therefore, the results are highly dependent upon "who does the analyzing" and "how the analyzing is done". It is proposed that some of the old tornado movies, including the Xenia movie, be re-analyzed in order to extract the maximum information based on the latest knowledge, experience, and skill in particle trackings.

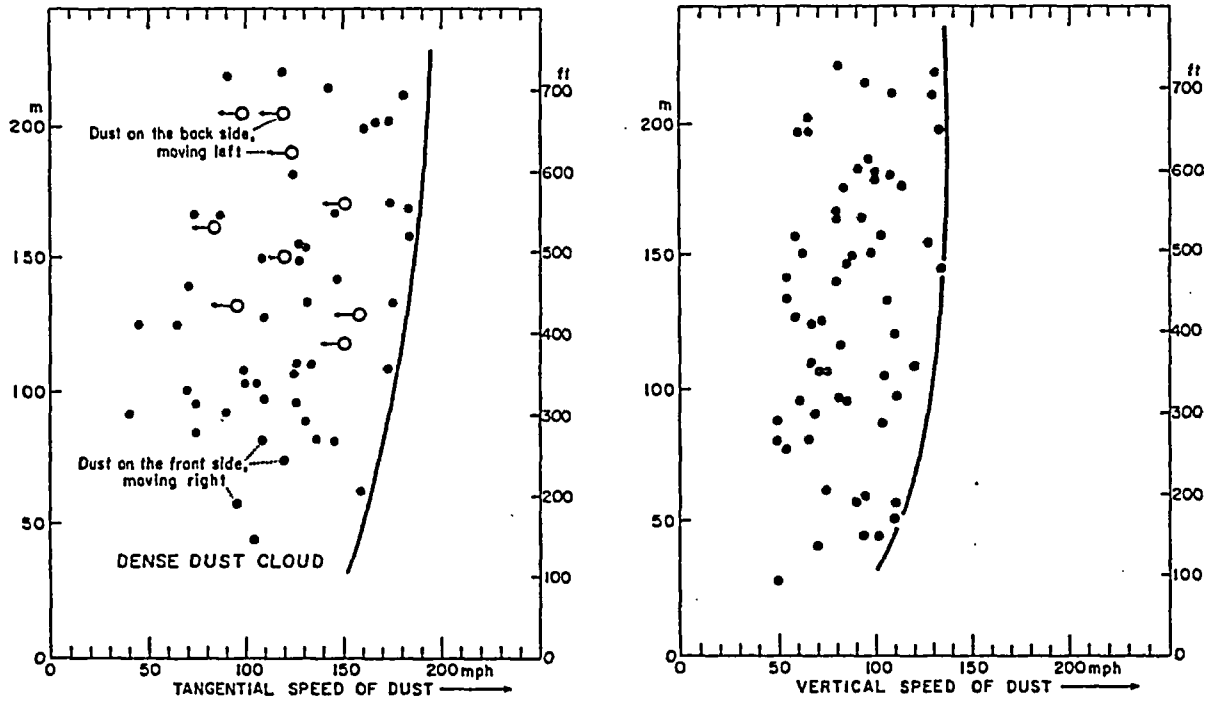


Figure 3.14 Vertical (right) and horizontal (left) velocities of dust clouds in the Xenia tornado plotted as functions of height above the ground. The maximum values are indicated by the heavy lines in the diagrams.

CHAPTER FOUR

AERIAL SURVEY FOR STORM STRUCTURE

Aircraft is extremely useful in inspecting damages caused by various types of windstorms. In most cases, however, aerial survey is limited to the inspection and assessment of structural damages. The flight paths are chosen to cover populated areas where the dollar damages are expected to be the highest.

Our extensive aerial survey revealed, on the contrary, that the structure of windstorms can be studied by flying over relatively flat areas where signatures of undisturbed windstorms are likely to be found.

About 10,000 aerial photographs were taken by the author and his associates since the Palm Sunday (April 11), 1965 tornadoes. The knowledge gained by analyzing these aerial photos now permit us to determine the storm structure based on aerial photography and subsequent mapping.

1. Microburst

Full-grown corn fields are found to be the best vegetation which respond to 40 to 100 mph winds. When corn is young and short, one to two feet in height, it can withstand a 70 mph wind (2 ft-tall corn at Yorkville, Illinois was not damaged by a recorded windspeed of 32 m/sec = 72 mph).

An example of a microburst to the south of Danville, Illinois, is shown in Figure 4.1. Picture (left) reveals an overall pattern of corn damage and a map

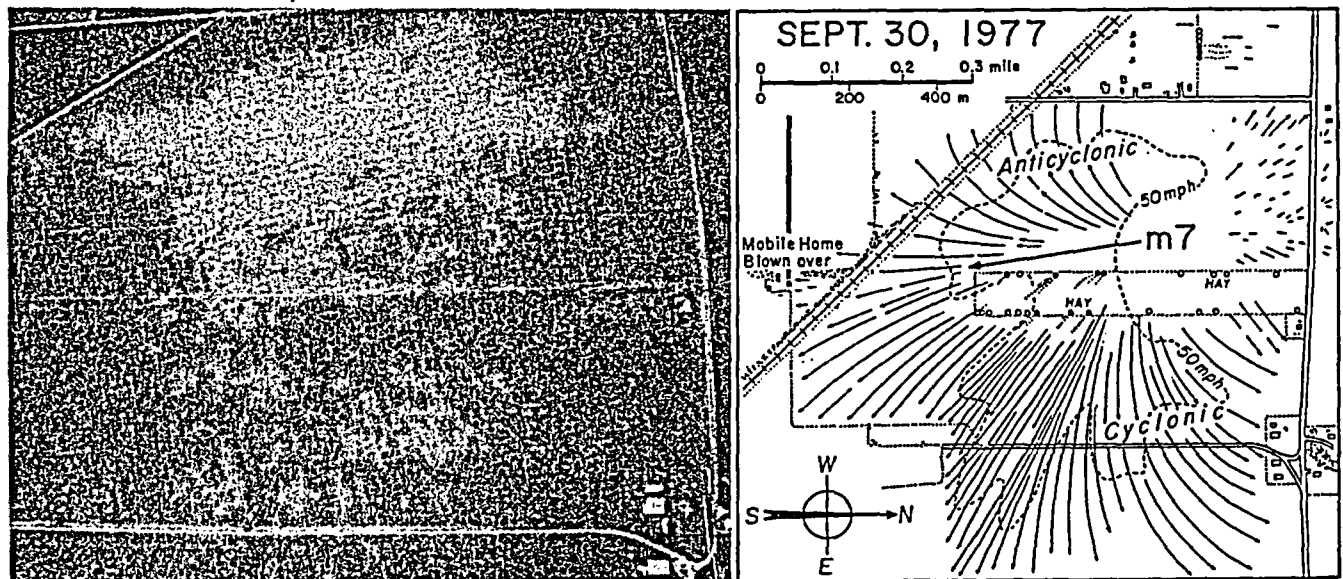


Figure 4.1 An aerial photograph taken from 6,000 ft AGL (left) and mapped trajectories of high winds (right) of Danville, Illinois microburst of September 30, 1977. Anticyclonic and cyclonic curvatures resulted from the movement of the microburst from right to left (north to south). The displacement vector of the downburst center during its lifetime (only 1 to 2 minutes) is shown by a heavy arrow.

(right) was made by combining about 20 pictures taken from various altitudes (500 to 6000 ft AGL) and viewing angles. This microburst was rated as F0 with maximum windspeed of about 70 mph. Corn crops are tall and old late in September when this microburst occurred.

The next example in Figure 4.2 occurred on August 19, 1977 in west-central Wisconsin near Cornell. The microburst area was only 0.2 x 0.3 mile in a forest. It uprooted about 1,500 trees probably in about one minute.

The pattern of winds was divergent. A left-turn curvature near the upper end of the flow was induced by a combination of translational and diverging motions of the microburst.

Microburst signatures are found frequently after the passage of a severe thunderstorm. Its intensity is usually less than F 2.

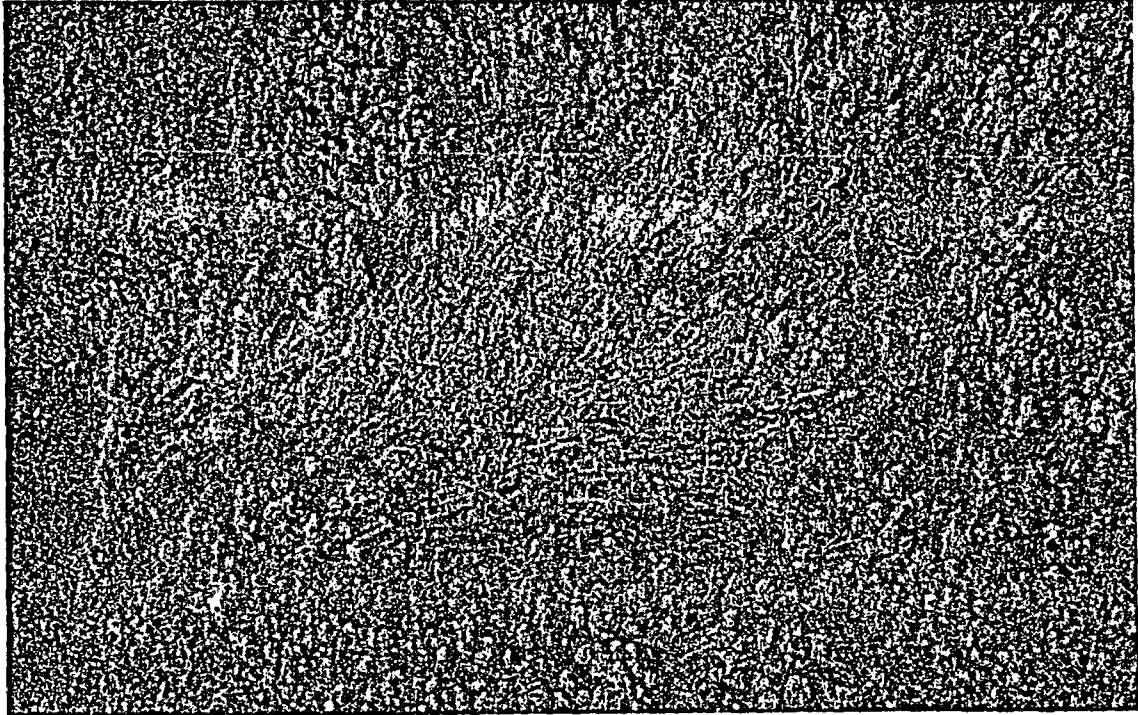


Figure 4.2 A strong (F2) microburst to the west of Cornell, Wisconsin. About 1,500 trees in forest uprooted by strong winds diverged out of the downburst center. Damage area was only 0.3 mile long and 0.2 mile wide.

2. Downbursts

Because of its relatively large horizontal dimensions, a downburst is often characterized by parallel flow field. This is why this type of windstorm has long been classified simply as "straight-line winds".

Detailed aerial mapping of so-called straight-line winds reveal that straight lines often diverge out of relatively small areas where the descending air hits the surface.

Figure 4.3 was taken in northern Wisconsin where the 4th of July, 1977 downbursts damaged a number of county areas causing several million dollars of damage.

Downburst damage seen from the air is very similar to that by a large tornado. A barn in Figure 4.4 (at A) was completely lifted off its foundation. Debris of the barn is scattered downwind in the corn field.

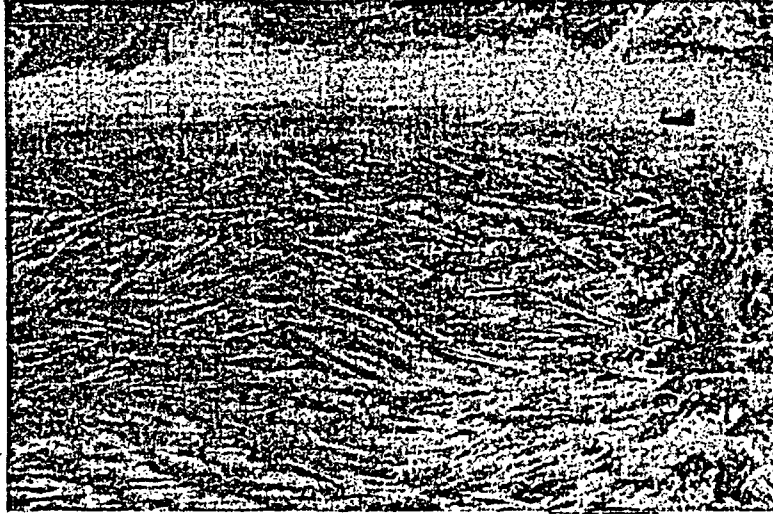


Figure 4.3 A pine forest flattened by the northern Wisconsin downburst of July 4, 1977. This aerial photo was taken just to the west of Flambeau River looking south toward Phillips-Winter Highway.

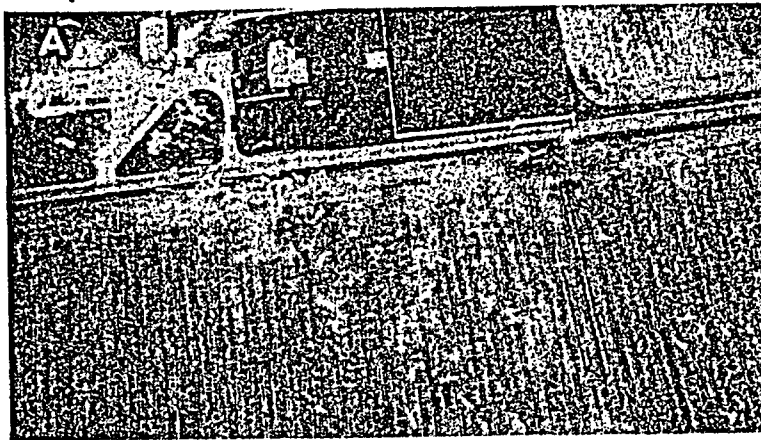


Figure 4.4 Tool shed debris from a downburst near Wallace, Fountain County, Indiana. Estimated damage scale is F1.

Hurricane winds can locally be strong when downbursts are imbedded inside the overall hurricane circulation. On August 3, 1970, when hurricane Celia was located to the north of Corpus Christi, Texas, the southwestern portion of the eye-wall turned into a group of thunderstorms. Downbursts from these thunderstorms induced strong west-southwest winds over the entire city. A motel complex in Figure 4.5 was unroofed by the hurricane/downburst winds.



Figure 4.5 A motel and trailers west of downtown Corpus Christi damaged by downburst winds in Hurricane Celia. Damaging winds estimated to be upper F1 or lower F2 came from WSW. The hurricane center, to the north of the city, was moving WNW at 16 mph.

Mobile homes will receive various degrees of damage by downburst winds. Sometimes, nobody can tell the difference between tornado and downburst damage on mobile homes unless an extensive mapping of environmental flow patterns is performed. Figure 4.6 shows one of the worst mobile home damages by downburst.

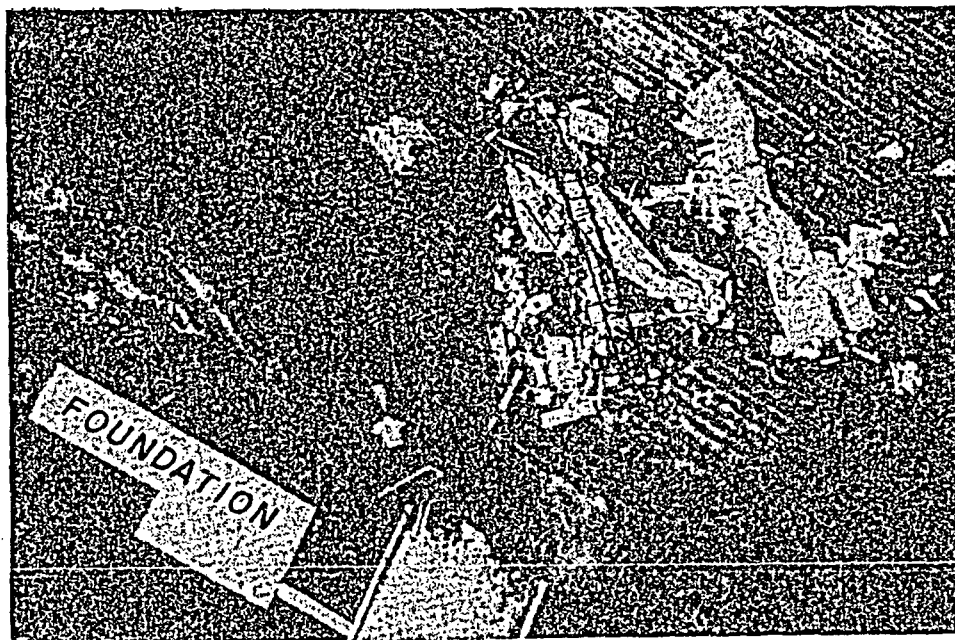


Figure 4.6 A mobile home smashed by a downburst south of Somonauk, Illinois. This was the worst mobile home damage by downburst photographed by the author.

3. Small Tornado

The core diameter of small tornadoes can be as small as several feet, characterized by features somewhat like strong dust devils. In many cases, however, one could see a small, rope-shaped funnel, extending into the parent cloud (see Figure 4.7).

An example of a small tornado is shown in Figure 4.8. It is seen that the rope-shaped funnel stretches semi-horizontally into the wall cloud to the upper right. The vortex axis near the surface is vertical, due to the horizontal swirl motion of the air just above the surface.

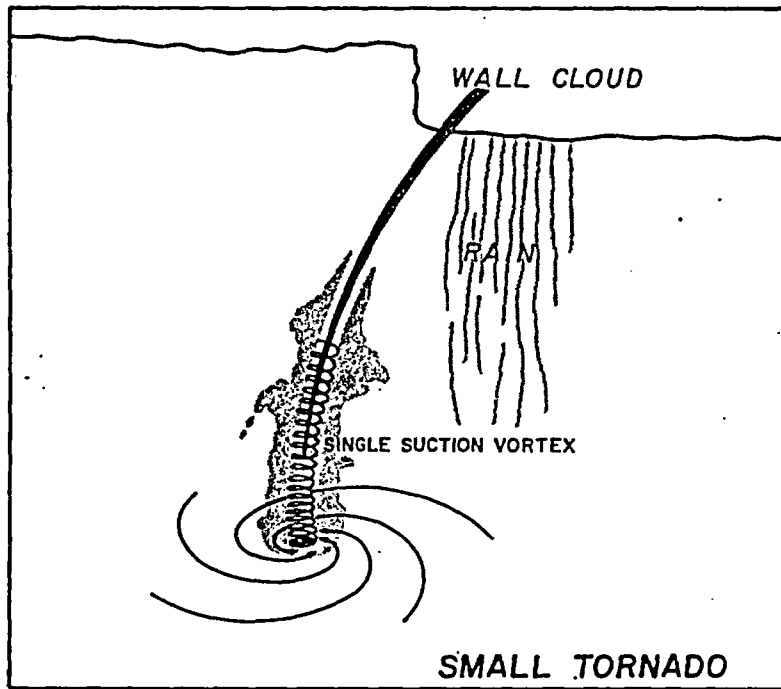


Figure 4.7 Schematic view of a small tornado with its funnel cloud extending into the wall cloud.

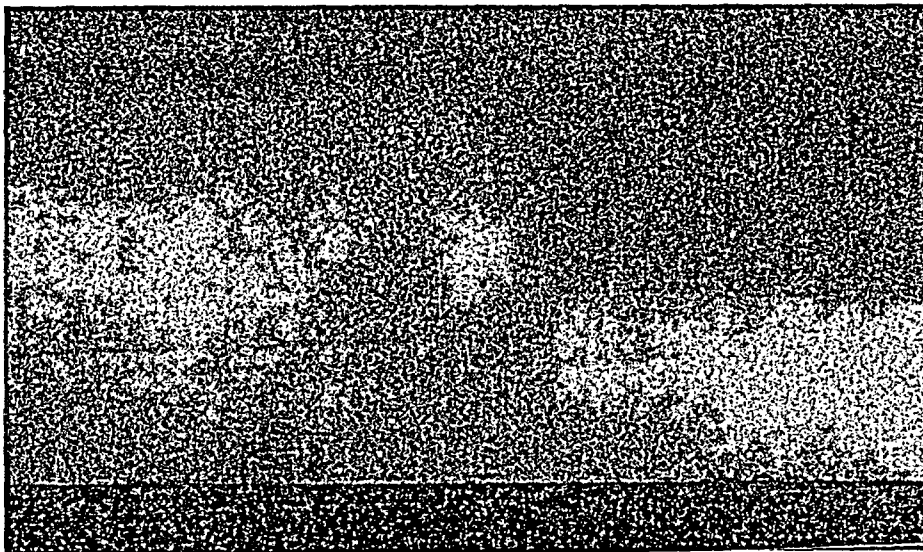


Figure 4.8 A photograph of the Farmersville tornado (March 20, 1976), Illinois. Picture was taken by Ivan Weber shortly before it moved through the Jordan Farm (see Figure 4.9).

An aerial survey revealed that a narrow dark line extended across the Thomas Jordan Farm, near Farmersville, Illinois (see Figure 4.9). It was a dark line only one to five feet wide (see Figure 4.10).

We visited the farm in order to learn how the tornado looked like during its farm crossing. Mr. and Mrs. Jordan saw a giant, dark dust devil was coming

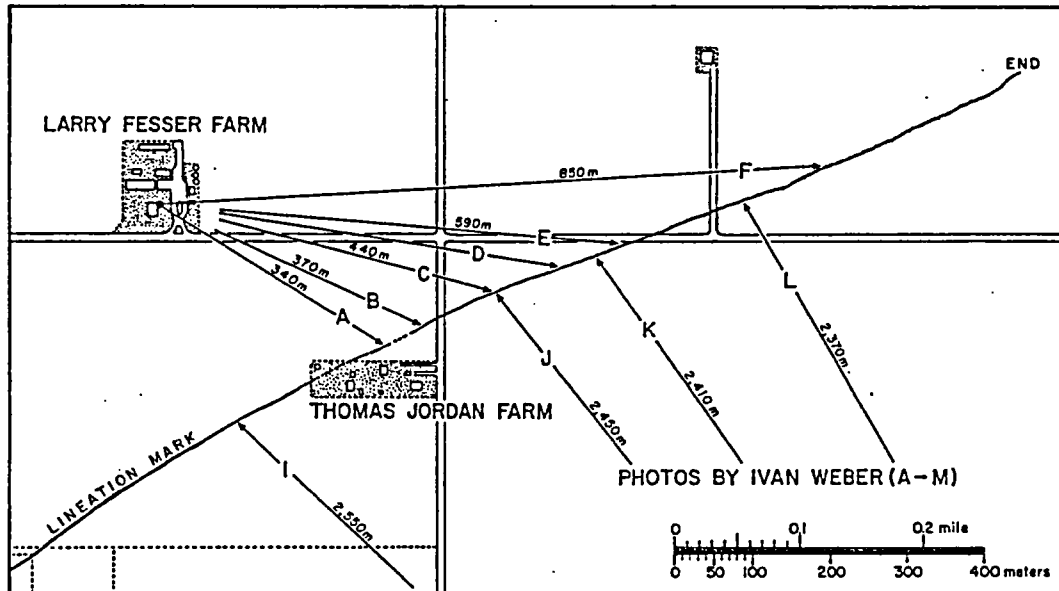


Figure 4.9 The path of a small tornado (Farmersville tornado) across the northwest corner of Thomas Jordan Farm in central Illinois.

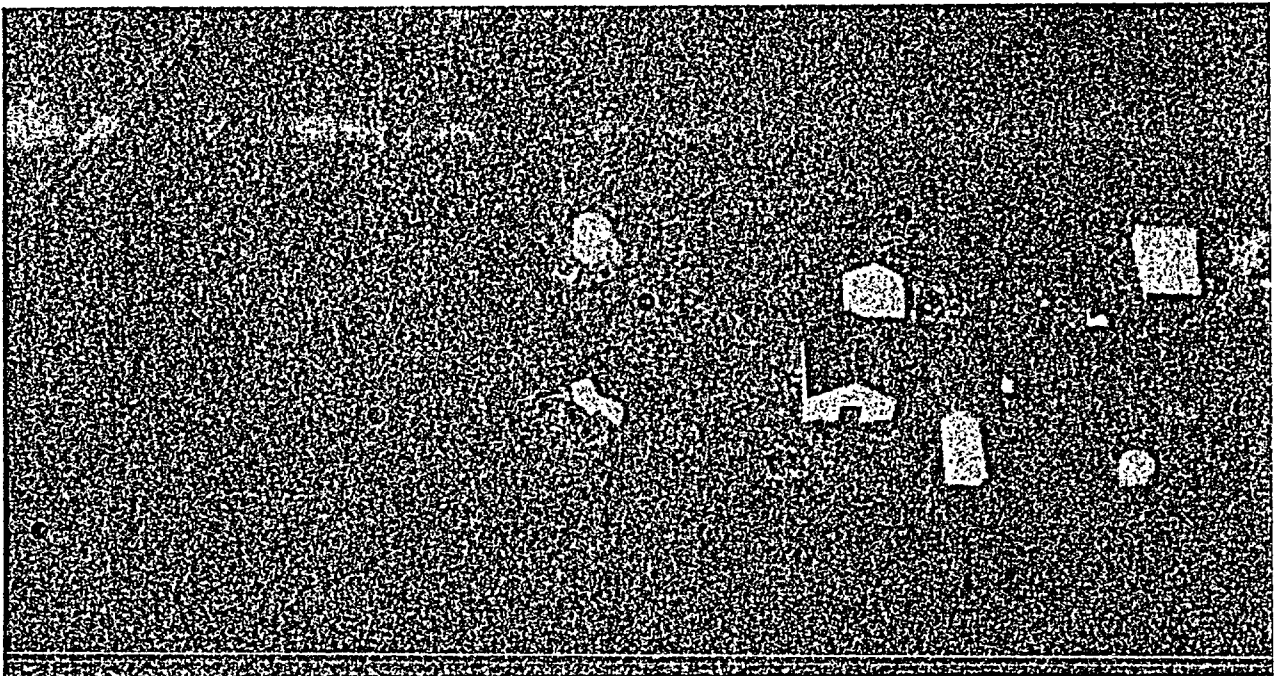


Figure 4.10 An aerial photograph of Thomas Jordan Farm. Path of the tornado is indicated by a series of dots.

toward them. They went down into the basement. There was a loud roar and the air became extremely dusty. After the roar was over, they came out of the basement to find practically no damage to the structure.

The small tornado passed between their metal silo and a barn (see Figure 4.10). Only a small branch of a tree next to the silo was blown down. The damage was much less than expected from the loud roar and blinding dust (see Figure 4.11).

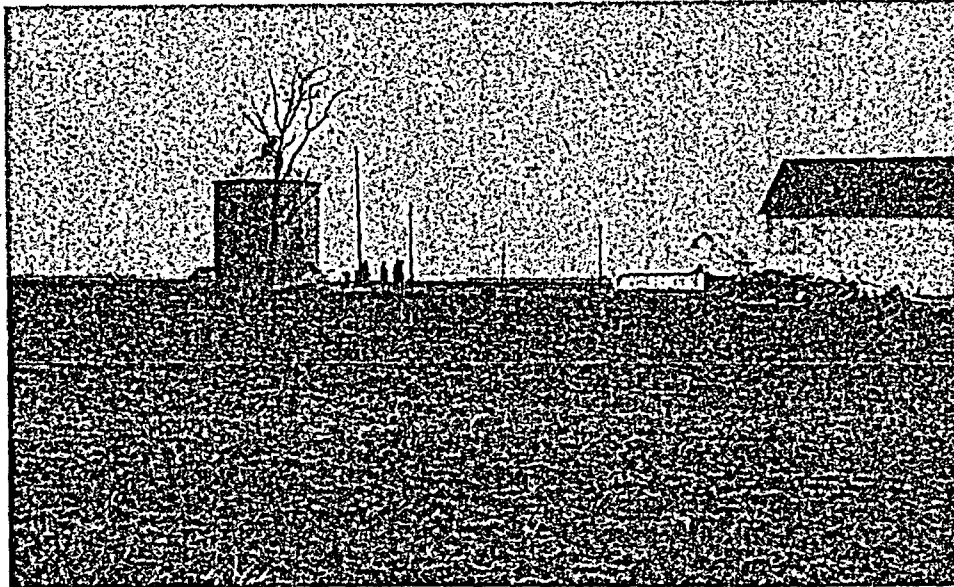


Figure 4.11 A ground photograph of Thomas Jordan Farm. The tornado passed between a metal silo and a barn without damaging either of them.

Mr. Larry Fesser watched the tornado from his farm 330 m (1000 ft) away. One of the pictures (see Figure 4.12) he took revealed the existence of a rope-shaped funnel, 2 to 5 feet in diameter, extending down to about 30 m (100 ft) above the ground. The maximum windspeed of this tornado was probably about 100 mph in order to produce the funnel cloud and swirling thick dust. The radius of maximum wind estimated from photographs was less than 3 m (10 ft), small enough to move between two structures without damaging either one of them. The damage could have been entirely different if it had moved directly over one of the barns.

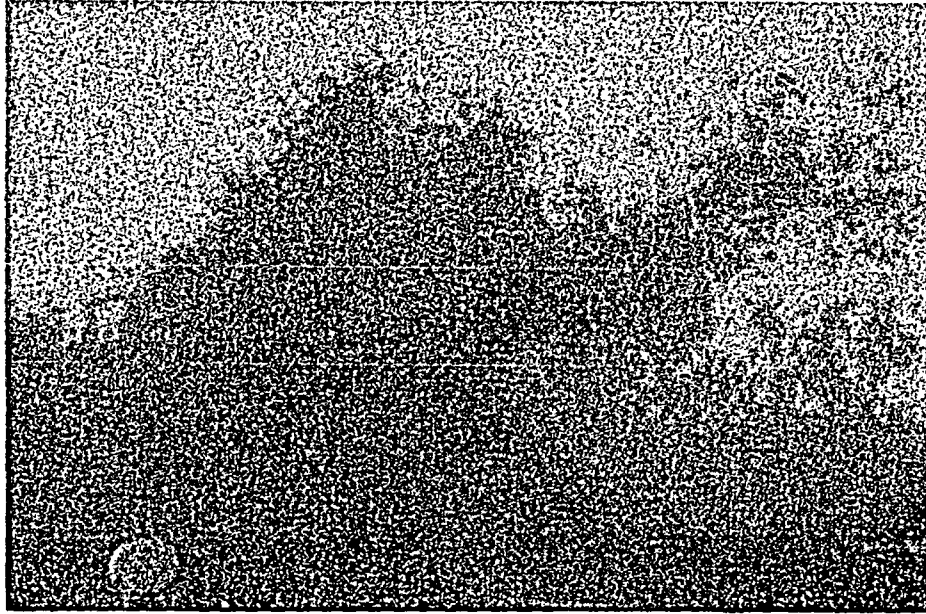


Figure 4.12 A picture of the tornado immediately after it passed through Thomas Jordan Farm. A rope-shaped funnel is seen along the center axis.

4. Large Tornado

Numerous photographic evidences have been accumulated to support the existence of multiple sub-tornado scale vortices hidden inside a large tornado (see Figure 4.13).

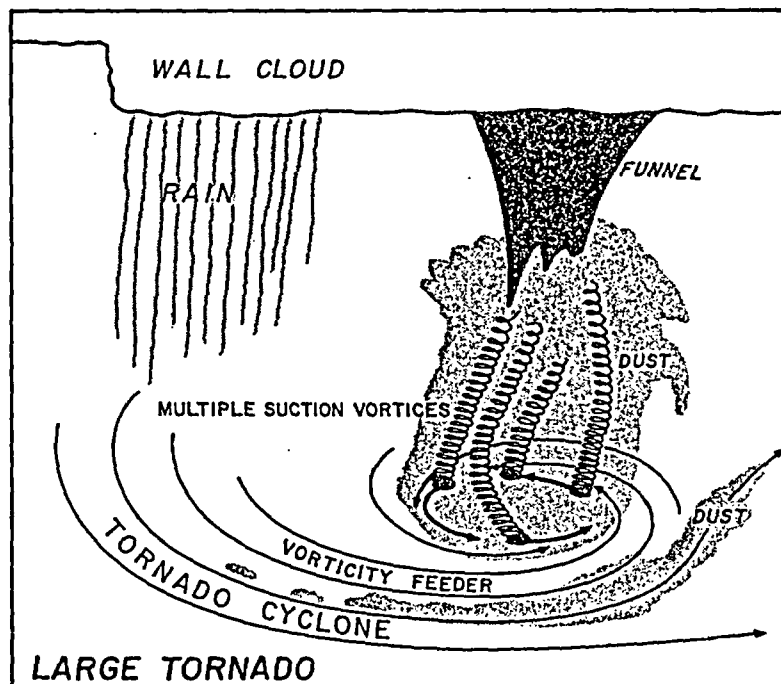


Figure 4.13 A schematic view of a large tornado with suction vortices.

These small vortices, called suction vortices, are characterized by fast translational velocity, up to 100 mph maximum tangential velocity, and their small diameter.

A huge dust column of the Sadorus, Illinois, tornado (see Figure 4.14) gives an impression of a single-vortex, giant tornado. It was moving from left (west) to right at about 45 mph.

An aerial survey of the field swept by this giant dust swirl showed a number of cycloidal curves likely to be caused by a number of suction vortices which moved around the fast-traveling tornado (see Figure 4.15).

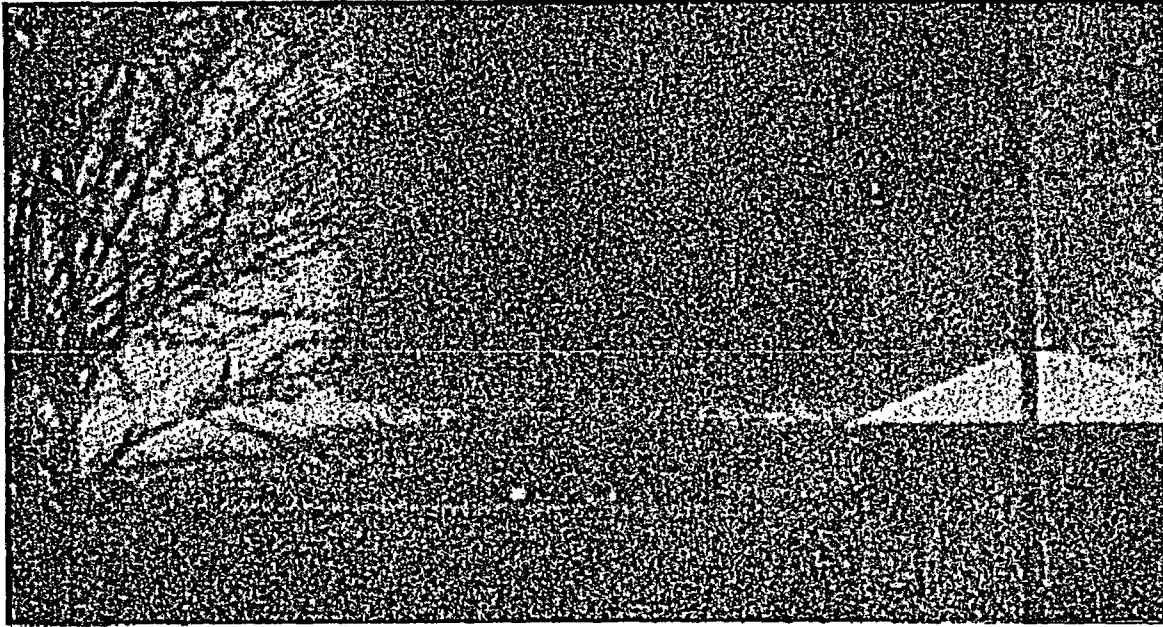


Figure 4.14 Dust column of the Sadorus tornado of March 20, 1976. This is an enlargement of a frame of a movie taken by Mr. Wilson southwest of Sadorus, Illinois.

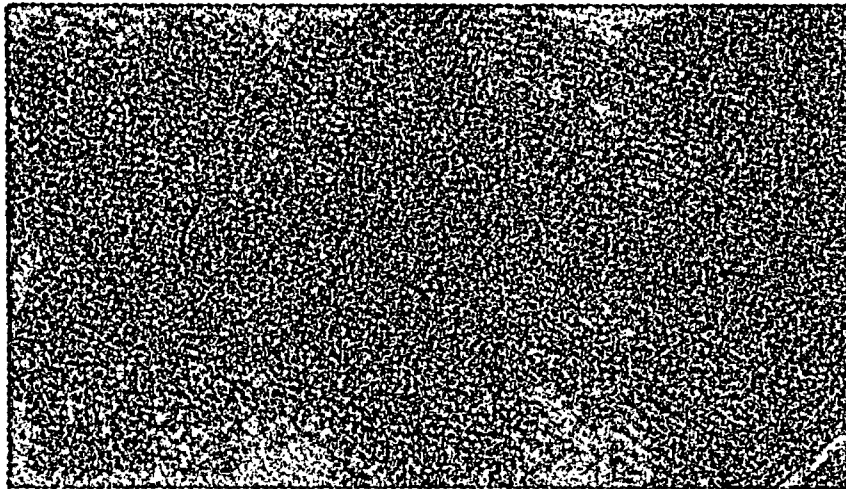


Figure 4.15 An aerial photograph of the ground swept by the Sadorus tornado in Figure 4.14. Cycloidal ground marks suggest an existence of suction vortices.

5. Suction Vortex

Suction vortices hidden deep inside large tornado can rarely be seen. One of the rare views of suction vortices in action was photographed by Mr. Hubbard of WISH-TV, Indianapolis, Indiana.

Aerial photographs reveal frequently an existence of cycloidal marks on open field (see Figure 4.16). Occurrences of these marks are quite common despite the fact that they had been assumed to be rare.

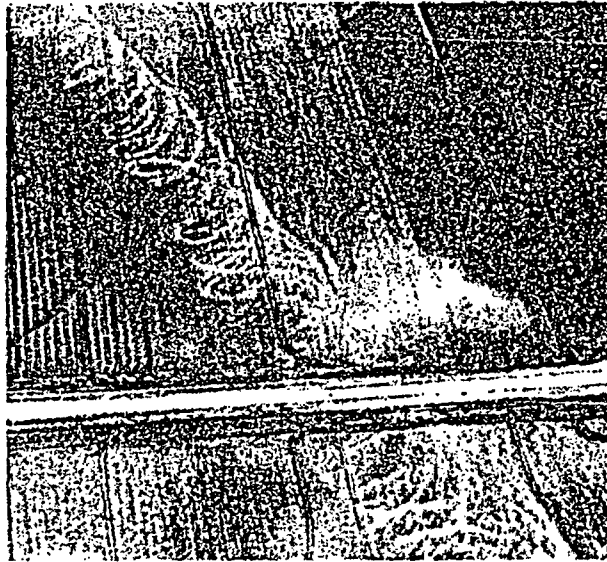


Figure 4.16 Cycloidal ground marks left behind by the Anchor, Illinois, tornado of April 3, 1974.

An example of a vertical view of cycloidal marks is shown in Figure 4.17. These lines are perfect cycloids obtained by combining a rotational with a translational motion. The ratio of these two velocities (motions) can be computed from their geometric features.

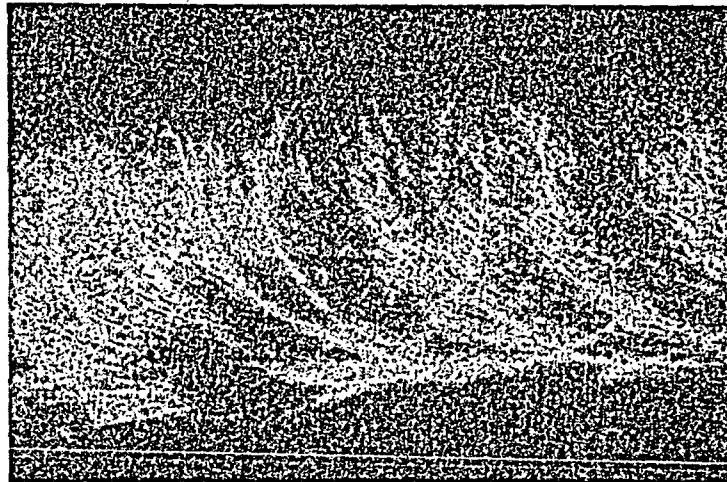


Figure 4.17 Cycloidal ground marks by the Magnet, Nebraska tornado of May 6, 1975. Ground survey reveals, almost always, that light-colored marks are low piles of debris collected and left behind by suction vortices.

What are these cycloidal marks? Ground survey shows that they consist of the deposit of light objects (see Figure 4.18). A suction vortex, spinning 50-100 mph, collects these objects caught inside the inflow air. Most of the objects become airborne and are thrown out of the vortex as they are lifted inside the swirling updraft. Those accumulated around the vortex center above the ground (below 5 inches) remain on the ground because the windspeed "at the ground" is zero.

The circle of maximum tangential wind passes over the low-height deposit without removing the light objects. After the passage of a suction vortex, a deposit line (band) is left behind, revealing the path of the vortex center. When lines are light in color, the deposit usually consists of corn stubbles or pieces of straw. Dark lines are of piles of dark soil only two to three inches deep. It is rather hard to identify these deposit lines on the ground even if we know where to look for. Aerial inspection and photography are the only means of their detection.

Swirl marks of a suction vortex can be found in a field of low grass. One- to three-foot tall grass is ideal. Duane Stiegler took a beautiful color picture of a swirl mark (see Figure 4.19) on a grass land in Wisconsin. A suction vortex moving from left to right ended suddenly within a few milliseconds.

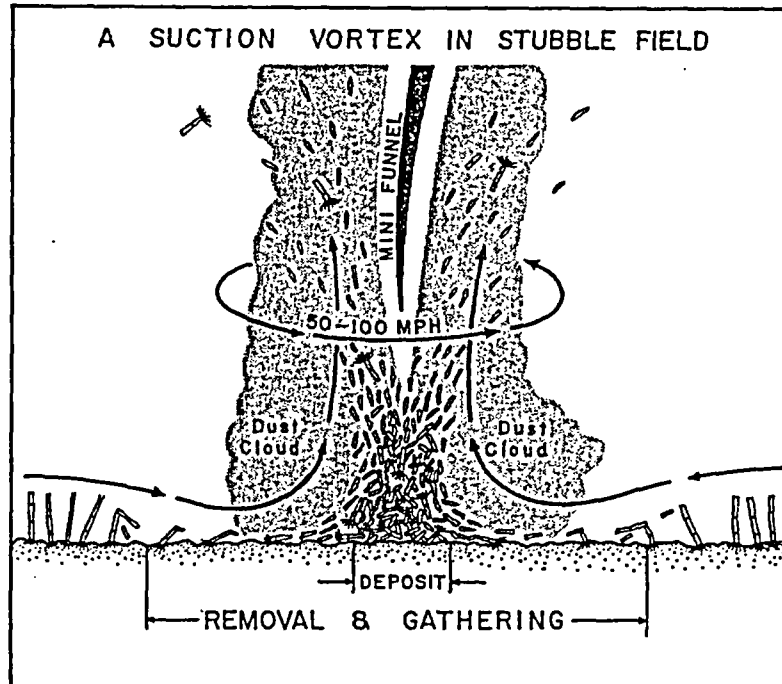


Figure 4.18 Schematic cross section of a suction vortex which collect small debris as it swirls on the field. Due to low-wind-speed just above the ground, a part of the collected debris is left behind along the vortex paths.

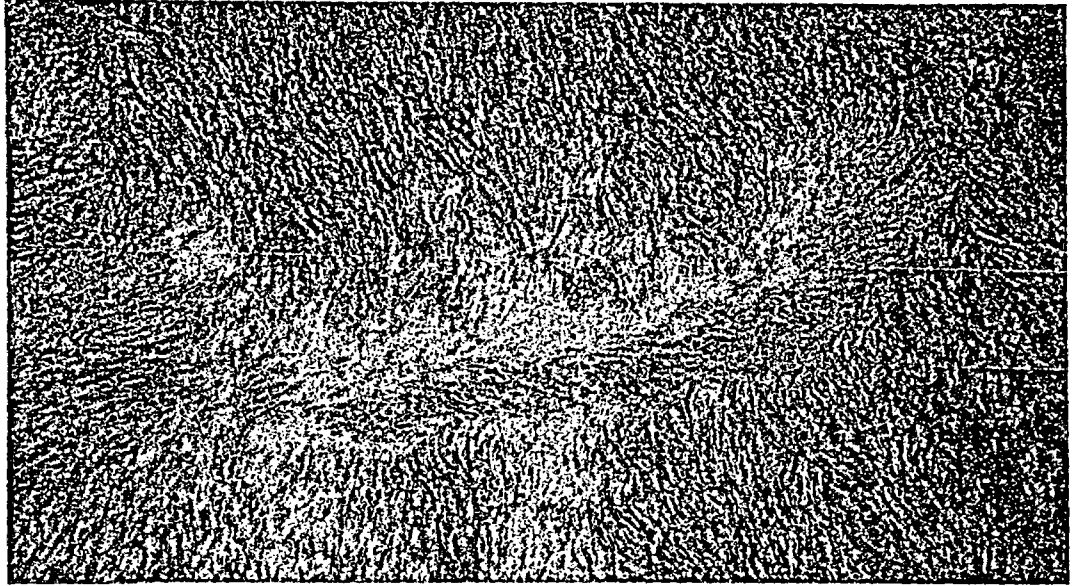


Figure 4.19 Suction vortex marks left in a grass field near Haricon Marsh, Wisconsin. Photo by Duane Stiegler from 500 ft AGL.

A suction vortex in a very large tornado is likely to split into a pair of twin vortices. The cycloidal marks of twin vortices appear like a railroad track. They form parallel lines. Due to the vortex interactions, however, these parallel lines, sooner or later, cross each other suggesting that twin vortices rotate around their common center of the vortex circulation (see Figure 4.20).

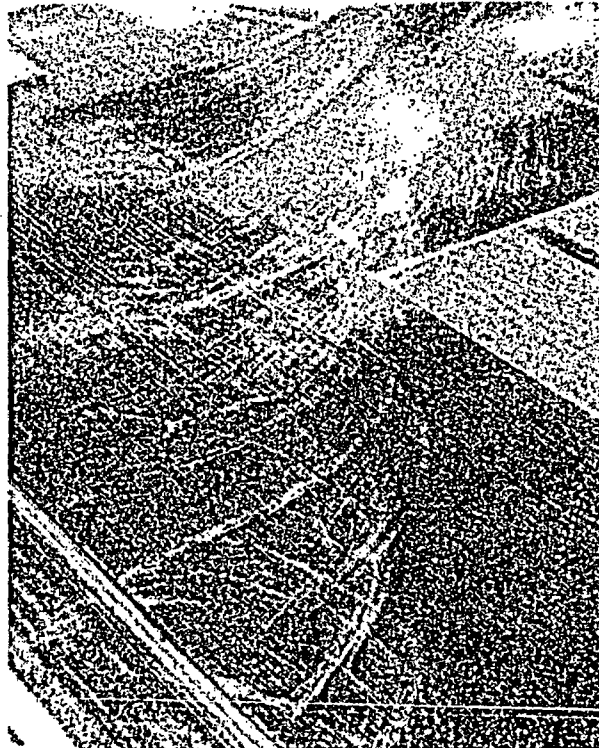


Figure 4.20 Unusual cycloidal marks generated by twin suction vortices. Some of the marks are characterized by double lines only 5 to 10 ft apart.

Sometimes, a suction vortex remains at one location for a short time and dies out. The swirl mark of this type of vortex is shown in Figure 4.21. It should be noted that a small, weak-wind area, is located near the vortex center, suggesting that there is a vortex eye.

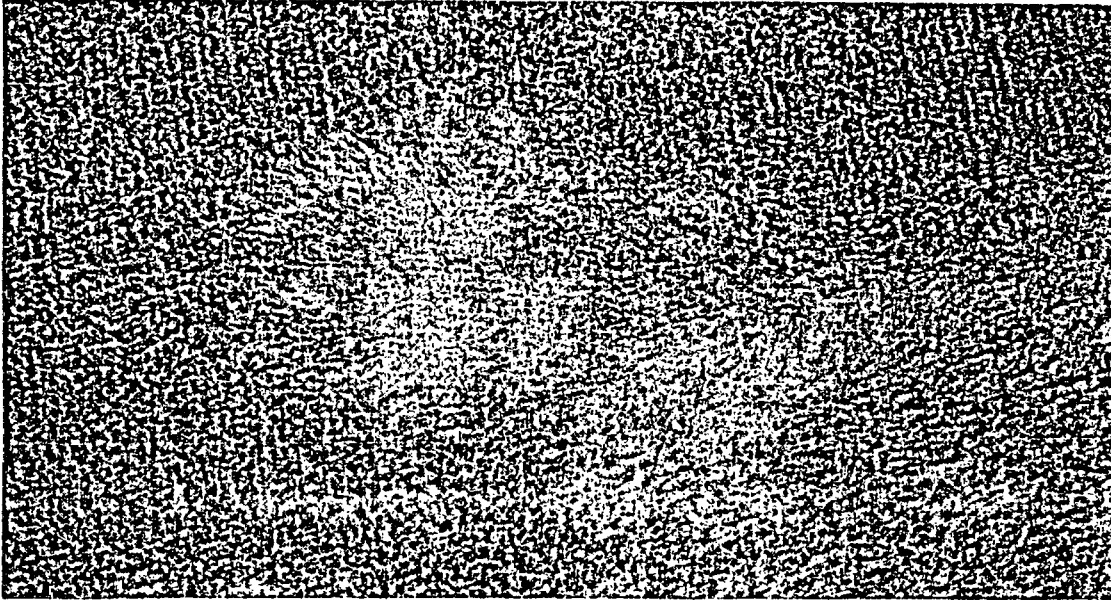


Figure 4.21 A swirl pattern produced by a stationary suction vortex. A weak-wind region, somewhat like a vortex eye, is seen near the center of the swirl mark.

Considerable experience and skill are required in detecting and photographing suction-vortex marks left on the ground. When marks are viewed toward the directions of

- a. Antisolar point, directly opposite from the sun, and
- b. forward scattering of sunlight,

most marks appear brighter than their environment (see Figure 4.22).

When the same marks are photographed from different directions, they may appear to be darker than their environment (see Figure 4.23).

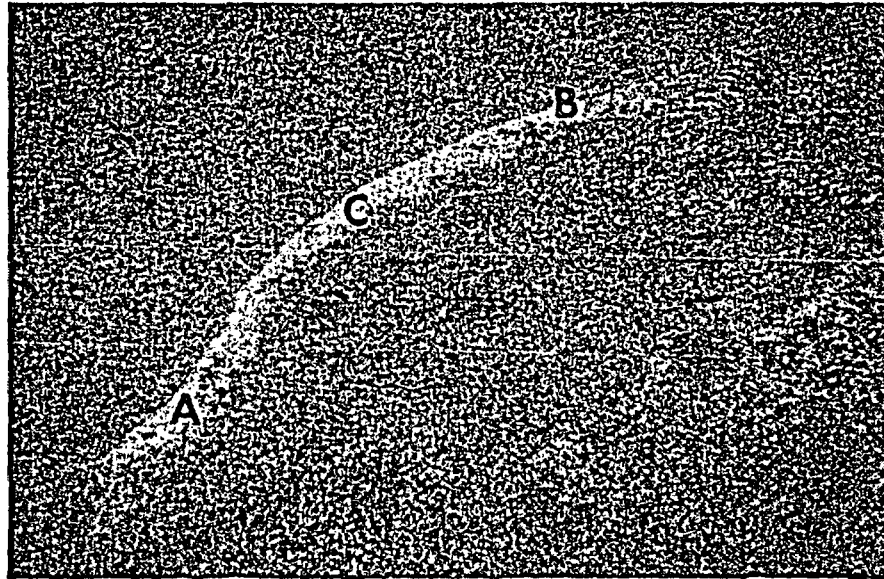


Figure 4.22 A suction vortex mark viewed toward the antisolar point. No shadow appears toward this direction, resulting in a light vortex mark. Vortex mark also appears bright when viewed toward the direction of forward scattering.

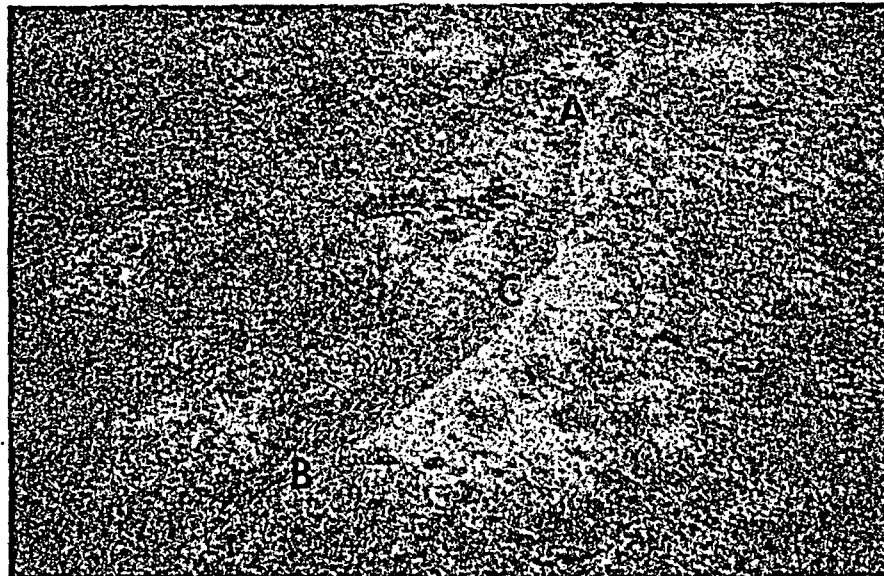


Figure 4.23 The same vortex mark viewed toward 90 degrees from the antisolar point. Effect of shadows turn the vortex mark into gray.

This means that suction-vortex marks are not always visible unless proper directions of view are selected by those who survey the tornado area. The author and his associates found numerous vortex marks where other aerial inspectors had failed to find any sign of these vortex marks.

6. Aerial Survey of Grand Gulf Tornado

The author performed an aerial survey and photography of the Grand Gulf Nuclear Power Plant (under construction) hit by the April 17, 1978 tornado. Refer to Fujita (1978) and McDonald (1978).

Figure 4.24 shows the flow pattern of the first wind on the front side of the approaching tornado. Flow lines, which may not represent streamlines or trajectories, were drawn based on damage directions shown by solid arrows.

The second wind mapped in Figure 4.25 was on the rear side of the tornado. Note that most areas of the power plant were hit twice, by the first and second winds.

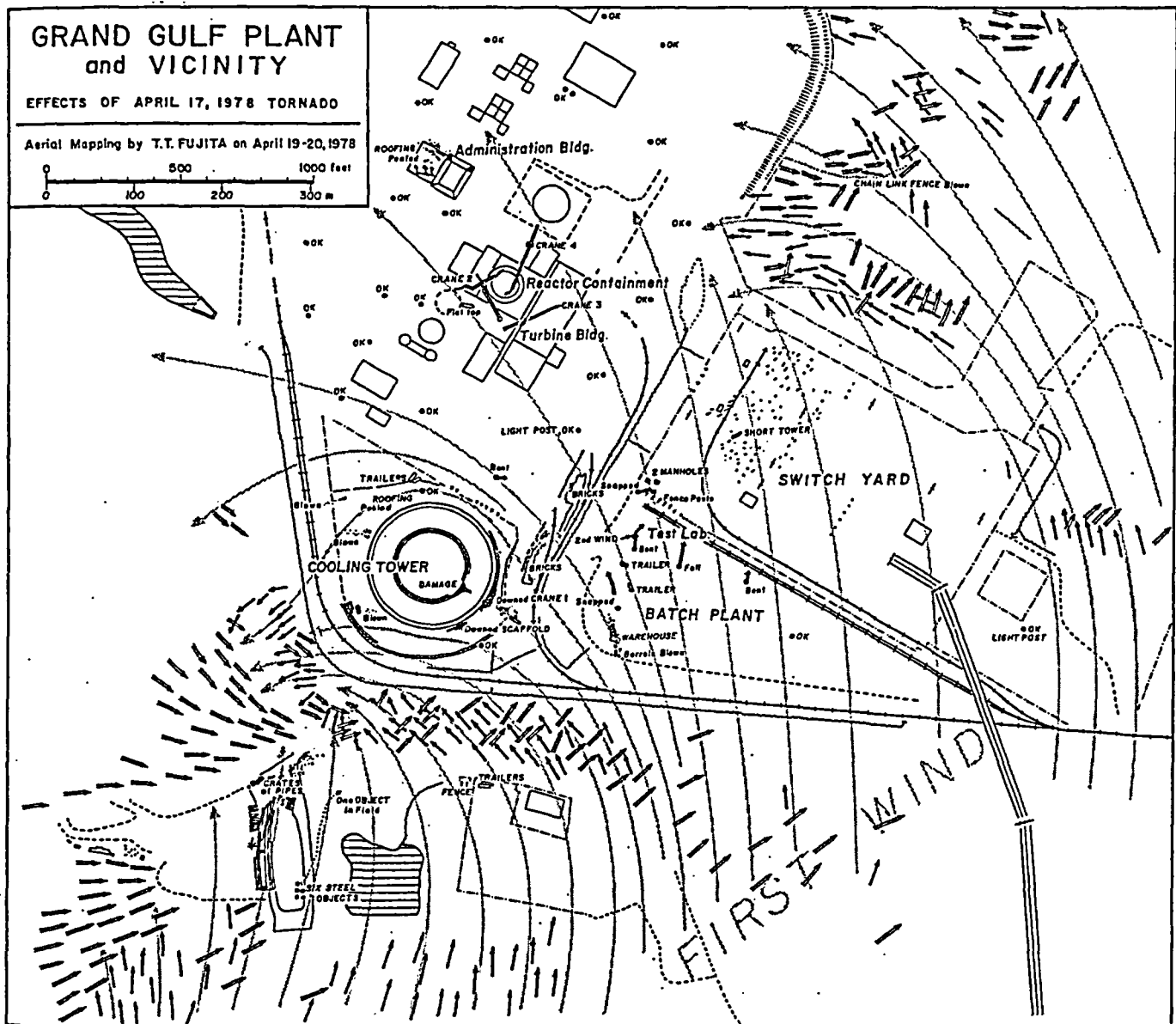


Figure 4.24 Airflow (close to trajectory) on the front side of the Grand Gulf tornado of April 17, 1978.

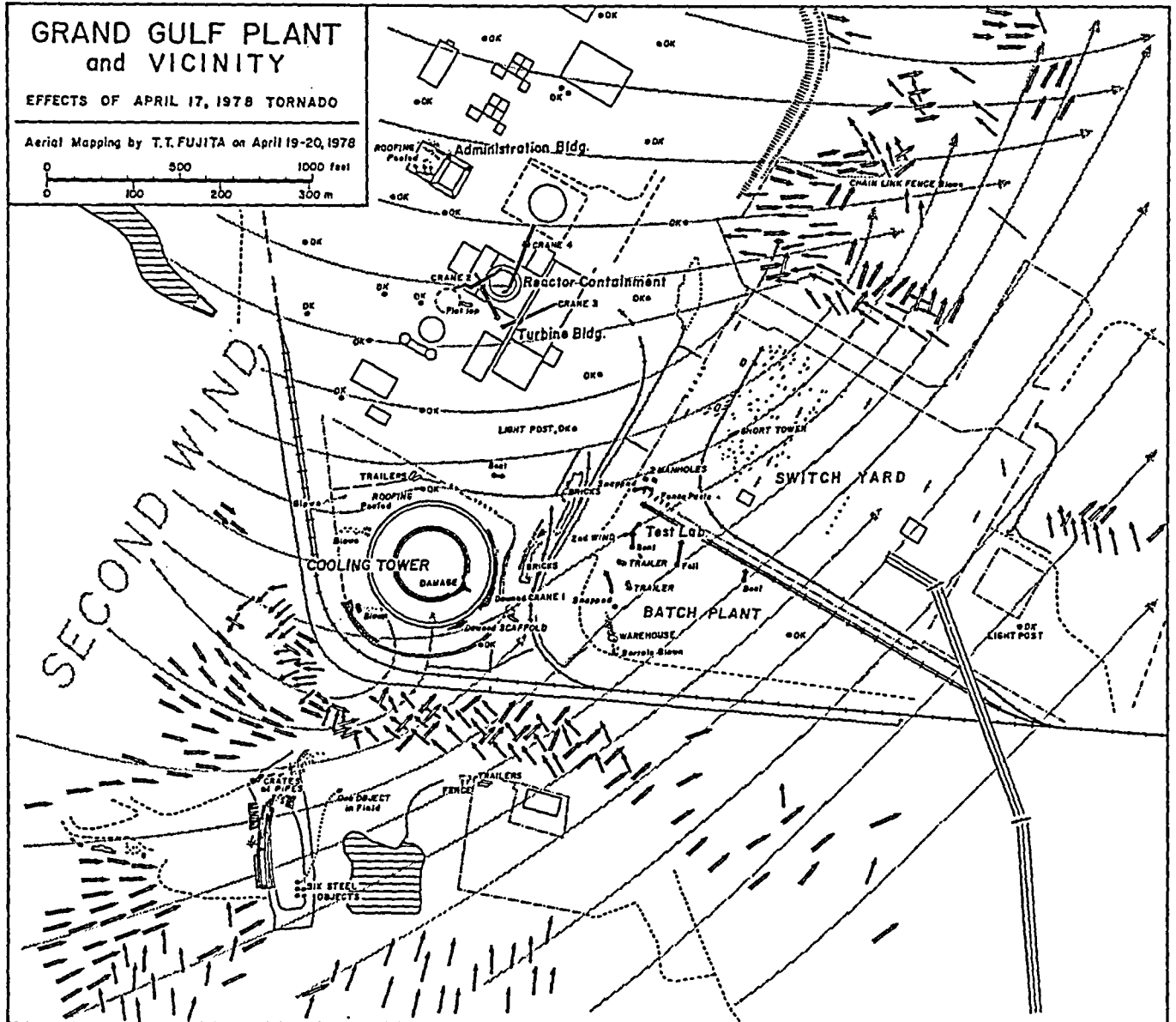


Figure 4.25 Airflow (close to trajectory) on the rear side of the Grand Gulf tornado of April 17, 1978.

Close-up views of the damaged cooling tower (under construction) are shown in Figures 4.26 (from outside) and 4.27 (toward outside). These pictures were taken by the author aboard Cessna 182.

A steep banking maneuver of the aircraft is necessary while taking high-oblique pictures. A 20 to 45 degree bank is commonly used by the author. The airspeed during such photography is chosen to be less than 110 kts as long as the speed is kept above the level of the stall alarm.

Continuous turning around a photographic object should be avoided, because an aircraft does not approach the object. An airborne photographer must tell the pilot first to move away from the object a few tenths of a mile, then approach straight toward the intended location where the camera shutter is pressed.

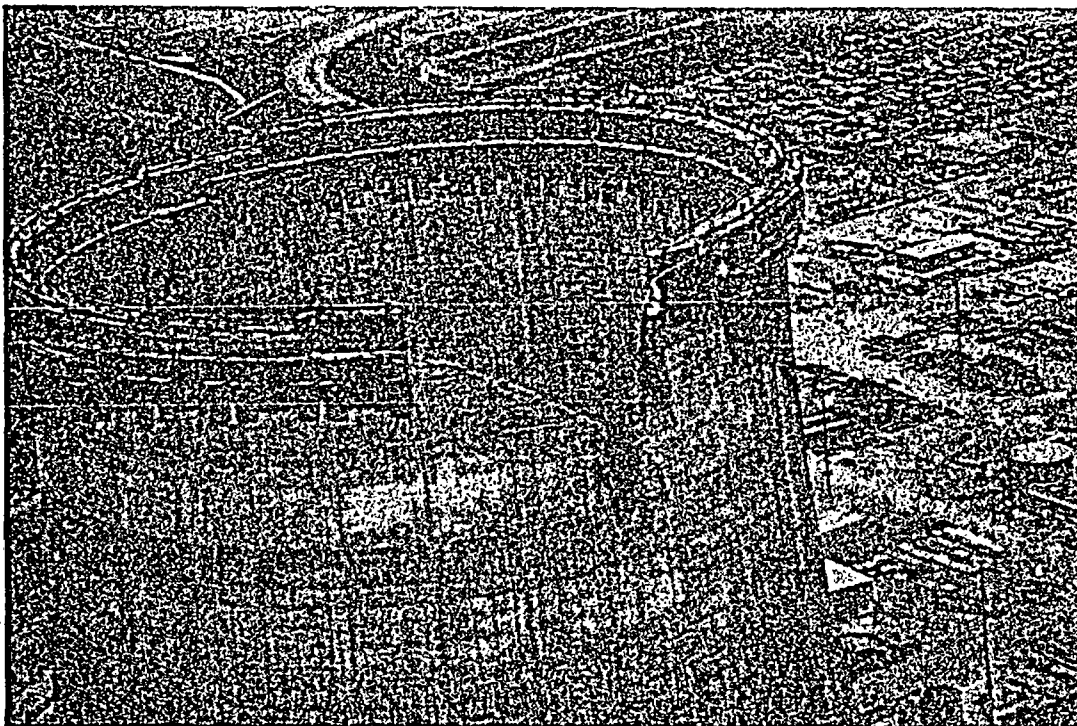


Figure 4.26 A telephoto view of the scaffold/wall damage of the cooling tower under construction. Observe a small, dark hole, on the wall.

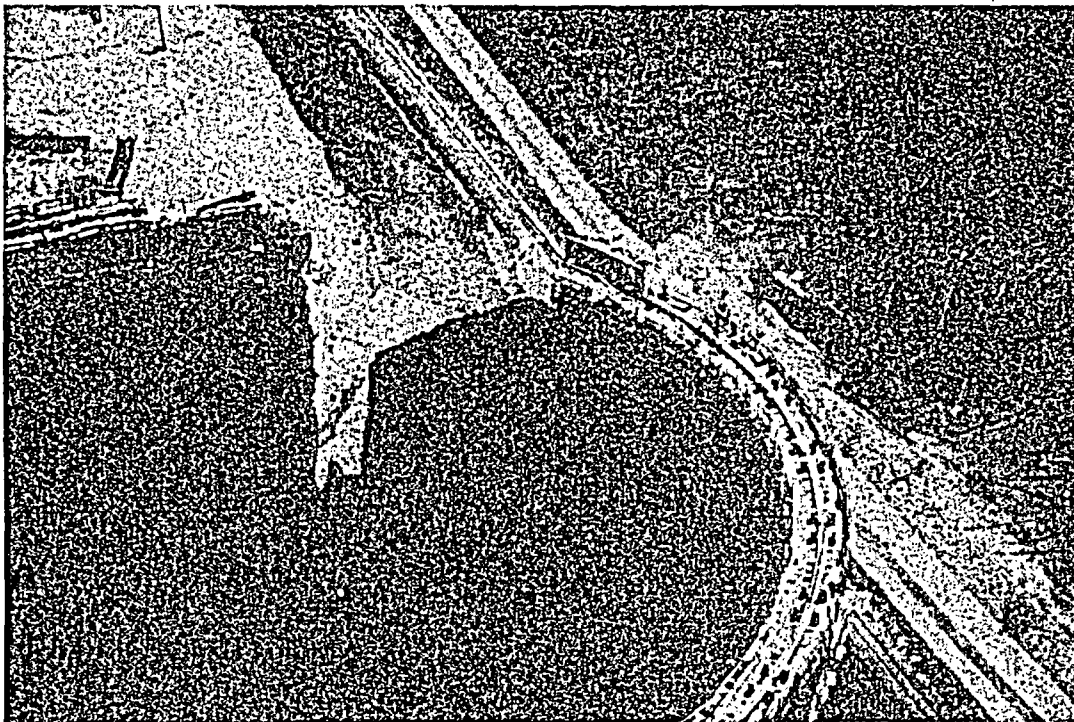


Figure 4.27 A high-oblique view of the cooling tower. A small hole on the wall is white against the background viewed toward the outside.

The line of the flight is highly sensitive to the wind direction and speed which causes a significant drift of low-air-speed aircraft.

Upon reaching the intended photographic spot, banking of the aircraft is executed immediately. After confirming the field of photographic angles through the view finder, the shutter is pressed during a steep bank. During a banking period of 2 to 5 seconds, several frames can be exposed by pressing down the shutter one after another.

The shutter speed is kept at 1/250 sec for regular photos and at 1/500 sec, for telephoto views. Since the author tried to float (with one-inch airspace) above the seat when the shutter is pressed, less than 1/500 sec shutter speed has never been used. Note that 1/1000 and 1/2000 sec speeds are often inaccurate.

It is extremely important to keep enough air space above photographic objects. The upwind side of a large object, such as this cooling tower, is always less turbulent than the wake region. Furthermore, the turbulence in each traverse is different, because the wind gust and subsequent airflow around the object change in a time scale of 10s of seconds.

Stick pieces of black tapes around the camera lens with a UV (ultra violet) filter on it. Tapes will avoid reflection and protect the aircraft window from being scratched. The author wears dark-colored shirt during his aerial photographic missions.

Since his first aerial survey of the Palm Sunday tornadoes, April 11, 1965, the author has flown over 20,000 miles in Cessna 172, 182, or 210. More than 250 paths of tornadoes and downbursts were flown over, taking more than 5,000 pictures.

CHAPTER FIVE

TORNADO STATISTICS AND DATA BASE

Since 1916 when the official collection of tornado data began, the numerical counts of tornadoes or so-called "tornado frequencies" have been used in assessing the tornado risk.

It has been known, on the other hand, that some tornadoes are small, short-lived, and weak while others are large, long-lived, and violent.

In an attempt to assess the "true tornado risk," rather than the "frequency-oriented risk," Fujita and his associates at the University of Chicago began mapping the paths of tornadoes and classifying each tornado using the Fujita scale (F scale) outlined in Chapter 1.

In the meantime, the frequency, N , and the path length, P , within each $15' \times 15'$ subbox were obtained through the painstaking process of mapping and plotting of all reported tornadoes during the 62-year period, 1916 through 1977.

The total values of both n and p within the $\Delta\phi \times \Delta\theta$ square are computed from

$$N = \sum_{\phi}^{\phi + \Delta\phi} \sum_{\theta}^{\theta + \Delta\theta} n \quad (n, \text{ count of tornadoes})$$

and

$$P = \sum_{\phi}^{\phi + \Delta\phi} \sum_{\theta}^{\theta + \Delta\theta} p \quad (p, \text{ path length of each tornado})$$

where N denotes the total number and P the total path length of tornadoes within the $\Delta\phi \times \Delta\theta$ square of latitude and longitude. When $\Delta\phi = \Delta\theta = \text{one degree}$, N and P are expressed by

$$N_1 = \sum_{\phi}^{\phi + 1^\circ} \sum_{\theta}^{\theta + 1^\circ} n$$

and

$$P_1 = \sum_{\phi}^{\phi + 1^\circ} \sum_{\theta}^{\theta + 1^\circ} p$$

where N_1 and P_1 are the total number and the total path length of tornadoes within the "one-degree square".

We may, likewise, define $N_2, P_2; N_3, P_3$; etc. which denote the values within $2^\circ, 3^\circ$, etc. squares of latitudes and longitudes. (Note that Marsden, early in the 19th Century, devised "squares" of latitudes and longitudes. A Marsden square represents $1^\circ, 2^\circ, 3^\circ$, etc of latitudes and longitudes). In this workbook, $15' \times 15'$ squares are called "sub-squares" or "sub-boxes".

Figure 1 shows the distribution of P_i during the 62 years, 1916-77. Values were obtained by computing the total path lengths within each 1° , non-overlapping Marsden square.

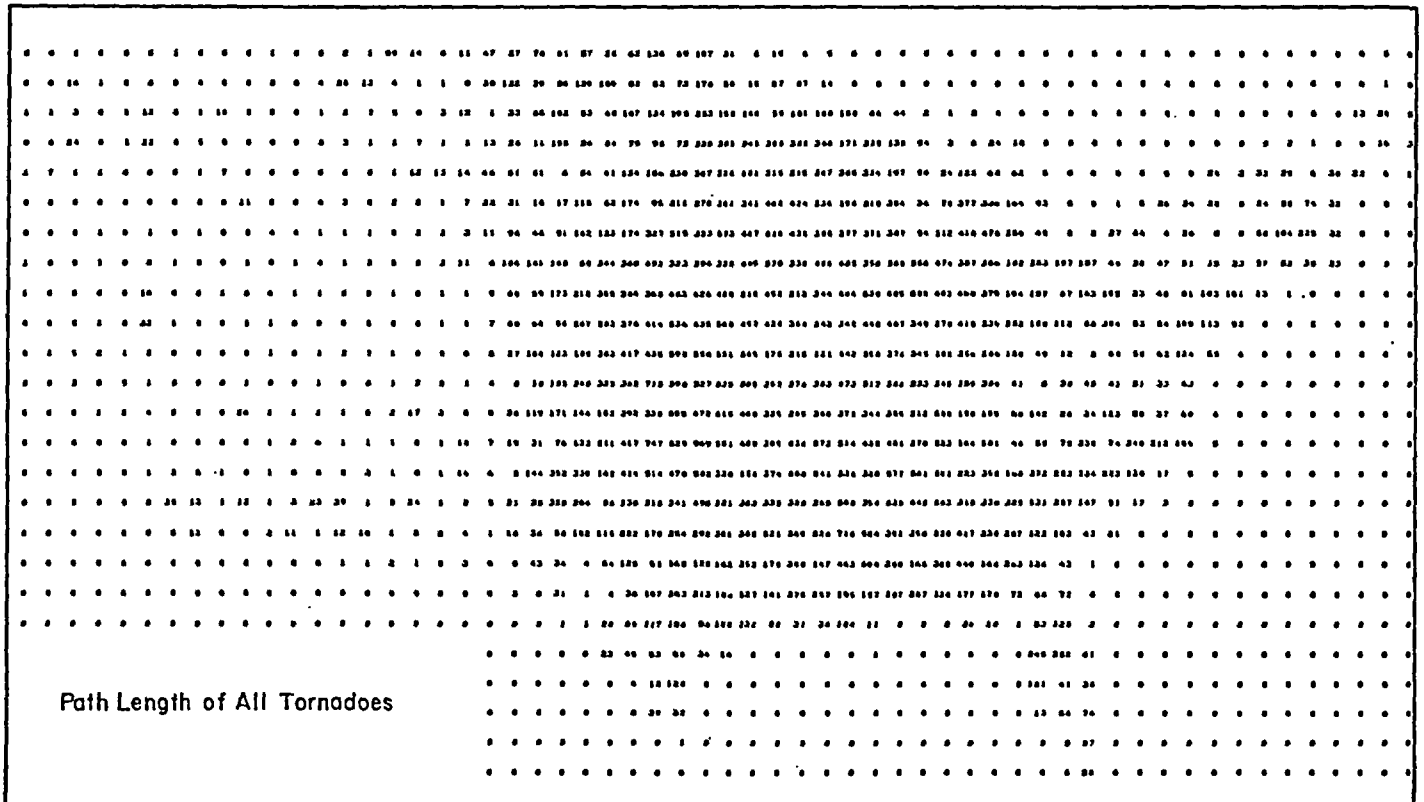


Figure 5.1 Path length of all tornadoes, 1916-1977, within non-overlapping, 1° Marsden squares.

Since computer printouts are made on rectangular coordinates, the U.S. map was distorted to fit to the computer-printout coordinates (CPC). The U.S. map, thus constructed, is called the CPC map (see Figure 5.2).

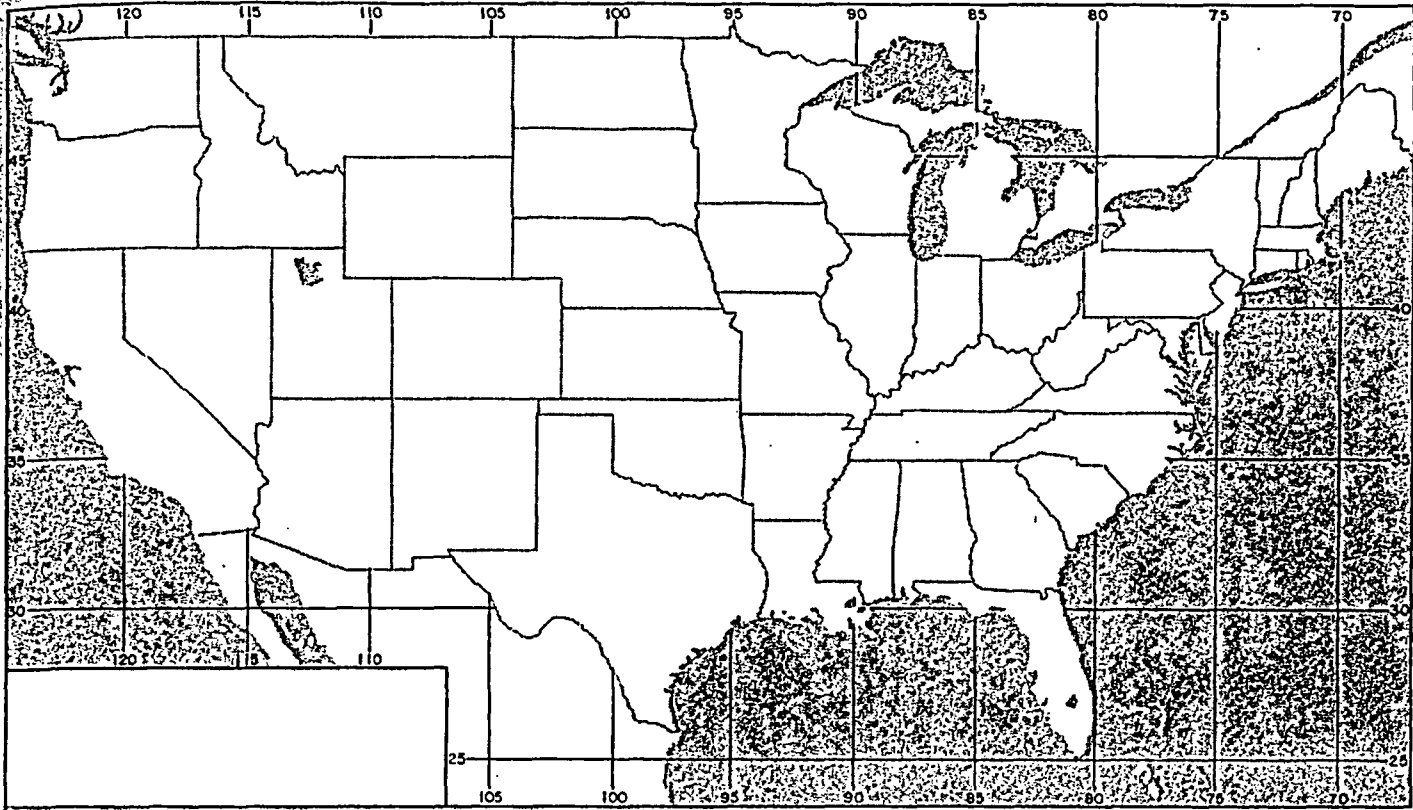


Figure 5.2 Map of the United States distorted to the computer-printout coordinates (GPC), or the GPC map.

A running total within overlapping Marsden squares were computed from

$$N_i = \sum_{\phi}^{\phi+1^{\circ}} \sum_{\theta}^{\theta+1^{\circ}} n$$

by changing

$$\begin{aligned} &= 67^{\circ}, 68^{\circ}, 69^{\circ}, \dots 124^{\circ} \text{W} \\ &= 24^{\circ} 00', 24^{\circ} 15', 24^{\circ} 30', \dots 48^{\circ} 00' \text{N}. \end{aligned}$$

Computed values of N_i were normalized to the area of the Marsden square at $= 37^{\circ}$, thus

$$\bar{N}_i = N_i \frac{\text{Cos } 37^{\circ}}{\text{Cos}(\phi + 0.5^{\circ})}$$

where \bar{N}_i is the latitude-corrected number. The identical correction was applied to P to obtain P_i , the latitude-corrected path length.

Results of computations of N_i and P_i are presented in the following figures.

MAPS OF	FIG. NO.
All (24,148) tornadoes	5.3
F0 + F1 (weak) tornadoes	5.4
F2 + F3 (strong) tornadoes	5.5
F4 + F5 (violent) tornadoes	5.6
Jan. and Feb. tornadoes	5.7
Mar. and Apr. tornadoes	5.8
May and June tornadoes	5.9
July and Aug tornadoes	5.10
Sept. and Oct. tornadoes	5.11
Nov. and Dec. tornadoes	5.12
00 - 03 LST tornadoes	5.13
03 - 06 LST tornadoes	5.14
06 - 09 LST tornadoes	5.15
09 - 12 LST tornadoes	5.16
12 - 15 LST tornadoes	5.17
15 - 18 LST tornadoes	5.18
18 - 21 LST tornadoes	5.19
21 - 24 LST tornadoes	5.20

A brief explanation of the above statistics are given in each of the figure captions.

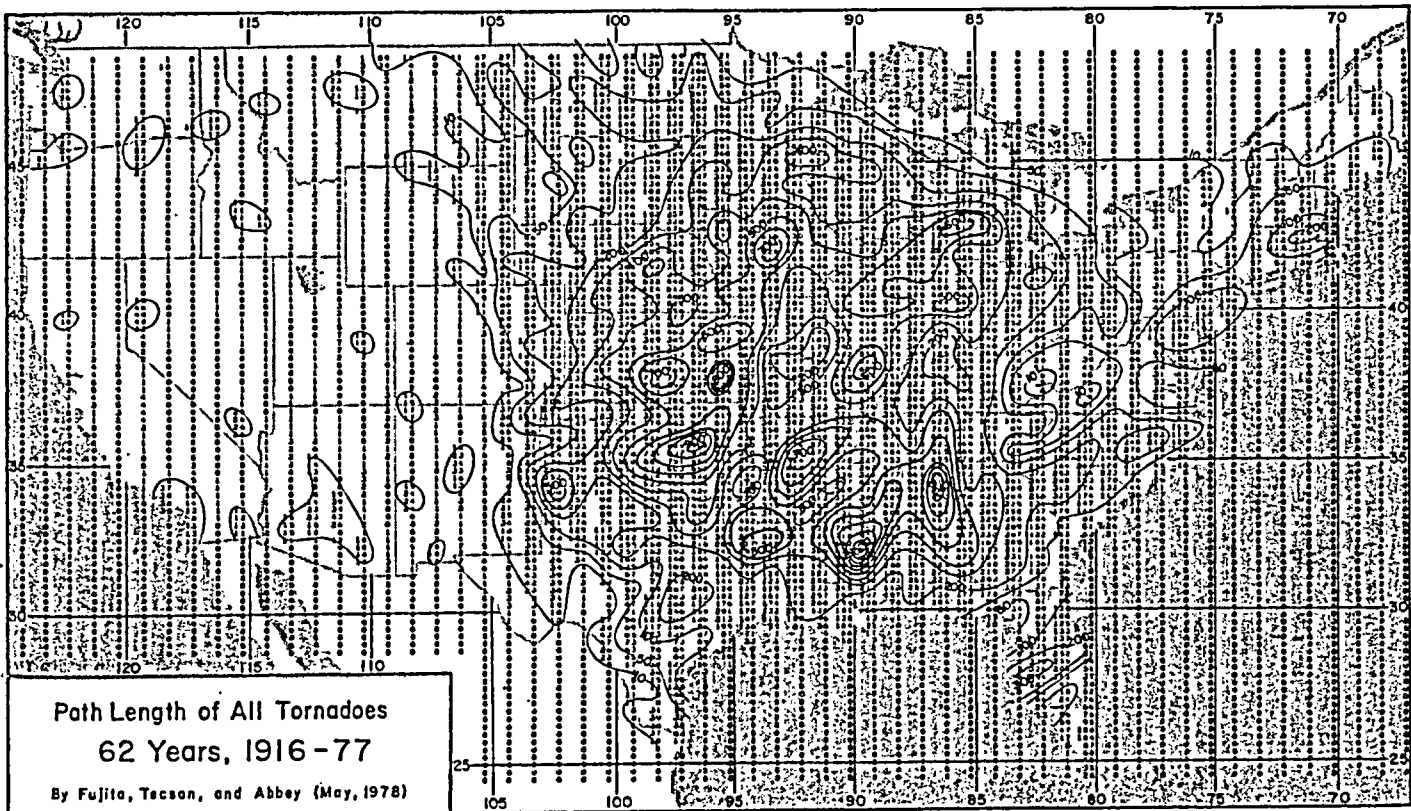
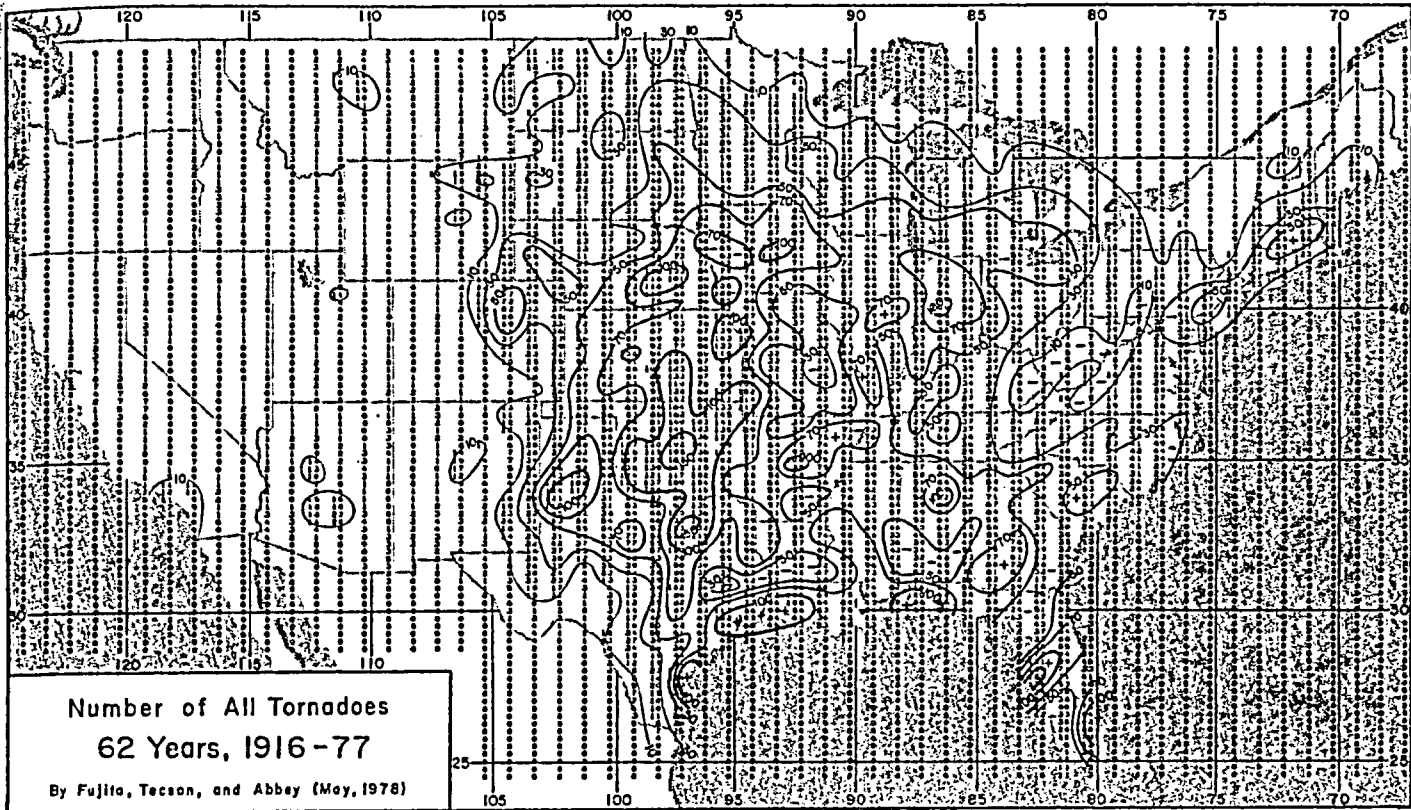


Figure 5.3 The maximum number (195) of tornadoes is seen in central Oklahoma while the maximum path length (1011 miles) is located in Mississippi where number is only 95. There is a significant minima both in N and P in central Missouri and in eastern Kentucky to West Virginia. These minima are resulted by blocking of the low-level moisture by the Ozark and Appalachian mountains.

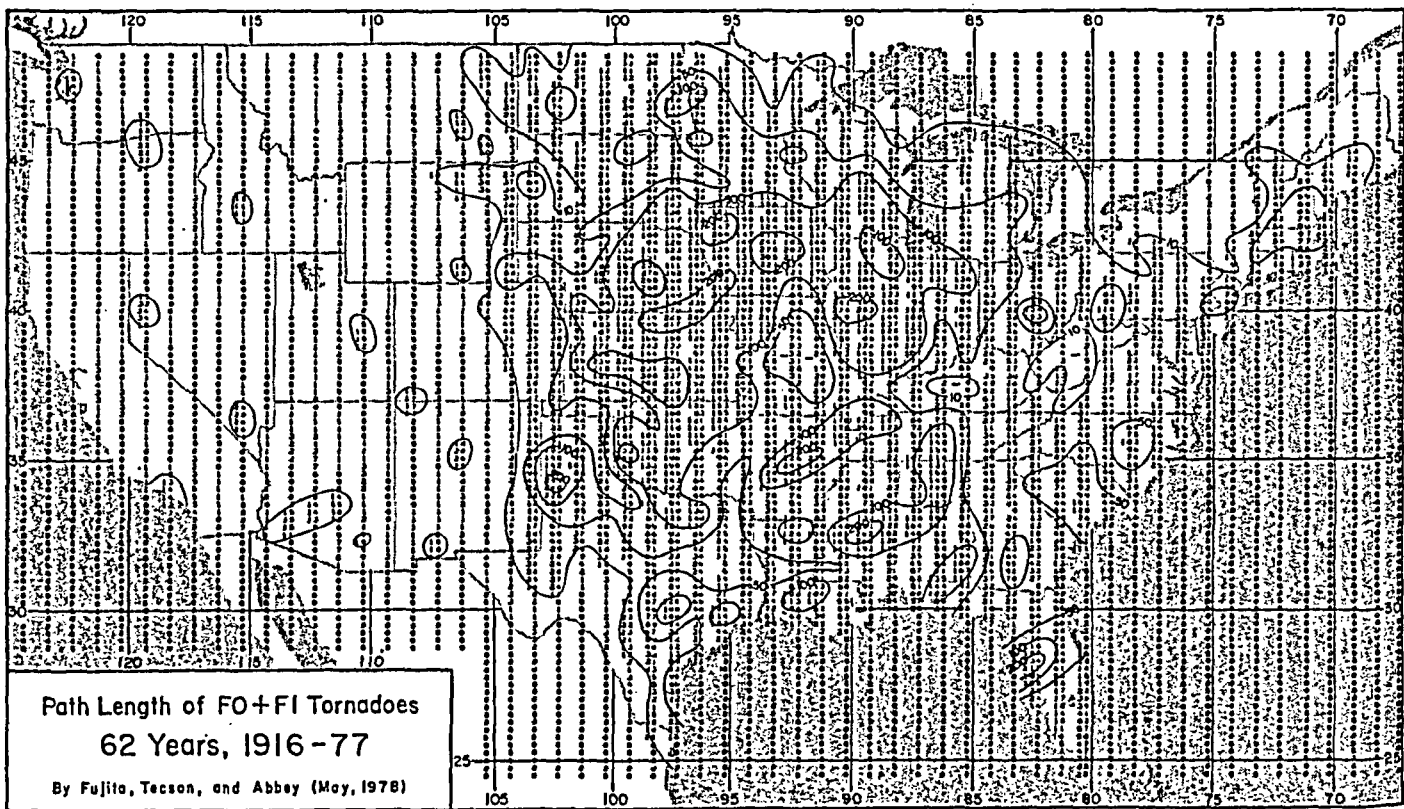
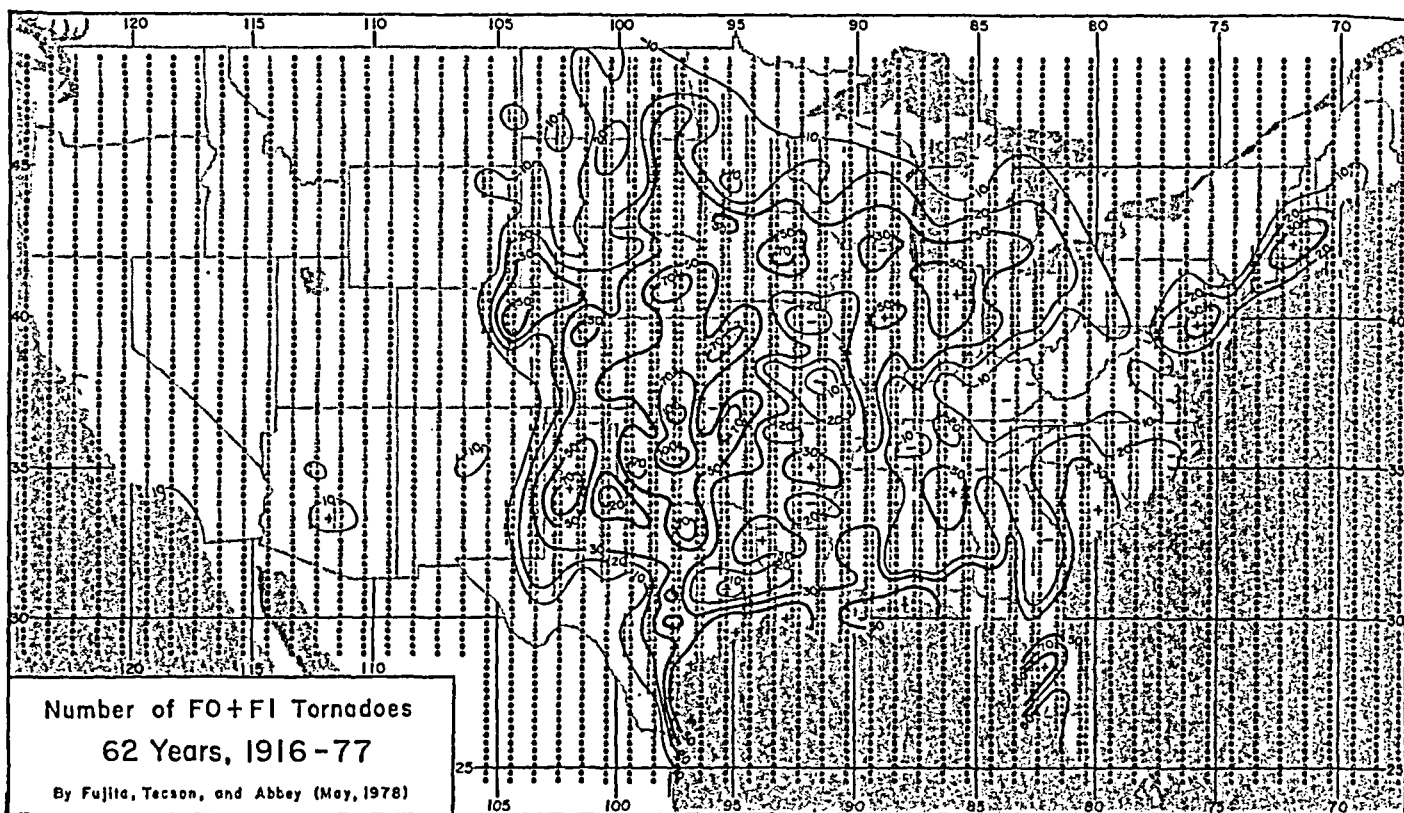


Figure 5.4 Numbers and path lengths of weak (FO + F1) tornadoes. The maximum numbers are seen in Oklahoma-Kansas area while the maximum path lengths are located in Kansas-Iowa-Illinois areas. High numbers are seen along the Gulf coast where hurricane-induced tornadoes occur.

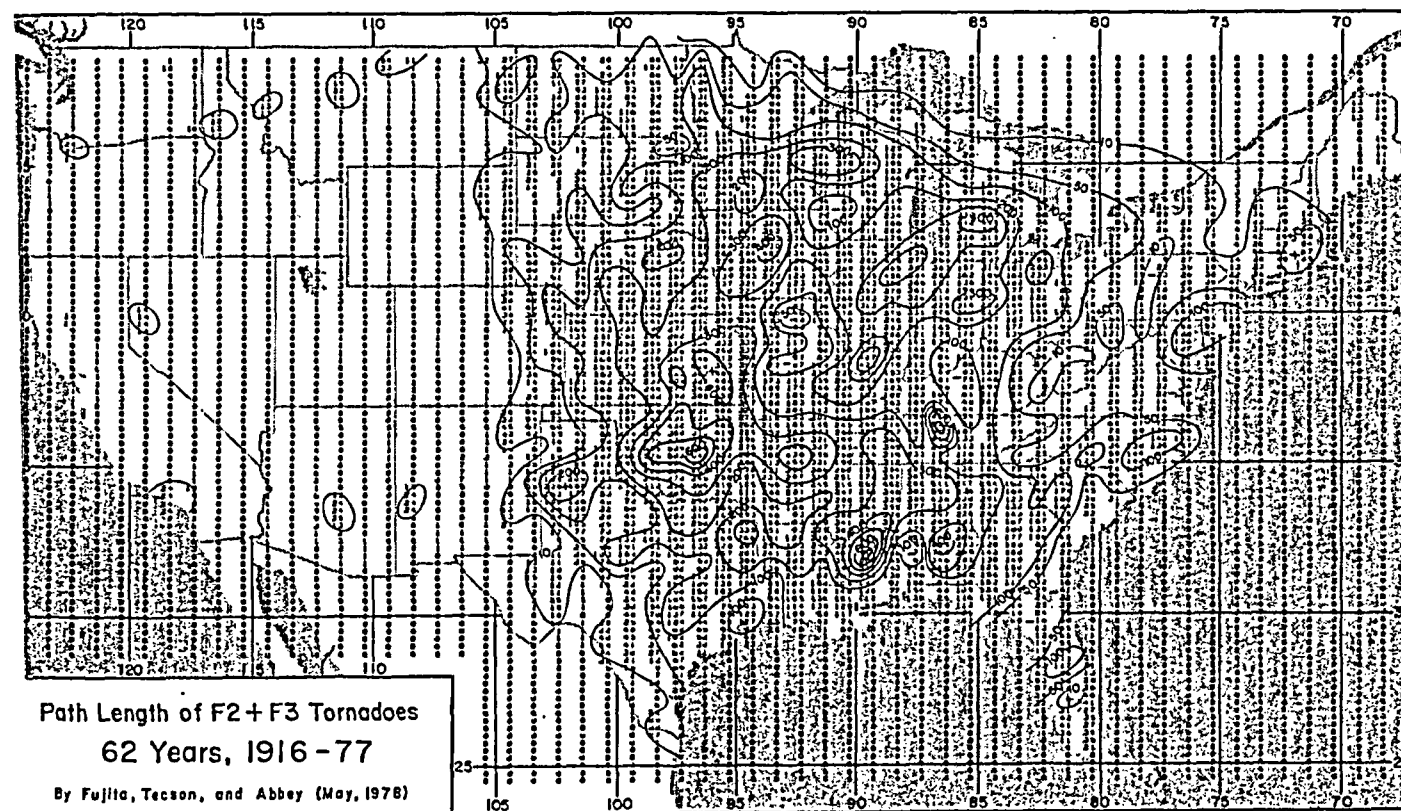
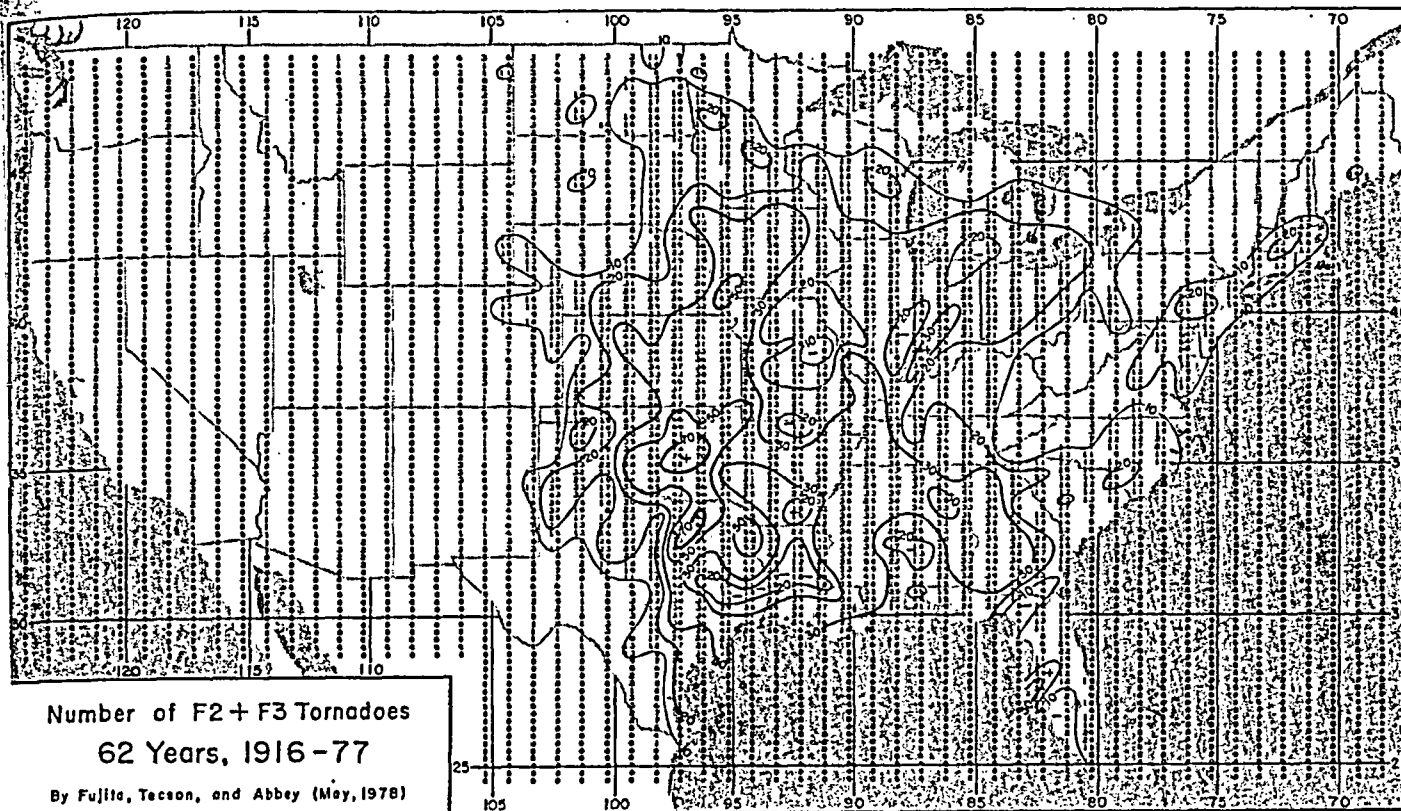


Figure 5.5 Numbers and path lengths of strong (F2 + F3) tornadoes. The maximum numbers are seen in Oklahoma while the maximum path lengths are in Mississippi.

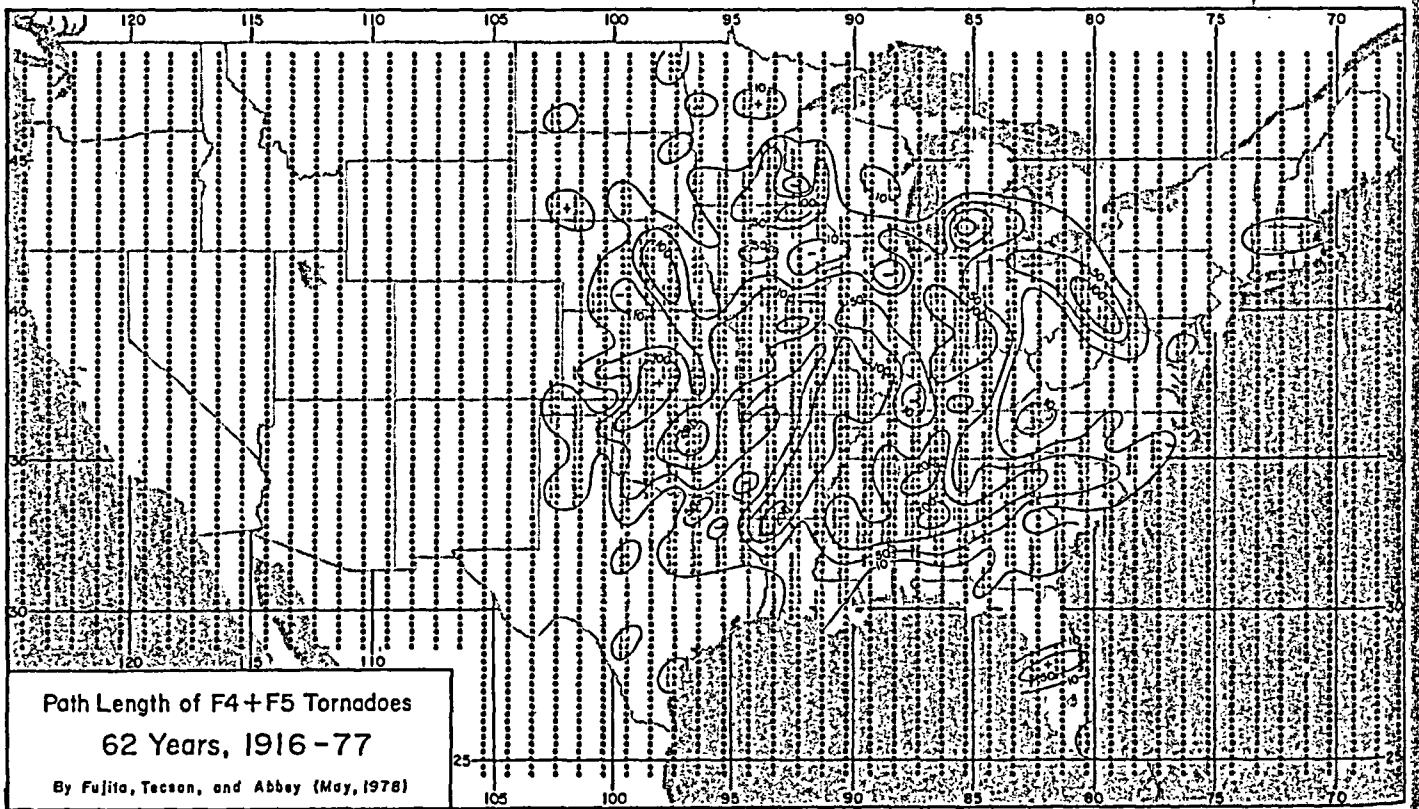
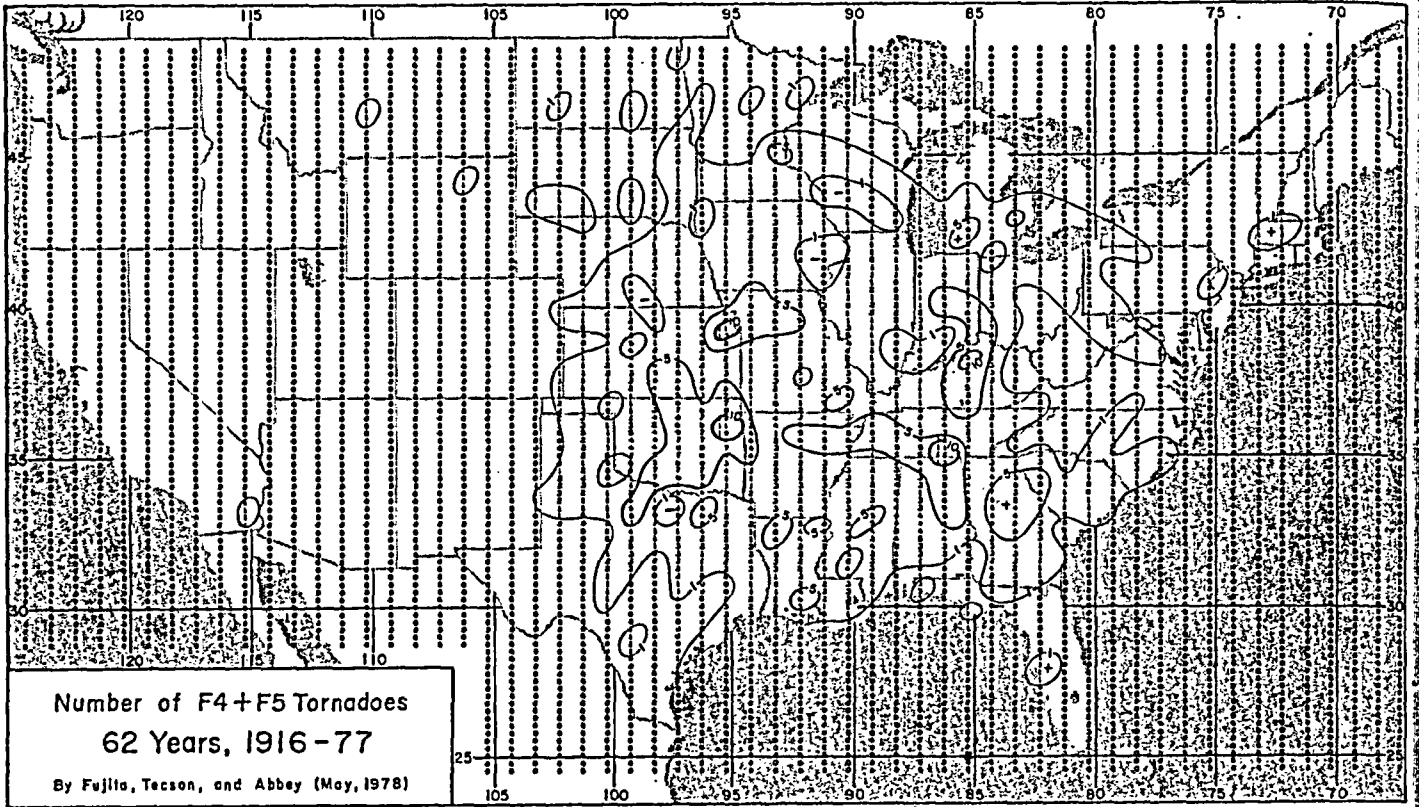


Figure 5.6 Numbers and path lengths of violent (F4 + F5) tornadoes. Both N and P of those violent tornadoes distribute rather uniformly over a circular area over the central Midwest. Maximum numbers of 10 to 11 are seen in Oklahoma, Kansas, Kentucky, and Tennessee.

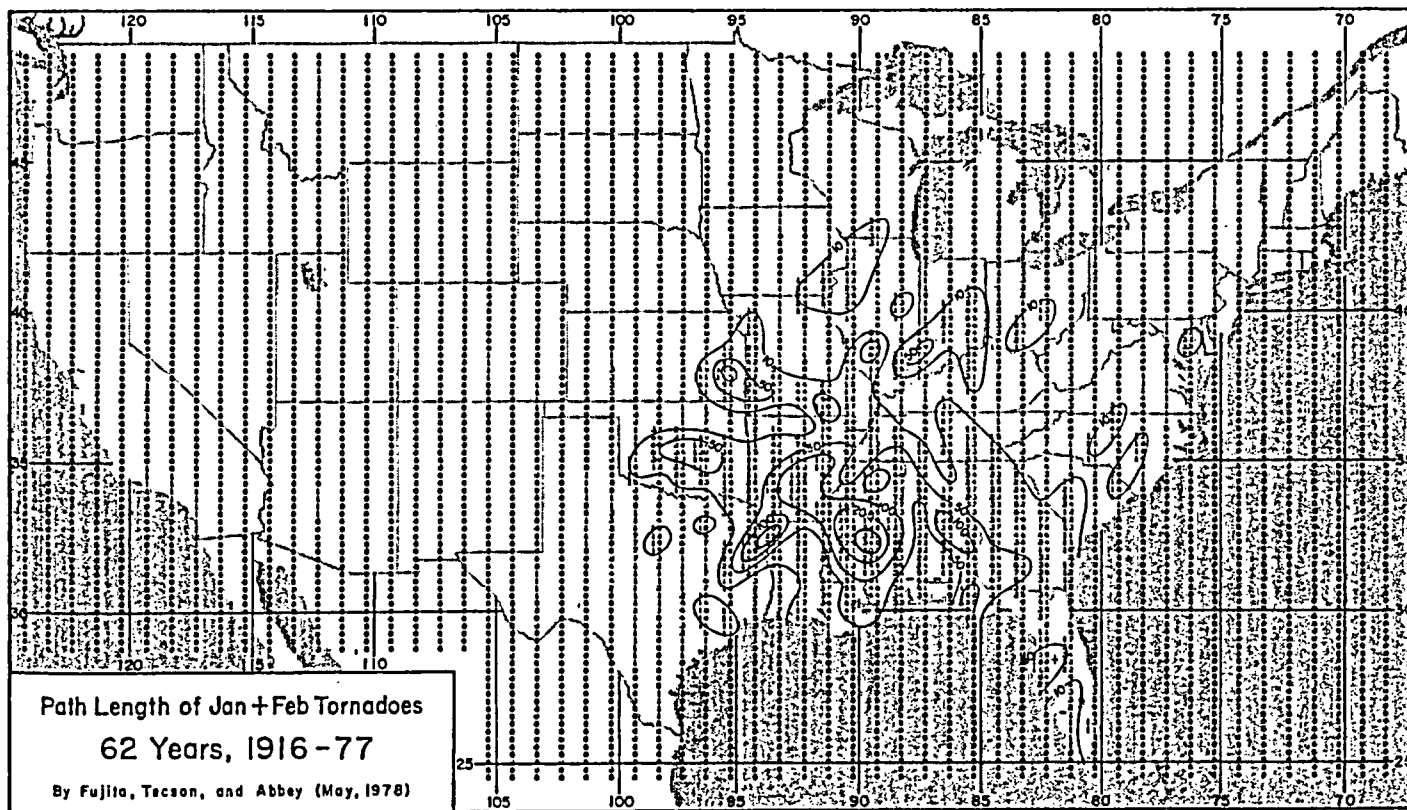
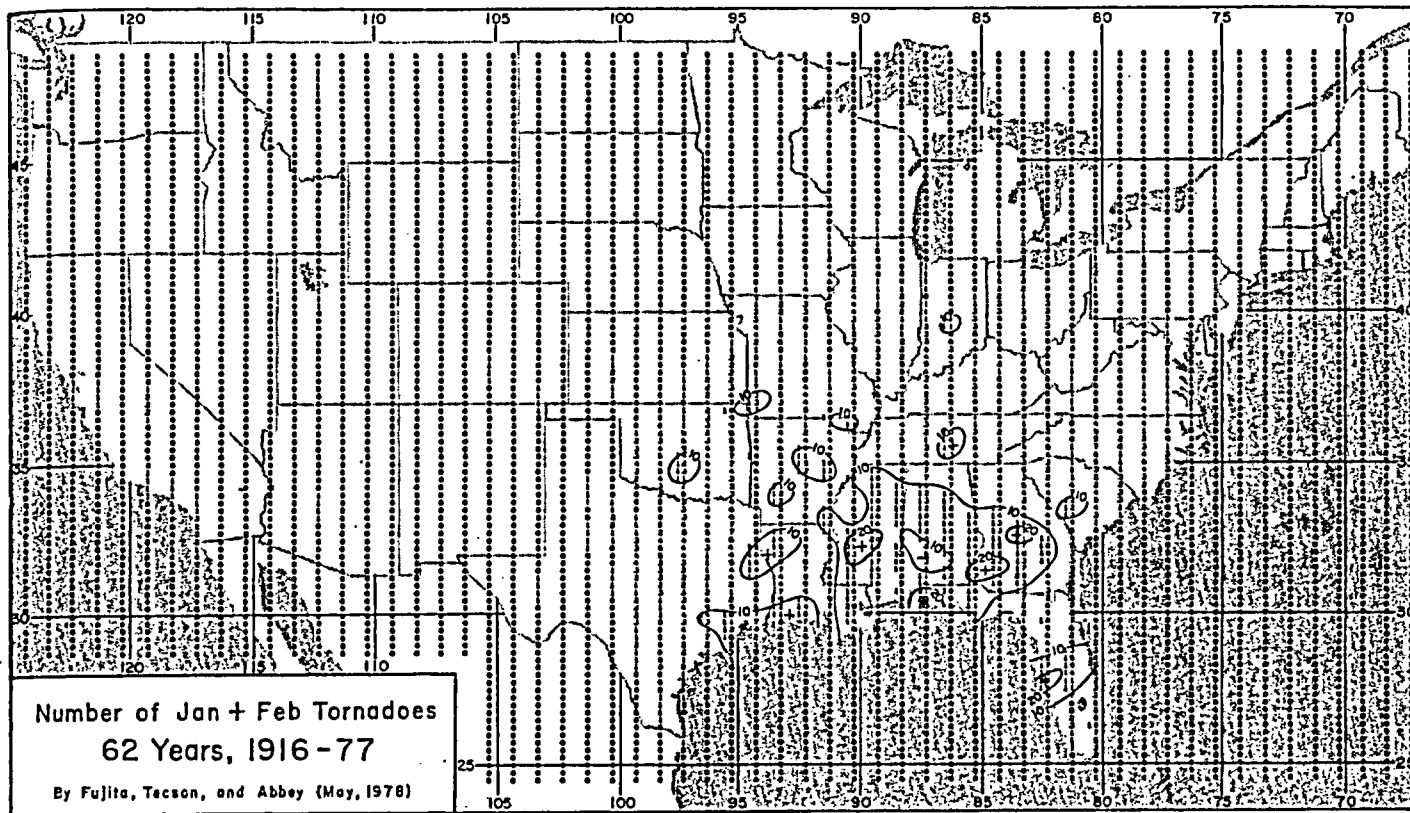


Figure 5.7 Numbers and path lengths of January and February tornadoes. Highest numbers and path lengths are seen in central Mississippi.

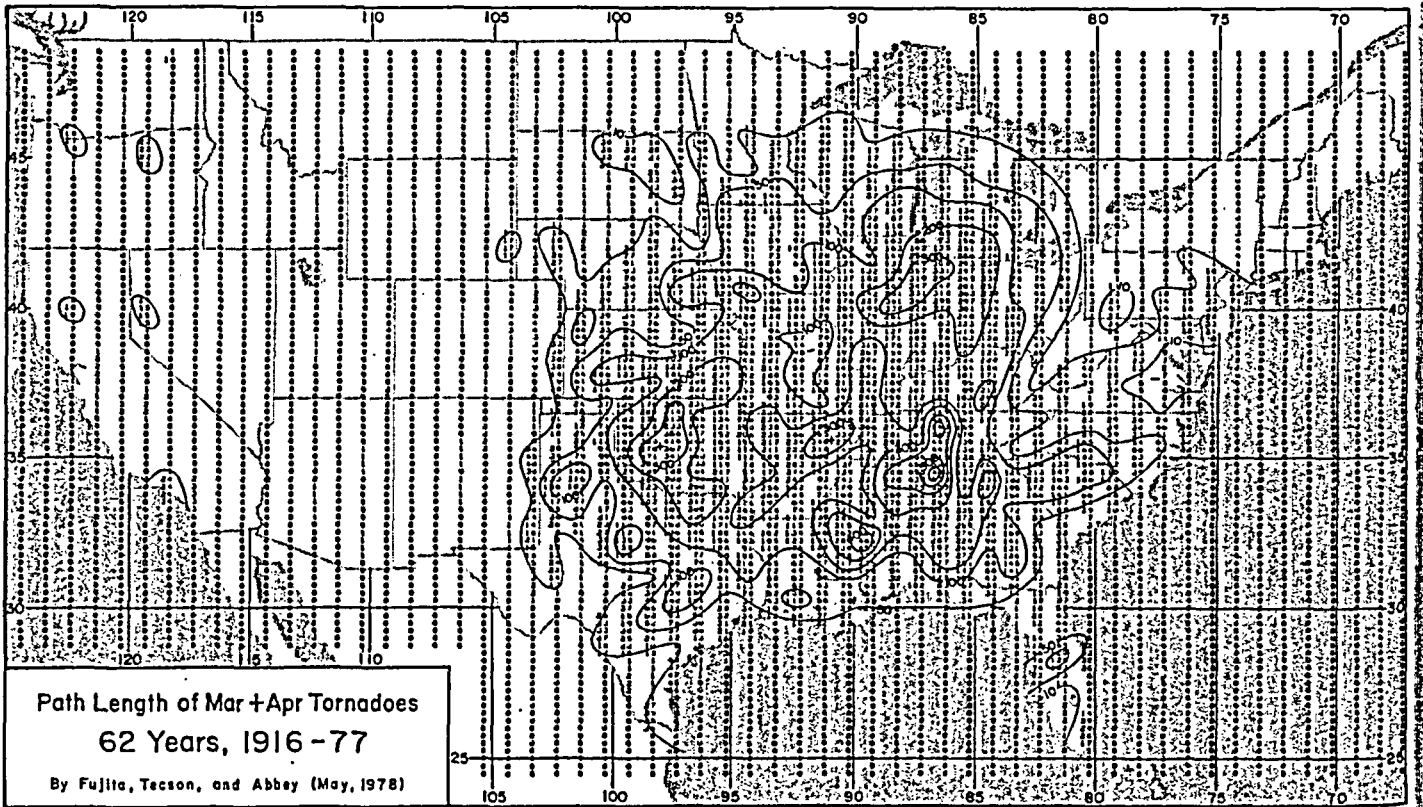
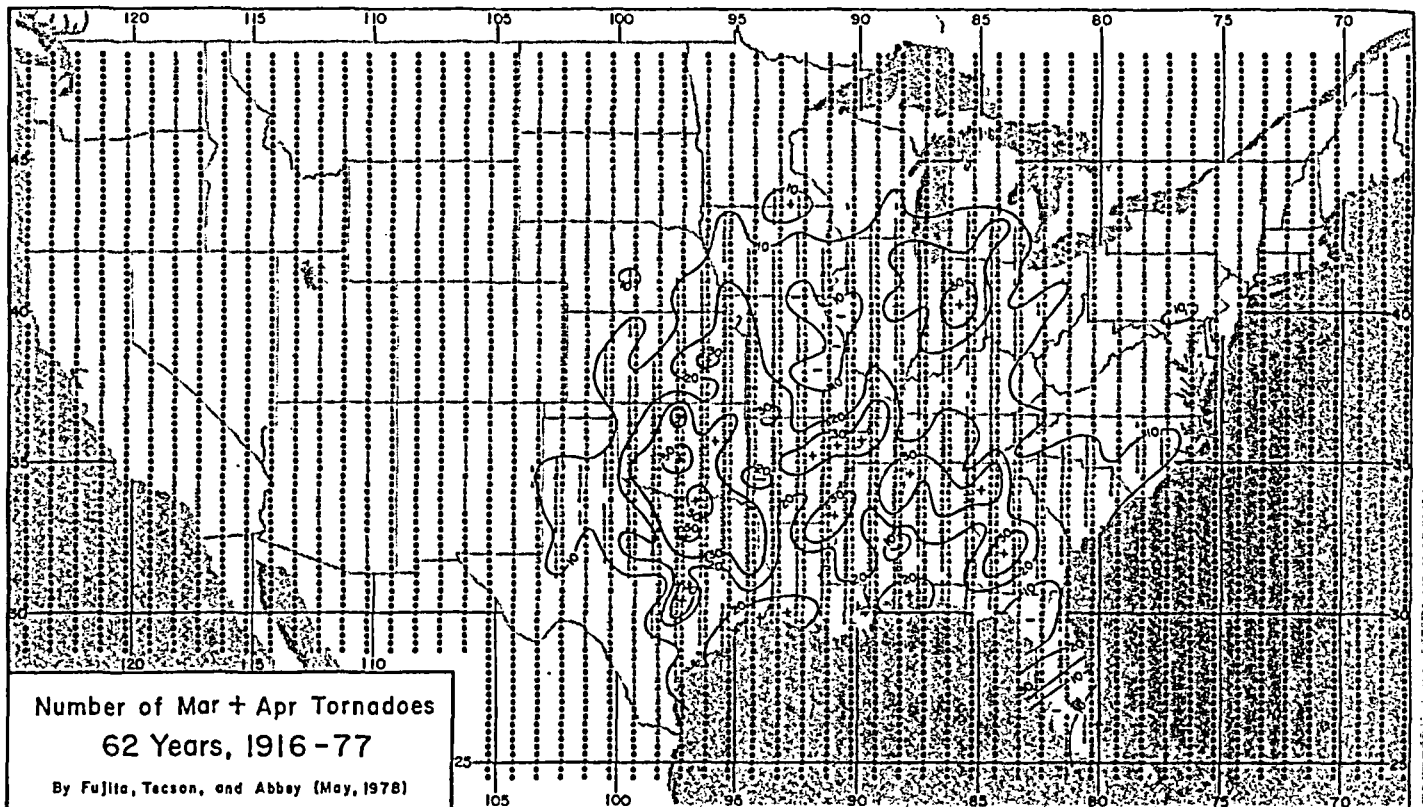


Figure 5.8 Numbers and path lengths of March and April tornadoes. Although the highest numbers are seen in Texas to Oklahoma area, the largest path lengths are located in Tennessee-Alabama area.

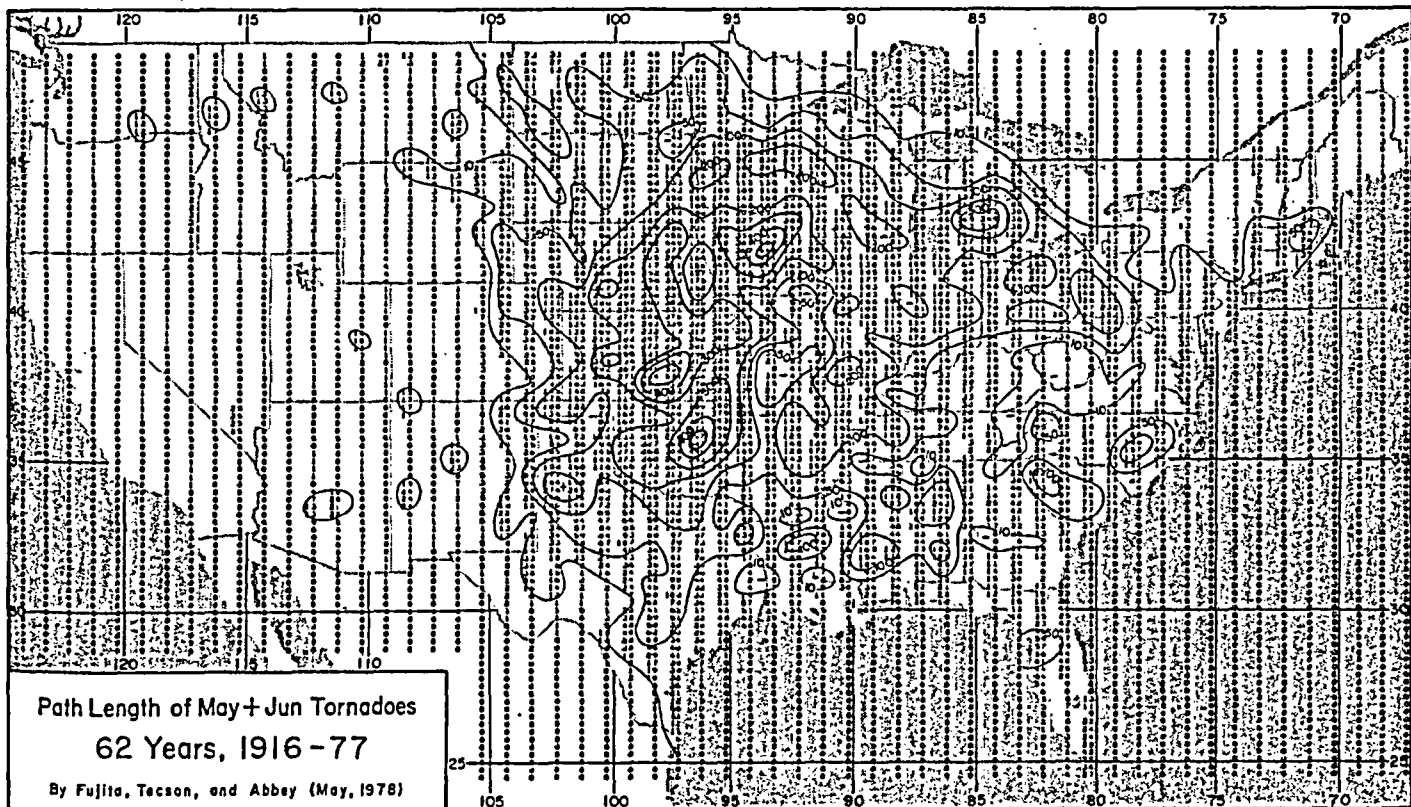
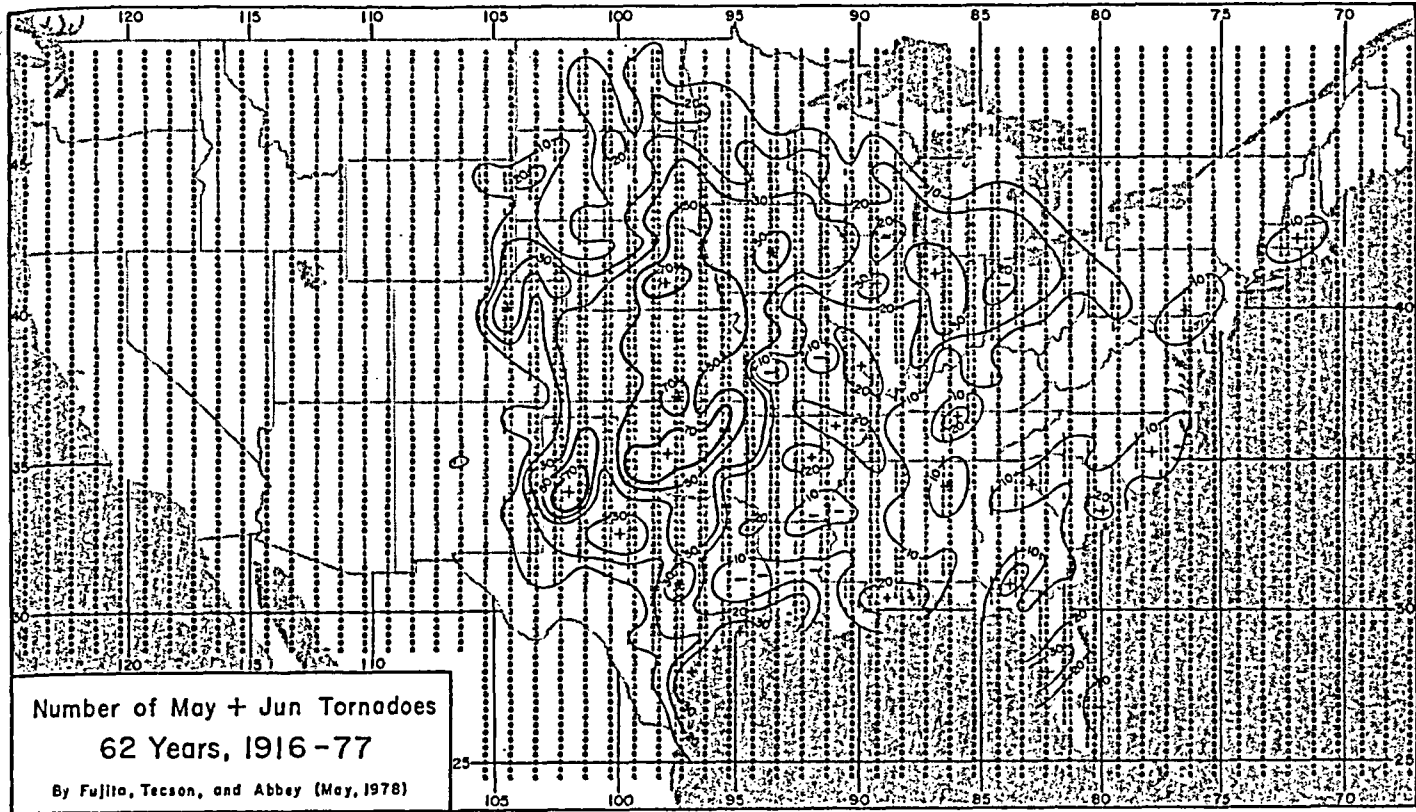


Figure 5.9 Numbers and path lengths of May and June tornadoes. Oklahoma-Kansas-Nebraska are affected by highest numbers. Largest path lengths extend into central Iowa.

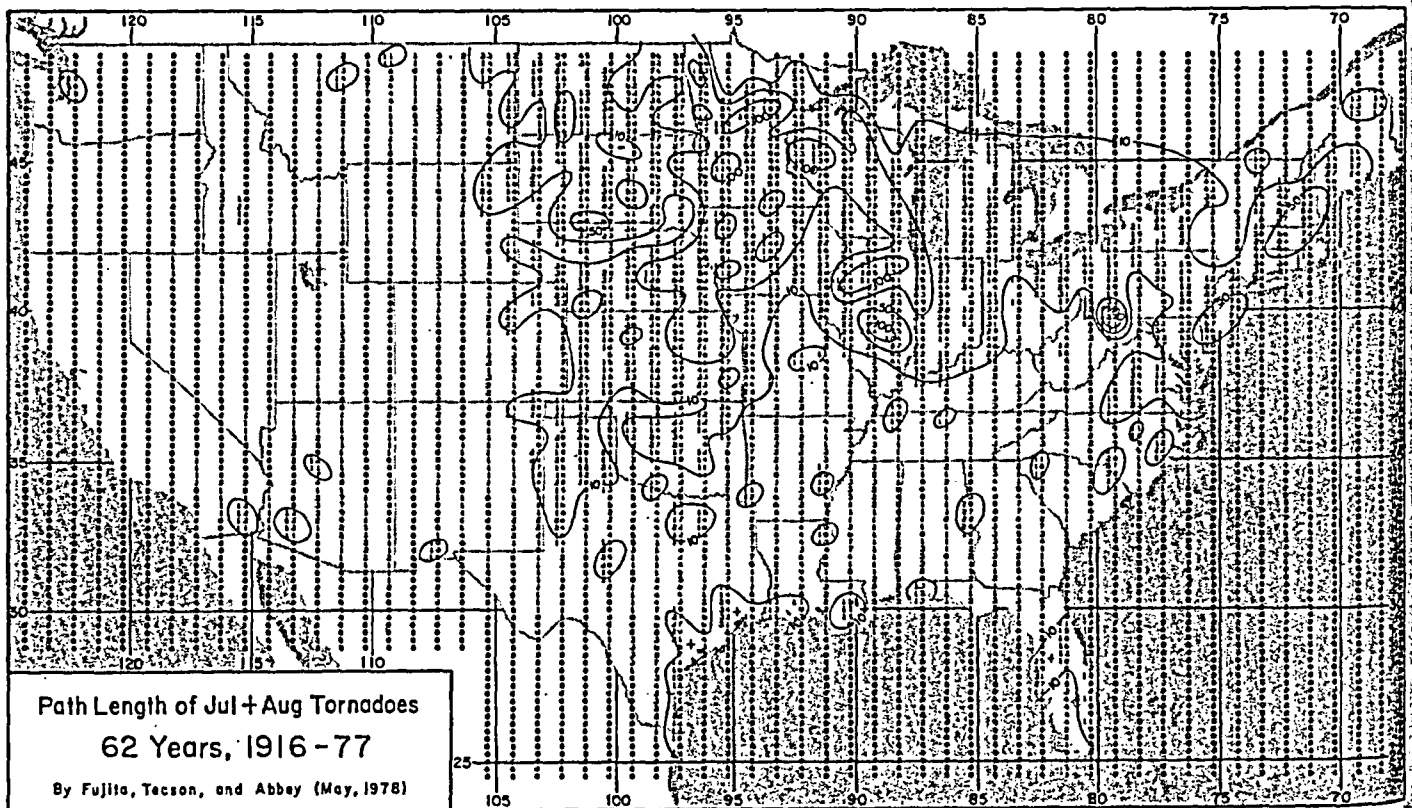
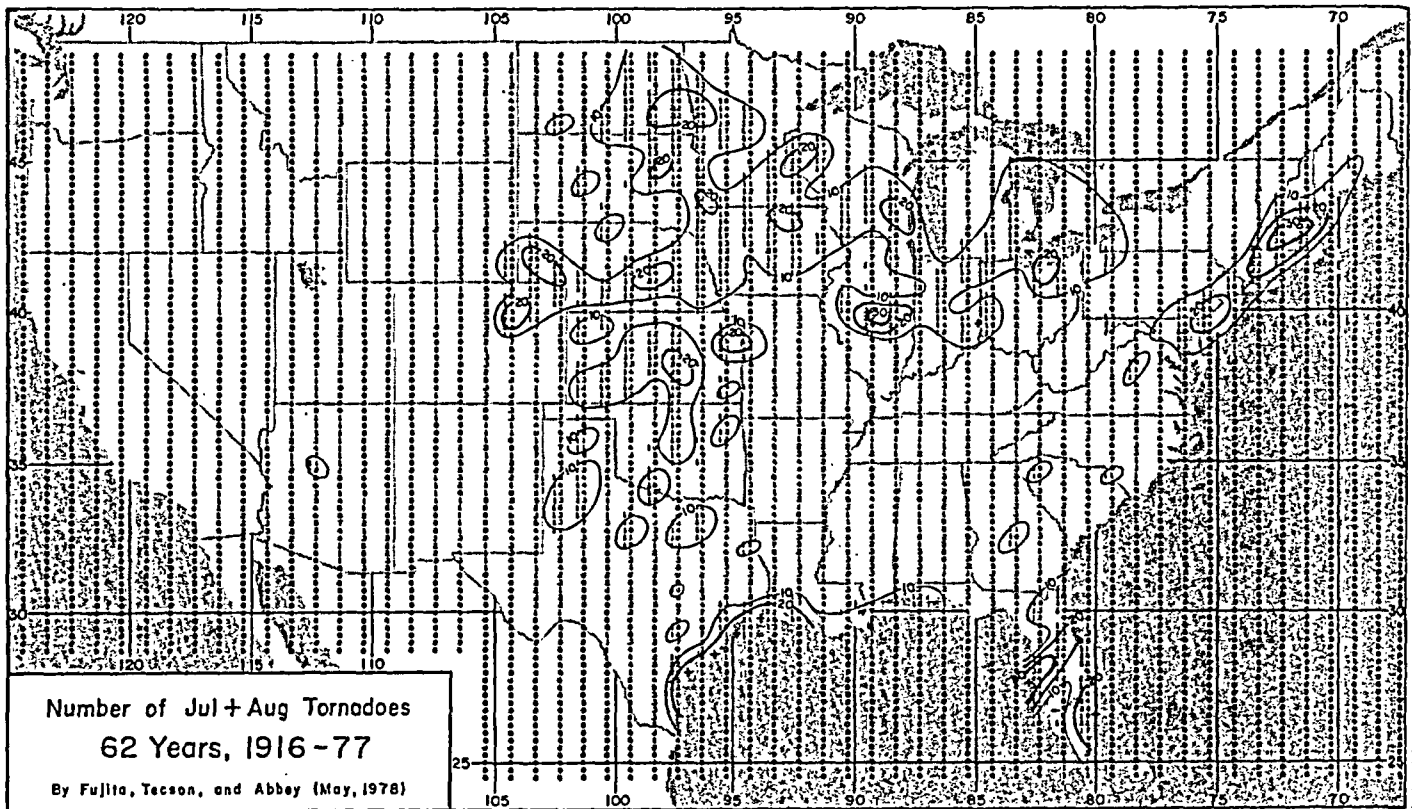


Figure 5.10 Numbers and path lengths of July and August tornadoes. Maximum values of N and P shift toward the northern Midwest. Hurricane-induced tornadoes are seen along the Gulf coast.

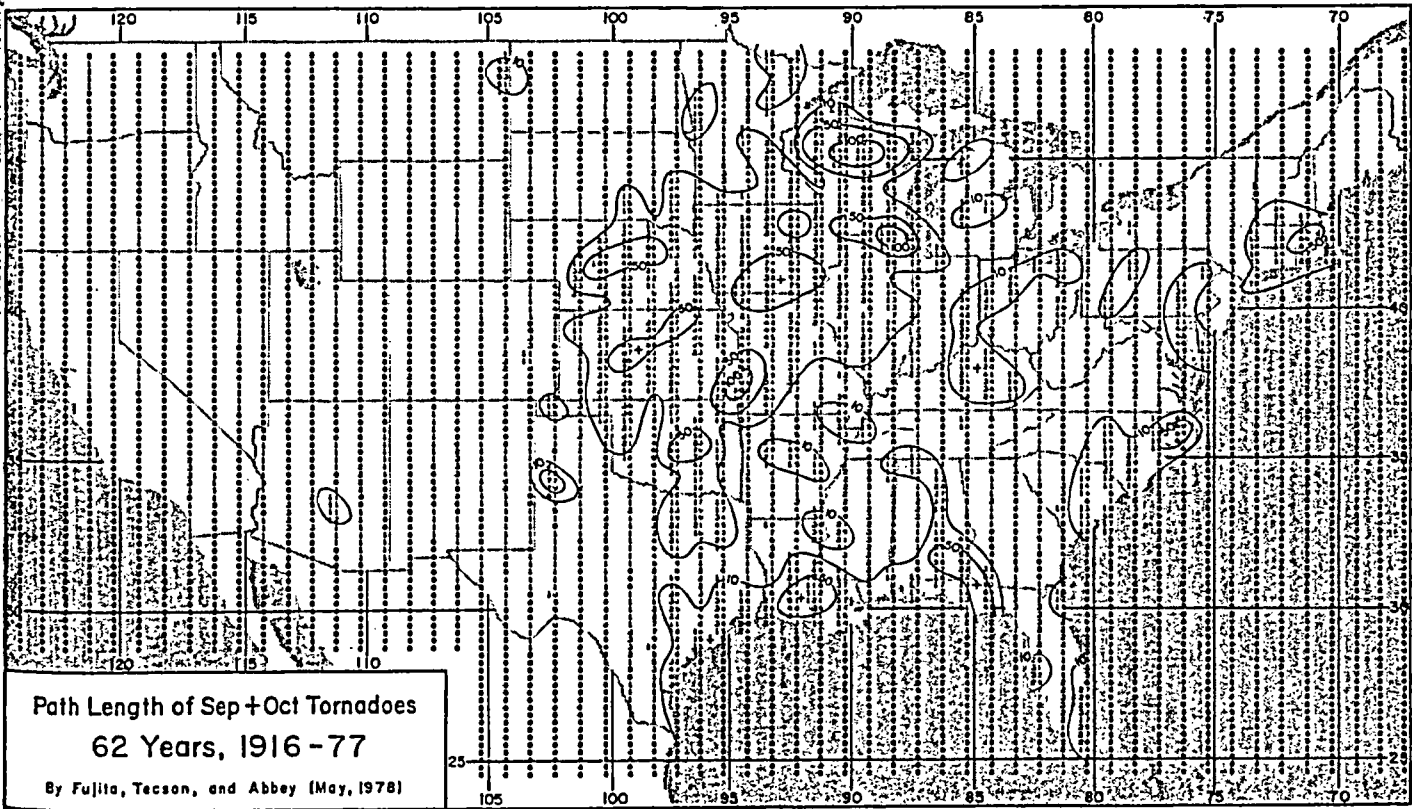
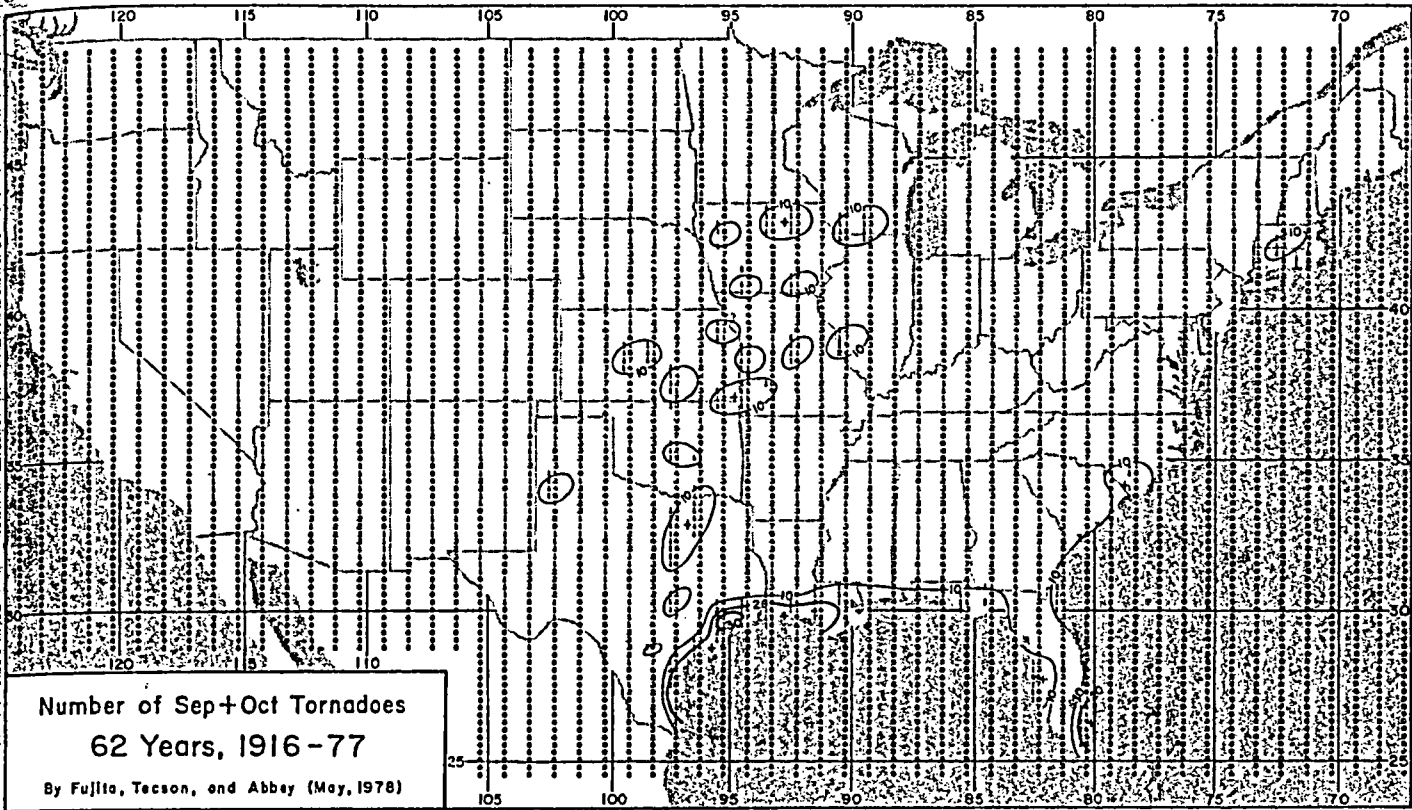


Figure 5.11 Numbers and path lengths of September and October tornadoes. Maximum numbers in the northern Midwest begin shifting toward the south. Hurricane-induced tornadoes are seen along the southern coast.

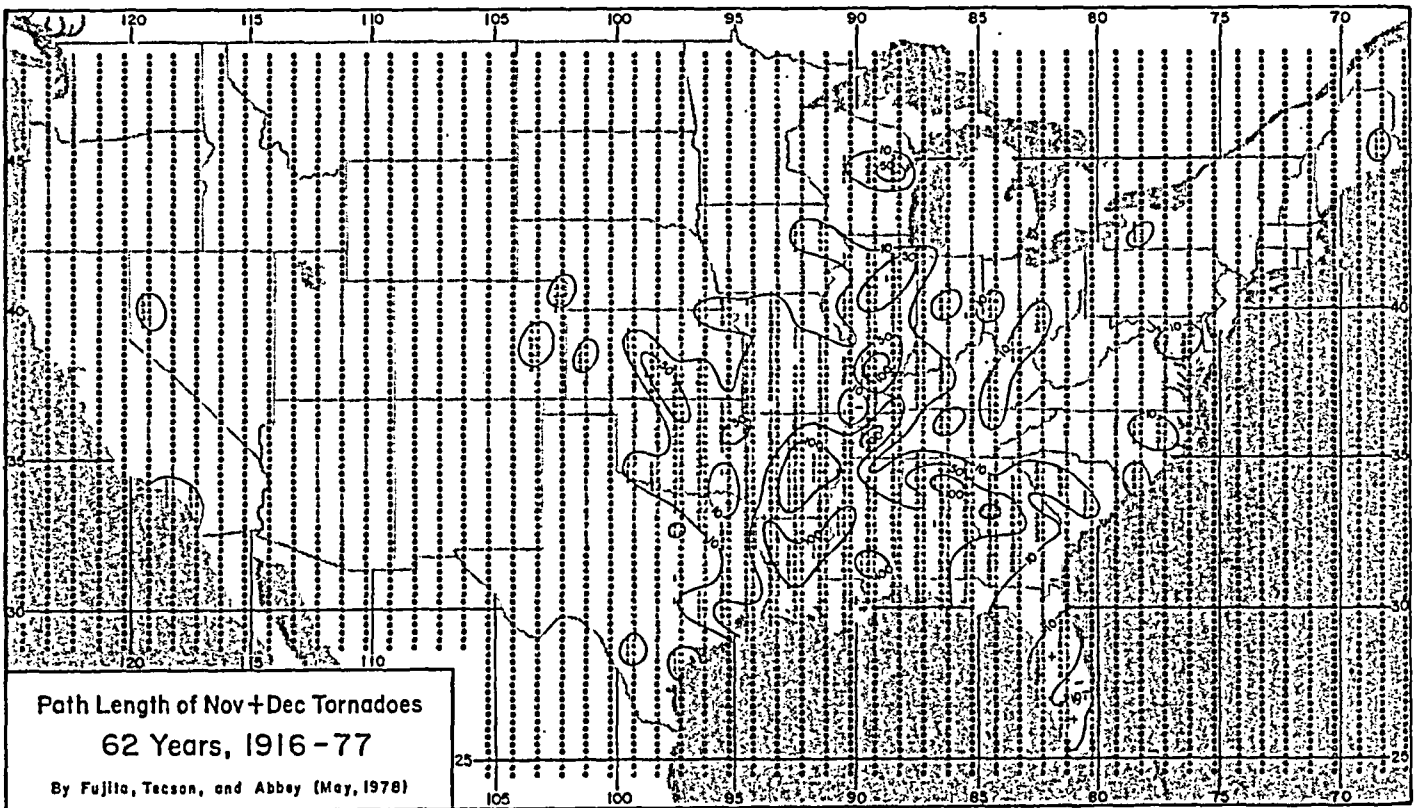
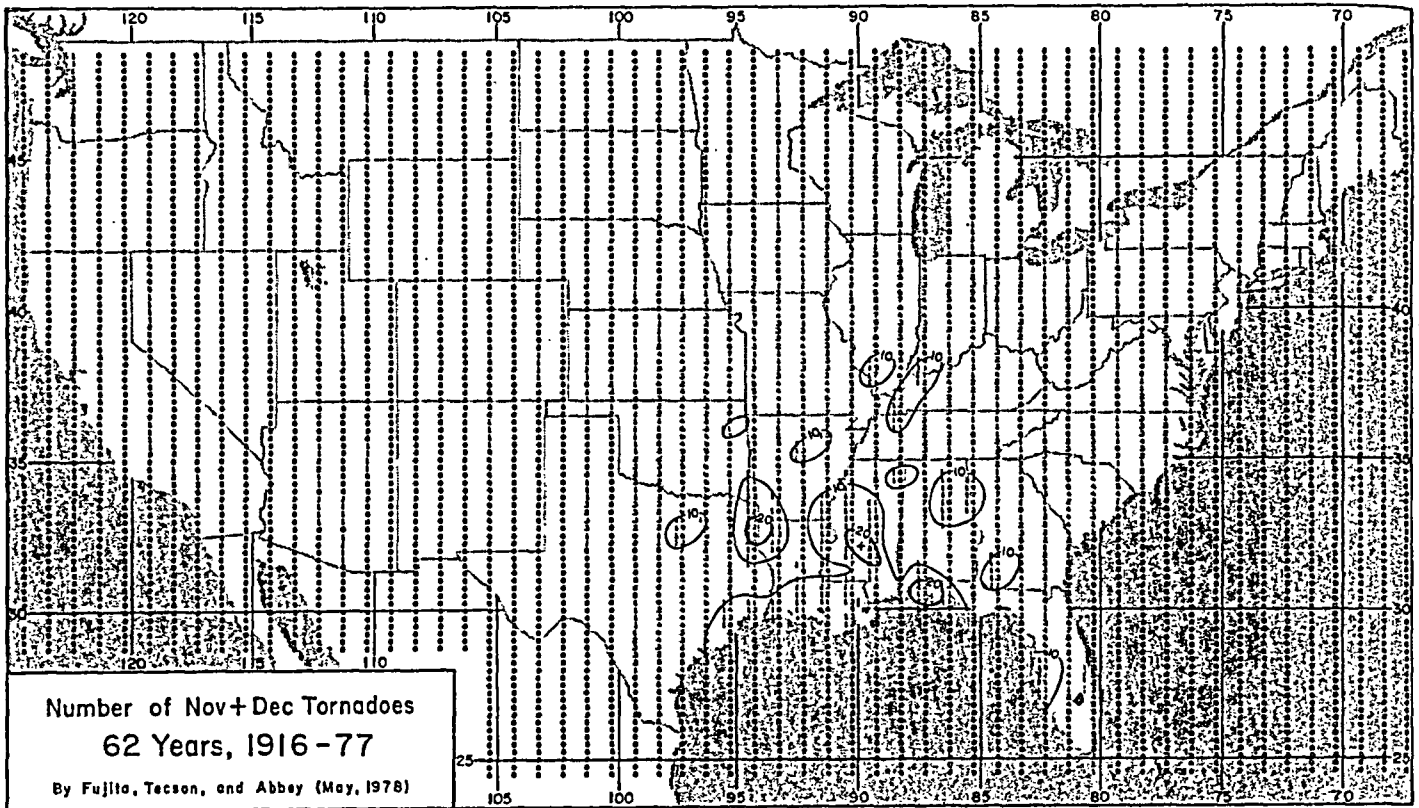


Figure 5.12 Numbers and path lengths of November and December tornadoes. Tornado activities are centered in the Mississippi valley.

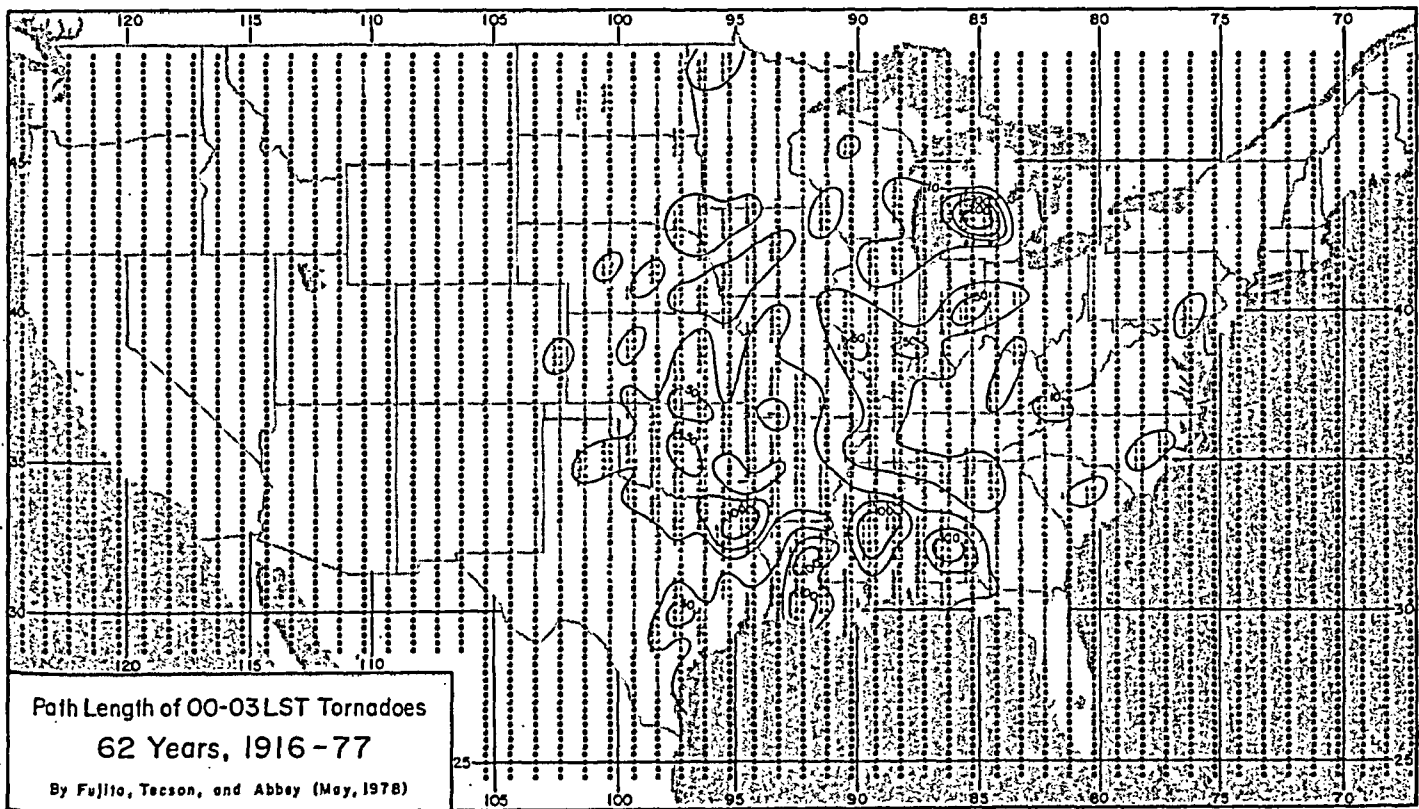
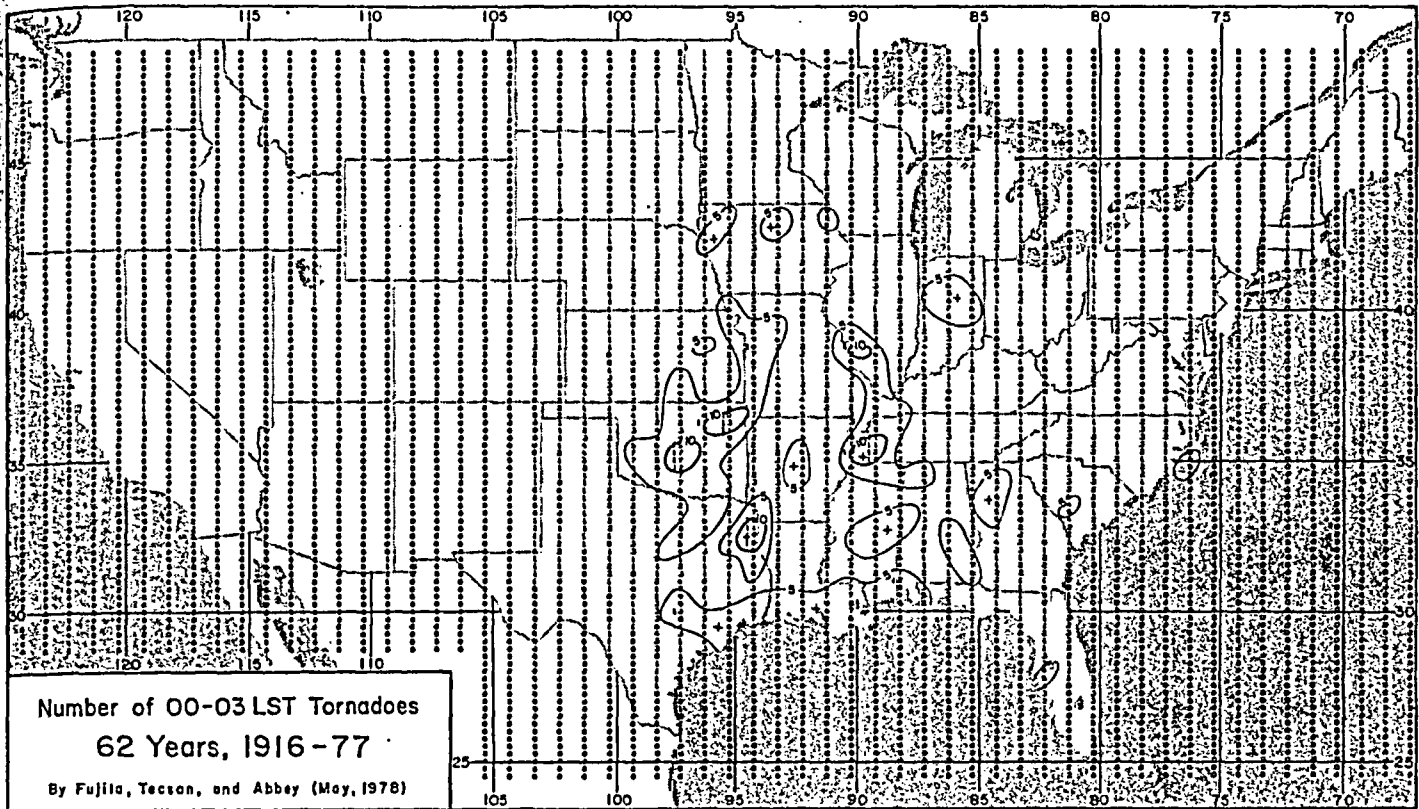


Figure 5.13 Numbers and path lengths of tornadoes between 00 and 03 Local Standard Time. These midnight tornadoes are located in the central Midwest. There is a significant path-length maximum in Michigan.

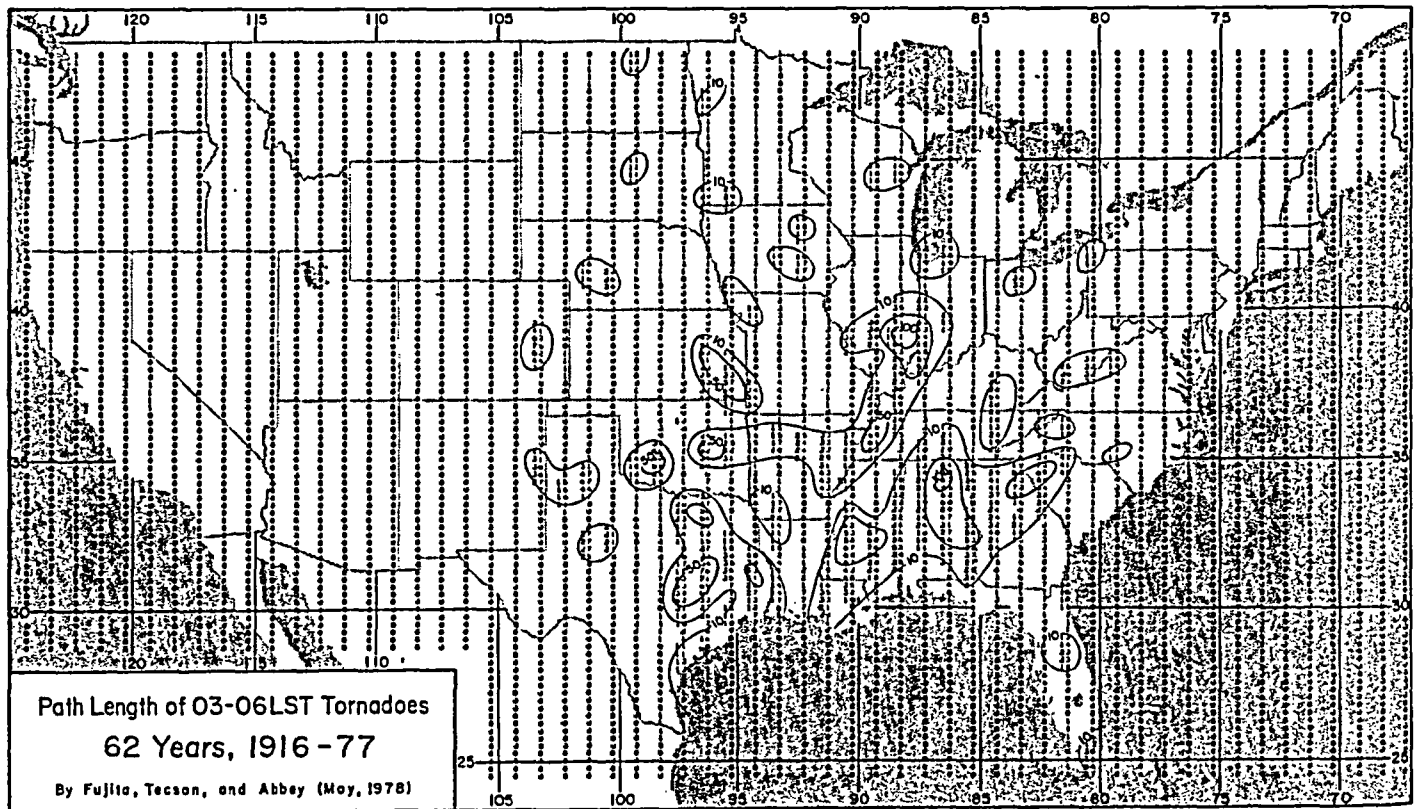
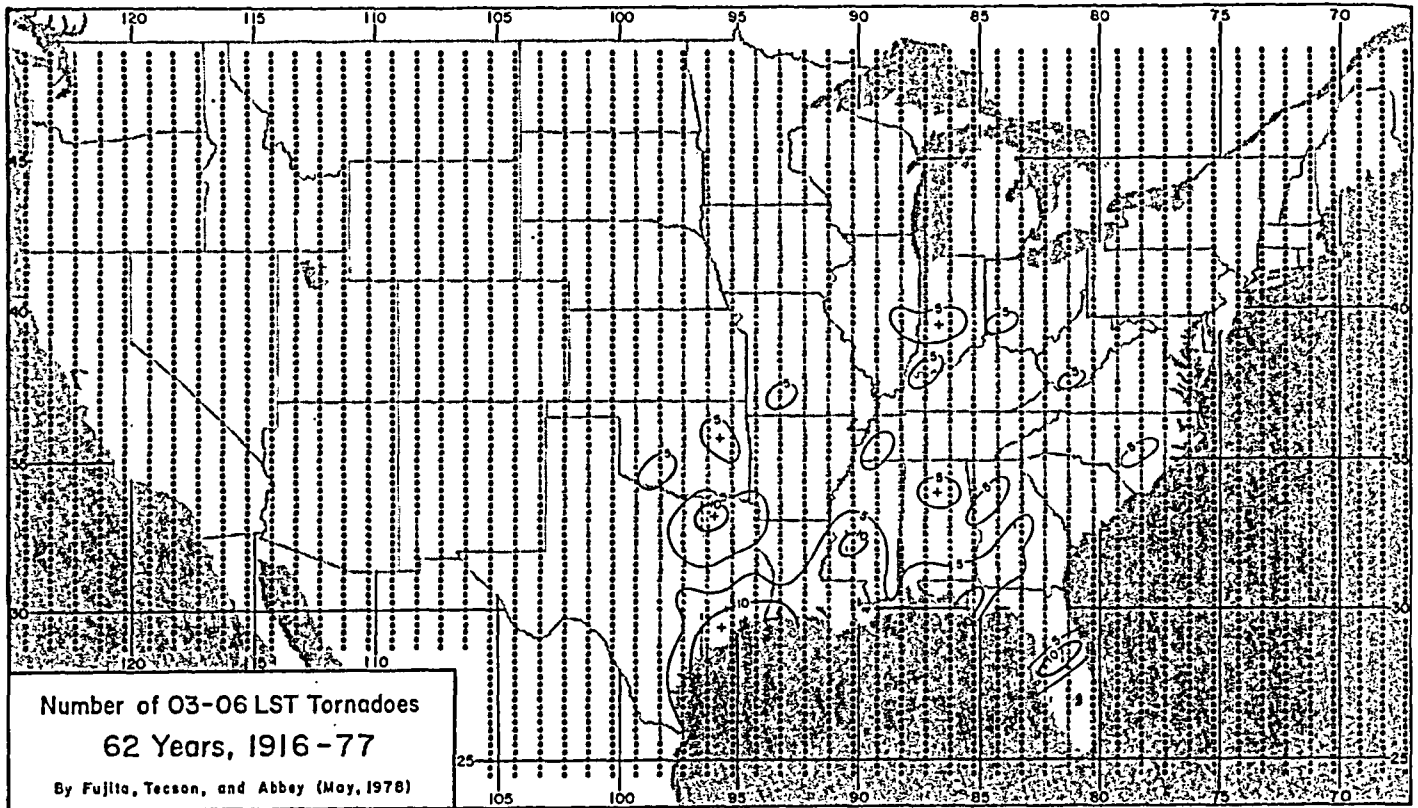


Figure 5.14 Numbers and path lengths of tornadoes between 03 and 06 Local Standard Time. These are pre-dawn tornadoes with their highest numbers along the Gulf coast. Largest path lengths are seen in and around the Mississippi valley.

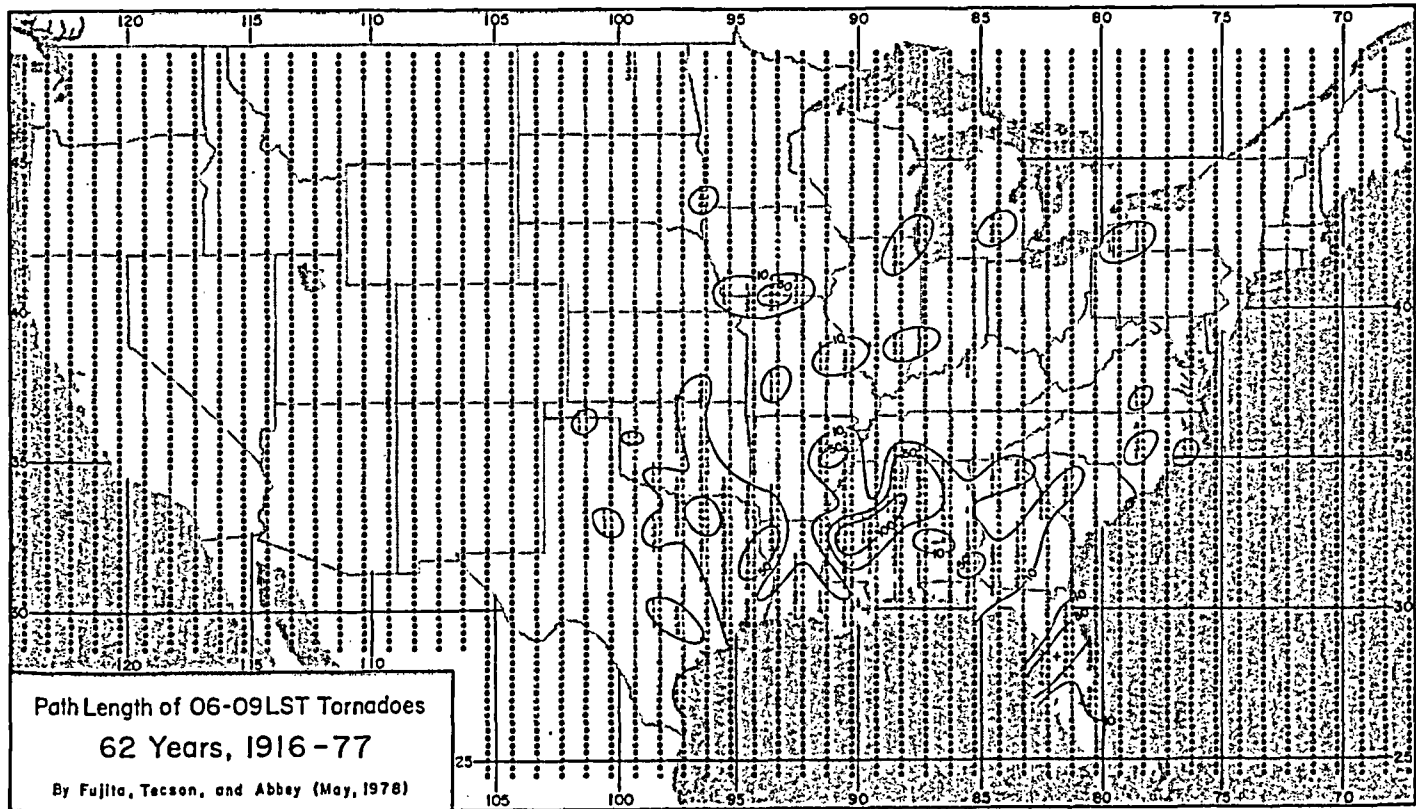
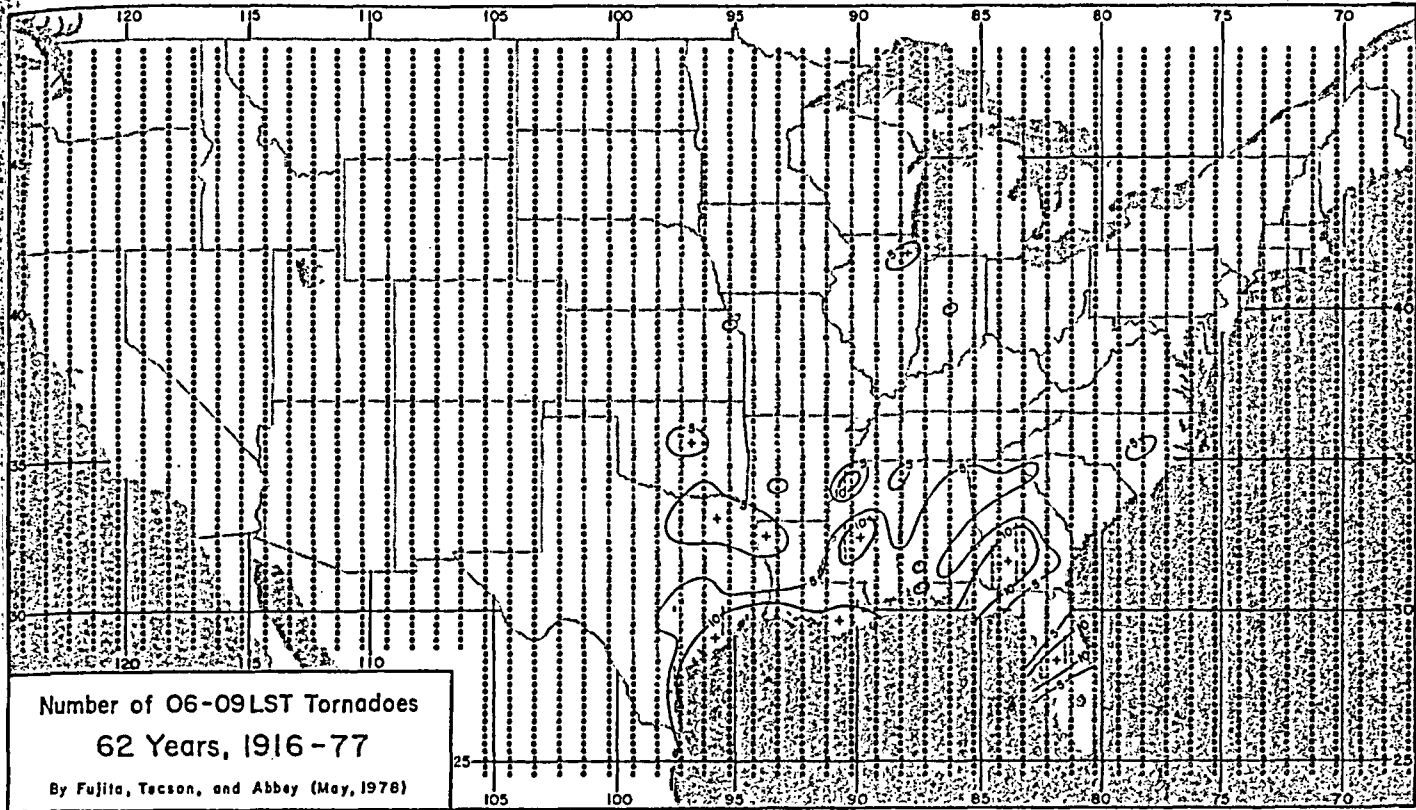


Figure 5.15. Numbers and path lengths of tornadoes between 06 and 09 Local Standard Time. The highest numbers are seen along the Gulf coast while the largest path lengths are located in Mississippi.

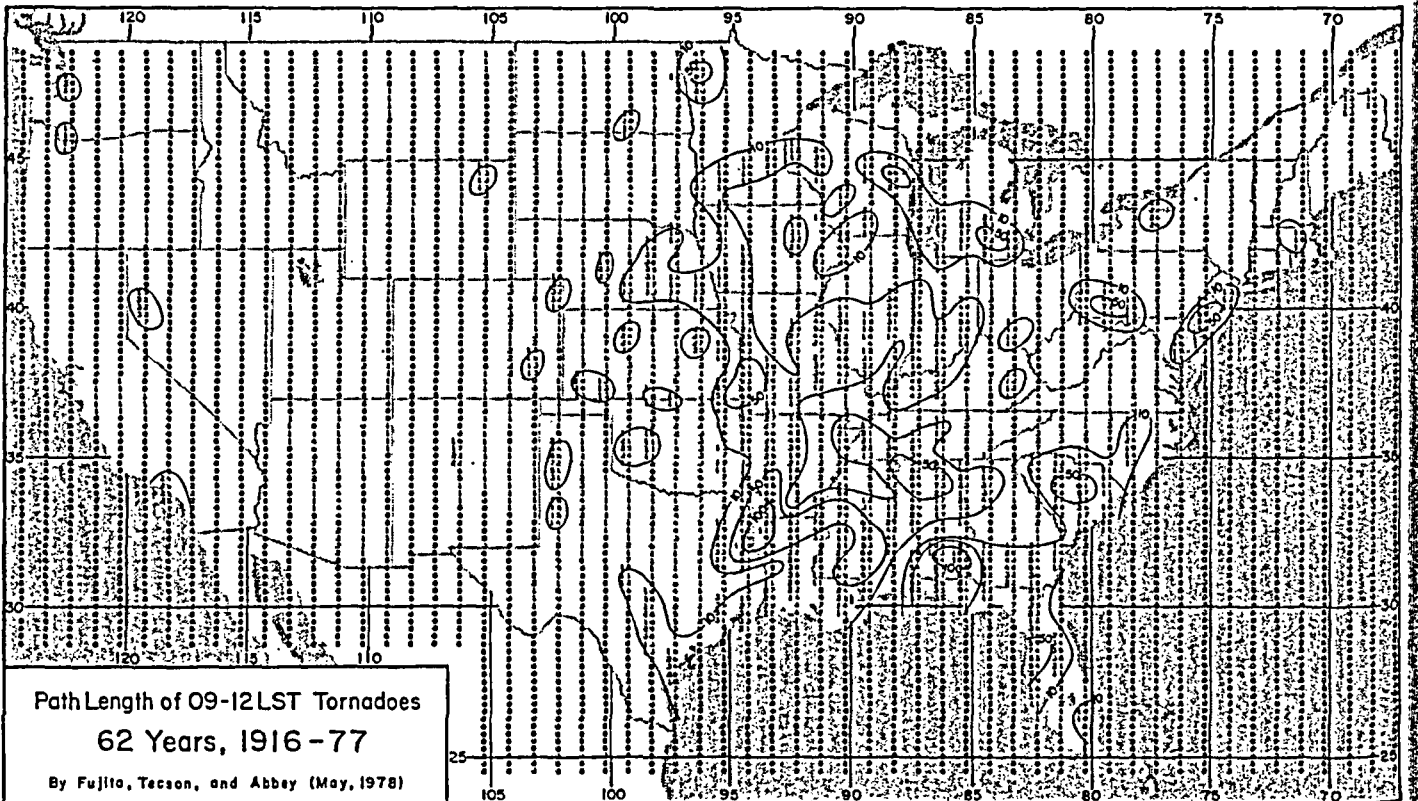
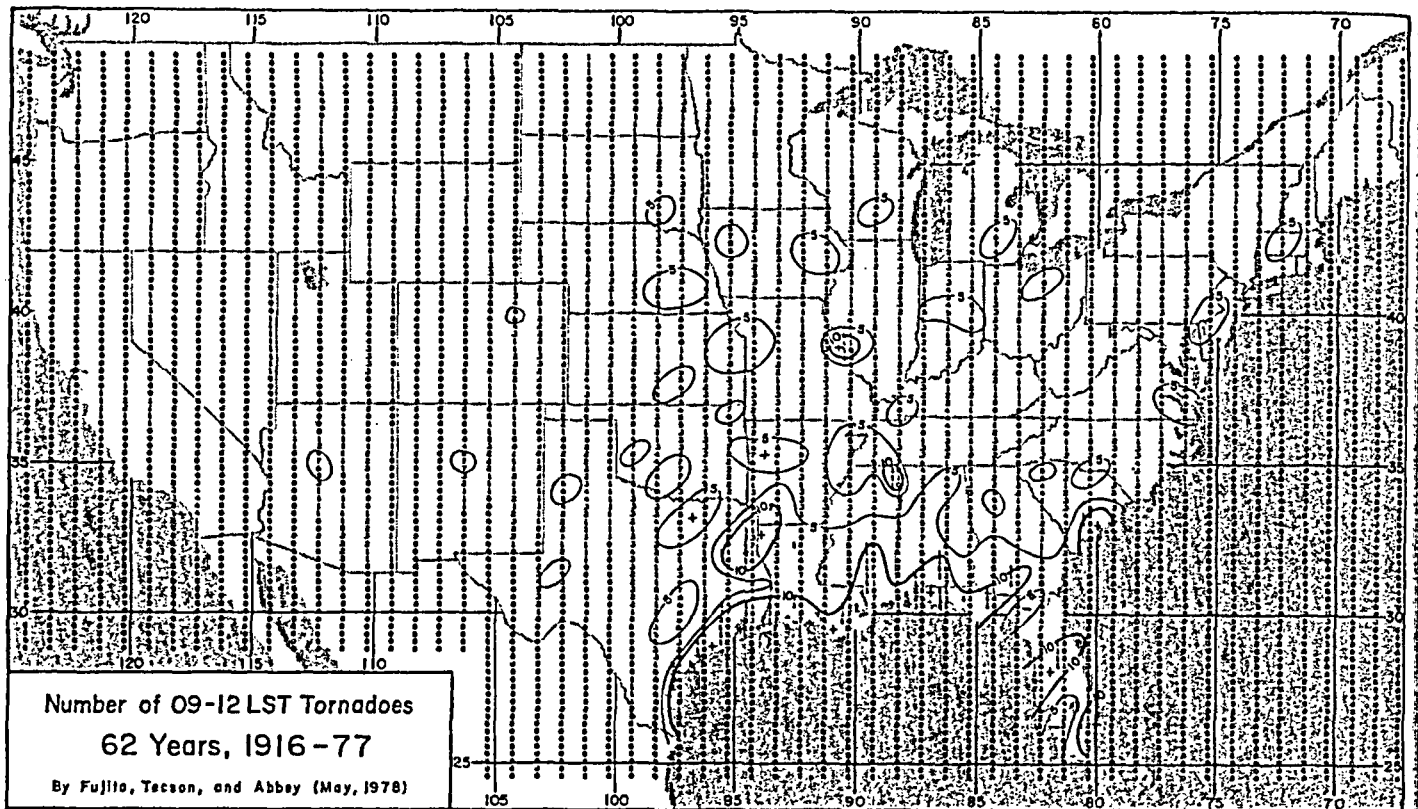


Figure 5.16 Numbers and path lengths of tornadoes between 09 and 12 Local Standard Time. The highest numbers are located along the Gulf coast while the largest path lengths are seen 100 to 200 miles inland.

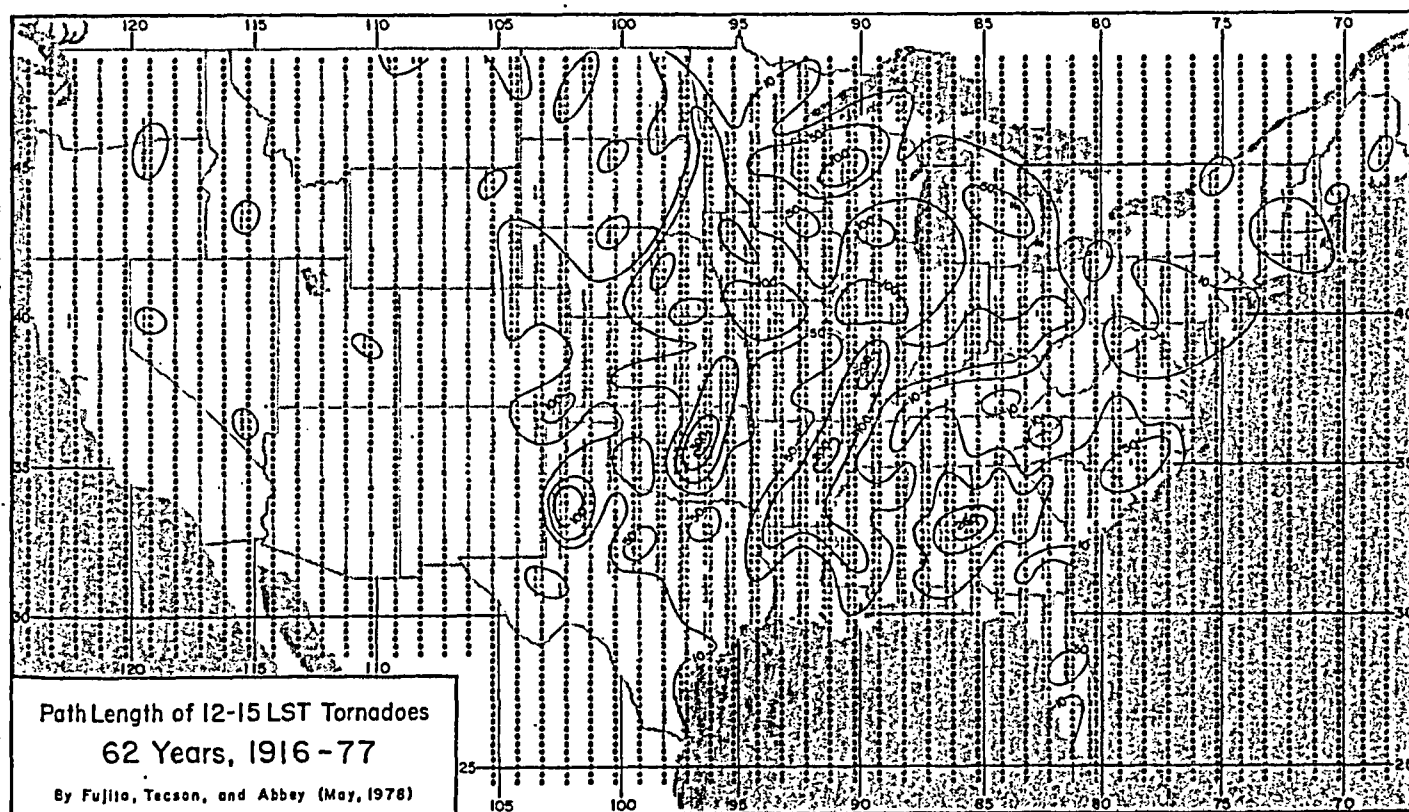
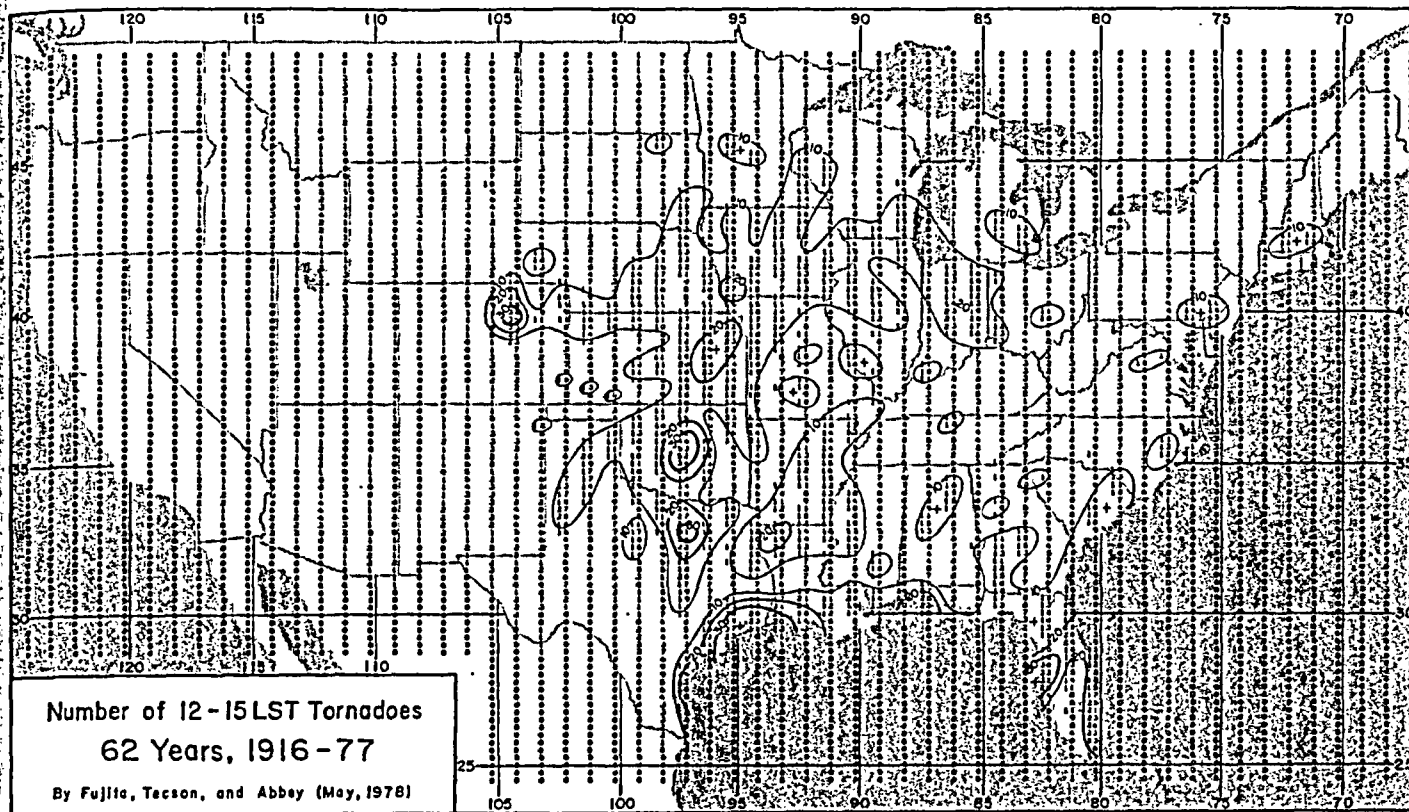


Figure 5.17 Numbers and path lengths of tornadoes between 12 and 15 Local Standard Time. These early afternoon tornadoes are seen along the Gulf coast (numbers) and in the central Midwest (path lengths).

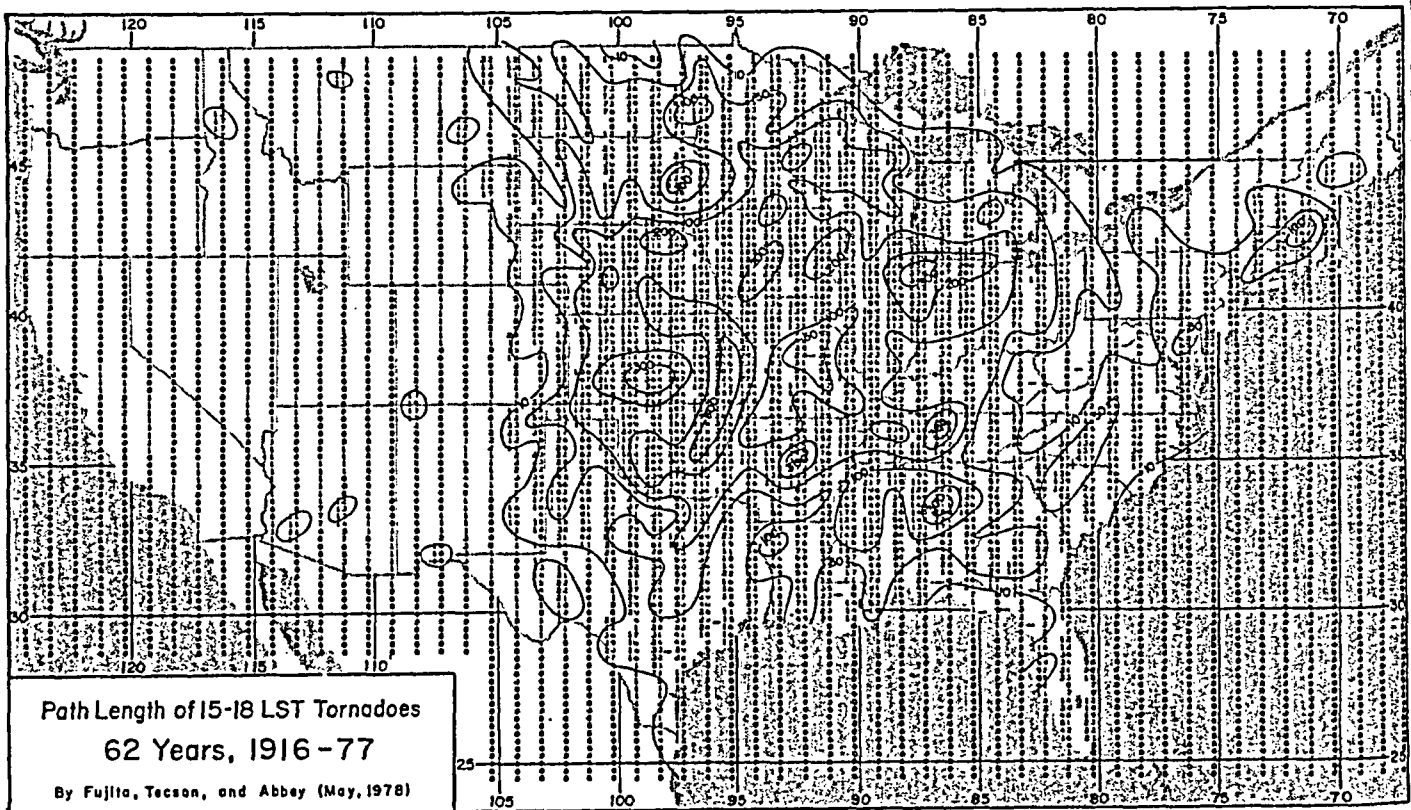
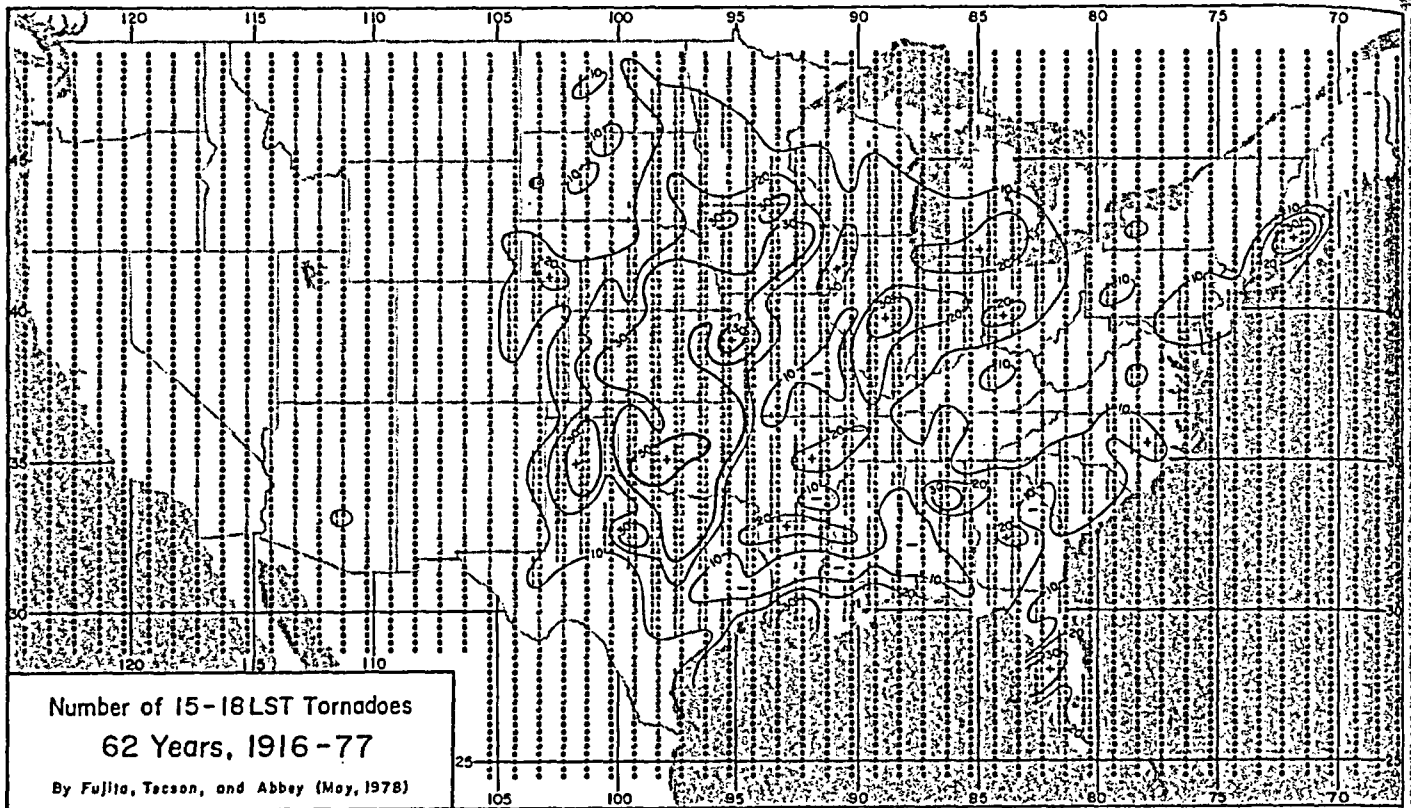


Figure 5.18 Numbers and path lengths of tornadoes between 15 and 18 Local Standard Time. These late afternoon tornadoes are characterized by the maximum values over the west central Midwest.

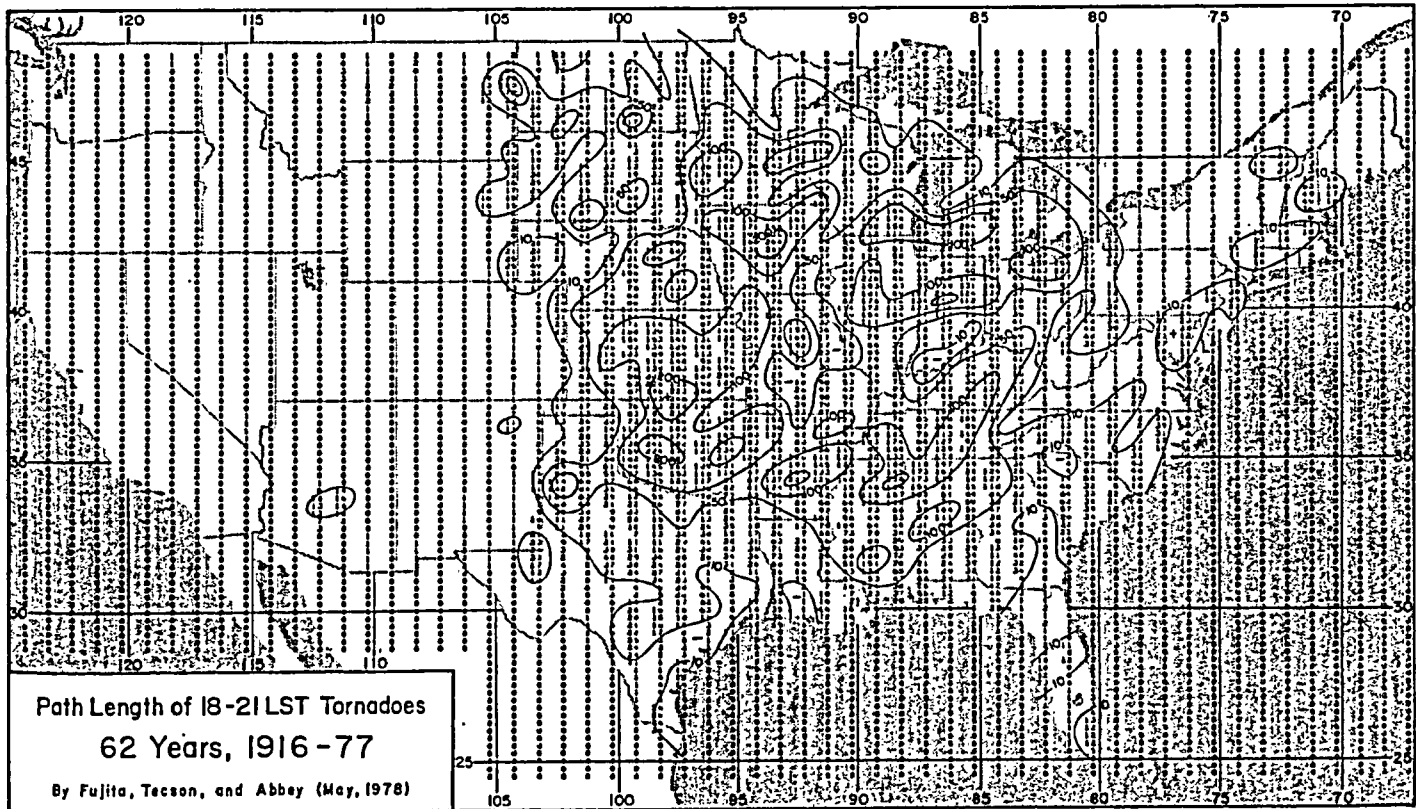
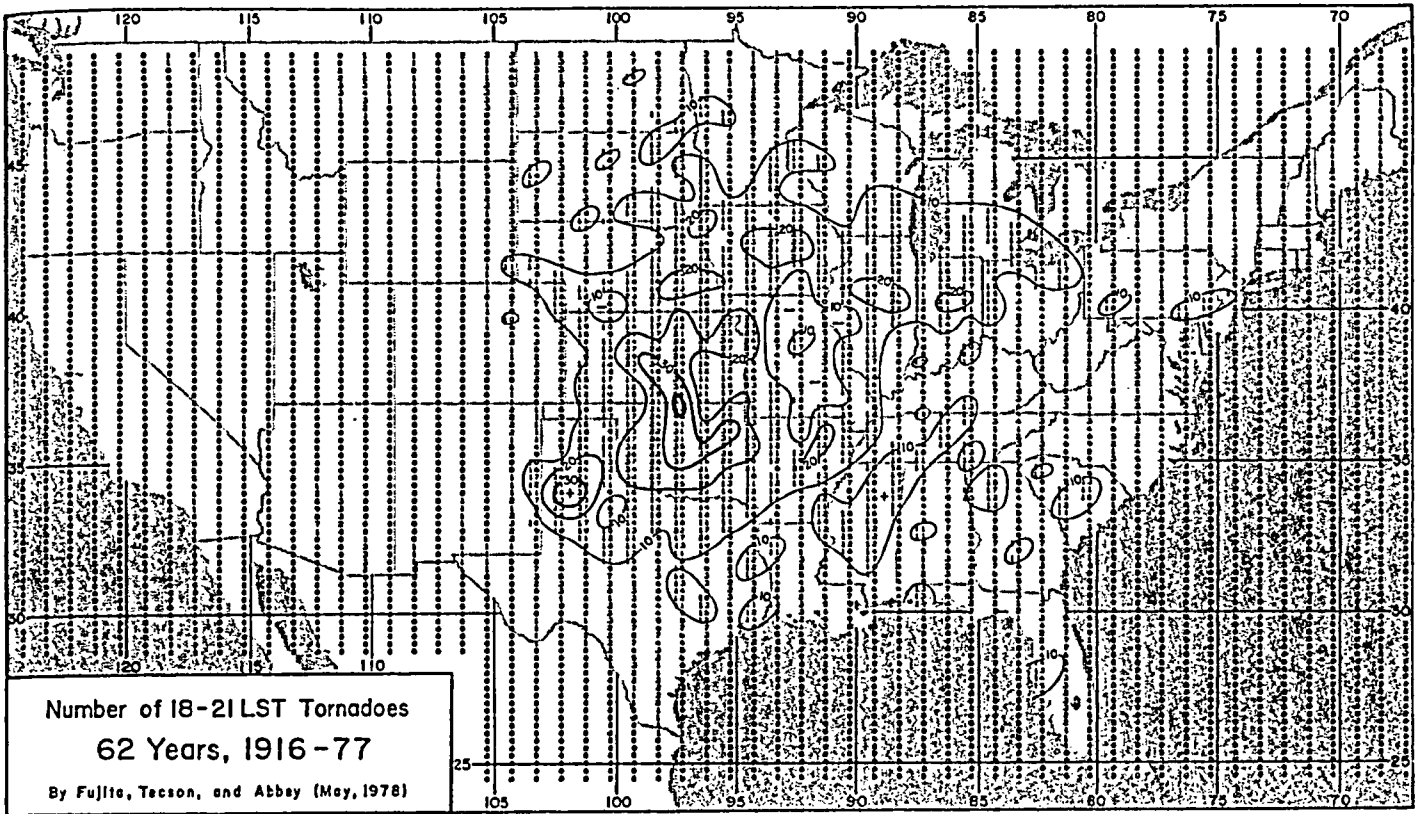


Figure 5.19 Numbers and path lengths of tornadoes between 18 and 21 Local Standard Time. These early evening tornadoes show the maximum numbers in Kansas-Oklahoma area. Path-length maxima are seen everywhere in the Midwest.

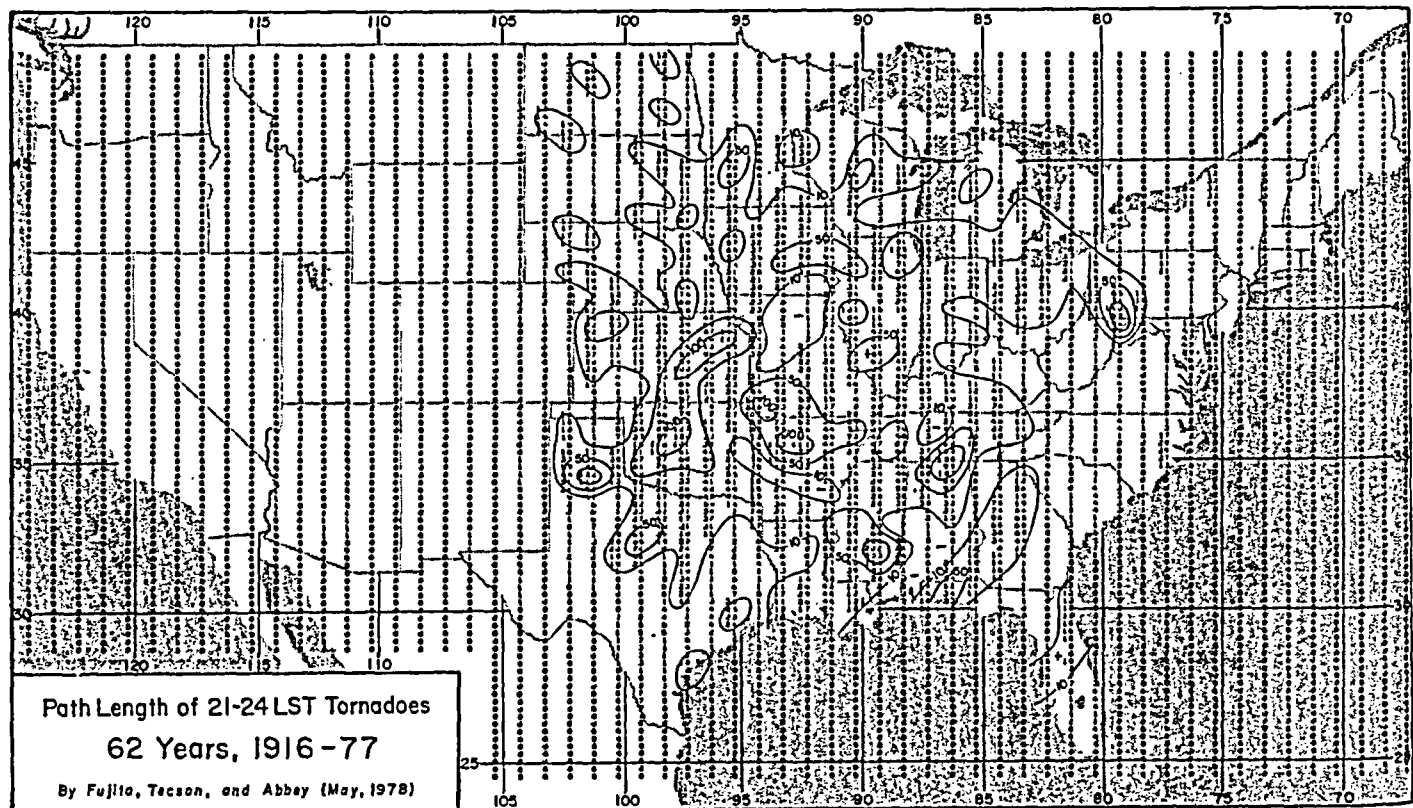
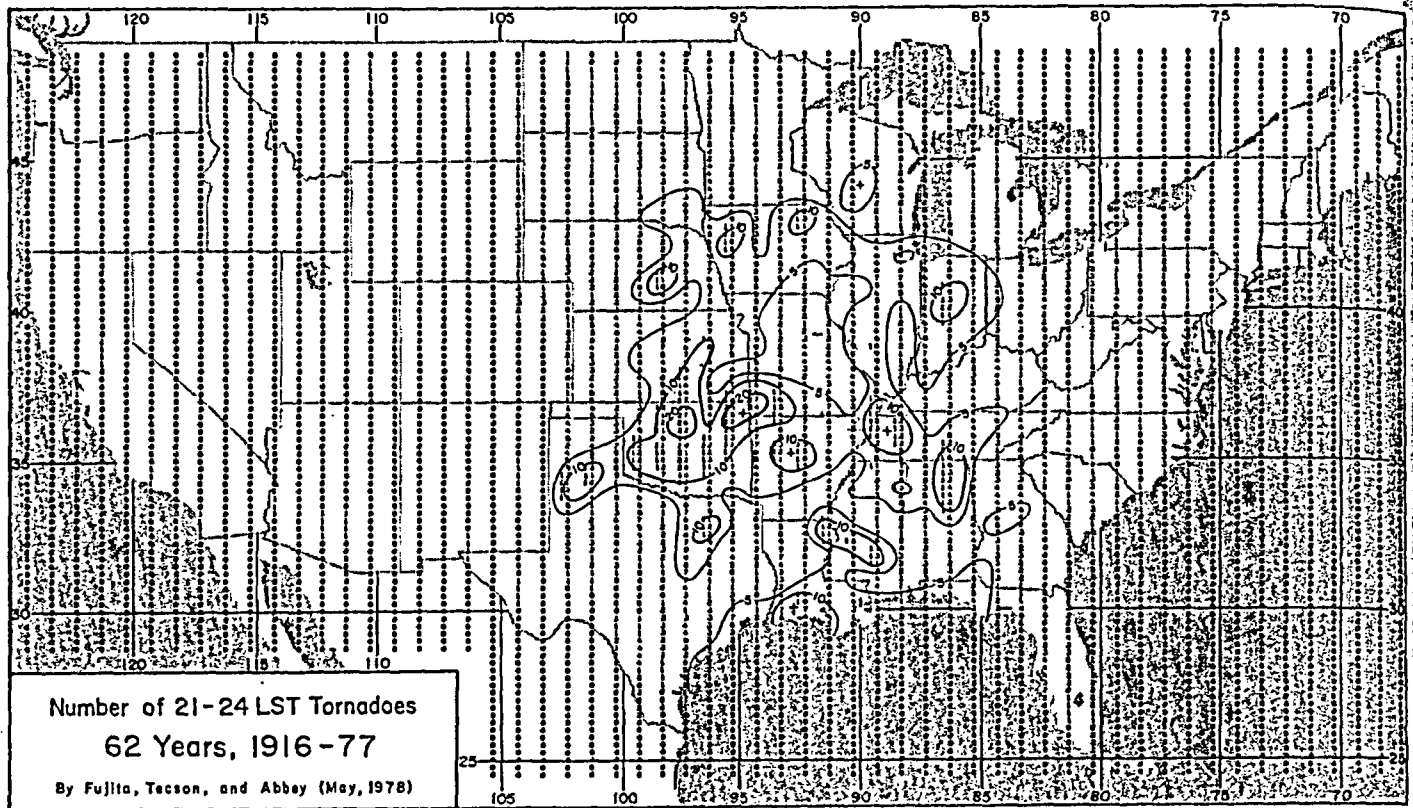


Figure 5.20 Numbers and path lengths of tornadoes between 21 and 24 Local Standard Time. The maximum numbers are located near the Oklahoma-Missouri border. Path-length maxima are seen at various locations.

CHAPTER SIX

ANALYTICAL MODEL OF TORNADOES

The concept of this design-basis tornado was originated early in 1976 under NRC Contract AT(49-24)-0239, leading to the formulation of the basic equations.

In view of the urgent requirements for a Review of Severe Weather Meteorology for Argonne National Laboratory, the tornado model identified as DBT-77 was finalized in the summer of 1977 under ANL Contract No. 31-109-38-3731.

1. Geometric Features

A schematic diagram of DBT-77 presented in Figure 6.1 reveals that the model tornado is an axially-symmetric vortex with a cylindrical core. The vertical core is divided into two parts:

The inner core with its radius, R_n , and
The outer core with its radius, R_o .

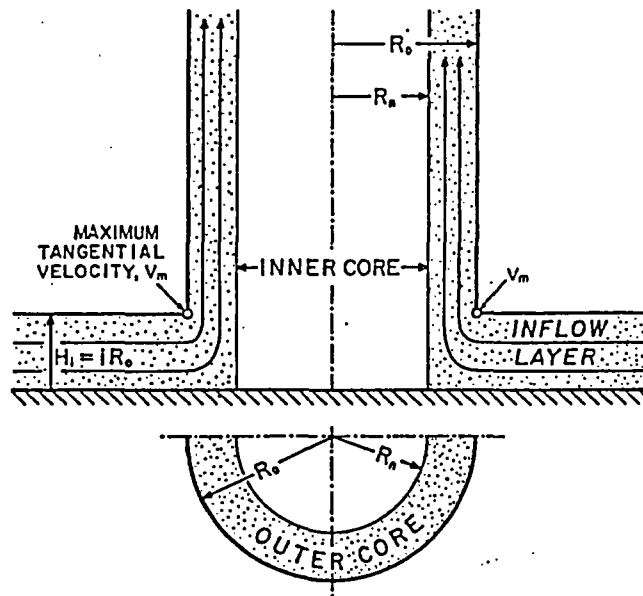


Figure 6.1 A schematic diagram of DBT-77. In this simplified model, the core is divided into inner and outer portions. Vertical motions are concentrated inside the outer core while the inner core is assumed to rotate like solid discs stacked up into a cylinder.

It is assumed that the inner core rotates like solid discs stacked into a cylinder, surrounded by an outer core in which air currents spiral upward. Inflow into the outer core takes place within a shallow layer with its top at H_1 .

The ratio of inner- and outer-core radii, called the "core ratio",

$$n = R_n / R_o \quad (6.1)$$

varies with the core radius. In this model, we assume that $n = 0.2$ when $R_o = 0$ and that n is between 0.5 and 0.6 when $R_o = 150$ m, and $n = 0.9$ when R_o approaches infinity. The equation adopted to express such a variation of core radius is

$$n = 0.9 - 0.7 e^{-0.005 R_o} \quad (6.2)$$

where R_o is the core radius in meters.

The depth of the inflow in relation to core radius varies with R_o . Evidence shows that the non-dimensional quantity,

$$i = H_1 / R_o \quad (6.3)$$

called the "inflow index" decreases with increasing core radii.

Without using an arbitrary function relating i with R_o , a specific relationship between i and n ,

$$E = \frac{i}{1 - n^2} = 0.55, \quad (6.4)$$

called the "core-shape parameter" was adopted in this model.

2. Definition of Windspeeds

Windspeed in a strict sense is the displacement of air molecules excluding their internal, thermal motions. It can be measured by anemometers or estimated from wind damage to structures or objects. Motions of debris also may be used in estimating tornado windspeeds. Strictly speaking, however, we have to identify the nature of windspeeds in relation to their computation methods. We shall first discuss the three types of windspeeds to be used in this paper.

- A. TRUE WINDSPEED (V_{TRU}) denotes the actual motion of air relative to the earth or to a moving wind system. A measured windspeed without proper corrections does not always represent the true windspeed, mainly because the air density varies with both time and space.
- B. DYNAMIC WINDSPEED (V_{DYN}) is the windspeed computed from dynamic pressure of an impinging flow. Dynamic and true windspeeds are interrelated by

$$\frac{1}{2} \rho V_{DYN}^2 = \frac{1}{2} \rho V_{TRU}^2 \quad (6.5)$$

where ρ denotes the true density of the airflow and ρ_s , a standard density of the airflow used in calibrating the pressure-type anemometer.

C. MODEL WINDSPEED (V_{MDL}) is a hypothetical windspeed which can be computed under the assumption of constant density. Such an assumption permits us to use the equation of continuity with a standard density, ρ_s , which can be taken out of integration. Model and true windspeeds are interrelated by

$$\rho_s V_{MDL} = \rho V_{TRU} \quad (6.6)$$

The three windspeeds discussed above can be related to each other by using the standard density such as that at 0°C and 1 atmospheric pressure. Equations to relate these speeds are

$$V_{TRU} = \rho_s / \rho V_{MDL} \quad (6.7)$$

$$V_{DYN} = \sqrt{\rho_s / \rho} V_{MDL} \quad (6.8)$$

It is seen that both true and dynamic windspeeds are faster than model windspeeds, especially at a high altitude or near the tornado center where air density is low. True and dynamic windspeeds at various altitudes of NASA standard atmosphere are shown in Table 6.1.

Table 6.1 Relationships between true, dynamic, and model windspeeds as a function of air density. The air density at sea level with 760 mm.Hg.(29.921 inch Hg.) pressure and 15°C (59°F) temperature was used as ρ_s , the standard density.

Altitude of the Standard Atmosphere		Air density kg/m ³	Model windspeed	True windspeed	Dynamic windspeed
0 km	0 ft	1.226	1.000	1.000	1.000
1	3,281	1.112	1.000	1.103	1.050
2	6,562	1.007	1.000	1.217	1.103
3	9,843	0.909	1.000	1.349	1.161
4	13,123	0.819	1.000	1.497	1.223
5	16,404	0.736	1.000	1.666	1.291
6	19,685	0.660	1.000	1.858	1.363
7	22,966	0.590	1.000	2.078	1.442
8	26,247	0.525	1.000	2.335	1.529
9	29,528	0.466	1.000	2.631	1.622
10	32,808	0.413	1.000	2.969	1.723

3. Tangential Velocity, V

Tangential velocity, as used in this model, is expressed by a product of two functions, each of which varies with height and radius, respectively. The equation of tangential velocity is

$$V = F(r) F(h) \cdot V_m \quad (6.9)$$

where V_m is the maximum tangential velocity commonly used by engineers. $F(r)$ and $F(h)$ are identified as "radial function" and "height function" and expressed by

$$F(r) = r^{+1} \quad \text{when } r < 1 \quad (6.10)$$

$$F(r) = r^{-1} \quad \text{when } 1 < r \quad (6.11)$$

$$F(h) = h^{k_0} \quad \text{when } h < 1 \quad (6.12)$$

$$F(h) = e^{-k(h-1)} \quad \text{when } 1 < h \quad (6.13)$$

where $k_0 = 1/6$ and $k = 0.03$ are used in this model. These values are subject to change as observational data are accumulated in the future.

Radial and height functions computed from these equations are tabulated in Table 6.2. (See Figures 6.2 and 6.3 for graphical representations of these functions.)

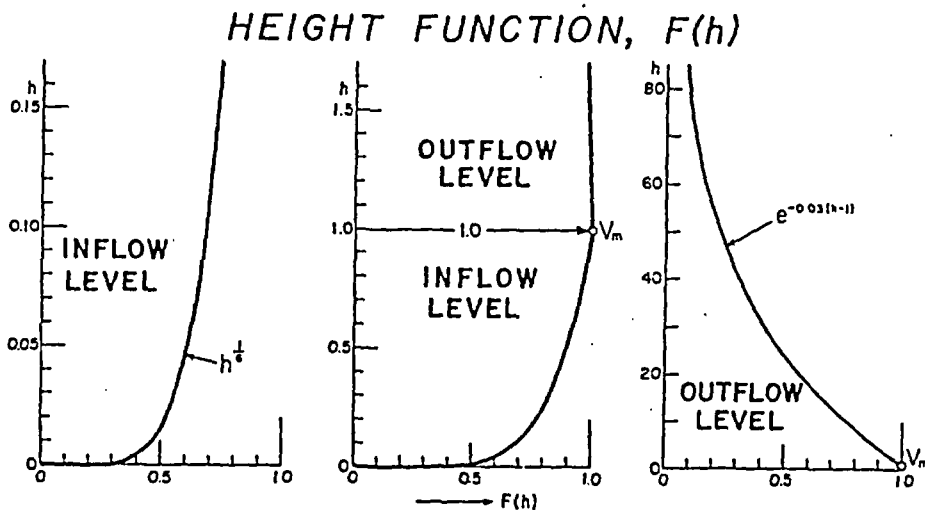


Figure 6.2 Height function, $F(h)$ used in DBT-77. Lowest layers of inflow (left) and outflow layers (right) are shown separately.

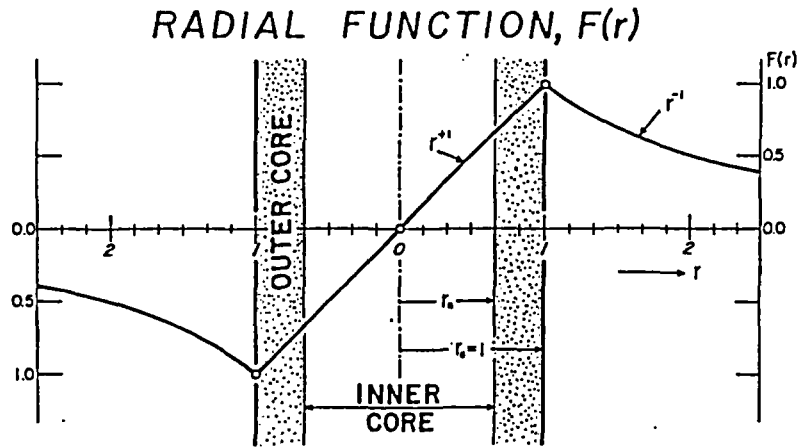


Figure 6.3 Radial function, $F(r)$ used in DBT-77.

Table 6.2 Radial function, $F(r)$ and height function, $F(h)$ for computing tangential velocities. From Eqs.(6.10) through (6.13).

Normalized radius, r	Radial function $F(r)$	Normalized height, h	Height function $F(h)$
0.0	0.000	0.00	0.000
0.1	0.100	0.01	0.464
0.3	0.300	0.03	0.557
0.5	0.500	0.05	0.607
0.7	0.700	0.07	0.642
0.9	0.900		
		0.1	0.681
1.0	1.000	0.3	0.818
1.1	0.909	0.5	0.891
1.3	0.769	0.7	0.942
1.5	0.667	0.9	0.983
1.7	0.588		
		1	1.000
2.0	0.500	3	0.942
3	0.333	5	0.887
4	0.250	7	0.835
5	0.200		
		10	0.763
6	0.167	30	0.419
7	0.143	50	0.230
8	0.125	70	0.126
9	0.111	100	0.051
10	0.100	150	0.011
20	0.050	200	0.003
Infinity	0.000	Infinity	0.000

4. Radial Velocity, U

Radial velocity is the radial component of the airflow and is expressed in this model by

$$U = V \tan \alpha \quad (6.14)$$

where α defined in Figure 3.5 denotes the crossing angle, positive outward (outflow) and negative inward (inflow). V has been defined by Eqs. (6.9) through (6.13).

In this model α is assumed to be zero inside the inner core. It increases or decreases outward within the outer core, reaching α_0 at its outer edge. Outside the core α_0 remains constant everywhere. These assumptions can be expressed by

$$\alpha = 0 \quad \text{inside the inner core} \quad (6.15)$$

$$\alpha \text{ varies } 0 \text{ to } \alpha_0 \quad \text{within the outer core} \quad (6.16)$$

$$\alpha = \alpha_0 \quad \text{outside the core} \quad (6.17)$$

The horizontally uniform α_0 outside the core is expressed in this model by two equations:

$$\tan \alpha_0 = -A_m \left(1 - h^{\frac{3}{2}}\right) \quad \text{inside inflow layer} \quad (6.18)$$

$$\tan \alpha_0 = B_m \left[1 - e^{-k(h-1)}\right] \quad \text{inside outflow layer} \quad (6.19)$$

where A_m and B_m are positive, non-dimensional quantities called the "maximum inflow tangent" and "maximum outflow tangent", respectively, and k is the constant in Eq. (6.13). These values represent the tangents of the maximum inflow and outflow angles located, respectively, at $h = 0$ and infinity.

Since the air entering the outer core must diverge outward before reaching the vortex top, assumed at infinity, A_m and B_m satisfy the equation of mass balance,

$$\int_0^1 U_0 \, dh + \int_1^\infty U_0 \, dh = 0 \quad (6.20)$$

where U_0 denotes the radial velocity at R_p . Making use of Eqs. (6.14), (6.18), and (6.19) we integrate Eq. (6.20) thus

$$-A_m \int_0^1 h^{\frac{1}{6}} \left(1 - h^{\frac{3}{2}}\right) dh + B_m \int_1^\infty \left[e^{-k(h-1)} - e^{-2k(h-1)}\right] dh = 0 \quad (6.21)$$

Thus, we equate inflow and outflow as

$$A_m \left[\frac{6}{7} h^{\frac{7}{6}} - \frac{3}{8} h^{\frac{8}{3}} \right]_0^1 = \frac{B_m}{2k} \left[-2e^{-k(h-1)} + e^{-2k(h-1)} \right]_1^\infty \quad (6.22)$$

which can be reduced to

$$\frac{B_m}{A_m} = \frac{27}{28} k = 0.02892. \quad (6.23)$$

This equation simply means that A_m and B_m cannot be chosen independently. The selection of a large A_m will result in a large value of B_m , because large inflow angles must be balanced by large outflow angles. Estimated inflow angles near the surface are between 30° and 40° . Based on this estimate, $A_m = 0.75$ was chosen in this model.

Putting $h = 0$ into Eq. (6.18), we obtain the maximum inflow angle, α_m , at the surface,

$$A_m = 0.75, (\alpha_m = -36.87^\circ) \quad \text{inflow} \quad (6.24)$$

Equation (6.23) and $A_m = 0.75$ result in the value of the maximum outflow tangent of

$$B_m = 0.02892 \quad A_m = 0.0217, (\alpha_m = 1.24^\circ) \quad \text{outflow} \quad (6.25)$$

Radial velocity outside the core can be obtained by combining Eqs. (6.12), (6.13), (6.14), (6.18), and (6.19) into

$$U_o = -A_m h^{\frac{1}{6}} (1 - h^{\frac{3}{2}}) F(r) V_m \quad \text{in flow layer} \quad (6.26)$$

$$\text{and} \quad U_o = +B_m e^{-k(h-1)} [1 - e^{-k(h-1)}] F(r) V_m \quad \text{outflow layer} \quad (6.27)$$

At the outer edge of the outer core, where $r = 1$, these equations can be reduced into

$$u_o = -A_m h^{\frac{1}{6}} (1 - h^{\frac{3}{2}}) \quad \text{inflow levels} \quad (6.28)$$

$$\text{and} \quad u_o = +B_m e^{-k(h-1)} [1 - e^{-k(h-1)}] \quad \text{outflow levels} \quad (6.29)$$

where $u_o = U_o/V_m$ denotes the normalized radial velocity at R_o . Numerical values and graphical representation of u_o appear in Table 6.3 and Figure 6.4.

The maximum values of u_o along the vertical occur where

$$\left(\frac{\partial u}{\partial h}\right)_{r=1} = -A_m \left(\frac{1}{6} h^{-\frac{5}{6}} - \frac{5}{3} h^{\frac{2}{3}}\right) = 0$$

$$\text{or} \quad h = 0.1^{\frac{2}{3}} = 0.215 \quad \text{inflow layer} \quad (6.30)$$

and where

$$\left(\frac{\partial u}{\partial h}\right)_{r=1} = B_m k [-e^{-k(h-1)} + 2e^{-2k(h-1)}]$$

$$\text{or} \quad h = 1 + k \ln 2 = 24.10 \quad \text{outflow layer} \quad (6.31)$$

where $k = 0.03$ is a constant assumed in this model.

The maximum value of U_o at these heights is computed by putting these heights into Eqs. (6.28) and (6.29). The maximum radial velocities thus obtained are

$$U_m = -0.6968 A_m V_m = -0.523 V_m \quad \text{inflow layer} \quad (6.32)$$

$$\text{and} \quad U_m = +0.250 B_m V_m = +0.00543 V_m \quad \text{outflow layer} \quad (6.33)$$

Table 6.3 Normalized radial velocity, $u_o = U_o/V_m$ at R tabulated as functions of normalized height, h . From Eqs.(6.28) and (6.29).

Normalized height, h	Normalized radial velocity, u_o	Normalized height, h	Normalized radial velocity, u_o
0.00	0.000	1	0.00000
0.01	0.348	3	0.00119
0.03	0.416	5	0.00217
0.05	0.450	7	0.00299
0.07	0.473	10	0.00393
0.1	0.495	24.10	0.00543 Max
0.215	0.523 Max	30	0.00527
0.3	0.513	50	0.00383
0.5	0.432	70	0.00239
0.7	0.293	100	0.00104
0.9	0.108	150	0.00024
1.0	0.000	200	0.00007

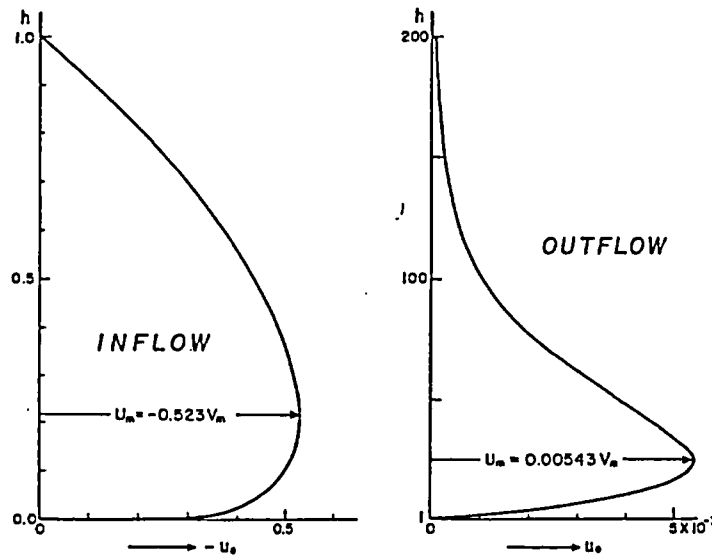


Figure 6.4 Normalized radial velocities within inflow (left) and outflow layers (right). The maximum inflow velocity, $0.523 V_m$ at $h=0.213$ is 96 times larger than the maximum outflow velocity, $0.00543 V_m$ at $h=24.10$.

5. Crossing Angle, α

The crossing angle of inflow and outflow outside the core are assumed to be horizontally uniform everywhere. The crossing angle, α_0 , already expressed by Eqs. (6.18) and (6.19) is given in Table 6.4.

By virtue of a constant crossing angle, trajectories of the airflow outside the core are logarithmic spirals expressed by

$$r = e^{2\pi f \tan \alpha_0} \quad (6.34)$$

$$\text{where } f = (\theta - \theta_0) / 2\pi$$

denotes the number of rotations around the tornado center.

Equation (6.34) permits us to compute normalized radii of air parcels as a function of the number of rotations. Table 6.5 reveals that an air parcel at $h = 0.215$, for example, departs from $r = 69.3$ in order to reach the core after completing a single rotation around the center. At $h = 24.10$ a parcel moves out only to $r = 1.23$ after rotating as many as three times around the tornado center. Thus, the outflow air moves out very slowly while rotating around the core.

The crossing angle inside the outer core can be obtained by equating

$$\frac{R U}{R^2 - R_n^2} = \frac{R_0 U_0}{R_0^2 - R_n^2} \quad (6.35)$$

each of which represents horizontally uniform divergence inside the outer core. Substituting U_0 and U in this equation by

$$U_0 = V_0 \tan \alpha_0 \quad \text{and} \quad U = V_0 r \tan \alpha$$

$$\text{and} \quad R_n = n R_0,$$

we obtain the ratio

$$a = \frac{\tan \alpha}{\tan \alpha_0} = \frac{r^2 - n^2}{r^2(1 - n^2)} \quad (6.36)$$

where a is called the "tangent ratio" in this model. This equation reveals that the tangent ratio is always positive and less than 1.0 (see Table 6.6 and Figure 6.5).

It is seen that a parcel which enters the outer core with crossing angle α_0 finally wraps around the inner core while α gradually decreases to zero.

Table 6.4 Crossing angles of airflow outside the core computed from Eqs.(6.18) and (6.19) with constants, $A_m = 0.75$ and $B_m = 0.0217$.

Normalized height, h	Crossing angles α_0	Normalized height, h	Crossing angles α_0
0.00	-36.9 degrees	1	+0.00 degrees
0.01	-36.8	3	+0.07
0.03	-36.7	5	+0.14
0.05	-36.6	7	+0.21
0.07	-36.4	10	+0.29
0.1	-36.0	24.10	+0.62
0.215	-34.0	30	+0.72
0.3	-32.1	50	+0.96
0.5	-25.9	70	+1.09
0.7	-17.3	100	+1.18
0.9	- 6.3	150	+1.23
1.0	- 0.0	200	+1.24

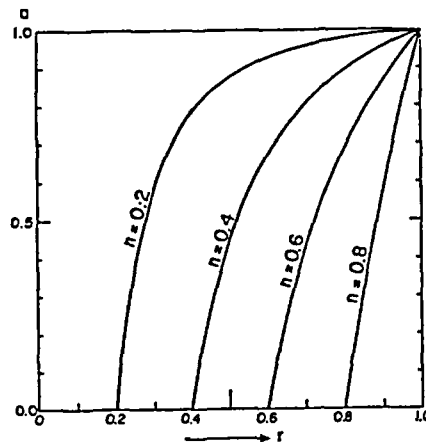


Figure 6.5 Variation of crossing angles inside the outer core in order to produce horizontally uniform divergence (or convergence) assumed in this model.

6. Vertical Velocity, W

Vertical velocity inside the inner core and outside the outer core is assumed zero. Inside the outer core, the vertical velocity is assumed horizontally uniform. Now we write

$$\pi (R_o^2 - R_n^2) W_{(h)} = 2 \pi R_o \int_0^h -U_o dh \quad (6.37)$$

Using $n = R_n/R_o$ from Eq. (6.1) and $H = h H_1$, where h is the normalized height and H_1 , the inflow height, we write

$$(1 - n^2) W = -2i \int_0^h U_o dh$$

or

$$W = \frac{-2i}{1 - n^2} \int_0^h U_o dh \quad (6.38)$$

where $i = H_1 / R_o$.

Putting U_o in Eq. (6.26) we have

$$\begin{aligned} w_o(\text{at } h) &= \frac{2i}{1 - n^2} A_m \left[-\frac{6}{7} h^{\frac{7}{6}} - \frac{3}{8} h^{\frac{8}{3}} \right]_0^h \\ &= W_m / V_m \quad \text{at inflow heights} \end{aligned} \quad (6.39)$$

where w_o denotes the normalized vertical velocity expressed by

$$\begin{aligned} w_o &= \frac{3}{28} \frac{i}{1 - n^2} A_m (16h^{\frac{7}{6}} - 7h^{\frac{8}{3}}) \\ &= 0.0442 (16h^{\frac{7}{6}} - 7h^{\frac{8}{3}}). \end{aligned} \quad (6.40)$$

For constants, n , i , and A_m , refer to Eqs. (6.1), (6.3), and (6.24).

Vertical velocity at outflow heights is obtained by putting $U_o = u_o V_m$ from Eq. (6.29) into Eq. (6.38) and integrating downward from infinity to level h . Thus we obtain

$$\begin{aligned} W_o(\text{at } h) &= \frac{-2i}{1 - n^2} B_m \left[-\frac{1}{k} e^{-k(h-1)} + \frac{1}{2k} e^{-2k(h-1)} \right]_{\infty}^h V_m \\ &= w_o V_m \quad \text{at outflow heights} \end{aligned} \quad (6.41)$$

where w_o denotes the normalized vertical velocity expressed by

$$\begin{aligned} w_o &= \frac{i}{1 - n^2} \frac{B_m}{k} [2e^{-k(h-1)} - e^{-2k(h-1)}] \\ &= 0.398 [2e^{-k(h-1)} - e^{-2k(h-1)}] \end{aligned} \quad (6.42)$$

Normalized vertical velocities computed from Eqs. (6.40) and (6.42) are given in Table 6.7 and described in graphical form in Figure 6.6.

The maximum vertical velocity can be obtained by putting $h = 1$ into either Eq. (6.40) or (6.42). The identical result obtained is

$$W_m = \frac{i}{1 - n^2} \left(\frac{27}{28} A_m \right) V_m = 0.398 V_m \quad (6.43)$$

Table 6.7 Normalized vertical velocity, $w_o = W_o/V_m$ computed from Eqs. (6.39) and (6.41). Eqs. (6.40) and (6.42) show that the maximum vertical velocity is independent of core radius.

Normalized height, h	Normalized vertical velocity, w_o	Normalized height, h	Normalized vertical velocity, w_o
0.00	0.000	1	0.398
0.01	0.003	3	0.397
0.03	0.012	5	0.393
0.05	0.021	7	0.387
0.07	0.031	10	0.376
0.1	0.047	30	0.263
0.3	0.161	50	0.162
0.5	0.266	70	0.094
0.7	0.347	100	0.040
0.9	0.392	150	0.009
1.0	0.398	200	0.000

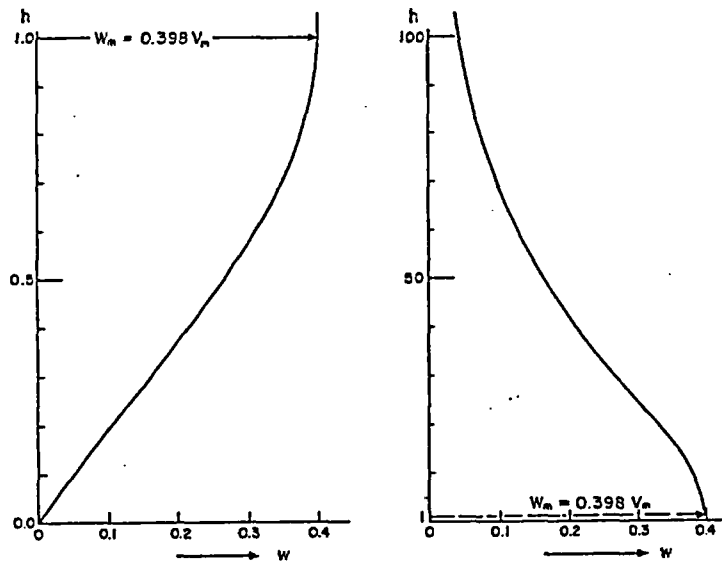


Figure 6.6 Normalized vertical velocity, W_o/V_m applicable to any tornado. From Table 6.7.

7. Summary of Three Component Velocities

Three component velocities used in this model are proportional to V_m , the maximum tangential velocity, making it possible to normalize each component velocity with respect to V_m . We shall summarize the normalized velocities applicable to DBT-77. These velocities $u_o = U_o/V_m$, $v_o = V_o/V_m$, and $w_o = W_o/V_m$ are

At INFLOW HEIGHTS where $h < 1$

$u_o = -A_m h^{\frac{1}{6}} (1 - h^{\frac{3}{2}})$	From: Eq. (6.28)
$v_o = h^{\frac{1}{6}}$ Eq. (6.12)
$w_o = \frac{3}{28} E A_m (16 h^{\frac{7}{6}} - 7 h^{\frac{8}{3}})$ Eq. (6.40)

where $E = \frac{i}{1 - n^2}$ and $A_m = -\tan \alpha_m$

At OUTFLOW HEIGHTS where $1 < h$

$u_o = \frac{27}{28} k A_m (e^{-k_1} - e^{-2k_1})$	From: Eq. (6.29)
$v_o = e^{-k_1}$ Eq. (6.13)
$w_o = \frac{27}{28} E A_m (2 e^{-k_1} - e^{-2k_1})$ Eq. (6.42)

where $E = \frac{i}{1 - n^2}$ and $k_1 = k(h - 1)$

At the INFLOW TOP where $h = 1$

$$\begin{aligned} u_o &= 0 \\ v_o &= 1 \\ w_o &= \frac{27}{28} E A_m \end{aligned}$$

This means that the vertical velocity varies in proportion to the product $E A_m$. Although the maximum inflow tangent, $A_m = 0.75$, and the core-shape parameter $E = 0.55$ were used in this model, these values can be changed individually or together as more tornado data become available.

CHAPTER SEVEN

TORNADO PARAMETERS FOR ENGINEERING

The so-called explosive damage by tornadoes has long been considered to be the result of a pressure drop inside the tornado funnel. Engineering assessments in recent years have revealed, however, that explosive damage can be caused by the hydrodynamic lift force induced by high-speed airflow above the structures. In other words, a downburst and straight-line winds are capable of producing structural damages similar to that caused by tornadoes.

When the vortex diameter is small in relation to a structure, however, the direction of damaging winds impinging upon the structure at any instant is no longer uniform. For small tornadoes and suction vortices, the effects of pressure and its variation with time becomes important. Figure 7.1 shows a small tornado in action.



Figure 7.1 A Japanese tornado in action. This small tornado formed beneath a towering cumulus in winter monsoon. The roof of a boat shed was lifted straight upward while small debris were thrown out in all directions.

Specific parameters for engineering assessments of tornado-induced damage are

- A. Radius of tornado's outer core, R_o .
- B. Translational velocity, T .
- C. Maximum tangential velocity, V_m .
- D. Maximum pressure drop due to vortex, ΔP_m .
- E. Maximum rate of pressure change $(dP/dt)_m$.

In the past, these parameters were estimated for tornadoes which were assumed to be axisymmetric. Evidence accumulated in recent years suggests a need for the inclusion of suction vortices in assessing possible tornado damage to structures.

1. Core Diameters of Tornado and Suction Vortex

Aerial surveys conducted during the past 13 years have revealed that most of the large tornadoes are accompanied by multiple suction vortices which may or may not be visible from outside.

Figure 7.2 shows three suction vortices rotating around the common center of the Muncie tornado, Indiana, of April 3, 1974. Funnel clouds inside these suction vortices are not visible at the time of this picture.

A few minutes later the same tornado was photographed by Mr. Anderson against the bright background, revealing the existence of two distinct condensation funnels (see Figure 7.3).

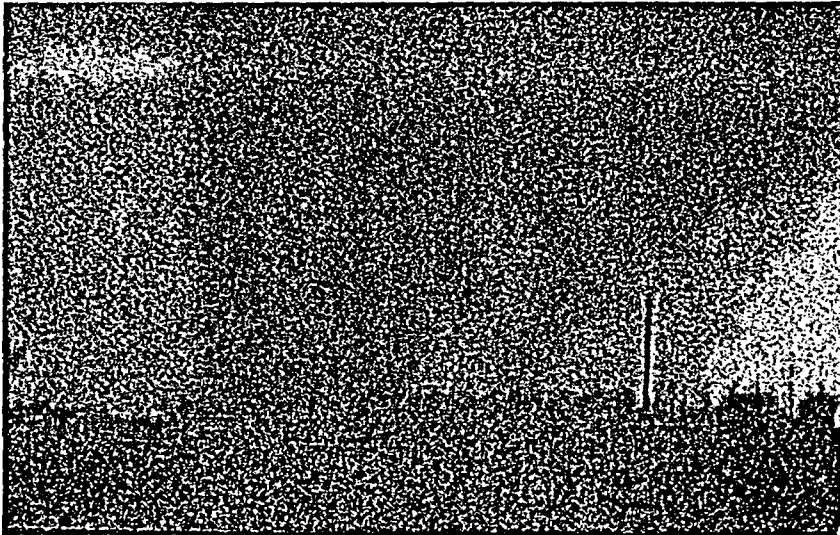


Figure 7.2 Three suction vortices rotating around the common center of Muncie tornado of April 3, 1974. One frame of a movie by Mr Hubbard, WISH-TV.

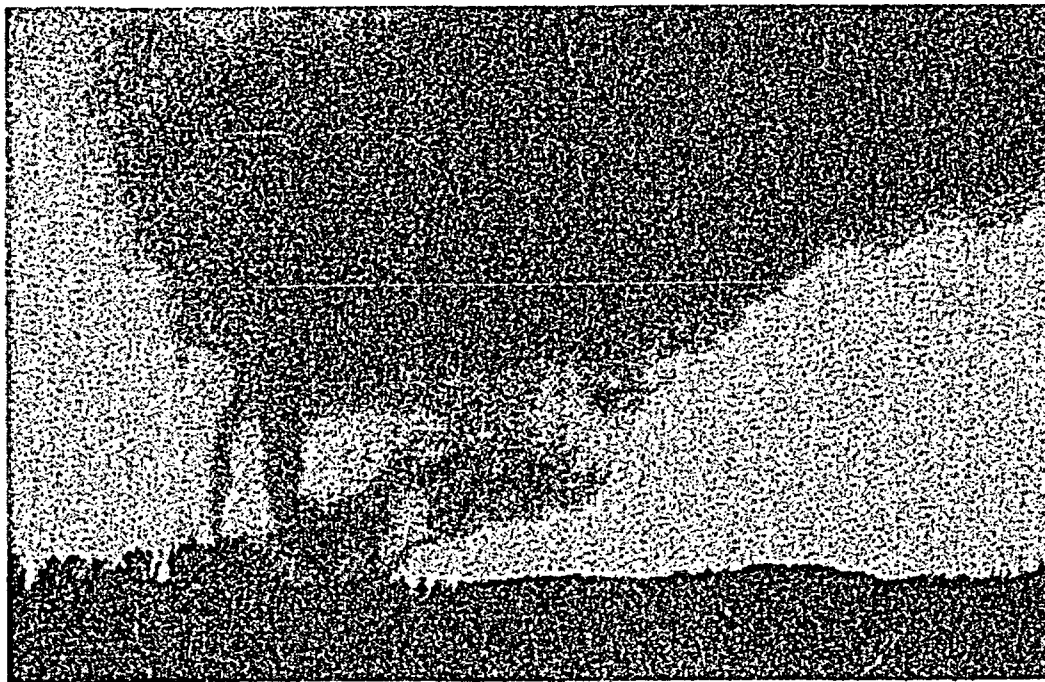


Figure 7.3 A few minutes after the picture in Figure 7.2, funnel clouds appeared inside suction vortices. Photo by Mr. Anderson.

It will probably take years before we can establish an engineering model of multiple-vortex tornadoes. Since we cannot wait until we obtain a complete solution of such tornadoes, a "first-guess" model has been worked out by the author. The author's generalized model includes the following parameters:

CORE RADIUS, R_o , OF TORNADO (but not of suction vortex) is assumed to vary with the maximum tangential velocity, V_m . This assumption can be expressed by

$$R_o = J V_m = 0.8 V_m \quad (7.1)$$

where J is a constant, 0.8, when R_o is expressed in meters and V_m in mph.

CORE RATIO, $n = R_n / R_o$, OF TORNADO is a non-dimensional value defined as the ratio of the radii of inner and outer core expressed by

$$n = 0.9 - 0.7 e^{-0.005 R_o} \quad (7.2)$$

This equation is identical to Eq. (6.2) in Chapter Six.

CORE RADIUS, \dot{R}_o , OF SUCTION VORTEX is computed assuming that a circular suction vortex occupies the annular space of the outer core of the parent tornado. Thus we write

$$\dot{R}_o = \frac{1}{2} (R_o - R_n) = \frac{1}{2} (1 - n) R_o. \quad (7.3)$$

Numerical values of the above three quantities are given in Table 7.1. Presently, a 150 m core radius is used as that of the design-basis violent tornado. It will be found later in this chapter that the maximum tangential velocity of an F5 tornado is less than 208 mph. This means that a tornado with $V_m = 250$ mph may be regarded as unrealistic.

The core radii of suction vortices are 0.6 to 0.2 times those of the parent tornadoes. Formerly, the radii of suction vortices were assumed to be one order of magnitude smaller than those of the parent tornadoes. This estimate was made by the narrow band of debris deposit left behind suction vortices. The core diameter of a vortex should be several times the width of the deposit band. In view of our re-evaluation, the core radii of suction vortices in Table 7.1 appear to be reasonable.

Table 7.1 Core diameters of tornado and embedded suction vortices given as functions of V_m , the maximum tangential velocity of the tornado.

Max. tan. vel. V_m	Tornado core radius R_o	S.V. core radius R_s	Core ratio $n = R_n/R_o$
50 mph	40 m	13 m	0.327
100	80	23	0.431
150	120	29	0.516
200	160	33	0.585
250	200	36	0.642

2. Maximum Total Windspeed

As has been discussed in Chapter Three, the maximum windspeed of a tornado occurs at the top of the inflow layer.

MAXIMUM HORIZONTAL WINDSPEED, M_H , OF TORNADO occurring on the right side of a traveling tornado at the top of the inflow layer is expressed by

$$M_H = T + V_m \quad (7.4)$$

where T is the translational velocity and V_m , the maximum tangential velocity. Based on an assumption that violent tornadoes travel at high speed, we express both T and V_m as simple functions of M_H . These functions are

$$T = \frac{1}{4} M_H \text{ and } V_m = \frac{3}{4} M_H . \quad (7.5)$$

The center of the suction vortex is located halfway between the outer edges of the inner and outer cores. The edge of a circular suction vortex makes contact with these core boundaries.

REVOLVING RADIUS, $\overset{\circ}{E}$, OF SUCTION VORTEX is computed by

$$\overset{\circ}{E} = \frac{1}{2} (R_o + R_n) = \frac{1}{2} (1+n) R_o . \quad (7.6)$$

It should be noted that both R_o and n vary with V_m , the maximum tangential velocity.

REVOLVING VELOCITY OR TRANSLATIONAL VELOCITY, $\overset{\circ}{T}$, OF SUCTION VORTEX around the parent tornado is assumed to be the mean tangential velocity of the tornado flow inside the inflow layer. Now we express

$$\overset{\circ}{T} = \frac{\overset{\circ}{E}}{R_o} \int_0^1 V_m h^{\frac{1}{6}} dh = \frac{6}{7} \frac{\overset{\circ}{E} V_m}{R_o} \quad (7.7)$$

which can be combined with Eq. (7.6) to obtain

$$\overset{\circ}{T} = \frac{3}{7} (1+n) V_m . \quad (7.8)$$

MAXIMUM TANGENTIAL VELOCITY, $\overset{\circ}{V}_m$, OF SUCTION VORTEX is assumed to be one-half of V_m . That is

$$\overset{\circ}{V}_m = \frac{1}{2} V_m . \quad (7.9)$$

This means that a suction vortex inside a $V_m = 200$ mph tornado rotates at a 100 mph tangential velocity.

MAXIMUM HORIZONTAL VELOCITY, M_H , OF SUCTION VORTEX is a sum of three velocities,

$$\overset{\circ}{M}_H = T + \overset{\circ}{T} + \overset{\circ}{V}_m . \quad (7.10)$$

This velocity occurs at the top of the inflow layer, on the right side of a suction vortex. This equation can be rewritten into

$$\begin{aligned}\dot{M}_H &= \frac{1}{4} M_H + \frac{3}{7} (1+n) \frac{3}{4} M_H + \frac{1}{2} \frac{3}{4} M_H \\ &= \left[\frac{5}{8} + \frac{9}{28} (1+n) \right] M_H \\ &= \left[\frac{5}{6} + \frac{3}{7} (1+n) \right] V_m .\end{aligned}\quad (7.11)$$

Since the smallest value of n is 0.2, \dot{M}_H should always be larger than $1.01 M_H$. This means that the maximum total horizontal windspeed inside a suction vortex is always larger than that of the parent tornado itself.

MAXIMUM VERTICAL VELOCITY, \dot{W}_m , OF SUCTION VORTEX is expressed by

$$\dot{W}_m = 0.397 \dot{V}_m = 0.199 V_m . \quad (7.12)$$

Tornado and suction-vortex parameters given in Eqs. (7.4) through (7.12) are computed as functions of V_m , the basic tornado parameter for engineering purposes (see Table 7.2).

Table 7.2 Tornado and suction-vortex parameters computed as functions of V_m .

Tornado parameters				Suction-vortex parameters			
V_m	T	W_m	M_H	\dot{V}_m	\dot{T}	\dot{W}_m	\dot{M}_H
50 mph	17 mph	20 mph	67 mph	25 mph	28 mph	10 mph	70 mph
100	33	40	140	50	61	20	144
150	50	60	210	75	97	30	222
200	67	79	279	100	136	40	303
250	83	99	349	125	175	50	383

MAXIMUM TOTAL WINDSPEED, M_T , OF TORNADO occurring at the same location of M_H is written as

$$M_T^2 = M_H^2 + W_m^2 \quad (7.13)$$

where W_m denotes the maximum vertical velocity at the top of the inflow layer. From Eq. (6.43) we have

$$W_m = 0.397 V_m = 0.298 M_H . \quad (7.14)$$

Thus we rewrite

$$\begin{aligned}M_T^2 &= (1 + 0.298^2) M_H^2 \\ \text{or } M_T &= 1.043 M_H = 1.391 V_m .\end{aligned}\quad (7.15)$$

MAXIMUM TOTAL VELOCITY, \dot{M}_T , OF SUCTION VORTEX is obtained by combining Eqs. (7.11) and (7.12). Thus we have

$$\dot{M}_T^2 = \dot{M}_H^2 + \dot{W}_m^2$$

or
$$\dot{M}_T = \dot{\mu} V_m$$

where
$$\dot{\mu} = \left[\left\{ \frac{5}{6} + \frac{3}{7}(1+n) \right\}^2 + 0.199^2 \right]^{\frac{1}{2}}. \quad (7.16)$$

The smallest value of $\dot{\mu}$ occurring when $n = 0.2$ is 1.362.

The above equations of tornado and suction-vortex parameters now permit us to express the maximum total velocities as functions of V_m (see Table 7.3).

Table 7.3 Maximum total velocities of tornado and suction vortex computed as functions of V_m , the maximum tangential velocity of tornado.

Tornado parameters		Suction-vortex parameters		
V_m	M_T	$\dot{\mu}$	\dot{M}_T	$\dot{M}_T - M_T$
50 mph	70 mph	1.415	71 mph	1 mph
100	139	1.459	146	7
150	209	1.496	224	15
200	278	1.525	305	27
250	348	1.550	388	40

This table reveals that the maximum total velocity of the suction vortex embedded inside a tornado is larger than that of the parent tornado. The difference in velocities increases significantly with V_m , indicating that the stronger the tornado, the larger the difference.

The effect of winds upon structures is proportional to the square of the wind-speed impinging upon them. Table 7.4 shows the increased wind effects in suction vortices when tornadoes of various V_m are characterized by these model suction vortices. A 10 to 20% increase in wind effect is expected to occur inside these suction vortices. This is why severe damage to structures is often found along the paths of suction vortices.

Table 7.4 Percent increase in the wind effect upon structure when tornadoes of various windspeeds are characterized by model suction vortices presented in this paper.

V_m	M_T^2	\dot{M}_T^2	% increase
50	$0.49 \times 10 \text{ mph}^2$	$0.50 \times 10 \text{ mph}^2$	2 %
100	1.92	2.13	11
150	4.37	5.02	15
200	7.73	9.30	20
250	12.11	15.05	24

The F-scale assessments of tornado damages are based on the maximum total velocities at structure levels. Assuming that the worst structural damage is caused by the maximum total wind inside the suction vortex, we compute maximum tangential velocities corresponding to each F scale windspeed.

Results in Table 7.5 indicate that the maximum tangential velocity of the top F 5 tornado is 207 mph. The core diameter increases with the F scale, reaching the largest value of 166 m.

Table 7.5 Maximum tangential velocities and core radii of tornado corresponding to F-scale windspeeds.

F scale	Windspeeds	Max.tan. velocities	Core radii
	$V_F = \dot{M}_T$	V_m	R_c
F 0	40 - 72 mph	29 - 51 mph	23 - 40 m
F 1	73 - 112	52 - 77	41 - 62
F 2	113 - 157	78 - 107	63 - 85
F 3	158 - 206	108 - 138	86 - 110
F 4	207 - 260	139 - 172	111 - 137
F 5	261 - 318	173 - 207	138 - 166

3. Maximum Pressure Drop

The maximum pressure drop inside a combined Rankine vortex is proportional to the air density and the square of the maximum tangential velocity. Since a suction vortex is small compared with its parent tornado, we assume that the total pressure field is the sum of the partial pressure field induced independently by these two types of Rankine vortices. These pressure drops are

$$\Delta P_m = \rho V_m^2 \quad \text{for tornado} \quad (7.17)$$

$$\text{and} \quad \Delta \dot{P}_m = \rho \dot{V}_m^2 \quad \text{for suction vortex.} \quad (7.18)$$

From the assumption in Eq. (7.9) we express Eq. (7.18) by V_m ; thus,

$$\Delta \dot{P}_m = \frac{1}{4} \rho V_m^2 \quad (7.19)$$

This means that the maximum pressure drop induced by this model suction vortex is only one-quarter of that induced by the parent tornado.

Equations (7.17) and (7.19) along with Table 7.6 now permit us to compute the maximum pressure drop by both tornado and embedded suction vortex. Table 7.7 was obtained by assuming the air density to be 1.226 kg/m³ (sea level).

Table 7.6 Maximum tangential velocities of tornado, core radii and maximum translational velocities of suction vortex corresponding to maximum total velocities of embedded suction vortices.

Max. total vel. \dot{M}_T	Max. tan. vel. V_m	Core radii R_o	Max. tran. vel. s.v. $T + \dot{T}$
50 mph	36 mph	29 m	32 mph
100	70	56	64
150	103	82	97
200	135	108	131
250	166	133	165
300	197	157	199

Table 7.7 Maximum pressure drops by tornado and embedded suction vortex at sea level ($\rho = 1.226 \text{ kg/m}^3$).

Max. total vel. \dot{M}_T	Tornado ΔP_m		Suction vortex $\Delta \dot{P}_m$	
50 mph	3.1 mb	0.04 psi	0.8 mb	0.01 psi
100	11.9	0.17	3.0	0.04
150	25.8	0.37	6.4	0.09
200	44.9	0.65	11.0	0.16
250	67.5	0.98	16.9	0.25
300	94.9	1.38	23.7	0.34

It should be noted that the amounts of the maximum pressure drop are much less than those computed by assuming that the maximum wind velocity inside a tornado is a simple addition of T and V_m . This generalized model by the author includes suction vortex as an additional swirl wind which increases the maximum windspeed. Therefore, it is not necessary for a tornado to be characterized by a large maximum pressure drop in order to create specific damage.

The maximum total pressure drop due to both the tornado and suction vortex is not the sum of ΔP_m and $\Delta \dot{P}_m$, because the pressure drop of the tornado at the revolving radius, \dot{E} , of the suction vortices is smaller than ΔP_m .

The pressure drop of the tornado at \dot{E} in Eq. (7.6) can be computed from

$$\Delta P_{\dot{E}} = \frac{1}{2} \Delta P_m + \rho \int_{\dot{E}}^{R_o} \frac{V^2}{R} dR \quad (7.20)$$

Putting $V = V_m \frac{R}{R_o}$ into this equation we integrate

$$\Delta P_{\dot{E}} = \left(1 - \frac{1}{2} \delta^2\right) \Delta P_m \quad (7.21)$$

where $\delta = \frac{1}{2} (1 + n) = \dot{E} / R_o$ from Eq. (7.6).

The maximum total pressure drop by both the tornado and the embedded suction vortex combined is

$$\Delta P_{mT} = \Delta P_{\xi} + \Delta \dot{P}_m \quad (7.22)$$

Values of ΔP_{mT} were computed as a function of maximum total velocity, \dot{M}_H , of embedded suction vortex (see Table 7.8).

It is of interest to find that the maximum total pressure drop of a 300 mph tornado turned out to be only 94.9 mb or 1.38 psi.

Table 7.8 Pressure drop, ΔP_{ξ} at revolving radius, maximum pressure drop, $\Delta \dot{P}_m$ by suction vortex, and maximum total pressure drop $\Delta P_{\xi} + \Delta \dot{P}_m$ by both tornado and suction vortex.

\dot{M}_T	ΔP_{ξ}	$\Delta \dot{P}_m$	$\Delta P_{\xi} + \Delta \dot{P}_m$
50 mph	2.5 mb 0.04 psi	0.8 mb 0.01 psi	3.3 mb 0.05 psi
100	9.1 0.13	3.0 0.04	12.1 0.18
150	19.1 0.28	6.4 0.09	25.5 0.37
200	32.4 0.47	11.0 0.16	43.4 0.63
250	47.5 0.69	16.9 0.25	64.4 0.93
300	65.2 0.95	23.7 0.34	88.9 1.29

4. Maximum Rate of Pressure Change

The maximum rate of pressure change caused by a combined Rankine vortex is expressed by

$$(dP/dt)_m = \frac{T}{R_o} \Delta P_m \quad (7.23)$$

where T denotes the translational velocity of the vortex; R_o , the core radius; and ΔP the maximum pressure drop. When T is expressed in mph and R_o in meters the rate per second is computed from

$$(dP/dt)_m = 0.447 \frac{T}{R_o} \Delta P_m \quad \text{sec}^{-1} \quad (7.24)$$

This equation is readily applicable to both a tornado and the embedded suction vortex. For a tornado we use Eqs. (7.1) and (7.5) to write

$$T = \frac{1}{4} M_H = \frac{1}{3} V_m \quad \text{and} \quad R_o = J V_m \quad (7.25)$$

and obtain the maximum rate of pressure change

$$(dP/dt)_m = 0.186 \Delta P_m \quad \text{sec}^{-1} \quad (7.26)$$

For the embedded suction vortex we replace T in Eq. (7.24) by $T + \dot{T}$ and R_o by \dot{R}_o to obtain

$$(d\dot{P}/dt)_m = 0.447 \frac{T + \dot{T}}{\dot{R}_o} \Delta \dot{P}_m \quad \text{sec}^{-1} \quad (7.27)$$

where $(d\dot{P}/dt)_m$ is the maximum rate of pressure change caused by the suction vortex. Using \dot{R}_o in Eq. (7.3) and \dot{T} in Eq. (7.8) we express Eq. (7.27) as a function of n and $\Delta \dot{P}_m$

$$(d\dot{P}/dt)_m = 0.447 \frac{0.333 + 0.429(1+n)}{0.4(1-n)} \Delta \dot{P}_m \quad \text{sec}^{-1} \quad (7.28)$$

The maximum rates of pressure change in Table 7.9 were computed from Eqs. (7.27) and (7.28). The maximum rate due to a tornado is only 8.4 mb/sec or 0.12 psi/sec when $\dot{M}_T = 200$ mph (top F3 tornado). This is why the pressure effect can be neglected for most tornadoes.

Table 7.9 Maximum rate of pressure change by tornado and embedded suction vortex computed as functions of \dot{M}_T .

Max. total vel. \dot{M}_T	Tornado $(dP/dt)_m$		Suction vortex $(d\dot{P}/dt)_m$		Ratio
50 mph	0.58 mb/s	0.01 psi/sec	1.09 mb/s	0.02 psi/sec	1.9
100	2.21	0.03	4.85	0.07	2.2
150	4.8	0.07	12.1	0.18	2.5
200	8.4	0.12	24.0	0.35	2.9
250	12.6	0.18	40.6	0.59	3.2
300	17.7	0.26	64.0	0.93	3.6

Pressure effects in a suction vortex are more serious than a tornado. The maximum rate in suction vortex is 2 to 4 times larger than that experienced in a tornado. On the other hand, the maximum amount of pressure drop by a tornado is 4 times larger than that by a suction vortex.

Table 7.10 Maximum tangential velocity, V_m given as a function of F-scale windspeed, V_F which is the maximum total velocity, \dot{M}_T of multiple-vortex tornadoes. V_m is the primary parameter of this tornado model, DBT-78 in computing n , the core ratio; R_o , the core radius; ρV_m^2 , the maximum pressure drop, etc. ($\rho = 1.226 \text{ kg/m}^3$)

	$V_F = \dot{M}_T$	V_m	n	R_o	T	ρV_m^2	\dot{R}_o	\dot{T}	$\rho \dot{V}_m^2$
FO	40 mph	28.7 mph	0.276	23.0 m	9.6 mph	2.0 mb	8.3 m	15.7 mph	0.5 mb
	41	29.4	0.278	23.5	9.8	2.1	8.5	16.1	0.5
	42	30.1	0.279	24.1	10.0	2.2	8.7	16.5	0.6
	43	30.8	0.281	24.6	10.3	2.3	8.9	16.9	0.6
	44	31.5	0.283	25.2	10.5	2.4	9.0	17.3	0.6
	45	32.2	0.285	25.8	10.7	2.5	9.2	17.7	0.6
	46	32.9	0.286	26.3	11.0	2.7	9.4	18.2	0.7
	47	33.6	0.288	26.9	11.2	2.8	9.6	18.6	0.7
	48	34.3	0.290	27.4	11.4	2.9	9.7	19.0	0.7
	49	35.0	0.291	28.0	11.7	3.0	9.9	19.4	0.7
FO	50	35.7	0.293	28.6	11.9	3.1	10.1	19.8	0.8
	51	36.4	0.295	29.1	12.1	3.2	10.3	20.2	0.8
	52	37.0	0.296	29.6	12.3	3.4	10.4	20.6	0.8
	53	37.7	0.298	30.2	12.6	3.5	10.6	21.0	0.9
	54	38.4	0.300	30.7	12.8	3.6	10.8	21.4	0.9
	55	39.1	0.301	31.3	13.0	3.7	10.9	21.8	0.9
	56	39.8	0.303	31.8	13.3	3.9	11.1	22.2	1.0
	57	40.5	0.305	32.4	13.5	4.0	11.3	22.7	1.0
	58	41.2	0.306	33.0	13.7	4.2	11.4	23.1	1.0
	59 ←	41.9	0.308	33.5	14.0	4.3	11.6	23.5	1.1
FO	60	42.6	0.310	34.1	14.2	4.4	11.8	23.9	1.1
	61	43.3	0.311	34.6	14.4	4.6	11.9	24.4	1.1
	62	44.0	0.313	35.2	14.7	4.7	12.1	24.8	1.2
	63	44.6	0.314	35.7	14.9	4.9	12.2	25.1	1.2
	64	45.3	0.316	36.2	15.1	5.0	12.4	25.6	1.3
	65	46.0	0.318	36.8	15.3	5.2	12.6	26.0	1.3
	66	46.7	0.319	37.4	15.6	5.3	12.7	26.4	1.3
	67	47.4	0.321	37.9	15.8	5.5	12.9	26.9	1.4
	68	48.1	0.323	38.5	16.0	5.7	13.0	27.3	1.4
	69	48.8	0.324	39.0	16.3	5.8	13.2	27.7	1.5
FO	70	49.4	0.326	39.5	16.5	6.0	13.3	28.1	1.5
	71	50.1	0.327	40.1	16.7	6.1	13.5	28.5	1.5
	72	50.8	0.329	40.6	16.9	6.3	13.6	29.0	1.6
	73	51.5	0.330	41.2	17.2	6.5	13.8	29.4	1.6
	74	52.2	0.332	41.8	17.4	6.7	13.9	29.8	1.7
	75	52.8	0.333	42.2	17.6	6.8	14.1	30.2	1.7
	76	53.5	0.335	42.8	17.8	7.0	14.2	30.6	1.8
	77	54.2	0.336	43.4	18.1	7.2	14.4	31.1	1.8
	78	54.9	0.338	43.9	18.3	7.4	14.5	31.5	1.8
	79	55.6	0.340	44.5	18.5	7.6	14.7	32.0	1.9
FI	80	56.2	0.341	45.0	18.7	7.7	14.8	32.3	1.9
	81	56.9	0.342	45.5	19.0	7.9	15.0	32.8	2.0
	82	57.6	0.344	46.1	19.2	8.1	15.1	33.2	2.0
	83	58.3	0.346	46.6	19.4	8.3	15.3	33.7	2.1
	84	59.0	0.347	47.2	19.7	8.5	15.4	34.1	2.1
	85	59.6	0.348	47.7	19.9	8.7	15.5	34.5	2.2
	86	60.3	0.350	48.2	20.1	8.9	15.7	34.9	2.2
	87	61.0	0.352	48.8	20.3	9.1	15.8	35.4	2.3
	88	61.6	0.353	49.3	20.5	9.3	15.9	35.8	2.3
	89	62.3	0.354	49.8	20.8	9.5	16.1	36.2	2.4
FT	90	63.0	0.356	50.4	21.0	9.7	16.2	36.6	2.4
	91	63.7	0.357	51.0	21.2	9.9	16.4	37.1	2.5
	92 ←	64.3	0.359	51.4	21.4	10.1	16.5	37.5	2.5
	93	65.0	0.360	52.0	21.7	10.3	16.6	37.9	2.6
	94	65.7	0.362	52.6	21.9	10.6	16.8	38.4	2.6
	95	66.4	0.363	53.1	22.1	10.8	16.9	38.8	2.7
	96	67.0	0.365	53.6	22.3	11.0	17.0	39.2	2.7
	97	67.7	0.366	54.2	22.6	11.2	17.2	39.7	2.8
	98	68.4	0.368	54.7	22.8	11.5	17.3	40.1	2.9
	99	69.0	0.369	55.2	23.0	11.7	17.4	40.5	2.9

	$V_F = \overset{\circ}{M}_T$	V_m	n	R_0	T	ρV_m^2	$\overset{\circ}{R}_0$	$\overset{\circ}{T}$	$\rho \overset{\circ}{V}_m^2$
	100	69.7	0.370	55.8	23.2	11.9	17.6	41.0	3.0
	101	70.4	0.372	56.3	23.5	12.1	17.7	41.4	3.0
	102	71.0	0.373	56.8	23.7	12.3	17.8	41.8	3.1
	103	71.7	0.375	57.4	23.9	12.6	17.9	42.3	3.1
	104	72.4	0.376	57.9	24.1	12.8	18.1	42.7	3.2
	105	73.0	0.377	58.4	24.3	13.1	18.2	43.1	3.3
	106	73.7	0.379	59.0	24.6	13.3	18.3	43.6	3.3
	107	74.4	0.380	59.5	24.8	13.6	18.4	44.1	3.4
	108	75.0	0.381	60.0	25.0	13.8	18.6	44.4	3.4
	109	75.7	0.383	60.6	25.2	14.0	18.7	44.9	3.5
	110	76.4	0.384	61.1	25.5	14.3	18.8	45.4	3.6
F1	111	77.0	0.386	61.6	25.7	14.5	18.9	45.8	3.6
F2	112	77.7	0.387	62.2	25.9	14.8	19.1	46.2	3.7
	113	78.3	0.388	62.6	26.1	15.0	19.2	46.6	3.8
	114	79.0	0.390	63.2	26.3	15.3	19.3	47.1	3.8
	115	79.7	0.391	63.8	26.6	15.6	19.4	47.6	3.9
	116	80.3	0.392	64.2	26.8	15.8	19.5	48.0	3.9
	117	81.0	0.394	64.8	27.0	16.1	19.6	48.4	4.0
	118	81.7	0.395	65.4	27.2	16.3	19.8	48.9	4.1
	119	82.3	0.396	65.8	27.4	16.6	19.9	49.3	4.1
	120	83.0	0.398	66.4	27.7	16.9	20.0	49.8	4.2
	121	83.6	0.399	66.9	27.9	17.1	20.1	50.2	4.3
	122	84.3	0.400	67.4	28.1	17.4	20.2	50.6	4.3
	123	84.9	0.402	67.9	28.3	17.7	20.3	51.0	4.4
	124	85.6	0.403	68.5	28.5	17.9	20.4	51.5	4.5
	125	86.3	0.404	69.0	28.8	18.2	20.6	52.0	4.6
	126	86.9	0.406	69.5	29.0	18.5	20.7	52.4	4.6
	127	87.6	0.407	70.1	29.2	18.8	20.8	52.9	4.7
	128	88.2	0.408	70.6	29.4	19.1	20.9	53.3	4.8
	129	88.9	0.409	71.1	29.6	19.4	21.0	53.8	4.8
	130	89.5	0.411	71.6	29.8	19.6	21.1	54.2	4.9
	131	90.2	0.412	72.2	30.1	19.9	21.2	54.6	5.0
F2	132	90.9	0.413	72.7	30.3	20.2	21.3	55.1	5.1
	133	91.5	0.415	73.2	30.5	20.5	21.4	55.5	5.1
	134	92.2	0.416	73.8	30.7	20.8	21.5	56.0	5.2
	135	92.8	0.417	74.2	30.9	21.1	21.6	56.4	5.3
	136	93.5	0.418	74.8	31.2	21.4	21.8	56.9	5.4
	137	94.1	0.420	75.3	31.4	21.7	21.8	57.3	5.4
	138	94.8	0.421	75.8	31.6	22.0	22.0	57.8	5.5
	139	95.4	0.422	76.3	31.8	22.3	22.1	58.2	5.6
	140	96.1	0.423	76.9	32.0	22.6	22.2	58.7	5.7
	141	96.7	0.425	77.4	32.2	22.9	22.3	59.1	5.7
	142	97.4	0.426	77.9	32.5	23.2	22.4	59.6	5.8
	143	98.0	0.427	78.4	32.7	23.5	22.5	60.0	5.9
	144	98.7	0.428	79.0	32.9	23.9	22.6	60.5	6.0
	145	99.3	0.429	79.4	33.1	24.1	22.7	60.9	6.0
	146	100.0	0.431	80.0	33.3	24.5	22.8	61.4	6.1
	147	100.6	0.432	80.5	33.5	24.8	22.9	61.8	6.2
	148	101.3	0.433	81.0	33.8	25.1	23.0	62.3	6.3
	149	101.9	0.434	81.5	34.0	25.4	23.1	62.7	6.4
	150	102.6	0.436	82.1	34.2	25.8	23.2	63.2	6.4
	151	103.2	0.437	82.6	34.4	26.1	23.3	63.6	6.5
	152	103.9	0.438	83.1	34.6	26.4	23.4	64.1	6.6
	153	104.5	0.439	83.6	34.8	26.7	23.4	64.5	6.7
	154	105.2	0.440	84.2	35.1	27.1	23.5	65.0	6.8
	155	105.8	0.442	84.6	35.3	27.4	23.6	65.4	6.9
F2	156	106.5	0.443	85.2	35.5	27.8	23.7	65.9	6.9
	157	107.1	0.444	85.7	35.7	28.1	23.8	66.3	7.0
F3	158	107.7	0.445	86.2	35.9	28.4	23.9	66.8	7.1
	159	108.4	0.446	86.7	36.1	28.8	24.0	67.3	7.2
	160	109.0	0.447	87.2	36.3	29.1	24.1	67.7	7.3
	161	109.7	0.449	87.8	36.6	29.5	24.2	68.2	7.4
	162	110.3	0.450	88.2	36.8	29.8	24.3	68.6	7.4
	163	111.0	0.451	88.8	37.0	30.2	24.4	69.1	7.5
	164	111.6	0.452	89.3	37.2	30.5	24.5	69.5	7.6
	165	112.3	0.453	89.8	37.4	30.9	24.6	70.0	7.7
	166	112.9	0.454	90.3	37.6	31.2	24.6	70.4	7.8
	167	113.5	0.455	90.8	37.8	31.5	24.7	70.9	7.9
	168	114.2	0.457	91.4	38.1	31.9	24.8	71.4	8.0
	169	114.8	0.458	91.8	38.3	32.3	24.9	71.8	8.1
	170	115.5	0.459	92.4	38.5	32.7	25.0	72.3	8.2
	171	116.1	0.460	92.9	38.7	33.0	25.1	72.7	8.2
	172	116.8	0.461	93.4	38.9	33.4	25.2	73.2	8.3
	173	117.4	0.462	93.9	39.1	33.8	25.2	73.6	8.4
	174	118.0	0.463	94.4	39.3	34.1	25.3	74.1	8.5

	$V_F = \overset{\circ}{M}_T$	V_m	n	R_0	T	ρV_m^2	$\overset{\circ}{R}_0$	$\overset{\circ}{T}$	$\rho \overset{\circ}{V}_m^2$
F3	175	118.7	0.465	95.0	39.6	34.5	25.4	74.6	8.6
	176	← 119.3	0.466	95.4	39.8	34.9	25.5	75.0	8.7
	177	120.0	0.467	96.0	40.0	35.3	25.6	75.5	8.8
	178	120.6	0.468	96.5	40.2	35.6	25.7	75.9	8.9
	179	121.2	0.469	97.0	40.4	36.0	25.7	76.4	9.0
	180	121.9	0.470	97.5	40.6	36.4	25.8	76.9	9.1
	181	122.5	0.471	98.0	40.8	36.8	25.9	77.3	9.2
	182	123.1	0.472	98.5	41.0	37.1	26.0	77.7	9.3
	183	123.8	0.473	99.0	41.3	37.5	26.1	78.3	9.4
	184	124.4	0.474	99.5	41.5	37.9	26.2	78.7	9.5
	185	125.1	0.476	100.1	41.7	38.3	26.2	79.2	9.6
	186	125.7	0.477	100.6	41.9	38.7	26.3	79.6	9.7
	187	126.3	0.478	101.0	42.1	39.1	26.4	80.1	9.8
	188	127.0	0.479	101.6	42.3	39.5	26.5	80.6	9.9
	189	127.6	0.480	102.1	42.5	39.9	26.5	81.0	10.0
	190	128.2	0.481	102.6	42.7	40.2	26.6	81.4	10.1
	191	128.9	0.482	103.1	43.0	40.7	26.7	82.0	10.2
	192	129.5	0.483	103.6	43.2	41.1	26.8	82.4	10.3
	193	130.2	0.484	104.2	43.4	41.5	26.9	82.9	10.4
194	130.8	0.485	104.6	43.6	41.9	26.9	83.3	10.5	
195	131.4	0.486	105.1	43.8	42.3	27.0	83.8	10.6	
196	132.1	0.487	105.7	44.0	42.7	27.1	84.3	10.7	
197	132.7	0.488	106.2	44.2	43.1	27.2	84.7	10.8	
198	133.3	0.489	106.6	44.4	43.5	27.2	85.2	10.9	
199	134.0	0.490	107.2	44.7	44.0	27.3	85.7	11.0	
200	134.6	0.491	107.7	44.9	44.4	27.4	86.1	11.1	
201	135.2	0.492	108.2	45.1	44.8	27.5	86.6	11.2	
202	135.9	0.494	108.7	45.3	45.2	27.5	87.1	11.3	
203	136.5	0.495	109.2	45.5	45.6	27.6	87.5	11.4	
204	137.1	0.495	109.7	45.7	46.0	27.7	88.0	11.5	
205	137.8	0.497	110.2	45.9	46.5	27.7	88.5	11.6	
F3	206	138.4	0.498	110.7	46.1	46.9	27.8	88.9	11.7
F4	207	139.0	0.499	111.2	46.3	47.3	27.9	89.4	11.8
	208	139.6	0.500	111.7	46.5	47.7	27.9	89.8	11.9
	209	140.3	0.501	112.2	46.8	48.2	28.0	90.3	12.0
	210	140.9	0.502	112.7	47.0	48.6	28.1	90.8	12.1
	211	141.5	0.503	113.2	47.2	49.0	28.2	91.2	12.3
	212	142.2	0.504	113.8	47.4	49.5	28.2	91.7	12.4
	213	142.8	0.505	114.2	47.6	49.9	28.3	92.2	12.5
	214	143.4	0.506	114.7	47.8	50.4	28.4	92.6	12.6
	215	144.1	0.507	115.3	48.0	50.9	28.4	93.1	12.7
	216	144.7	0.508	115.8	48.2	51.3	28.5	93.6	12.8
	217	145.3	0.509	116.2	48.4	51.7	28.6	94.0	12.9
	218	145.9	0.509	116.7	48.6	52.1	28.6	94.5	13.0
	219	146.6	0.511	117.3	48.9	52.6	28.7	95.0	13.2
	220	147.2	0.512	117.8	49.1	53.1	28.8	95.4	13.3
	221	147.8	0.512	118.2	49.3	53.5	28.8	95.9	13.4
	222	148.5	0.514	118.8	49.5	54.0	28.9	96.4	13.5
	223	149.1	0.514	119.3	49.7	54.4	29.0	96.9	13.6
	224	149.7	0.515	119.8	49.9	54.9	29.0	97.3	13.7
	225	150.3	0.516	120.2	50.1	55.3	29.1	97.8	13.8
	226	151.0	0.517	120.8	50.3	55.8	29.2	98.3	14.0
F4	227	← 151.6	0.518	121.3	50.5	56.3	29.2	98.7	14.1
	228	152.2	0.519	121.8	50.7	56.7	29.3	99.2	14.2
	229	152.9	0.520	122.3	51.0	57.3	29.3	99.7	14.3
	230	153.5	0.521	122.8	51.2	57.7	29.4	100.2	14.4
	231	154.1	0.522	123.3	51.4	58.2	29.5	100.6	14.5
	232	154.7	0.523	123.8	51.6	58.6	29.5	101.1	14.6
	233	155.4	0.524	124.3	51.8	59.1	29.6	101.6	14.8
	234	156.0	0.525	124.8	52.0	59.6	29.6	102.1	14.9
	235	156.6	0.526	125.3	52.2	60.1	29.7	102.5	15.0
	236	157.2	0.527	125.8	52.4	60.5	29.8	103.0	15.1
	237	157.9	0.528	126.3	52.6	61.1	29.8	103.5	15.3
	238	158.5	0.529	126.8	52.8	61.5	29.9	103.9	15.4
	239	159.1	0.530	127.3	53.0	62.0	29.9	104.4	15.5
	240	159.7	0.530	127.8	53.2	62.5	30.0	104.9	15.6
	241	160.4	0.531	128.3	53.5	63.0	30.1	105.4	15.7
	242	161.0	0.532	128.8	53.7	63.5	30.1	105.8	15.9
	243	161.6	0.533	129.3	53.9	64.0	30.2	106.3	16.0
	244	162.2	0.534	129.8	54.1	64.4	30.2	106.8	16.1
	245	162.8	0.535	130.2	54.3	64.9	30.3	107.2	16.2
	246	163.5	0.536	130.8	54.5	65.5	30.3	107.7	16.4
	247	164.1	0.537	131.3	54.7	65.9	30.4	108.2	16.5
	248	164.7	0.538	131.8	54.9	66.4	30.5	108.7	16.6
	249	165.3	0.539	132.2	55.1	66.9	30.5	109.1	16.7

	$V_F = \dot{M}_T$	V_m	n	R_0	T	ρV_m^2	\dot{R}_0	\dot{T}	$\rho \dot{V}_m^2$
	250	166.0	0.540	132.8	55.3	67.5	30.6	109.6	16.9
	251	166.6	0.541	133.3	55.5	68.0	30.6	110.1	17.0
	252	167.2	0.541	133.8	55.7	68.5	30.7	110.6	17.1
	253	167.8	0.542	134.2	55.9	69.0	30.7	111.0	17.2
	254	168.4	0.543	134.7	56.1	69.5	30.8	111.5	17.4
	255	169.1	0.544	135.3	56.4	70.0	30.8	112.0	17.5
	256	169.7	0.545	135.8	56.6	70.5	30.9	112.5	17.6
	257	170.3	0.546	136.2	56.8	71.0	30.9	112.9	17.7
	258	170.9	0.547	136.7	57.0	71.5	31.0	113.4	17.9
	259	171.5	0.547	137.2	57.2	72.0	31.0	113.9	18.0
F4	260	172.2	0.548	137.8	57.4	72.6	31.1	114.4	18.1
F5	261	172.8	0.549	138.2	57.6	73.1	31.2	114.9	18.3
	262	173.4	0.550	138.7	57.8	73.6	31.2	115.3	18.4
	263	174.0	0.551	139.2	58.0	74.1	31.3	115.8	18.5
	264	174.6	0.552	139.7	58.2	74.7	31.3	116.2	18.7
	265	175.3	0.553	140.2	58.4	75.3	31.4	116.8	18.8
	266	175.9	0.554	140.7	58.6	75.8	31.4	117.2	18.9
	267	176.5	0.554	141.2	58.8	76.3	31.5	117.7	19.1
	268	177.1	0.555	141.7	59.0	76.8	31.5	118.2	19.2
	269	177.7	0.556	142.2	59.2	77.3	31.6	118.6	19.3
	270	178.4	0.557	142.7	59.5	77.9	31.6	119.2	19.5
	271	179.0	0.558	143.2	59.7	78.5	31.7	119.6	19.6
	272	179.6	0.559	143.7	59.9	79.0	31.7	120.1	19.7
	273	180.2	0.560	144.2	60.1	79.5	31.7	120.6	19.9
	274	180.8	0.560	144.6	60.3	80.1	31.8	121.0	20.0
	275	181.4	0.561	145.1	60.5	80.6	31.8	121.5	20.1
	276	182.1	0.562	145.7	60.7	81.2	31.9	122.0	20.3
	277	182.7	0.563	146.2	60.9	81.7	31.9	122.5	20.4
F5	278	183.3	0.564	146.6	61.1	82.3	32.0	123.0	20.6
	279	183.9	0.565	147.1	61.3	82.8	32.0	123.4	20.7
	280	184.5	0.565	147.6	61.5	83.4	32.1	123.9	20.8
	281	185.1	0.566	148.1	61.7	83.9	32.1	124.4	21.0
	282	185.8	0.567	148.6	61.9	84.5	32.2	124.9	21.1
	283	186.4	0.568	149.1	62.1	85.1	32.2	125.4	21.3
	284	187.0	0.569	149.6	62.3	85.6	32.3	125.8	21.4
	285	187.6	0.569	150.1	62.5	86.2	32.3	126.3	21.5
	286	188.2	0.570	150.6	62.7	86.7	32.4	126.8	21.7
	287	188.8	0.571	151.0	62.9	87.3	32.4	127.2	21.8
	288	189.5	0.572	151.6	63.2	87.9	32.4	127.8	22.0
	289	190.1	0.573	152.1	63.4	88.5	32.5	128.3	22.1
	290	190.7	0.574	152.6	63.6	89.1	32.5	128.7	22.3
	291	191.3	0.574	153.0	63.8	89.6	32.6	129.2	22.4
	292	191.9	0.575	153.5	64.0	90.2	32.6	129.7	22.5
	293	192.5	0.576	154.0	64.2	90.8	32.7	130.1	22.7
	294	193.1	0.577	154.5	64.4	91.3	32.7	130.6	22.8
	295	193.8	0.578	155.0	64.6	92.0	32.7	131.2	23.0
	296	194.4	0.578	155.5	64.8	92.6	32.8	131.6	23.1
	297	195.0	0.579	156.0	65.0	93.1	32.8	132.1	23.3
	298	195.6	0.580	156.5	65.2	93.7	32.9	132.6	23.4
	299	196.2	0.581	157.0	65.4	94.3	32.9	133.0	23.6
	300	196.8	0.581	157.4	65.6	94.9	33.0	133.5	23.7
	301	197.4	0.582	157.9	65.8	95.4	33.0	134.0	23.8
	302	198.1	0.583	158.5	66.0	96.1	33.0	134.5	24.0
	303	198.7	0.584	159.0	66.2	96.7	33.1	135.0	24.2
	304	199.3	0.585	159.4	66.4	97.3	33.1	135.5	24.3
	305	199.9	0.585	159.9	66.6	97.9	33.2	136.0	24.5
	306	200.5	0.586	160.4	66.8	98.5	33.2	136.4	24.6
	307	201.1	0.587	160.9	67.0	99.0	33.2	136.9	24.8
	308	201.7	0.588	161.4	67.2	99.6	33.3	137.4	24.9
	309	202.3	0.588	161.8	67.4	100.2	33.3	137.8	25.0
	310	203.0	0.589	162.4	67.7	100.9	33.4	138.4	25.2
	311	203.6	0.590	162.9	67.9	101.5	33.4	138.9	25.4
	312	204.2	0.591	163.4	68.1	102.1	33.4	139.3	25.5
	313	204.8	0.591	163.8	68.3	102.7	33.5	139.8	25.7
	314	205.4	0.592	164.3	68.5	103.3	33.5	140.3	25.8
	315	206.0	0.593	164.8	68.7	103.9	33.5	140.8	26.0
	316	206.6	0.594	165.3	68.9	104.5	33.6	141.2	26.1
F5	317	207.2	0.594	165.8	69.1	105.1	33.6	141.7	26.3
F6	318	207.8	0.595	166.2	69.3	105.7	33.7	142.2	26.4

CHAPTER EIGHT

RISK COMPUTATION BY DAPPLE METHOD

(Co-authored by Robert F. Abbey, Jr.)

The DAPPLE (Damage Area Per Path Length) METHOD for calculating the probabilities of tornado risk was devised by Abbey and Fujita (1975). This method uses the Fujita - Pearson (FPP) tornado classification scheme based on intensity (F scale), path length (first P scale), and path width (second P scale).

Although the data bases of historical tornadoes are available in various publications, the new forms of data archiving listed below will be extremely useful to tornado researchers. Two major efforts are underway for the archiving of historical tornado data in the United States in "Tape" form. One is being carried out at the National Severe Storms Forecast Center (NSSFC) and the other at the University of Chicago. Parameters included in these tapes are:

NSSFC Tape (being directed by Allen D. Pearson)

- * Year, month, date, time, weather event
- * Longitudes and latitudes of beginning and ending points
- * Type of path, % on the ground, storm type and rotational sense
- * Path length and mean path width
- * Fatalities, injuries, and damage class
- * Affected states and counties
- * FPP scale

DAPPLE Tape (being directed by T. Theodore Fujita)

- * Year, month, date, and time
- * F scale
- * Fatalities and injuries
- * Affected sub-boxes identified by 1 x 1 degree, longitude and latitude boxes, each subdivided into 15-min sub-boxes
- * Path length, path types, and direction within each sub-box

These tapes may be made available to potential users at the cost of duplicating the tapes.

1. Weighted Mean F Scale

The range of windspeeds between the maximum and minimum speeds within each F scale increases from 32 mph (F0) to 57 mph (F5). It is necessary to define windspeeds which represent the center tendency value of each F-scale windspeed. For this purpose we divide one F-scale range into n equal parts of ΔF , or

$$\Delta F = \frac{1}{n} \quad (7.29)$$

where n is an arbitrary number of divisions.

By choosing $n = 10$, for example, the center F scales of successive divisions are expressed approximately by

$$\begin{aligned}
 C_1 &= F + 0.5 \Delta F \\
 C_2 &= F + 1.5 \Delta F \\
 C_3 &= F + 2.5 \Delta F \\
 &\dots\dots\dots \\
 &\dots\dots\dots \\
 C_n &= F + (n - 0.5) \Delta F
 \end{aligned} \tag{7.30}$$

where C denotes the center F scale of each division and F , an integer scale, 0, 1, 2, ... 5.

Arithmetic mean F scale is a simple average written as

$$\begin{aligned}
 \tilde{F} &= \frac{1}{n} (C_1 + C_2 + \dots + C_n) \\
 &= F + 0.5
 \end{aligned} \tag{7.31}$$

which means that this mean is the center value of each integer F -scale range.

Weighted mean F scale can be computed by multiplying a specific weighting function.

$$\bar{F} = \frac{\sum_1^n C N}{\sum_1^n N} \tag{7.32}$$

where N is a weighting function which varies with the center division, C . It is meaningful to choose N to be the number of tornadoes within each division of ΔF . N may, thus, be regarded as "spectral frequency of tornadoes".

Median F scale is defined by an equation

$$\hat{F} = F + m \Delta F$$

where

$$\sum_1^m N = \frac{1}{2} \sum_1^n N \tag{7.33}$$

which varies, like median income, according to the distribution of N within each integer F scale.

The latest results of the F -scale classification of 24,148 tornadoes between 1916 and 1977 (see Table 1.8) was used in determining the spectral distribution of tornado frequencies in Table 7.11 and Figure 7.4. Note that each integer F scale was divided into ten 0.1 fractional scales.

Table 7.11 Smoothed distribution of N, the number of tornadoes within each division of $\Delta F=0.1$. N may be regarded as a weighting function or a spectral distribution of F-scale tornadoes. Based on 1916-77 tornadoes in Table 1.8.

F 0		F 1		F 2		F 3		F 4		F 5	
C	N	C	N	C	N	C	N	C	N	C	N
0.05	125	1.05	791	2.05	823	3.05	461	4.05	117	5.05	29
0.15	290	1.15	809	2.15	807	3.15	403	4.15	102	5.15	25
0.25	410	1.25	825	2.25	785	3.25	354	4.25	89	5.25	21
0.35	500	1.35	837	2.35	761	3.35	302	4.35	78	5.35	17
0.45	565	1.45	845	2.45	732	3.45	259	4.45	68	5.45	13
0.55	621	1.55	848	2.55	698	3.55	223	4.55	57	5.55	9
0.65	665	1.65	850	2.65	663	3.65	184	4.65	48	5.65	6
0.75	706	1.75	849	2.75	621	3.75	172	4.75	41	5.75	4
0.85	738	1.85	845	2.85	574	3.85	152	4.85	37	5.85	2
0.95	768	1.95	835	2.95	521	3.95	134	4.95	33	5.95	1
Total	5388		8334		6985		2644		670		127

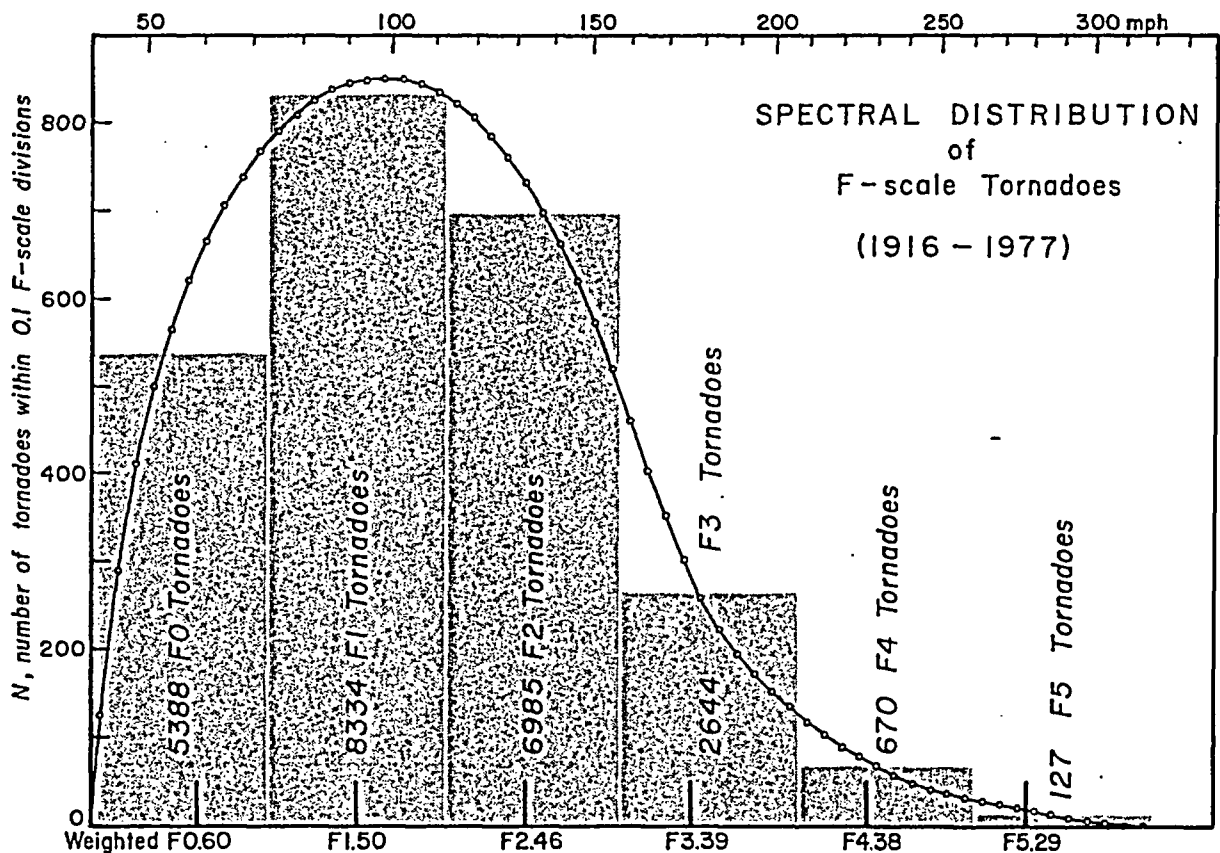


Figure 7.4 Spectral distribution of 24,148 tornadoes reported in the United States during the 62-year period ending 1977. The peak frequency is located between F 1.6 and 1.7. The distribution curve was extended to F 5.9 where N was assumed to reach zero.

Table 7.12 shows the variations of the mean values computed from Eqs. (7.31) through (7.33). It is evident that the median values as well as the weighted values are higher than arithmetic means when N increases within an integer F scale. On the other hand, the former is smaller than the latter when N decreases. For $F5$ tornadoes, for instance, the mean F scale windspeed is 290 mph. The weighted mean windspeed is 278 mph and the median windspeed is as low as 275 mph.

Mean intensities of F -scale tornadoes are important in assessing tornado risks because the use of the maximum windspeed within each F scale always results in an overestimate of the risk, while the minimum windspeed results in an underestimate. Properly, the weighted mean values should be used as the representative intensities.

Table 7.12 Three values of averaged F scale and corresponding windspeeds. Based on 1916-77 tornadoes.

F scale	Extreme values		Arith. mean		Weighted mean		Median	
	F_{min}	F_{max}	\bar{F}	V_F	\bar{F}	V_F	\hat{F}	V_F
F 0	40 mph	72 mph	0.50	56 mph	0.60	59 mph	0.63	60 mph
F 1	73	112	1.50	92	1.50	92	1.51	93
F 2	113	157	2.50	135	2.46	133	2.44	132
F 3	158	206	3.50	182	3.39	176	3.33	174
F 4	207	260	4.50	234	4.38	227	4.33	225
F 5	261	318	5.50	290	5.29	278	5.25	275

2. Definition of Damage Area

A typical area of tornado damage extends from the beginning point to the ending point (see Figure 8.1). These points vary according to the intensity of damage. In general, light to moderate damage occurs prior to the beginning and after the end of severe or devastating damage.

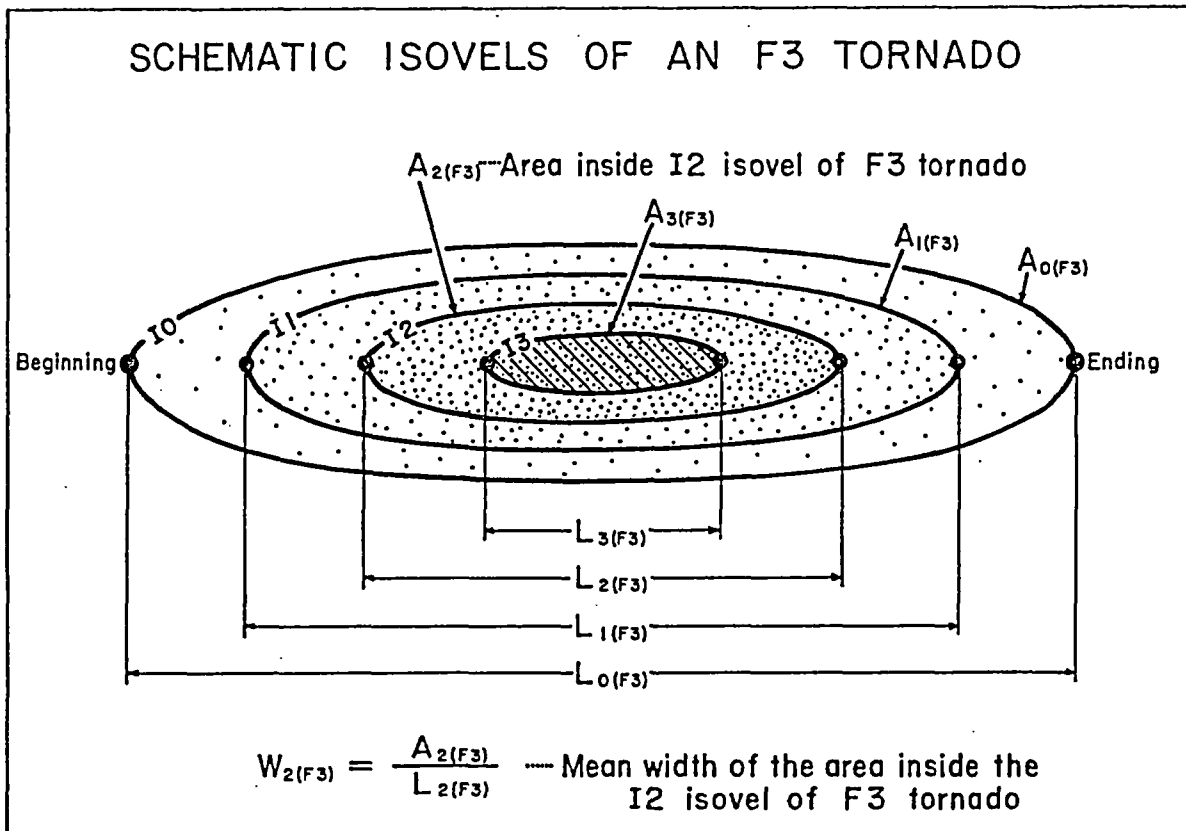


Figure 8.1 Iso-lines of maximum velocities (ISOVELS) drawn inside the damage area of an F 3 tornado. Although the selection of velocities is, more or less, arbitrary, an extensive F-scale assessment will permit us to draw isovels of F-scale windspeeds. I 2 isovel, for example, denotes that of the F 3 windspeed.

The path length, the length of the path between beginning and ending points, is a function of the intensity of damage or, in general, that of windspeed induced by a storm. As for one specific storm, the length of the F0 damage is the longest, followed by those of higher F-scale damage. The so-called path length of a tornado denotes F0 length.

If there were numerous anemometers over a tornado area measured windspeeds would permit us to draw contour lines of the maximum winds. Such a contour line is called, in this paper, the "isovel" (iso-line of the velocity of damaging wind). Commonly used, "isotach" is a line connecting points of equal windspeed usually on a synoptic chart. The use of the term "isotach" is avoided in this chapter to prevent possible confusion.

Because we do not have wind stations dense enough to measure windspeeds during the passage of a tornado, isolines of F-scale contours are probably the best possible substitute. Therefore, the available isovels are limited only to the velocities corresponding to the lowest integer F scale. These isovels are

- I0 ... isovel of the lowest F0 windspeed (40 mph)
- I1 ... isovel of the lowest F1 windspeed (73 mph)
-
-
- I5 ... isovel of the lowest F5 windspeed (261 mph).

The path lengths can now be expressed as a function of isovels. Thus, we define

- L₀ ... Length of I0 isovel
-
-

By definition, the number of isovels inside a tornado area increases with the tornado's F scale up to F plus one. For example, an F0 tornado is characterized by only one isovel, an F4 tornado by 5. Figure 8.1 shows a method of expressing various path lengths; for instance,

- L_{3(F3)} ... Length of I3 isovel area of an F3 tornado
- L_{0(F5)} ... Length of I0 isovel area of an F5 tornado.

We define, likewise, both averaged width and areas of isovels inside the area of a tornado with F-scale intensity. They are, for example,

- A_{0(F3)} ... Area inside I0 isovel of F3 tornado
- A_{1(F5)} ... Area inside I1 isovel of F5 tornado.

The averaged width of the area inside a specific isovel is defined by

$$W_x = \frac{A_x}{L_x} \tag{8.1}$$

where A and L are the area and the path length of a specific isovel; and W, the width averaged over the path length of the same specific isovel, not over the entire path length of the tornado.

3. Concept of DAPPLE

Tornado risk probabilities per year are calculated by

$$P_{I(F)} = \frac{\sum A_{I(F0 \rightarrow F5)}}{(\text{Total Area}) \times (\text{Statistical Years})} \tag{8.2}$$

where the suffix I denotes a specific isovel; A, the area inside the isovel; and P, the probability per year of the velocity designated by the isovel.

As shown in Table 8.1 there are 21 types of isovels in F0 through F5 tornadoes. The area, path length, and averaged width corresponding to each of these isovels can be expressed as a combination of I and F.

$$A_{I(F)} , L_{I(F)} , \text{ and } W_{I(F)} \quad (8.3)$$

where isovel I varies between 0 and up to 5 while F varies between 0 and 5.

Table 8.1 Twenty-one kinds of isovels to be found inside the areas of F0 through F5 tornadoes.

	F scale of tornadoes					
	F 5	F 4	F 3	F 2	F 1	F 0
Isovels	I0(F5)	I0(F4)	I0(F3)	I0(F2)	I0(F1)	I0(F0)
	I1(F5)	I1(F4)	I1(F3)	I1(F2)	I1(F1)	--
	I2(F5)	I2(F4)	I2(F3)	I2(F2)	--	--
	I3(F5)	I3(F4)	I3(F3)	--	--	--
	I4(F5)	I4(F4)	--	--	--	--
	I5(F5)	--	--	--	--	--

Using the relationship of Eq. (8.1) we rewrite the summation in Eq. (8.2) into

$$\begin{aligned} \sum A_{I(F0-F5)} &= \sum W_{I(F0)} L_{I(F0)} + \dots + \sum W_{I(F5)} L_{I(F5)} \\ &= \bar{W}_{I(F0)} \sum L_{I(F0)} + \dots + \bar{W}_{I(F5)} \sum L_{I(F5)} \end{aligned} \quad (8.4)$$

where $\bar{W}_{I(F5)}$ denotes the "mean width" of a specific isovel area of a number of F5 tornadoes. It is expected that $\bar{W}_{I(F)}$ increases with F and decreases with I so that the value can be expressed by a function of I and F,

$$\bar{W}_{I(F)} = f_A (I, F) \quad (8.5)$$

Likewise, we express the sum of the path-lengths in (8.4) by

$$\sum L_{I(F)} = \bar{\psi}_{I(F)} \sum L_{0(F)} \quad (8.6)$$

where $\bar{\psi}_{I(F)}$ denotes the "mean path factor", $L_{0(F)}$, the path length of an F-scale tornado from its I0 beginning to the I0 ending (see Figure 8.1). We also expect that the mean path factor can be expressed by another function of I and F,

$$\bar{\psi}_{I(F)} = f_B (I, F) \quad (8.7)$$

A combination of Eqs. (8.2), (8.4), (8.6), and (8.7) now permits us to write

$$P_I = \frac{\bar{W}_{I(F)} \bar{\psi}_{I(F)} \sum L_{o(F)}}{(\text{Area}) \times (\text{Year})} \quad (8.8)$$

where the product of the "mean width" and the "mean path factor" is called the "DAPPLE". Thus, we write

$$\text{DAPPLE} = \bar{W}_{I(F)} \bar{\psi}_{I(F)} = f_c(I, F) \quad (8.9)$$

which can be used for calculating the risk probabilities as a function of I and F.

For a better understanding of the DAPPLE, Eq. (8.6) and (8.9) can be combined into

$$\text{DAPPLE} = \frac{\bar{W}_{I(F)} \sum L_{I(F)}}{\sum L_{o(F)}} \quad (8.10)$$

$$= \frac{A_{I(F)}}{\sum L_{o(F)}} \quad (8.11)$$

where $A_{I(F)}$ is the total area inside a specific isovel, I, of the tornadoes rated as a specific F scale. Equation (8.11) clearly shows that DAPPLE is the area of a specific windspeed damage averaged over the "entire" path length of tornadoes.

4. Determination of DAPPLE

Although "Storm Data", the basic source of tornado data published by NOAA, includes both path lengths and widths of most tornadoes, the publication does not include sufficient information for the determination of DAPPLE. This is why the past risk assessments were dependent heavily on "tornado frequencies" and "mean damage areas" which were readily available.

Equation (8.10) indicates that we must know, in addition to F0 path length, the path length of isovel patterns corresponding to each F-scale windspeed. Likewise, the path widths as a function of isovels are also required. These data will have to be obtained through detailed surveys of tornado areas. They are:

Breakdown of Path Lengths by I and F

147 tornadoes plus one downburst on April 3-4, 1974 were surveyed in detail. The result published in April 1975 as a super-outbreak color map includes F scale values along each tornado path.

Abbey and Fujita used the color map to obtain a breakdown of damage paths by F-scale isovels for the 147 tornadoes grouped together by their intensity scale, F0 through F5. The result in Table 8.2 is, so far, the best statistical data base of the path length breakdown necessary for DAPPLE value computations.

Table 8.2 Breakdown of path lengths based on 147 Superoutbreak tornadoes. Since it was not practicable to add up the lengths of the lowest F-scale tornadoes, F scale at the top of the table represents the weighted-mean F scale. Path lengths were computed based on the isovel of the windspeed of the weighted-mean F scale.

Isovels	Windspeeds	F $\bar{5}$	F $\bar{4}$	F $\bar{3}$	F $\bar{2}$	F $\bar{1}$	F $\bar{0}$
I $\bar{0}$	59 mph	302	858	710	360	295	46 miles
I $\bar{1}$	92	233	643	486	187	91	--
I $\bar{2}$	133	203	526	356	103	--	--
I $\bar{3}$	176	155	331	187	--	--	--
I $\bar{4}$	227	86	175	--	--	--	--
I $\bar{5}$	278	39	--	--	--	--	--
Number of tornadoes		6	24	35	30	31	21

Breakdown of Path Width by I and F

Distribution of tornado winds in the direction normal to the translational velocity should also be determined through detailed aerial and ground survey. However, an assessment of the lateral distribution of damage intensities requires an extensive zigzag flight and/or driving across damage areas. This type of survey is far more time consuming than F-scale assessments of heaviest damage along the damage swath.

Making use of the surveyed damage widths of the Superoutbreak tornadoes, Abbey and Fujita (1975) obtained an empirical formula,

$$W_{\bar{1}} = 2.4^{-F} W_{\bar{0}} \quad (8.12)$$

where $W_{\bar{0}}$ denotes the width of approximately 60 mph isovel area (weighted mean F0 windspeed = 59 mph) and $W_{\bar{1}}$, the width of the isovel area of weighted mean F-scale windspeed.

$W_{\bar{0}}$ values were estimated from the outermost boundaries of 147 Superoutbreak tornadoes to compute the mean width as a function of F scale intensity. A breakdown of path width by I and F, thus computed, is shown in Table 8.3.

The analytical model of tornadoes in Chapter 6 and of tornado parameters in Chapter 7 provide us with an independent means of computing the widths of isovel areas of tornadoes. This subject will be discussed later.

Table 8.3 Breakdown of path width based on Eq. (8.12).
Both Tables (8.2) and (8.3) are from Abbey and Fujita (1975).

Isovels	Windspeeds	$F \bar{5}$	$F \bar{4}$	$F \bar{3}$	$F \bar{2}$	$F \bar{1}$	$F \bar{0}$
$I \bar{0}$	59 mph	0.487	0.457	0.366	0.185	0.062	0.028 mile
$I \bar{1}$	92	0.203	0.190	0.153	0.077	0.026	--
$I \bar{2}$	133	0.085	0.079	0.064	0.032	--	--
$I \bar{3}$	176	0.035	0.033	0.026	--	--	--
$I \bar{4}$	227	0.015	0.014	--	--	--	--
$I \bar{5}$	278	0.06	--	--	--	--	--

5. Wind Fields of Tornadoes and Embedded Suction Vortices

The maximum tangential velocity, V_m , the basic tornado parameter, can be obtained from Table 7.10 which tabulates the total maximum windspeeds at one mile per hour intervals between 40 and 318 mph. The feature of the model tornado that can be determined from parameters derived from V_m is presented in Figure 8.2.

Translational velocity, T , in the figure denotes the rate of displacement of the tornado center, from left to right. Such a translational motion is provided by the deep layer of the airflow in which a tornado vortex is embedded. This airflow--called the "steering flow"--usually decreases toward the ground, reaching theoretical "zero" at the ground. Observational evidence shows that air is usually calm before a tornado; then winds pick up suddenly to destructive levels.

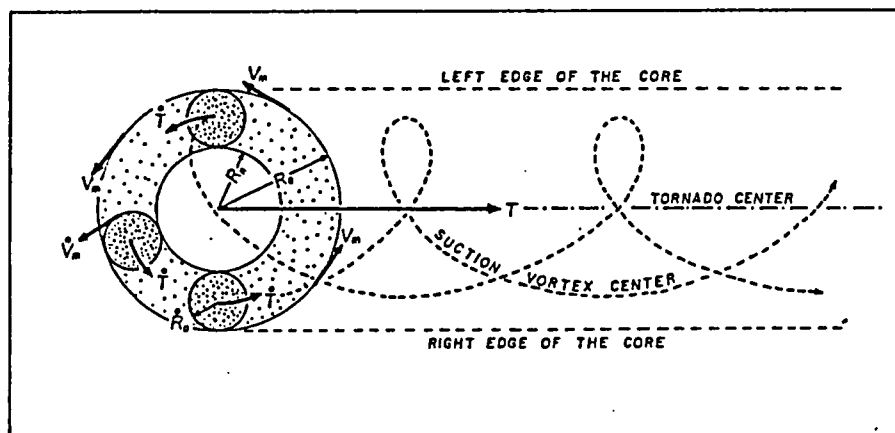


Figure 8.2 Fujita's latest model of multiple-vortex tornadoes for engineering applications. The design-basis tornado model in Chapter 6 developed in 1977 was identified as "DBT-77". Design-basis suction-vortex parameters in Chapter 7 were added to the DBT-77 in constructing this latest analytical model, to be identified as "DBT-78".

It is not reasonable, therefore, to assume that a uniform vector of T extends far away into a tornado environment. Namely, vector T must decrease with increasing radius from the tornado center.

For the purpose of further computations, the translational velocity at the level of H_i is assumed to decrease outward from the tornado center as expressed by the functions

$$T = \text{constant inside the tornado core}$$

$$T_e = T r^{-1} \quad (r = R / R_o) \quad (8.13)$$

where T_e is the vector field of the translational velocity in the tornado environment.

Based on logic similar to that of tornado environment, the translational velocity, T , outside the embedded suction vortex is expressed by

$$\dot{T} = \text{constant inside the s.v. core}$$

$$\dot{T}_e = \dot{T} \dot{r}^{-1} \quad (\dot{r} = \dot{R} / \dot{R}_o) \quad (8.14)$$

where the suffix "o" denotes suction-vortex parameter.

The maximum tangential velocity, V_m , of the model tornado occurs at H_i , the top of the inflow layer, which can be computed from Eqs. (6.2), (6.3), (6.4), (6.9) and (7.1) as a function of V_m .

Table 8.4 reveals that H_i increases from 17m or 55 ft (mean F0 tornado) to 55m or 180 ft (mean F5 tornado).

Table 8.4 H_i , heights of the maximum tangential velocities of the weighted mean tornadoes.

Tornado F scale	Weighted mean F	Corresponding velocity, \dot{M}_T	Tornado parameters			
			V_m	R_o	H_i	
F 0	0.60	59 mph	41.9 mph	34 m	17 m	55 ft
F 1	1.50	92	64.3	51	25	81
F 2	2.46	133	91.5	73	33	109
F 3	3.39	176	119.3	95	41	135
F 4	4.38	227	151.6	121	49	160
F 5	5.29	278	183.3	147	55	180

The height of the maximum tangential velocity of suction vortex is assumed to occur at the top of the inflow layer of the vortex. Thus, we use Eqs. (6.1) through (6.4), which are also applicable to tornadoes, to compute the inflow heights as a function of the core radius for suction vortices (refer to Table 7.10). Table 8.5 was obtained by using these core radii and maximum tangential velocities of suction vortices from Eq. (7.9).

Table 8.5 \dot{H}_i , heights of the maximum tangential velocities of suction vortices embedded inside the weighted mean tornadoes.

Tornado F scale	Weighted mean F	Corresponding velocity, \dot{M}_T	Suction-vortex parameters		
			\dot{V}_m	\dot{R}_o	\dot{H}_i
F $\bar{0}$	0.60	59 mph	21.0 mph	12	6 m 20 ft
F $\bar{1}$	1.50	92	32.1	17	8 28
F $\bar{2}$	2.46	133	45.8	21	11 36
F $\bar{3}$	3.39	176	59.7	26	13 42
F $\bar{4}$	4.38	227	75.8	29	15 48
F $\bar{5}$	5.29	278	91.7	32	16 52

It should be noted that the angular velocity of the spinning motion (spin rate) of suction vortex is not constant. On the other hand, the spin rate of the parent tornado from Eq. (7.1) is constant,

$$\omega = \frac{V_m}{R_o} = J^{-1} \quad (8.15)$$

where J is 0.8 when R_o is expressed in meters and V_m in mph. The numerical value and the unit of J is, therefore, 1.79 sec or

$$J^{-1} = 0.559 \text{ sec}^{-1}. \quad (8.16)$$

The spin rate of suction vortices from Eqs. (7.1), (7.3), and (7.9) is

$$\dot{\omega} = \frac{\dot{V}_m}{\dot{R}_o} = \frac{\frac{1}{2} J^{-1} R_o}{\frac{1}{2} (1-n) R_o} = (1-n)^{-1} J^{-1} \quad (8.17)$$

The computed spin rates of weighted mean tornadoes and embedded suction vortices are presented in Table 8.6. It is seen that the spin rates of suction vortices are 45 to 130% larger than their parent tornadoes. This means that the model tornado is accompanied by fast-spinning suction vortices.

Table 8.6 Spin rates of tornadoes and embedded suction vortices. From Eqs. (8.15) and (8.16)

Spin rates	Weighted mean F scale					
	F $\bar{0}$	F $\bar{1}$	F $\bar{2}$	F $\bar{3}$	F $\bar{4}$	F $\bar{5}$
Tornado (ω)	0.559	0.559	0.559	0.559	0.559	0.559 sec ⁻¹
S. vortex ($\dot{\omega}$)	0.808	0.872	0.956	1.047	1.160	1.282 sec ⁻¹

Localized Damage by Suction Vortex

By virtue of its small core radius and fast spinning motion, a suction vortex is accompanied by strong winds at a relatively low level above the surface. Figure 8.3 shows the vertical distribution of the maximum total windspeeds of the weighted mean F4 tornado and embedded suction vortex.

The maximum total windspeed of the suction vortex is 227 mph which is only 17 mph larger than the maximum total windspeed of the parent tornado. At the 15 m level, however, the tornado windspeed is only 167 mph -- 60 mph slower than that of suction vortex. This is why frame houses and mobile homes inside the suction-vortex swaths are often found to be seriously damaged.

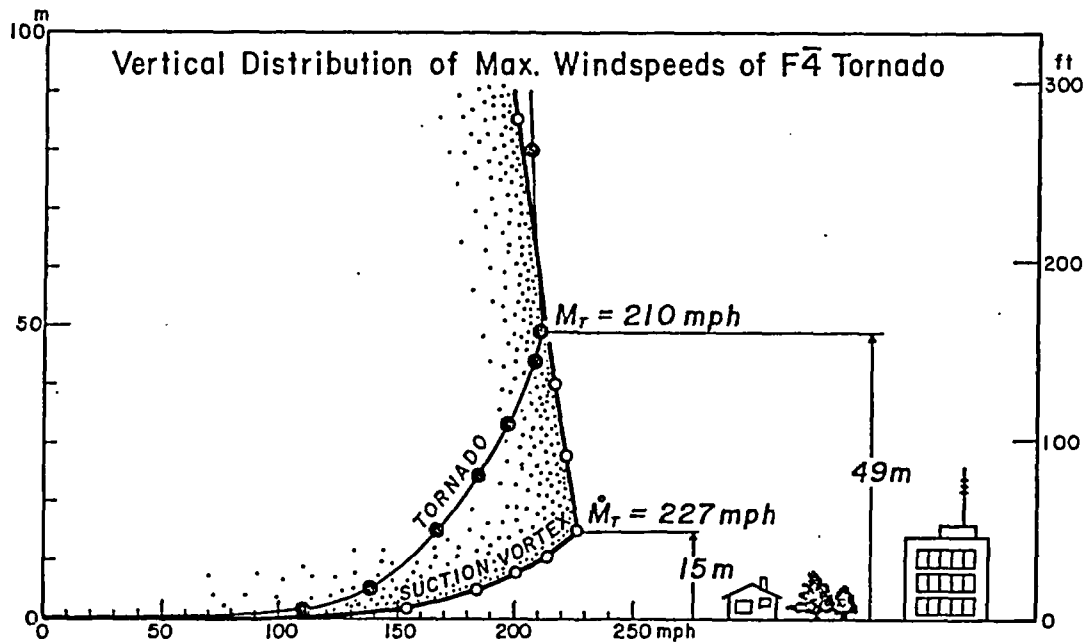


Figure 8.3 Vertical distribution of maximum total windspeeds inside tornado and embedded suction vortices. This figure shows that damaging winds of suction vortex is closer to the ground than those of the parent tornado, the maximum windspeeds of which often stay way above structure heights.

While the airflow in tornadoes can often be approximated as straight-line winds, the turning radii of the air inside suction vortices are very small. Meanwhile, the inflow air gains vertical velocity while swirling around the vortex center.

The vertical acceleration of the air at 3 m AGL, the height of frequent missile generations, is relatively small in a tornado. Inside the model suction vortices in Table 8.7, the vertical acceleration increases rapidly with the tornado's F scale, reaching the maximum value of $0.61 \times g$.

Table 8.7 Vertical acceleration of the air swirling up inside the tornado and embedded suction vortex. Vertical acceleration induced by tornado is larger than that by suction vortex, but it occurs at high level. At 3m AGL, suction vortex induces much larger vertical acceleration than tornado.

		Weighted F scale of parent tornado					
		F 0	F 1	F 2	F 3	F 4	F 5
TORNADO	Outer core, R_o	33.5	51.4	73.2	95.4	121.3	146.6 m
	Inner core, R_n	10.3	18.4	30.4	44.5	62.8	82.7 m
	Max. vert. acc. occurs at (AGL)	0.27	0.44	0.66	0.91	1.23	1.59xg
	Acc. at 3 m AGL	9.0	13.3	18.0	22.2	26.3	29.7 m
S.VORTEX	Outer core, R_o	0.11	0.12	0.12	0.12	0.13	0.14xg
	Inner core, R_n	11.6	16.4	21.4	25.5	29.2	32.0 m
	Max. vert. acc. occurs at (AGL)	2.8	4.2	5.8	7.2	8.6	9.6 m
	Acc. at 3 m AGL	0.19	0.32	0.50	0.72	1.02	1.38xg
		3.2	4.5	5.9	7.0	7.9	8.6 m
		0.19	0.27	0.33	0.39	0.48	0.61xg

Such an enormous acceleration cannot possibly be created by the so-called "buoyancy" force which may generate up to $0.1 \times g$ acceleration. The swirling air in a suction vortex is literally "sucked up" or "pushed up" by the vertical gradient of the non-hydrostatic pressure, the pressure induced by dynamical effects of atmospheric motions.

Suction vortices are likely to produce small "DAPPLES" of high-speed isovels. The patterns of isovels left behind suction vortices are complicated (see Figure 8.4).

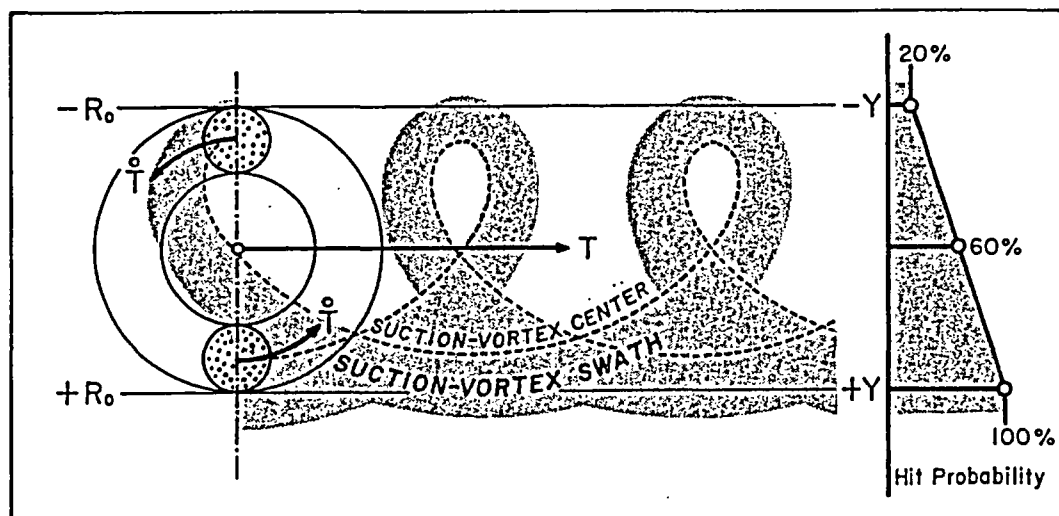


Figure 8.4 Localized swaths of suction vortices. Wind effects of suction vortices are frequently far more severe than those of the parent tornado, resulting often in so-called "skipping damage". The hit probability by suction vortices inside a tornado swath increases from $-Y$ to $+Y$.

Unfortunately, it is rare to find only one suction vortex inside a tornado. Usually 3 to 5 suction vortices swirl simultaneously around the tornado center.

A concept of "hit probability" was devised for computing DAPPLE values of suction vortices. If a structure were on the right side of the tornado at the distance $Y = +R$ in Figure 8.4, the hit probability was assumed 100% or 1.0. On the left side of the center the probability should be small. Thus we assumed

$$\begin{aligned} \sigma &= 0.2 && (Y \leq -R_0) \\ \sigma &= 0.6 + 0.4 \frac{Y}{R_0} && (-R_0 \leq Y \leq +R_0) \\ \sigma &= 1.0 && (Y \geq +R_0) \end{aligned} \quad (8.18)$$

where σ is the hit probability by suction vortices.

6. Computation of Isovel Widths from DBT-78

An analytical model, DBT-78 provides us with the tornado's wind field as a function of the maximum total velocity including embedded suction vortices. It is now feasible to compute the widths of isovel areas, abbreviated as "isovel width," based on DBT-78.

The maximum total velocity, M_θ , as defined in Figure 8.5 occurring at the outer-core boundary is computed by

$$\begin{aligned} M_\theta^2 &= (T + V_m \cos \theta)^2 + (V_m \sin \theta)^2 + W_m^2 \\ &= (1.269 + \frac{2}{3} \cos \theta) V_m^2 \end{aligned} \quad (8.19)$$

where θ is the argument of the tornado-centric vector measured from $+Y$ axis which extends toward the right of a traveling tornado. Values of T and W_m , in relation to V_m , are defined by Eqs. (7.5) and (7.14), respectively. Substituting $\cos \theta$ by Y / R_0 , we have

$$M_\theta = (1.269 + \frac{Y}{R_0})^{\frac{1}{2}} V_m \quad (8.20)$$

where Y is positive on the right side and negative on the left side of the tornado center.

The maximum total windspeeds outside the swath of tornado core can be expressed simply by

$$M_R = (V_m + T) \frac{R_o}{Y} = \frac{4}{3} \frac{R_o}{Y} V_m \quad (8.21)$$

and
$$M_L = (V_m - T) \frac{R_o}{Y} = \frac{2}{3} \frac{R_o}{Y} V_m \quad (8.22)$$

where M_R and M_L are the maximum total windspeeds on the right and on the left side, respectively. Note that both T_e and V decreased outward from tornado core inversely proportional to the distance from the tornado center.

The velocity profile at the top of the inflow level across the swath of the tornado core is shown in Figure 8.5. A jump in the velocity on the core boundary is due to the addition of vertical velocity, W_m .

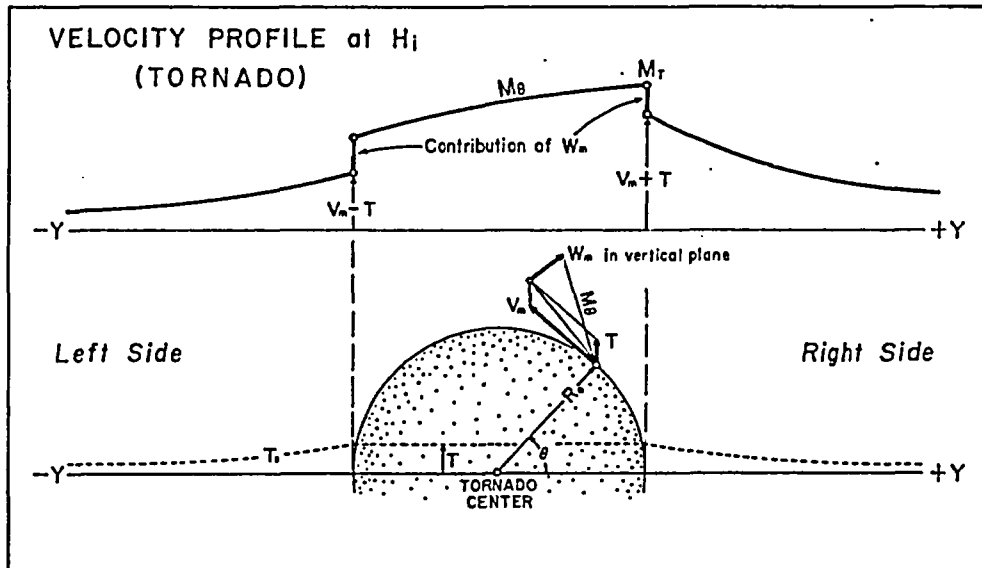


Figure 8.5 Profile of the θ -dependent maximum velocity across the path of a tornado. Isovels corresponding to various windspeeds can be computed from such a velocity profile.

A similar velocity profile for a suction vortex is presented in Figure 8.6. The maximum total velocity, in this case, includes four basic parameters,

$$\hat{V}_m = \frac{1}{2} V_m \quad \text{Eq. (7.9)}$$

$$\hat{W}_m = 0.397 \hat{V}_m \quad \text{Eq. (7.12)}$$

$$\hat{T} = \frac{3}{7} (1 + n) V_m \quad \text{Eq. (7.8)}$$

$$T = \frac{1}{3} V_m \quad \text{Eq. (7.4)}$$

The θ -dependent, maximum total velocity, M_θ can now be given by

$$\begin{aligned} \dot{M}_\theta^2 &= [(\dot{V}_m + \dot{T}) \cos \theta + T]^2 + (\dot{V}_m + \dot{T})^2 \sin^2 \theta + \dot{W}_m^2 \\ &= (K^2 + 0.269 + \frac{2}{3} K \cos \theta) V_m^2 \end{aligned} \quad (8.23)$$

$$\text{where } K = (\dot{V}_m + \dot{T}) / V_m = \frac{13}{14} + \frac{3}{7} n. \quad (8.24)$$

Substituting $\cos \theta$ by Y / R_o , we have

$$\dot{M}_\theta = (K^2 + 0.269 + \frac{2}{3} K \frac{Y}{R_o})^{\frac{1}{2}} V_m. \quad (8.25)$$

The maximum total windspeeds by suction vortex on both sides of the tornado core are expressed by

$$\dot{M}_R = (\dot{T} + T) \frac{R_o}{Y} + \frac{\dot{R}_o}{Y - \dot{E}} \dot{V}_m \quad (8.26)$$

$$\text{and } \dot{M}_L = (\dot{T} - T) \frac{R_o}{Y} - \frac{\dot{R}_o}{Y - \dot{E}} \dot{V}_m \quad (8.27)$$

where \dot{M}_R and \dot{M}_L are the maximum total windspeeds on the right and left sides, respectively.

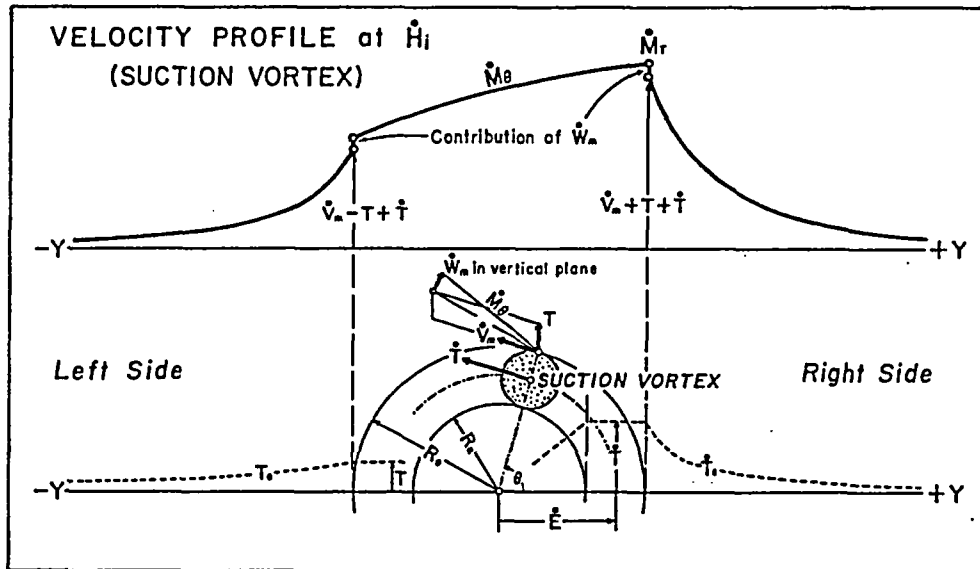


Figure 8.6 Profile of the θ -dependent maximum velocity of suction vortex. As shown in Figure 8.4, some locations inside the swath of a tornado core escape damage by the maximum velocities of suction vortices.

Equations (8.19) through (8.27) derived from the DBT-78 model will permit us to compute the isovel widths of given windspeeds. These widths, however, represent the values at the levels of the maximum total velocities which vary according to the inflow heights of tornadoes and embedded suction vortices.

Since F-scale assessments of storm damages are based primarily on trees and structures with their usual heights of 5 to 15m AGL (above ground level), isovel widths computed from DBT-78 will have to be at the heights of the objects for F-scale assessments.

10m AGL was, thus, chosen as the height for computing isovel widths. The DAPPLE values to be computed are identified as "DAPPLE at 10m AGL".

Computation of velocities at 10m AGL can be achieved by substituting V_m , W_m , T , etc. by height- and radius-dependent quantities.

When R is equal to or larger than R_o , we use Eq. (6.9) to write

$$V(r, h) = \frac{R_o}{R} F(h) V_m \quad (\text{see also Table 6.2})$$

where $F(h)$ is the height function specified by Eqs. (6.12) and (6.13). Likewise, the vertical velocity can be expressed by

$$W(\text{at } h) = 0.0442 (16 h^{\frac{7}{6}} - 7 h^{\frac{8}{3}}) \quad (\text{see Table 6.7})$$

where W is constant horizontally inside the outer core. These equations and tables are applicable also to suction vortices.

Since T_e and \dot{T}_e must reach zero at the surface, the height function of these parameters were chosen as

$$\begin{aligned} T_e(\text{at } h) &= T \frac{R_o}{R} F(h) \\ \text{and} \quad \dot{T}_e(\text{at } h) &= \dot{T} \frac{R_o}{R} F(h). \end{aligned} \quad (8.28)$$

Velocity profiles at 10m AGL computed from these equations of DBT-78 are presented in Figure 8.7. The five profiles in this figure represent those of the weighted mean tornadoes F0 through F5 with embedded suction vortices.

At 10m AGL, suction vortices induce higher windspeeds than their parent tornadoes. The difference increases with F scale, revealing that suction vortices induce a small DAPPLE of high windspeed.

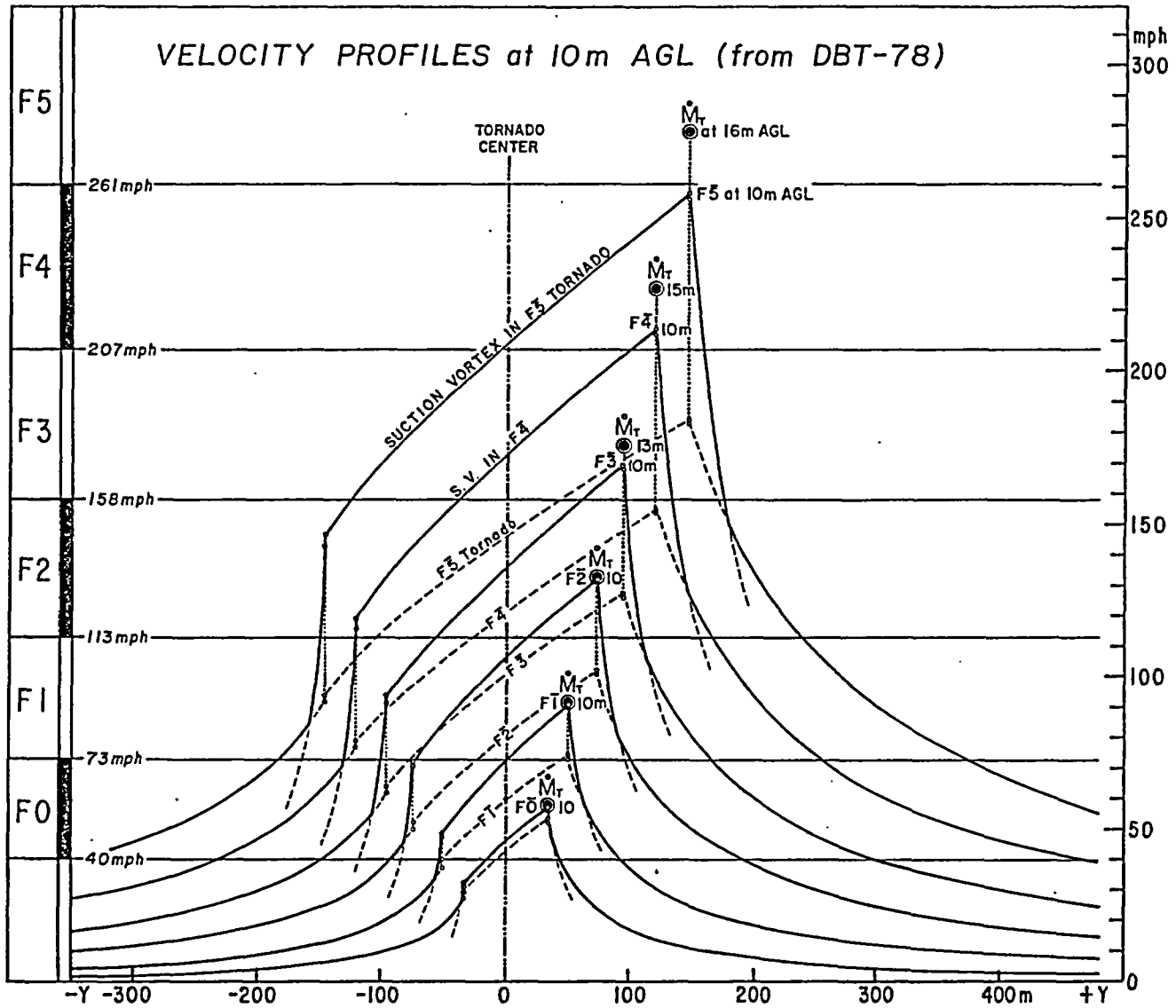


Figure 8.7 Velocity profiles of F $\bar{0}$ through F $\bar{5}$ tornadoes at 10 m AGL. Profiles were computed from equations of the DBT-78 model.

Isovel widths computed from DBT-78 are presented in Table 8.8. It should be noted that the isovel widths of the highest velocity range of each tornado category are contributed exclusively by suction vortex, not by tornado. The total isovel widths in meters and miles were computed by applying the hit probabilities. Note that isovel widths were computed for the lowest F-scale windspeeds, rather than the weighted mean F-scale windspeeds.

Table 8.8 Isovel widths of F0 through F5 tornadoes at 10m AGL. Fractional numbers in () represent the hit probability by suction vortices applicable to each width. Based on DBT-78.

Isovels	WIDTHS CAUSED BY		Total widths	
	Tornado	Suction vortex		
I5(F5)	--	--	--	--
I4(..)	--	152m(0.79), 12m(1.00)	132m	0.082mi
I3(..)	128	167 (0.49), 6 (1.00)	216	0.134
I2(..)	343	42 (0.26), 3 (0.20)	355	0.221
I1(..)	554	--	554	0.344
I0(..)	1,011	--	1,011	0.628
I4(F4)	--	21m(0.97), 2m(1.00)	22m	0.014mi
I3(..)	--	159 (0.72), 13 (1.00)	127	0.079
I2(..)	193	92 (0.36), 1 (0.20)	259	0.161
I1(..)	383	--	383	0.238
I0(..)	699	--	699	0.434
I3(F3)	--	33m(0.93), 2m(1.00)	33m	0.021mi
I2(..)	67	98 (0.58), 3 (1.00)	127	0.079
I1(..)	243	17 (0.23) 4 (0.20)	248	0.154
I0(..)	447	--	447	0.278
I2(F2)	--	58m(0.85), 3m(1.00)	52m	0.032mi
I1(..)	127	47 (0.39),	145	0.090
I0(..)	276	--	276	0.172
I1(F1)	6	43m(0.76), 5m(1.00)	44m	0.027mi
I0(..)	145	-- 2 (0.20)	145	0.090
I0(F0)	53	7m(0.74)	58m	0.036mi

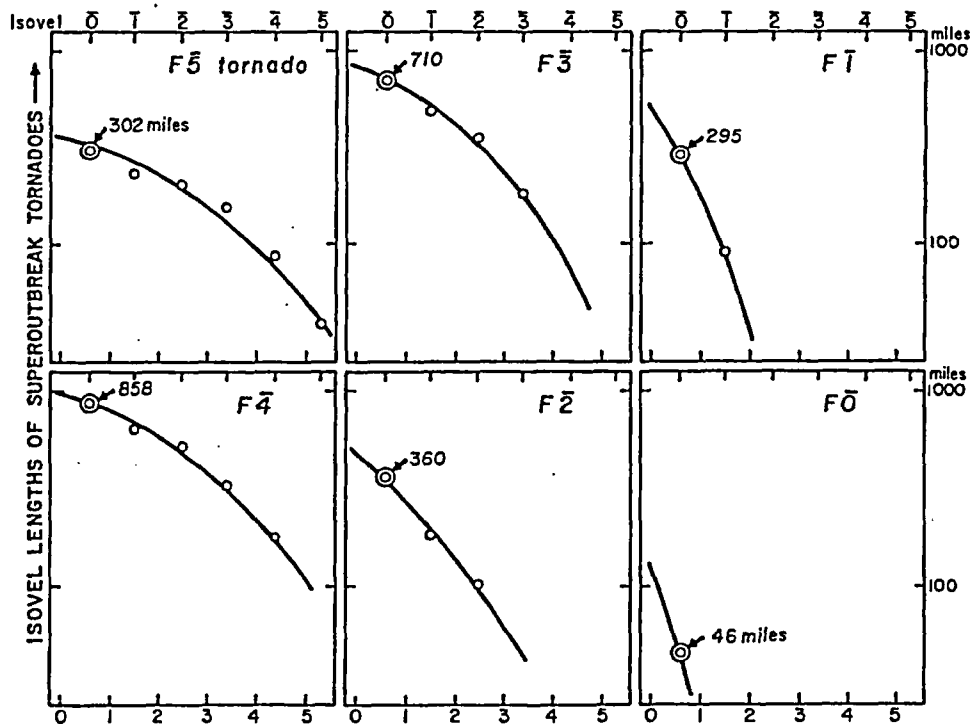


Figure 8.8 Heavy curves which represent smoothed isovel lengths of Superoutbreak tornadoes of April 3-4, 1974. Data point with mileage denote the isovel length of the I0 windspeed of F0 through F5 tornadoes (Refer to Table 8.2).

For computing isovel areas as a function of I and F, the path lengths in Table 8.2 from Abbey and Fujita (1975) were smoothed and interpolated (see Figure 8.8). Equation (8.10) was then written as

$$DAPPLE = \frac{W_{I(F)} \sum L_{I(F)}}{\sum L_{\bar{O}(F)}} \quad (8.29)$$

for use in computing DAPPLE as a function of the isovels of the lowest F-scale windspeeds and weighted mean F scale of tornadoes (see Table 8.9).

The total path length of a tornado is theoretically the isovel length of the F0 windspeed (40 mph). Survey experiences and "Storm Data" show, however, that it is not practical to determine the lengths of 40 mph isovels, because damage to trees and structures by a 40 mph wind is barely visible.

Table 8.9 DAPPLE at 10m AGL computed from smoothed and interpolated isovel lengths of Superoutbreak tornadoes and from isovel widths of DBT-78 tornadoes. **I \bar{O} denotes original value of Superoutbreak tornadoes.

Tornado F scale	Isovels I(F)	Velocities V _F	I S O V E L D A T A			DAPPLE D _F
			L _F	W _F	A _F	
F 5	**I \bar{O}	59mph	302mi			
	I 5	261	52	0.000mi	0.0mi ²	0.0000mi
	I 4	207	93	0.082	7.6	0.025
	I 3	158	155	0.134	20.8	0.069
	I 2	113	234	0.221	51.7	0.171
	I 1	73	302	0.344	103.9	0.344
	I 0	40	370	0.628	232.3	0.769
F 4	**I \bar{O}	59mph	858mi			
	I 4	207	224	0.014mi	3.1mi ²	0.0036mi
	I 3	158	380	0.079	30.0	0.035
	I 2	113	589	0.161	94.8	0.110
	I 1	73	813	0.238	193.5	0.225
	I 0	40	954	0.434	414.0	0.483
F 3	**I \bar{O}	59mph	710mi			
	I 3	158	240	0.021mi	5.0mi ²	0.007mi
	I 2	113	427	0.079	33.7	0.047
	I 1	73	631	0.154	97.2	0.137
	I 0	40	871	0.278	242.1	0.340
F 2	**I \bar{O}	59mph	360mi			
	I 2	113	141	0.032mi	4.5mi ²	0.012mi
	I 1	73	269	0.090	24.2	0.067
	I 0	40	489	0.172	84.1	0.234
F 1	**I \bar{O}	59mph	295mi			
	I 1	73	178	0.027mi	4.8mi ²	0.016mi
	I 0	40	501	0.090	45.1	0.153
F 0	**I \bar{O}	59mph	46mi			
	I 0	40	125	0.036mi	4.5mi ²	0.098mi

The so-called path lengths of tornadoes are likely to be the isovel lengths of the F0 (59 mph) winds if detailed surveys are performed. If not, the reported path lengths might represent isovel lengths of much higher windspeeds. For this reason, the DAPPLE in Eq. (8.29) was computed by using the isovel lengths of F0 damage in Table 8.2.

Finally, the DAPPLE at 10m AGL of the violent, strong, and weak tornadoes was determined by using the number of F-scale tornadoes as a weighting function (see Table 8.10).

Table 8.10. DAPPLE at 10 m AGL of violent(F5+F4), strong(F3+F2), and weak(F1+F0) tornadoes. Values from Table 8.9 were used in computing the weighted DAPPLE in this table. N, the number of tornadoes in each F category was used as weighting function.

Isovels I _F	F-scale speeds V _F	F5 tornadoes N ₅ = 127	F4 tornadoes N ₄ = 670	Violent tornadoes weighted DAPPLE
I5	261mph	0.0000mi	0.0000mi	0.0000mi
I4	207	0.025	0.0036	0.0070
I3	158	0.069	0.035	0.040
I2	113	0.171	0.110	0.120
I1	73	0.344	0.225	0.244
I0	40	0.769	0.483	0.528

Isovels I _F	F-scale speeds V _F	F3 t nadoes N ₃ = 2644	F2 tornadoes N ₂ = 6985	Strong tornadoes weighted DAPPLE
I3	158mph	0.007	0.000	0.0019
I2	113	0.047	0.012	0.0022
I1	73	0.137	0.067	0.086
I0	40	0.340	0.234	0.263

Isovels I _F	F-scale speeds V _F	F1 tornadoes N ₁ = 8334	F0 tornadoes N ₀ = 5388	Weak tornadoes weighted DAPPLE
I1	73mph	0.016	0.000	0.0097
I0	40	0.153	0.098	0.131

7. Comparison of DAPPLE Values from AF-75 and DBT-78

Path length data used in computing DAPPLE by AF-75 and DBT-78 were obtained from the superoutbreak tornadoes of April 3-4, 1978.

In computing isovel widths, AF-75 used the empirical formula of Eq. (8.12), while the isovel widths of the DBT-78 were obtained by solving analytic functions of the model. Namely, the major difference between these independent computations are the methods of estimating the isovel widths as a function of I and F.

DAPPLE values computed from these two methods were plotted in 6 graphs for comparison purposes. The results, as presented in Figure 8.9, are encouraging. In spite of a number of assumptions and inevitable uncertainties, these two independent DAPPLEs are now found to be very close indeed.

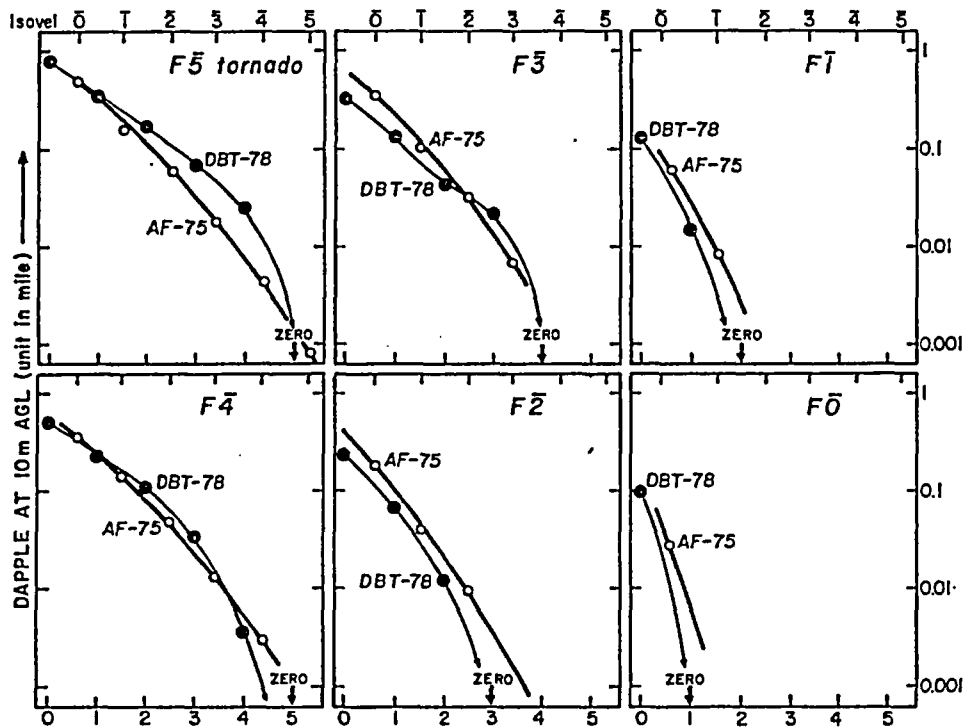


Figure 8.9 Comparison of DAPPLE values obtained by Abbey and Fujita (1975), abbreviated as AF-75, and those computed from DBT-78 model.

DAPPLE at 50-mph intervals from AF-75 has been used in assessing tornado risks at several sites in the United States. The new DAPPLE values by DBT-78 in Table 8.10 were also computed at 50-mph intervals of F-scale windspeeds and tabulated along with the AF-75 DAPPLE (see Table 8.11 and Figure 8.10).

This table reveals that the differences between these two sets of DAPPLE values are rather small, especially when windspeeds are low within each category of tornadoes. AF-75 always gives higher DAPPLE for high windspeeds because the analytic function, Eq. (8.12) becomes small but remains finite, no matter how large the input F scale may be. On the other hand, the output from DBT-78 results in "zero width" when isovel windspeeds exceed the maximum total windspeed of a specific tornado at a given height for DAPPLE computations.

Table 8.11 Comparison of DAPPLE values from Abbey and Fujita (1975) or AF-75 and those computed from DBT-78. DAPPLE from AF-75 was used by Fujita for site evaluations until August 31, 1978. The "MEAN DAPPLE" in this table will be used effective September 1, 1978.

Tornadoes in 3 categories	Maximum total windspeeds at 10 m AGL						
	50	100	150	200	250	300	318 mph
VIOLENT TORNADOES							
AF-75	0.51	0.14	0.036	0.0081	0.0016	0.00023	0.00010 mile
DBT-78	0.43	0.16	0.050	0.0101	0.00014	0.00000	0.00000
MEAN DAPPLE	0.47	0.15	0.043	0.0091	0.0009	0.00012	0.00005
STRONG TORNADOES							
AF-75	0.43	0.062	0.0098	0.0012	0.000087	--	--
DBT-78	0.19	0.035	0.0037	0.0000	0.000000	--	--
MEAN DAPPLE	0.31	0.049	0.0068	0.0006	0.000044	--	--
WEAK TORNADOES							
AF-75	0.074	0.0028	0.000052	--	--	--	--
DBT-78	0.076	0.0000	0.000000	--	--	--	--
MEAN DAPPLE	0.075	0.0014	0.000026	--	--	--	--

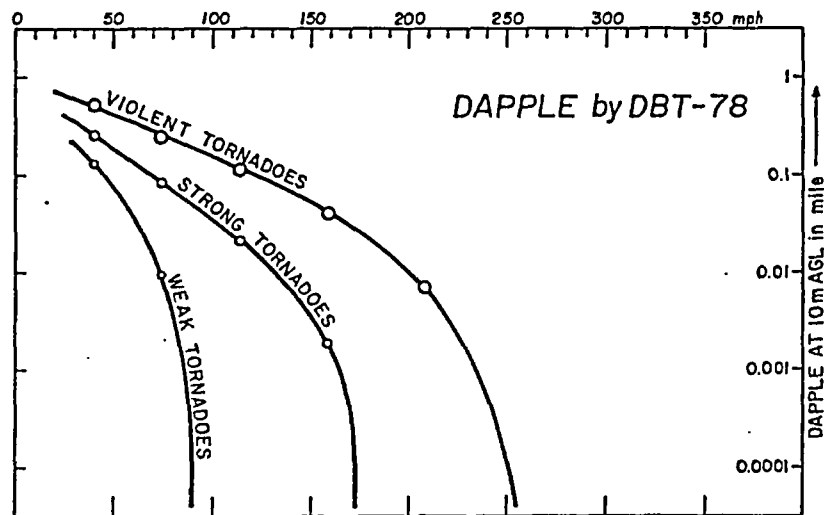


Figure 8.10 DAPPLE computed by DBT-78 as functions of the three categories of tornadoes. The three categories are: violent (F3+ F4), strong (F3+ F2), and weak (F1+ F0) tornadoes.

How can we resolve such a difference? The answer to this question may not be forthcoming soon, because it is not possible for anyone to specify the maximum possible windspeeds of tornadoes which include suction vortices.

The best possible approach, at the present time, is to use the "MEAN DAPPLE" of AF-75 and DBT-78 until further progress in DAPPLE computations is made through investigations of the wind effects of more tornadoes.

However, the present state of the art in risk computations is not as inaccurate as it may appear to be. The extremely small DAPPLE within the high velocity ranges results in the probability of the top F 5 (318 mph) windspeed as being less than 10^{-7} per year in most areas of the midwestern United States.

It may be concluded that the use of the "MEAN DAPPLE" presented in this workbook will give engineers a reasonable guideline for the structural protection needed against the extreme winds of tornadoes and embedded suction vortices.

READING LIST

1. Abbey, R. F., Jr. and T. T. Fujita (1975): Use of Tornado Path Lengths and Gradations of Damage to Assess Tornado Intensity Probabilities. Preprints, Ninth Conference on Severe Local Storms, Norman, Oklahoma, October 21-23, 286-293. Published by American Meteorological Society, Boston, Mass.

A method is presented to assess tornado hazard probabilities which empirically incorporate windspeed variation across and along the tornado path. Only approach to date that allows tornado severity to vary as a function of path length.
2. Abbey, R. F., Jr. (1977): NRC's Research Program in Severe Phenomena. Designing to Survive Severe Hazards, November 1-3, Chicago, IL, 263-287. Available from IIT Research Institute, 10 West 35th Street, Chicago, IL 60616.

Presents the severe storm research program supported by the Office of Nuclear Regulatory Research, USNRC.
3. Asp, M. O. (1963): History of Tornado Observations and Data Sources. Key to Meteor. Records Doc. No. 3.131, U. S. Weather Bureau, Washington.

Provides summary of previous attempts to describe the tornado hazard and outlines cautions which must be exercised in assessing past tornado data and histories.
4. Brinkmann, W. A. R. (1975): Severe Local Storm Hazard in the United States: A Research Assessment. Program on Technology, Environment and Man Monograph No. NSF-RA-E-75-011, Inst. of Behavioral Science, Univ. of Colorado, Boulder, Colorado.

An assessment of the current status of severe storm research in U. S. from the perspective of developing adequate warning and emergency response procedures.
5. Court, A. (1970): Tornado Incidence Maps. ESSA Tech. Memo. ERL/TM-NSSL 49, National Severe Storms Laboratory, Norman, OK.

A perceptive and witty account of 109 representations of tornado incidence listings, enumerations, graphs, and charts. Indicates limitations in past tornado data record.
6. Davies-Jones, R. P. and E. Kessler (1974): Tornadoes in Weather and Climate Modification, ed. by W. N. Hess, Wiley, N. Y., 552-595.

Provides succinct description of tornado characteristics, measurement techniques, and vortex theory through 1973. Significant advances in tornado knowledge have occurred since this article.

7. Forbes, G. S. (1978): Three Scales of Motions Associated with Tornadoes. Ph.D. dissertation, The University of Chicago, NUREG -
8. Fujita, T. T. (1971): Proposed Characterization of Tornadoes and Hurricanes by Area and Intensity. SMRP Res. Paper No. 91, Univ. of Chicago, Chicago, IL 60637, 42 pp.

This is the original paper of the F-scale classification scheme to rate tornadoes by the damage they produced. This system is being used by NOAA and the University of Chicago to assign intensity rating to all reported tornadoes in U. S.

9. Fujita, T. T. (1972): Proposed Mechanism of Suction Spots Accompanied by Tornadoes. Preprints, Seventh Conf. on Severe Local Storms, Kansas City, MO., Oct. 5-7, 1971, 208-213.

Advances theory to explain observed "suction swaths" in path of tornado damage. Later confirmed by visual observation and movie of tornadoes, laboratory model, and vortex theory.
10. Fujita, T. T. (1973): Experimental Classification of Tornadoes in FPP Scale. SMRP Res. Paper No. 98, Univ. of Chicago, IL., 15 pp.

Revises 1971 paper on the F-scale rating system by adding path length and path width, thus producing the FPP (Fujita-Pearson) scale for classifying tornado intensity and path dimensions.
11. Fujita, T. T. (1974): Jumbo Tornado Outbreak of 3 April 1974. Weatherwise, 27, 116-126.

Brief overview of the 147 tornadoes that occurred on April 3-4, 1974--the largest, single tornado outbreak in recorded history.
12. Fujita, T. T., G. S. Forbes, and T. A. Umenhofer (1976): Close-up View of 20 March 1976 Tornadoes: Sinking Cloud Tops to Suction Vortices. Weatherwise, 29, 116-131.

Report of three meteorologists who flew around thunderstorms while tornadoes were in progress. Follow-up aerial surveys revealed the swaths of suction vortices left behind by tornadoes.
13. Fujita, T. T. (1977): Anticyclonic Tornadoes. Weatherwise, 30, 51-64.

A summary of seven anticyclonic tornadoes which rotated in a direction opposite to that of other ordinary tornadoes. Several tornadoes in each year have been reported to be anticyclonic.
14. Fujita, T. T. (1978): Manual of Downburst Identification for Project NIMROD. SMRP Res. Paper No. 156, Univ. of Chicago, IL, 104 pp.

This manual includes the definition of newly identified diverging wind called downburst. Aircraft accidents and downburst/tornado interactions are discussed.

15. Golden, J. H. (1974): Life Cycle of Florida Keys' Waterspouts. NOAA Tech. Memo ERL NSSL-70. National Severe Storms Laboratory, Norman, OK.
16. Hoecker, W. H., Jr. (1960): Wind Speed and Air Flow Patterns in the Dallas Tornado of April 2, 1957. Mon. Wea. Rev., 88, 167-180.
 Classic and oft-cited paper presenting an analysis of the wind-speeds and flow field of the famous Dallas, Texas, tornado. Photogrammetric analysis techniques have improved greatly in the past 18 years, but this pioneering paper remains a significant contribution to our knowledge of tornadoes.
17. Howe, G. M. (1974): Tornado Path Sizes. J. Appl. Meteor., 13, 343-347.
 Excellent statistical analysis of tornado path area by states and regions.
18. McDonald, J. R. (1978): Tornado-Generated Missiles.
 An addendum to this workshop.
19. Mehta, K. C., et al. (1976): Tornadoes. J. Struc. Div., Proc. Am. Soc. Civil Eng., 102, 1709-1724.
20. Mehta, K. C., et al. (1975): Engineering Aspects of the Tornadoes of April 3-4, 1974. National Academy of Sciences, Washington, D. C.
21. Minor, J. E., et al. (1977): The Tornado: An Engineering-Oriented Perspective. NOAA Tech. Memo ERL NSSL-82. National Severe Storms Laboratory, Norman, OK.
 Analyses of tornado damage and inferred windspeeds from the engineering perspective. Assessments from this viewpoint are needed in order to merge near-ground tornado flow fields deduced by fluid dynamics with engineering observations made at ground level.
22. Morton, B. (1966): Geophysical Vortices. Prog. in Aeronautical Sci., 7, 145-193.
 An insightful review and synthesis of geophysical vortex theory and observations. Compares dust devils, waterspouts, and tornadoes.
23. Thom, H. C. S. (1963): Tornado Probabilities. Mon. Wea. Rev., 91, 730-736.
 As Hoecker (1960) is to tornado flow fields and windspeeds, this paper is to tornado probability assessments. However, the limited data used restricts the usefulness and general applicability to concepts and techniques rather than conclusions.

24. Symposium on Tornadoes: Assessment of Knowledge and Implications for Man, June 22-24 (1976); Lubbock, TX. Proceedings available from: Institute for Disaster Research, Texas Tech University, P. O. Box 4089, Lubbock, TX 79409.

Invaluable standard reference, defining the current state-of-knowledge on tornadoes, written by world experts in their respective fields. For the purposes of this workshop, the following should most certainly be consulted.

Windspeeds in Tornadoes

- Golden, J. H. --- An assessment of windspeeds in tornadoes, P 5 - 42.
- Fujita, T. T. --- Photogrammetric analyses of tornadoes, P 43 - 88.
- Mehta, K. G. --- Windspeed estimates: engineering analyses, P 89 - 103.

Tornado Vortex Models

- Lewellen, W. S. --- Theoretical models of the tornado vortex, P 107 - 143.

Assessment of Risk

- Abbey, R. F., Jr. --- Risk probabilities associated with tornado windspeeds, P 177 - 236.

Tornado-Structure Interaction: Engineering Implications

- Shanahan, J. A. --- Evaluation of and design for extreme tornado phenomena, P 251 - 282.
- Cermak, J. E. and R. E. Akins --- Wind load on structures, P 283 - 312.
- Gregory, W. S., et al. --- Effects of tornadoes on mechanical systems, P 313 - 328.

Tornado-generated Missiles and Their Effects

- McDonald, J. R. --- Tornado-generated missiles and their effects, P 331 - 348.
- Costello, J. F. --- Trajectories of tornado-borne missiles, P 349 - 362

S U B J E C T I N D E X

Aerial photograph	60	Funnel aloft	10
Air density	85	Gust front	
Beaufort force	3,5	definition	11
Bow echo	17	F scale	13
Buoyancy	18,19,125	parent cloud	12
Circulation	9	Hook echo	17
Computer printout coordinates		Instantaneous center	
bi-month distribution	69-74	of rotation	6
CPC map	62	Isotach	35
diurnal variation	75-82	Isovel	
1916-77 tornadoes	65	area	116,117,132
strong tornadoes	67	definition	116
violent tornadoes	68	F scale	117
weak tornadoes	66	length	116,117,131,132
Crossover height	19	width	116,117,126,127,131,132
DAPPLE		Microburst	
by AF-75	133,134,135	aerial photograph	43,44
by DBT-78	132,133,135	aircraft accidents	22
concept	117	Danville microburst	43
definition	119	definition	12
mean DAPPLE	135	F scale	13
tornado tape	16,115	Model windspeed	85
Deformation	8	NIMROD	21
Divergence	8,10	NSSFC tape	115
Doppler radar	20	Outflow	9
Downburst		Overshooting top	19
aerial photograph	27,45,46	Rotation	8,10
cloud model	19	Streak line	6
definition	12	Streamline	6
Northern Wisconsin downburst	45	Suction vortex	
observation	20	aerial pictures	27,56
tornado interaction	22,26	core radius	99,100,108-111
wind record	21	core ratio	99
Down-slope wind	11	cycloidal mark	51,52,54,121,125
Dust devil		definition	11
definition	11	formation	22
F-scale	13	hit probability	125,126
parent cloud	12	in tornado	50,121,125
Dynamic windspeed	84,85	inflow height	123
Fujita scale		inner and outer core	125
damage pictures	7	pressure change, rate of	106
downburst	13	pressure drop	104,105,108-111
gust front	11,13	revolving radius	101
median F	113	spin rate	123
spectral distribution	114	swirl pattern	55
tornado	10,13		
waterspout	13		
weighted mean	112,113		
windspeeds	5		

